BATTERY MANAGEMENT OF RECHARGEABLE ZINC-AIR BATTERIES

ANDRE LÖCHTE

A dissertation submitted to

UNIVERSIDAD
DE GRANADA

for the degree of
Doctor of Science
Doctoral Programme in Information
and Communication Technologies
(Tecnologías de la Información
y de las Comunicaciones)

SUPERVISORS:
Ignacio Rojas Ruiz
Peter Glösekötter

September 2021

Editor: Universidad de Granada. Tesis Doctorales
Autor: Andre Löchte
ISBN: 978-84-1117-173-1
URI: http://hdl.handle.net/10481/72051

ABSTRACT

The demand for energy storage is increasing massively due to the electrification of transport and the expansion of renewable energies. Current battery technologies cannot satisfy this growing demand because they are difficult to recycle, because the necessary raw materials are mined under precarious conditions, and because the energy density is insufficient. Metal-air batteries offer a high energy density because there is only one active mass inside the cell and the cathodic reaction uses the ambient air. Various metals can be used, but zinc is very promising because of its disposability, non-toxic behavior, and because operation as a secondary cell is possible. Typical characteristics of zinc-air batteries are flat charge and discharge curves. On the one hand, this is an advantage for the subsequent power electronics, which can be optimized for smaller and constant voltage ranges. On the other hand, the state determination of the system becomes more complex, since the voltage level is not sufficient to determine the state of the battery. In this context, electrochemical impedance spectroscopy is a promising candidate since the resulting impedance spectra depend on the state of charge, working point, state of aging, and temperature. Therefore, in this thesis, an electrochemical model of the zinc-air cell is developed and parameterized using measured electrochemical impedance spectra. The modification of the parameters enables to successfully determine the state of charge when the cell is being discharged and provide a charge termination detection. In addition, electrochemical impedance spectroscopy is combined with various artificial intelligence techniques to also determine successfully the state of charge during charging of the cell. Furthermore, an analysis of the oxygen consumption and the cell performance at different oxygen concentrations is performed, such that with a control of the electrolyte management a demonstrator consisting of several zinc-air cells could be successfully put into operation.

RESUMEN

La demanda de almacenamiento de energía está aumentando masivamente debido a la electrificación del transporte y la expansión de las energías renovables. Las actuales tecnologías de baterías no pueden satisfacer esta creciente demanda porque son difíciles de reciclar, porque las materias primas necesarias se extraen en condiciones precarias y porque la densidad energética es insuficiente. Las baterías metal-aire ofrecen una alta densidad energética porque sólo hay una masa activa dentro de la celda y la reacción catódica utiliza el aire del ambiente. Se pueden utilizar varios metales, pero el zinc es muy prometedor por su carácter desechable, su comportamiento no tóxico y porque es posible su funcionamiento como celda secundaria. Una característica típica de las baterías de zinc-aire son las curvas planas de carga y descarga. Por un lado, esto es una ventaja para su uso en electrónica de potencia, ya que puede optimizarse para rangos de tensión más pequeños y constantes. Por otro lado, la determinación del estado del sistema se vuelve más compleja, ya que el nivel de tensión no es suficiente para determinar el estado de la batería. En este contexto, la espectroscopia de impedancia electroquímica es un candidato prometedor, ya que los espectros de impedancia resultantes dependen del estado de carga, el punto de trabajo, el desgaste acutal y la temperatura. Por lo tanto, en esta tesis se desarrolla y parametriza un modelo electroquímico de la celda de zinc-aire utilizando los espectros de impedancia electroquímica medidos. La modificación de los parámetros permite determinar con éxito el estado de carga cuando la celda se está descargando y proporcionar una detección de ausencia de carga. Además, la espectroscopia de impedancia electroquímica se combina con varias técnicas de inteligencia artificial para determinar también con éxito el estado de carga durante la carga de la celda. Asimismo, se realiza un análisis del consumo de oxígeno y del rendimiento de la celda a diferentes concentraciones de oxígeno, de manera que, con un control de la gestión del electrolito, se podría poner en funcionamiento con éxito un moelo de demostración compuesto por varias celdas de zinc-aire.

ACKNOWLEDGMENTS

My work in the field of energy storage systems started as a student assistant under the supervision of Peter Glösekötter. I would like to thank him very much for his support, appreciation and ideas during my studies and while working on this project. Without his outstanding commitment this thesis would not have been possible.
Another person I would like to thank is Ignacio Rojas, who made difficult problems suddenly much less difficult after every discussion. A special thanks also goes to Klaus Kallis, who supported all his co-workers with great appreciation and from the bottom of his heart and who sadly passed away much too early.
Also I would like to thank all the staff of the Laboratory for Semiconductor Devices and Bus Systems and the Chair for Intelligent Microsystems, who supported and still support me with much interest. In particular, I would like to thank Ludwig Horsthemke, Daniel Heming, Marcel Gebing, Jan-Ole Thranow and Ole Gebert.
Last, but not least, I would like to thank the project partners and funding institutions. Only through the active support and valuable insights of 3e Batterie Systeme GmbH, Kunkel und Partner GmbH, EMG Automation and Stadtwerke Steinfurt the success of the projects and the cell technology is possible. Special thanks also go to the project funding Projektträger ETN, Leitmarktagentur.NRW, which is now funding the project after project number *EFRE-0800072* in a follow-up project *EFRE-0801585*, making the research possible in the first place.

Funding:

EFRE.NRW
Investitionen in Wachstum und Beschäftigung

EUROPÄISCHE UNION
Investition in unsere Zukunft
Europäischer Fonds für regionale Entwicklung

Leitmarkt Agentur.NRW

Partners:

FH MÜNSTER
University of Applied Sciences

KUNKEL+ PARTNER
MIT UNS KOMMT QUALITÄT ZUM TRAGEN

3e Batterie Systeme GmbH

EMG

Stadtwerke Steinfurt
... spürbar nah!

CONTENTS

LIST OF FIGURES

LIST OF TABLES

LISTINGS

ACRONYMS

AC Alternating Current
ADC Analog Digital Converter
ANN Artificial Neural Networks
BEV Battery Electric Vehicle
BMS Battery Management System
BUT Battery Under Test
CCCV Constant Current Constant Voltage
CNLS Complex-Nonlinear Least-Squares
DAC Digital Analog Converter
DC Direct Current
DMA Direct Memory Access
EIS Electrochemical Impedance Spectroscopy
GDE Gas Diffusion Electrode
GPIO General Purpose Input Output
IoT Internet of Things
KF Potassium Fluoride
KOH Potassium Hydroxide
LiF Lithium Fluoride
LSB Least Significant Bit
MSB Most Significant Bit

NiMH Nickel-Metal Hydride

PCA Principle Component Analysis

PCB Printed Circuit Board

PGA Programmable Gain Amplifier

PHEV Plug-in Hybrid Electric Vehicle

PTFE PolyTetraFluoroEthylene

PV Photo Voltaic

RTC Real Time Clock

RMSEP Root Mean Squared Error of Prediction

RMSE Root Mean Squared Error

S&H Sample-and-Hold

SoC State of Charge

SoH State of Health

SVR Support Vector Regression

Part I

INTRODUCTION

1 INTRODUCTION

Renewable energies depend heavily on environmental conditions. Therefore, the energy storage is a very important topic for the society. Due to high environmental impact and costly or rare materials, current battery technologies reach their limits. A promising future alternative are zinc-air secondary batteries as the zinc is the 24th most available element with an expected content of 0.02 % of materials on earth[33]. Furthermore, a high theoretical energy density of up to 888 $\frac{\mathrm{Wh}}{\mathrm{kg}}$ reinforces the high potential[102]. The two main components of the galvanic cell are zinc and oxygen which is extracted by the ambient air.
Metal air batteries provide a high energy density as the cathodic reaction uses the surrounding air. Different metals can be used but zinc is very promising due to its disposability and nontoxic behavior. Typical characteristics of zinc-air batteries are flat charging and discharging curves. On the one hand this is an advantage for the following power electronics which can be optimized for smaller voltage ranges. On the other hand, state estimation of the system becomes more complex as the voltage level is not sufficient to identify the state of the battery. A critical aspect of a Battery Management System (BMS) is state estimation. In this context, the Electrochemical Impedance Spectroscopy (EIS) tends to be a promising candidate, as the resulting spectra depend on the State of Charge (SoC), working point, State of Health (SoH), temperature and the oxygen content.

1.1 IMPORTANCE OF BATTERY TECHNOLOGY

Luigi Galvani, an Italian doctor and researcher, started the electricity revolution around 1780 in his laboratory in Bologna. He experimented with frogs' legs and noticed that muscles contract when they come into contact with copper and iron as long as copper and iron are also connected. Thus, he created an electric circuit. This consisted of two metals and the salt water in the frog's leg which works as electrolyte. The muscle contractions indicate the electric current. Although the correlations were still unclear to him, he nevertheless laid the fundamentals of the battery with his discovery. Since today, batteries are still based on the principle of converting chemical energy into electrical energy using two different electrodes and an electrolyte. Because of his discovery, this combination is also called a galvanic cell today.
Based on the galvanic cell, the Italian physicist Alessandro Volta developed his voltaic pile around 1800. Volta realized that the contracting

frog legs in Galvani's experiment had a physical basis, he then studied the contact voltage of various metals and developed the galvanic voltage series. He stacked several layers of copper and zinc plates on top of each other, as well as pieces of cardboard or leather soaked in salt water. The series connection added up the voltages and enabled real research in electricity through the first continuous current source. Together with the galvanic cell, the voltaic pile caused a boom around electricity in chemistry in the 19th century. Thus, for a long time, battery technology was the only way to perform electrical experiments. The German physicist Johann Wilhelm Ritter took the voltaic pile as a basis for his own invention in 1802. He also formed a stack for this purpose. This consisted of copper and cardboard sheets layered on top of each other and soaked in salt. This was the first rechargeable battery, because the device could be charged, discharged and electrically recharged again.
In 1854, Wilhelm Josef Sinsteden developed the first lead acid battery. Sinsteden placed two large lead plates, not touching each other, in a container filled with diluted sulfuric acid. By connecting a voltage source and frequent discharging and charging of the battery, he achieved a detectable capacity after a certain time. This process is called battery formation. Lead dioxide formed on one of the plates, and pure lead on the other. In 1859, Gaston Planté recognized the basic requirements for an effective lead-acid battery:

- The insolubility and conductivity of lead dioxide on the positive electrode, while the deposition of hydrogen on the negative electrode leaves sponge-like, metallic lead;
- changes in chemistry of the active mass during charging and discharging[70].

He therefore developed lead acid cells with a new spiral arrangement of the lead plates. Lead acid batteries are still built according to this principle in more recent times[71]. Industrial demand for ways to store electrical energy increased rapidly due to the electric generator developed by Werner von Siemens in 1866. In 1880, the lead acid battery was further improved by Camille Alphonse Faure. By coating the battery with lead powder and sulfur, the lead acid battery reached a high capacity after only a few charging cycles. This resulted in a rechargeable battery that was truly suitable for mass use. This was mainly due to the fact that lead-acid batteries are cheap to produce and could store a lot of electricity at the same time.
Lead-acid batteries are still widely used. One of the most common applications is as a vehicle starter battery. They are used for starting, lighting and ignition of vehicles. However, lead-acid batteries are also commonly found apart from cars. Figure 1.1 shows the quantity sold in tons of lead-acid batteries in Germany for the years 2009 to 2019. Applications such as uninterruptible power supplies are also

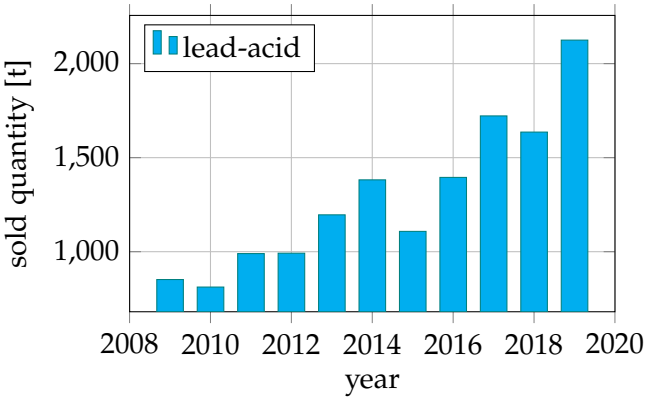

Figure 1.1: Sold quantity of lead-acid batteries as device batteries in Germany.[22]

leading to greater demand for battery technologies that are primarily stationary. Thus, the volume of lead-acid batteries sold has more than doubled in the last decade.
This was followed by the sealing of the battery, because up to this point the secondary cells still contained an electrolyte that changed during operation. The next step was taken by Waldemar Jungner in 1899, who patented the nickel-cadmium battery in that year, motivated by the idea of developing a gas-tight battery. At about the same time, Thomas Edison was also working on the nickel-cadmium battery, developing, among other things, the nickel-iron battery. By using cadmium instead of iron, Jungner was able to increase the energy and current output of his accumulator compared to Edison's predecessor. Since the electrolyte remains unchanged during charging and discharging of the battery, a gas-tight design was possible. Gas-tight cells ready for series production were available in the 1950s. This opened up new applications, such as remote controls or cordless telephones, in comparison with the lead acid battery, since portable operation was now simplified. By the 1990s, the NiCd battery had become the most widely used rechargeable battery for end users, as they could often replace alkaline-manganese primary cells[71].
A major disadvantage of nickel-cadmium batteries is the use of the toxic metal cadmium. From 1962 to 1982, Stanford Ovshinsky and Masahiko Oshitani developed the Nickel-Metal Hydride (NiMH) battery, which does not use toxic metals. This was an important step because such metals are now banned in most EU countries. As shown in Figure 1.2, the proportion of nickel-cadmium batteries sold is falling accordingly. At the same time, the number of NiMH batteries placed on the market is increasing and was about 200 times higher than nickel-cadmium batteries in Germany in 2019[50].
The general sales volume of device batteries in Germany for all battery technologies is shown in Figure 1.3. A rapidly increasing trend can be seen, the overall numbers are once again significantly higher than

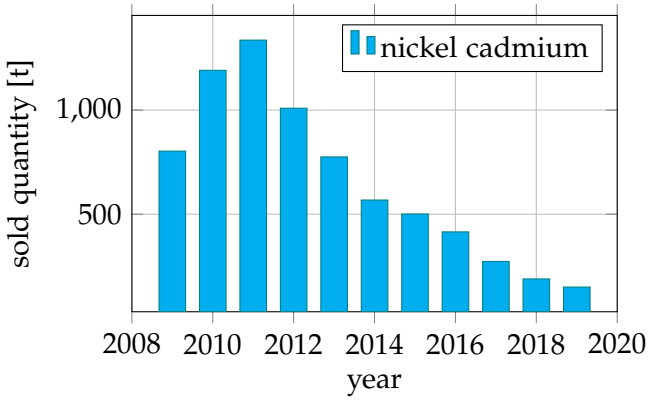

Figure 1.2: Sold quantity of nickel cadmium batteries as device batteries in Germany.[22]

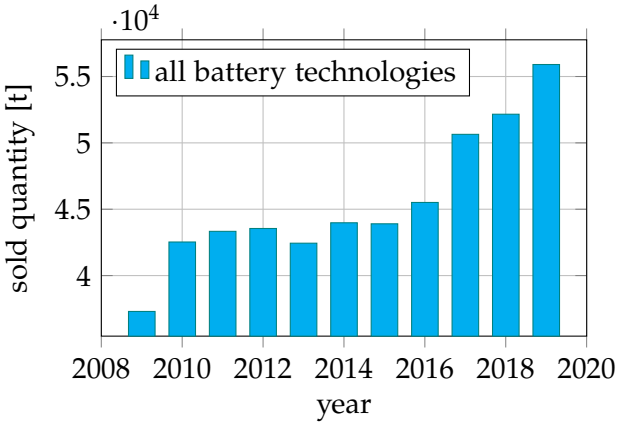

Figure 1.3: Total sold quantity of device batteries in Germany.[22]

the sum of the technologies presented so far. The reason for this is lithium-ion batteries, which were first brought to market by Sony in 1991. They offer high energy density and low weight, so lithium-ion technology currently dominates the market for device batteries. Another advantage is durability, as the technology is not based on the electrode material dissolving chemical reactions, but on the flow of lithium-ions between the anode and cathode. Lithium-ion batteries initially powered mainly portable devices with high energy requirements for which conventional nickel-cadmium or NiMH batteries were too heavy or too large, such as cell phones, digital cameras, notebooks or flashlights. They can now be found in almost all areas. They serve as energy storage for pedelecs, modern electric wheelchairs and Plug-in Hybrid Electric Vehicle (PHEV). They also established themselves early on in RC model making.
This trend is not expected to slow down, as topics such as the digitization of industry, ubiquitous computing and the Internet of Things (IoT) are only on the rise. Industry 4.0 is the name given to a future project for the comprehensive digitization of industrial production. With its

help, largely self-organized production is to become possible where people, machines, plants, logistics and products communicate and cooperate directly with each other in the Fourth Industrial Revolution. Networking will make it possible to optimize not just one production step, but an entire value chain. The network should also include all phases of the product life cycle, i.e. from the idea of a product through development, production, use and maintenance to recycling. Depending on the size, location and type of production facility, the requirements may only be possible with the help of battery-powered sensors and devices as well as with energy-autonomous systems that require a buffer battery. For example, it can be problematic to supply necessary sensor technology with power via cables because the distance is too great, because the sensor technology has no fixed location or because one would like to avoid wiring for aesthetic reasons. If necessary, an energy-autonomous setup can be made here, in which the energy is generated by solar panels or by pressure and heat differences. This often provides sufficient energy, but there are also times when the sun is not shining or the heating is switched off. Buffer batteries are therefore necessary to store the energy temporarily and still be able to work in these phases.

But digitization is also taking place in areas outside industry. As an example, Figure 1.4 shows the constantly growing number of smartphone users in Germany. Meanwhile, the use of smartphones is also increasing among older people and teenagers. The smartphone enables people to connect on the move and digitally. A similar trend can also be found in the digitization of things. In the IoT, objects are given a unique identity and can communicate with each other or accept commands. With the IoT, applications can be automated and tasks can be completed without outside intervention. Numerous applications of the IoT exist. In the private sector, the technology is used for building automation and the smart home, for example. Typical examples of applications include lighting control, alarm systems and remote monitoring, automatic heating and climate control, and smart electricity meters. Overall, the demand for battery capacity is therefore also growing outside industry.

However, Battery Electric Vehicle (BEV)s are the largest growth market for rechargeable batteries. Currently, the transportation sector within the EU is still largely based on fossil fuels and is responsible for more than 25% of Europe's greenhouse gas emissions. Excluding the Corona crisis, this share is even growing[93]. According to climate research, global warming is expected to cause sea ice and glacier melting, sea level rise, permafrost melting with the release of methane hydrate, growing drought zones, and increasing weather extremes. To some extent, the consequences are already being observed. According to current estimates, the current extinction rate of species caused by human activity exceeds the natural rate by a factor of 100 to 1000[113].

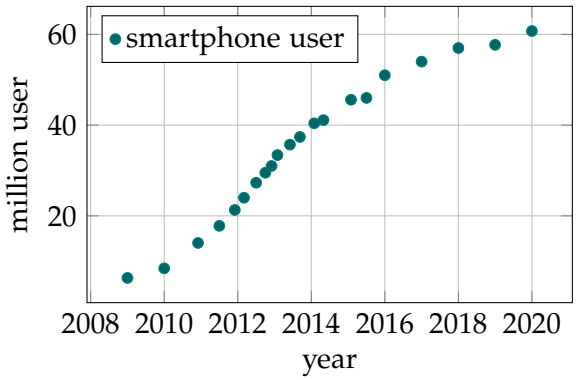

Figure 1.4: Smartphone user in Germany.[132]

In addition to global warming, vehicles with combustion engines also form a significant part contributing to air pollution. In particular, the proportion of particulate matter and nitrogen dioxide increases as a result of combustion engines[93]. As a result, driving restrictions have been imposed on high-polluting vehicles in numerous European cities[2].
Electrified or partially electrified vehicles can help here. In the case of electric cars, CO_2 emissions do not occur in the car itself, but in the generation of electricity and in the production of the BEV (the battery in particular). The level of greenhouse gas emissions over the entire vehicle life cycle therefore also depends to a large extent on the CO_2 balance of the generated electricity. Even with the current electricity mix within the EU, electric cars including batteries perform better than vehicles with internal combustion engines in terms of both energy consumption and greenhouse gas emissions when considering the entire product life cycle[93]. In addition, the climate advantage of electric cars will improve even further in the future with the expected decrease in emissions of electricity generation, so that in the future even the most inefficient electric cars will have a better climate footprint than the most efficient internal combustion vehicles. Overall, the switch to EVs will almost certainly reduce greenhouse gas emissions in most regions around the world[64]. An improvement in air quality can also be expected, as particulate emissions from electric cars are only generated to a small extent by tire abrasion and braking processes. Mechanical braking can be reduced by energy recovery systems. However, the greatest potential for reduction comes from the absence of exhaust gases from internal combustion engines, which means that no nitrogen dioxide is produced here either[69].
Even in the case of combustion vehicles, partial electrification in the form of a PHEV in combination with a battery can lead to an improvement in the environmental balance. The maximum efficiency of an Otto engine at optimum speed and load is approximately 37 %. At fixed rpm, efficiency is highest just under full load, depending heavily

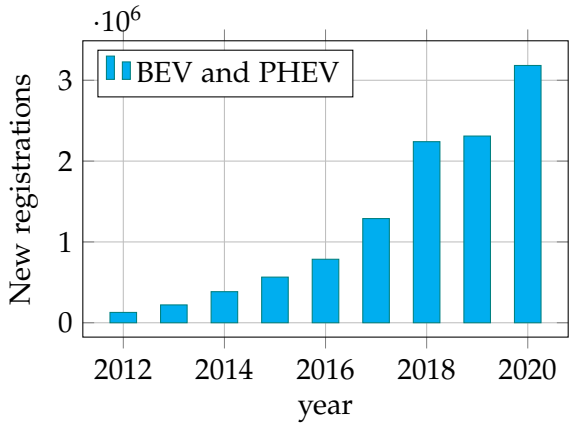

Figure 1.5: Worldwide new registrations of battery electric vehicles and plug-in hybrids (PHEV).[125].

on the load, and drops to zero by the time the engine reaches idling speed[12, 90]. Electric motors have a comparatively high efficiency of over 90 %. This remains high over a wide speed range[90]. Partial load and idling of the combustion engine occur frequently in urban traffic and can be largely avoided in PHEVs. The combustion engine can now be operated more frequently and for longer periods at high load with reasonable efficiency. The surplus energy produced is used for battery charging via a generator. During acceleration, the combustion engine and electric motor can work together, allowing a smaller combustion engine to be used. During braking and overrun, the greater part of the braking energy is recuperated in the battery. Especially in urban traffic, these recuperations help reduce consumption by up to 60 %[90].
In addition to the improved environmental footprint, tax advantages and a falling price are also leading to a growing number of BEVs worldwide, as can be seen in Figure 1.5. Along with this, the demand for battery capacity and the raw materials is also growing massively. Since electric cars mainly use lithium-ion cells, the demand for cobalt in particular is considered critical. This is because, as with many other ores, mining is partly carried out under precarious conditions. In particular, child labor in the often unsecured mines in the Democratic Republic of Congo is problematic. It is estimated that in the Congo, the country where a more than half of the world's cobalt is mined, around 20% of the cobalt is mined by hand. Complete electrification of all vehicles based on lithium-ion technology is therefore not justifiable.

The environmental footprint of BEV is particularly good when renewable electricity is used to charge the electric cars. Renewable energy sources are energy sources that are practically inexhaustible in the horizon of mankind for sustainable energy supply or are renewed relatively quickly[110, 112]. In contrast, fossil energy sources only regenerate over a period of millions of years. Uranium and other

nuclear fuels are also finite, so nuclear energy is not an alternative to fossil fuels because of limited resources[110]. Estimates are that uranium reserves will last until about 2070 if today's nuclear power plants continue to use the same amount of fuel. Furthermore, the disposal of the highly radioactive fuel elements or the residues from reprocessing is still unsecured. As of 2012, no final repository for highly radioactive materials is available worldwide[103]. Therefore, a sustainable energy policy must rely on biomass, geothermal energy, hydro power, ocean energy, solar energy and wind energy.
Since renewable energies are to a large extent not permanently available and depend, for example, on the weather, grid stability must also be considered when expanding renewable energies. For example, the locations and technical characteristics of the plants influence grid stability, and so does the quality of the grid. In addition, grid stability depends on the respective short-term power flows in the power grid, which in turn depend heavily on the weather in a renewable power supply. The grid is considered stable when frequency, voltage and angular stability are satisfied. Figure 1.6 explains these terms by comparing the time course of an unstable grid voltage with a sinusoidal curve. The period of the grid voltage differs here from the 20 ms of the sinusoidal curve. A power supply system whose frequency deviates significantly from the nominal value of 50 Hz does not meet the criterion of frequency stability. The same applies to voltage stability, too much deviation from the voltage target value (U_C) of the respective voltage level would lead to loss of voltage stability of the system. This is illustrated by the fact that the grid voltage does not reach the amplitude of the sine wave. This voltage deviation applies only to that particular location in the network being considered. At other points in the network, the voltage amplitudes may have other values at the same point in time. The voltage stability of a grid is only given if the voltage values at all points in the grid are within certain tolerance ranges around the voltage target values. Angular stability, on the other hand, is given when the angular velocity of machines (generators) connected to the grid is equal to the angular velocity of the grid voltage. The loss of this synchronism is illustrated in by a phase shift[65, 121].
While voltage stability can be maintained by distributed generation facilities and communication systems, maintaining frequency stability is more complex. So far, the rotating masses of the power generators support the grid frequency in the first moments of a power loss (frequency-response reserve). Such a power deficit can occur, for example, due to the failure of an offshore wind farm. The contribution of frequency-response reserve is not an active form of frequency maintenance, but rather a passive and essential feature of the power grid. The foreseeable absence of rotating masses raises the question of whether there will be sufficient frequency-response reserve in the

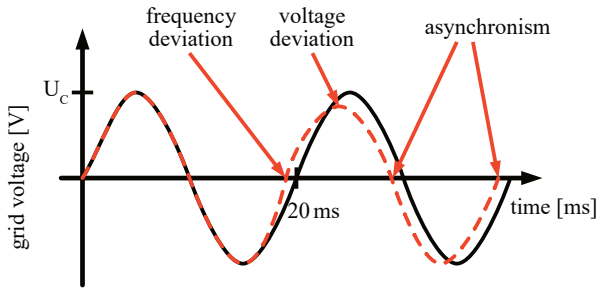

Figure 1.6: Illustration of the criteria for grid stability[65].

power system in the future, or whether the system will have sufficient inertia in the event of abrupt power plant or line failures to allow sufficient time for the deployment of spinning reserve[57, 65].
If the mismatch between consumed and generated energy exceeds the time horizon of the frequency response reserve, primary control power is used to ensure that frequency stability is not affected. If the energy demand is higher than predicted, power plants already in use are first operated at a higher working point and, if necessary, additional power plants that are in standby mode are brought online. The demand for control power that needs to be held in reserve increases with the increasing amount of weather-dependent renewable energies, whose output can only be predicted to a certain extent[38]. In principle, the possible power gradients of weather-dependent solar and wind power plants are sufficient to react quickly compared to large power plants. However, it should be noted that the availability of control power is only possible if there is sufficient wind or sun. Since the allocation of control power by weather-dependent renewable energies is only possible by throttling, free available energy remains unused, which applies to the allocation of negative and positive control power. In the case of positive control power, however, the extent is greater, since the plants must be permanently throttled in order to be able to increase output if necessary[65].
Hence, for a complete roll-out of renewable energies, alternatives for power control must also be considered in order to ensure a safe system state of the grid. Due to the fast activation and reaction time, battery systems are ideal for providing the necessary control power. The time required to provide or consume energy is mainly determined by the used power electronics and reaches full load in the range of 20 ms. This means that battery systems can provide both frequency response reserve and operating reserve. To a certain extent, it is even possible to generate the replacement reserve with batteries. In contrast, the alternatives are not as versatile. For example, pumped storage power plants require a longer period of time to start up. Flywheel storage is already more responsive, but still takes several minutes to start up and has a high self-discharge rate, so the energy is only available for a

very limited period of time[11, 56, 65]. Therefore, the energy transition can only be achieved by a massive expansion of battery storage power plants. Already today, battery storage power plants are used to a significant extent. For example, in 2017, about 700 battery storage power plants with a capacity of over 2.5 GW were in operation. The majority of these use lithium-ion batteries with the problems already described[34].

1.2 BENEFITS OF ZINC-AIR BATTERIES

As already explained in the previous chapter, lithium-ion accumulators are currently used in numerous battery applications. Especially when considering the further storage demand due to electromobility and the expansion of renewable energies, a shortage of the necessary cell materials is expected. In particular, cobalt, which is used for the production of the positive electrode, is only available on a small scale on earth and has a high toxicity. The problem is further intensified by the fact that the majority of cobalt deposits are located in countries with poor working conditions, making it difficult to switch to other suppliers. In the meantime, there are also alternative cell variants that use other materials for the positive electrode. Lithium iron phosphate batteries are a popular alternative. Although here there is no dependence on cobalt any more, the cell voltage is also reduced, so that they have a much lower energy density.
Zinc is a relatively frequent element on Earth, representing 76 ppm of the Earth's crust, making it the 24th most frequent element[48]. It is thus more common than lithium (60 ppm), cobalt (40 ppm) or lead (18 ppm)[13, 18, 48]. Consequently, the price of zinc per ton is much lower than that of lithium[44]. In addition, the deposits are distributed all over the world, so that better working conditions can be guaranteed. Large deposits exist in the United States, Canada, Australia and China, but there are also zinc deposits in Europe that are being actively mined[48]. Another major advantage of zinc is that it is completely recyclable. For example, it is estimated that in North America more than 33 % of the utilized zinc is made from recycled materials. Globally, the recycling rate is about 40 % of the produced zinc, with the recycling loops in Europe being largely closed for zinc recycling. This is mainly done with the help of the Waelz process. Therefore, a rotary kiln with a slowly rotating conveyor belt is used. The scrap passes through various zones, first being dried, then slowly heated up to 1400 °C.The zinc evaporates and can thus be extracted[59].
Another advantage of metal-air batteries and thus of zinc-air batteries as well are particularly high theoretical specific energies and theoreti-

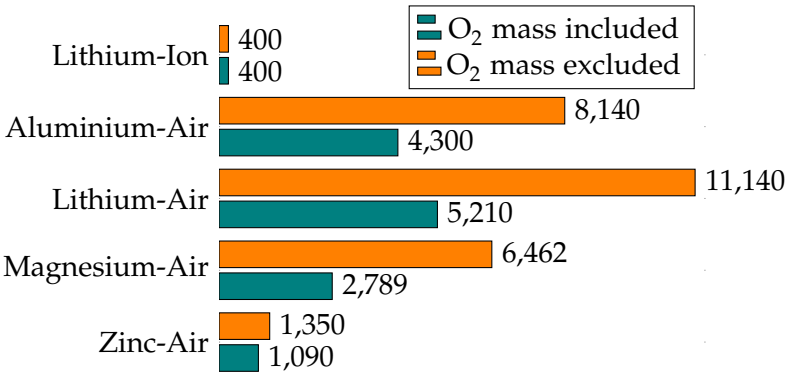

Figure 1.7: Theoretical specific energy of different battery technologies in $[\frac{\mathrm{W\,h}}{\mathrm{kg}}]$[78, 117].

cal energy densities[1, 78]. The theoretical specific energy is given by the equation

$$e = \frac{V_{\text{cell}} \cdot M_{\text{reaction}}}{\text{charge carrier transfer per mole}}, \tag{1.1}$$

where M_{reaction} is the mass of the reactants, for a substance amount of one mole. For illustration, Figure 1.7 shows the theoretical specific energies of different metal-air batteries in comparison to current battery technologies. It can be seen that the theoretical specific energy of metal-air batteries is several times higher than that of other battery technologies. For metal-air batteries, one differentiates whether the oxygen content is included or excluded in the calculation. This seems confusing at first, but is based on practical operation, since oxygen is usually used from ambient air and is not inside the cells. The lithium-air cells stand out with the highest specific energy. However, this is a primary cell technology. This means that lithium-air batteries can only be discharged once, as superoxide ions form during the discharge process and react with the electrolyte, preventing a recharge[52]. Aluminum-air batteries are also primary cells and cannot be recharged. In contrast, operation as a secondary cell is theoretically possible with magnesium-air batteries. Metallic magnesium even has the advantage that dendrite formation does not occur during the charging process. However, there are no commercial magnesium-air secondary cells yet, as research is currently being carried out on electrolytes and electrodes that work with magnesium ions[23].
Compared to the lithium-air primary cell, the theoretical specific energy of zinc-air cells is much smaller. In addition to the positive aspects of gaining raw materials, it also offers the advantage that secondary cell operation is possible. In relation to current secondary cell technologies, the theoretical specific energy is still much higher. However, it should be noted that the zinc-air battery as a secondary cell has not yet been optimized to the extent that lithium-ion technol-

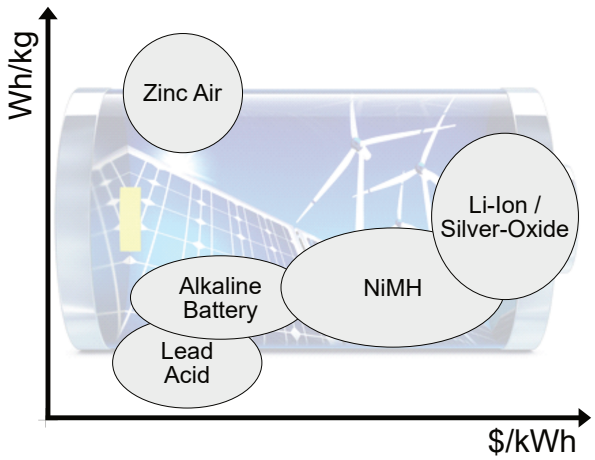

Figure 1.8: Quantitative comparison of specific energy and costs of different battery technologies[94].

ogy has. Therefore, the actual specific energies of current cells are approximately at the level of current lithium-ion cells[76].
Another advantage of the zinc-air technology is the low price. In two economic analyses by Brinker and Greßhoff, the manufacturing costs of zinc-air batteries are compared with the manufacturing costs of lithium-ion accumulators and other energy storage systems[19, 49]. Figure 1.8 gives a quantitative overview of the specific energy and the costs of different battery technologies. While the theoretical energy density of a zinc-air battery is about a factor of 2 greater than that of a lithium-ion cell, the difference in manufacturing costs is much greater. Thus, the expected production price of zinc-air in relation to the stored energy is a factor of 10 lower than that of lithium-ion cells. Since the production of zinc-air cells is not yet automated, Brinker compares the material costs of the cells. This should be a pessimistic estimate insofar as no complex processes are necessary to produce zinc-air cells. For example, no process takes place under vacuum. Cell prices alone are of course only comparable if an equal number of cycles can be guaranteed. Here, there is still a lot of potential for improvement due to the early stage of development. Nevertheless, the material price with respect to stored energy and number of cycles is already competitive with lithium-ion technology[19].

1.3 REQUIREMENT OF A BATTERY MANAGEMENT SYSTEM

Battery management systems are electronic circuits that ensure the safe state of the battery systems and monitor and control the charging and discharging processes of the batteries. Their protective functions include, for example, deep discharge protection, overcharge protection and overcurrent protection. Deep discharge protection is also necessary for lead-acid and lithium-ion batteries, as this can disable the

battery. In the case of lead-acid batteries, deep discharge can lead to sulfating of the active mass and thus to a loss of capacity. Furthermore, corrosion of the electrodes occurs due to the lower acid density. Over a longer period of time, recrystallization leads to the formation of coarsely crystalline lead sulfate, which can end in a short circuit of the cell. In lithium-ion batteries, even a slight deep discharge leads to irreversible damage and loss of capacity. In the case of a significant deep discharge, it is even likely that copper bridges will form, leading to a short circuit. In this condition, the cell becomes unstable and heats up very strongly, creating a fire hazard[9]. Deep discharge should also be avoided for zinc-air batteries. Although there is no fire hazard here, a loss of capacity, performance and lifetime is to be expected. In the charged state, the zinc anode consists mainly of metallic zinc and is therefore mechanically stable. During deep states of charge, the zinc oxidizes to zincate, which mixes within the electrolyte to form a viscous paste. Due to gravity, the anode mass now slowly sinks towards the bottom of the cell and the anode surface area decreases along with a loss of capacity and power. If the cell remains in a SoC that is too low for a longer period of time, more and more anode mass accumulates at the bottom of the cell and flows towards the counter electrode. Once this is reached, a short circuit occurs, preventing further battery operation. Therefore, zinc-air batteries must also be protected against deep discharge to ensure a long cycle life.
Overcharging can also damage batteries. When various lithium-ion batteries are overcharged, metallic lithium can be reduced and accumulated at the cathode; this can also result in the release of oxygen at the anode. In an ideal case, the produced oxygen will outgas through a safety valve. Otherwise, it reacts with the electrolyte or the anode. As a result, the accumulator heats up and can even catch fire[36, 126]. Other lithium-ion batteries such as the $LiFePO_4$ battery are thermally stable, but are also irreversibly damaged if overcharged[111]. Less critical is the electrolysis that occurs when a lead-acid battery is overcharged. The water component of the electrolyte outgasses during this process and the electrolyte level drops so that some of the anodes can no longer be used for battery operation. In an open cell, the loss of liquid can be compensated with distilled water. A similar overcharge behavior also exists for zinc-air batteries, as electrolysis starts here as well. In addition to the loss of liquid and capacity, the electrolyte concentration also increases. Typically, the initial concentration is selected to achieve maximum conductivity. The change in concentration therefore additionally leads to reduced cell performance by increasing losses. Although it is also possible with zinc-air batteries to compensate for the loss with distilled water, overcharging the cells should generally be avoided for the reasons mentioned.
So that these essential protective functions can work, the SoC of the respective cell must be known or determinable. In current cell tech-

nologies, the cell voltage is usually used for this purpose, because typically the cell voltage of an empty cell is lower than that of a full cell[101]. The Nernst equation can be used to estimate the resulting change of the open circuit voltage. The Nernst equation describes the dependence of the electrode potential of a redox couple on temperature and concentration[104, 120]:

$$E_{red} = E_{red}^{\Theta} - \frac{RT}{zF} \ln \frac{a_{Red}}{a_{Ox}} \tag{1.2}$$

Where E_{red}^{Θ} corresponds to the standard electrode potential at normal conditions, R is the universal gas constant, T specifies the absolute temperature, and z defines the number of electrons transferred in the reaction. In order to determine the voltage change due to the SoC, these variables can be considered constant. In contrast, the SoC is a key determinant of the activity of the redox partner (a_{Red} and a_{Ox}, respectively). The activity indicates the concentration corresponding to the behavior of a real mixture. As an approximation, the concentration of the reduced or oxidized species and thus the SoC can be used. The Nernst equation describes the behavior at one electrode at a time, so that the differences of both electrodes accumulate. In terms of a lead-acid battery, the voltage difference between a full and an empty cell is

$$V_{\mathrm{Pb,SoC,diff}} = V_{\mathrm{Pb}}(\mathrm{SoC} = 1) - V_{\mathrm{Pb}}(\mathrm{SoC} = 0) = 2.3\,\mathrm{V} - 1.8\,\mathrm{V} = 0.5\,\mathrm{V} \tag{1.3}$$

where $V_{\mathrm{Pb}}(\mathrm{SoC} = 1)$ is the cell voltage in the charged state and $V_{\mathrm{Pb}}(\mathrm{SoC} = 0)$ is the voltage in the empty state. Using the example of a lithium-ion battery the nominal voltage is 3.6 V, but a charging cycle of an empty battery starts at 3.4 V and finishes at 4.2 V. So that the resulting voltage difference due to the SoC is

$$\begin{aligned} V_{\mathrm{LiIon,SoC,diff}} &= V_{\mathrm{LiIon}}(\mathrm{SoC} = 1) - V_{\mathrm{LiIon}}(\mathrm{SoC} = 0) \\ &= 4.2\,\mathrm{V} - 3.4\,\mathrm{V} = 0.8\,\mathrm{V}. \end{aligned} \tag{1.4}$$

The typical regulated charging process of lead-acid batteries and lithium-ion batteries is divided into two sections by the maximum charging current and the end-of-charge voltage (see Figure 1.9). As long as the cell is still discharged enough that the end-of-charge voltage is not reached, charging takes place at a constant current. As the SoC increases, the cell voltage rises until the end-of-charge voltage is finally reached. From now on, the external cell voltage is regulated to the end-of-charge voltage. Due to the active charge current, the cell voltage measurable from the outside is not the current redox potential of the cell in no-load operation, but the voltage of the internal resistance V_{R_i} is also added to it. The resulting charge current I_{ch} in this section is therefore calculated as

$$I_{\mathrm{ch}} = \frac{(V_{\mathrm{cell}} - E_{red})}{R_i}. \tag{1.5}$$

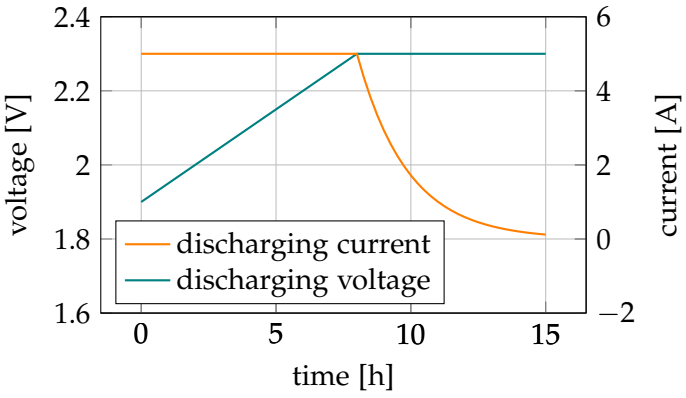

Figure 1.9: Qualitative illustration of a constant current - constant voltage charging process.

Since the redox potential in the open circuit increases with the SoC, the charge current becomes smaller and smaller. After it drops below a threshold value, the cell is considered to be fully charged. The discharge behavior is normally not controlled, since the discharge current depends on the application. To prevent deep discharge, the cell voltage is prevented from falling below the end-of-discharge voltage.
In both lead-acid batteries and lithium-ion cells, the voltage differences are therefore sufficiently high to enable simple detection of the SoC. In individual variants of lithium-ion batteries, the voltage difference can already be reduced in some areas. Lithium iron phosphate batteries, for example, show only a slight change in cell voltage in the state-of-charge range between 10 % and 90 % during both charging and discharging, making it difficult to determine the SoC.
When analyzing zinc-air batteries, the change in cell voltage as a function of the SoC is even less significant. Usually zinc-air batteries use oxygen from the ambient air. The amount of oxygen consumed during discharging or the amount released during charging is relatively small compared to the amount of oxygen in the air and therefore has only a very small influence on the partial pressure of oxygen in the ambient air. The redox potential of the air electrode therefore shows almost no dependence on the SoC of the cell. Instead, only the zinc anode contributes to the change in open circuit voltage. Applying the Nernst equation to the zinc anode, the activity of the oxidation partner can be assumed to be a constant concentration of Potassium Hydroxide (KOH) solution c_{KOH}. In contrast, the chemical activity of the reduction partner is strongly influenced by the SoC, as it is the ratio x_{ZnO} of zincate to zinc:

$$E_{red,ZnAir,anode} = E^{\Theta}_{red,ZnAir,anode} - \frac{RT}{zF} \ln \frac{x_{ZnO}}{c_{KOH}}. \tag{1.6}$$

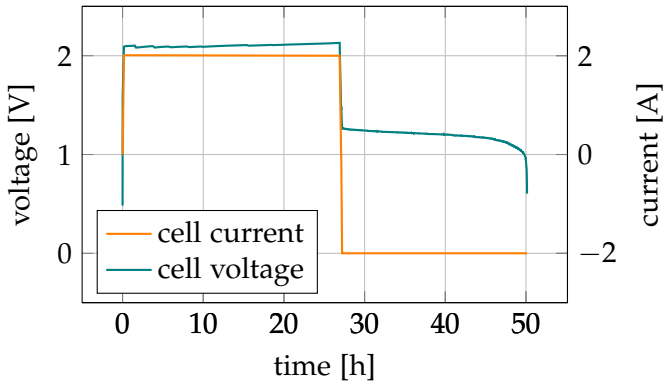

Figure 1.10: Successive charging and discharging of a zinc-air battery with constant current.

Unfortunately, the resulting impact is not very distinct as the redox potential difference between a fully charged and a nearly empty battery is about

$$\begin{aligned} V_{\text{ZnAir,SoC,diff}} &= E_{red,ZnAir,anode}(x_{ZnO} \to 0) - E_{red,ZnAir,anode}(x_{ZnO} = 1) \\ V_{\text{ZnAir,SoC,diff}} &\sim 60\,\text{mV}. \end{aligned} \tag{1.7}$$

The influence of the SoC is thus an order of magnitude smaller than with traditional technologies. In particular, the temperature and possible aging of the cell and especially of the electrolyte have a stronger effect on the cell voltage than the SoC. It is therefore not possible to determine the SoC from the open-circuit voltage of a zinc-air cell. Figure 1.10 shows the cell voltage of a zinc-air cell during an active charge and discharge cycle. Both the charging process and the discharging process are performed with a constant current. Even with an active charge current, the change in cell voltage over the charge cycle is so small that neither state-of-charge detection nor effective end-of-charge detection is possible from the cell voltage. In addition, it is problematic that towards the end of the charging process an accompanying electrolysis process starts at a similar voltage level, so that overcharging with gassing cannot be detected either. The voltage characteristic during the discharge process is also largely constant. Towards the end of the discharge process, however, there is a voltage drop, so that at least deep discharge detection is possible with the aid of a conventional voltage threshold. While SoC detection is very difficult this way, the behavior on the other hand has the advantage that applications using a zinc-air cell can be optimized for very constant voltage ranges.
In this work, therefore, the question is answered whether it is possible to develop a BMS based on zinc-air batteries with the help of alternative methods. First, an electrochemical model of the cell is developed to evaluate potential measurement methods. Furthermore, parasitic

effects that occur during the operation of zinc-air cells are investigated and the influence is classified. For critical effects, possible solutions are shown in order to treat them. For the reasons mentioned above, the most important sub-aspect is the determination of the SoC of the zinc-air cell. EIS turned out to be a promising measurement technique to obtain measurement data which depend on the SoC. Due to the special electrode arrangement of the used zinc-air cells, an adapted measurement hardware is presented. The acquired measurement data are then combined with different regression methods to determine the SoC as accurately as possible. In addition to the traditional fitting of the created electrochemical battery model, artificial intelligence methods are also applied.

Part II

THEORETICAL ASPECTS

2

THEORETICAL BACKGROUND OF BATTERIES

The first part of this chapter explains the basic structure, operation and behavior of conventional batteries. In addition, the advantages and disadvantages of the respective technology are pointed out. This is followed by a detailed description of zinc-air batteries. In addition to the structure of the cell and the description of the different cell components involved, the chemical reactions are also described and an overview of the current state of research is given. Finally, a description is given of the cell which is used to complete the research in this document.

2.1 CONVENTIONAL BATTERIES

Batteries are devices that allow the transformation of chemical energy into electrical energy. Typically these devices have got two terminals that are formed by the anode and the cathode, respectively. Batteries can be split into different groups. On the one hand, there are primary batteries that can be discharged only once. After assembling they are charged, but the electrochemical reactions that occur while discharging the battery are not reversible. On the other hand, there are secondary batteries that can be charged and discharged many times. Typically, these type of cell is more expensive than primary cells, but the total cost of a lifetime powering an electronic device is much lower since they can be charged inexpensively quite often.
In general, any combination of two different electrodes and an electrolyte is called a galvanic element. Figure 2.1 illustrates such a galvanic element. The function of the galvanic cell is based on a redox reaction. Reduction and oxidation take place physically separated each in a half cell (half element). When both electrodes are connected to each other via an electrical conductor, the different redox potentials of the electrodes ensure that the reaction can continue. Since the redox potential of the more noble metal is higher, more ions go into solution at the electrode of the less noble metal than at the other electrode. The electron gas remains in the electrode. Therefore, the negative charge of the base electrode is higher than the charge in the noble electrode, so a voltage is created where the electrons are "pushed" towards the noble electrode. This causes the dissolution of the noble atoms in the electrolyte to stop, instead the arriving electrons react with the ions of the noble electrolyte solution and cause them to attach to the noble electrode as normal atoms. The noble electrode is thus the cathode (electrode at which reduction takes place) and the positive pole of the

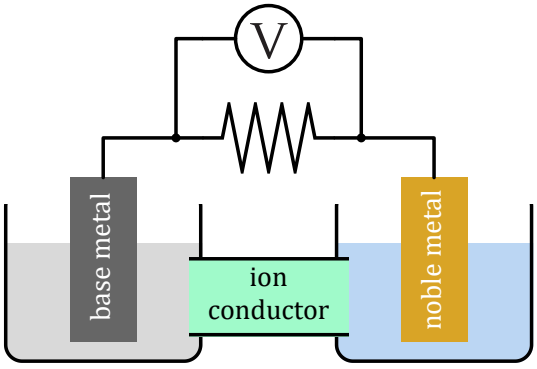

Figure 2.1: Galvanic cell

galvanic cell (absence of electrons). At the base electrode, on the other hand, oxidation takes place. The base electrode is therefore the anode and the negative pole of the galvanic cell (surplus of electrons). The electrode regions are connected to each other by an ion bridge (salt bridge), which is necessary to close the circuit. During the charging process of secondary cells, the chemical reactions at the poles are reversed: oxidation takes place at the positive pole, which is why it then functions differently as the anode - accordingly, the negative pole is then the site of reduction and thus the cathode[99]. The resulting voltage of the electric current can be calculated by the Nernst equation

$$\Delta E = \Delta E^0 - \frac{RT}{nF} \ln Q, \tag{2.1}$$

where Q depends on the activities (concentrations) of the reactants. Therefore, the voltage depends on the type of metal (ΔE^0) and the concentration[104]:

2.1.1 *Lead-Acid Battery*

The structure of a lead acid battery is shown in Figure 2.2. A lead acid battery consists of an housing and two lead plates or groups of plates, one of them serving as a positive electrode and the other as a negative electrode, and a filling of 37 % sulfuric acid (H_2SO_4) as electrolyte[71, 118]. The ground electrode made of Pb-PbO paste in the lead grid at the negative pole has a high hydrogen overvoltage, so that gassing occurs only when the cell is overcharged. The use of 0.5% barium sulfate forms crystallization seeds for $PbSO_4$, which should act against sulfation[71]. In order for the plates to be as close together as possible, there are separators between them, for example made of polyvinyl chloride, which prevent the electrodes from touching each other directly and thus preventing a short circuit[118].
The principle of operation of the lead acid battery can be illustrated by

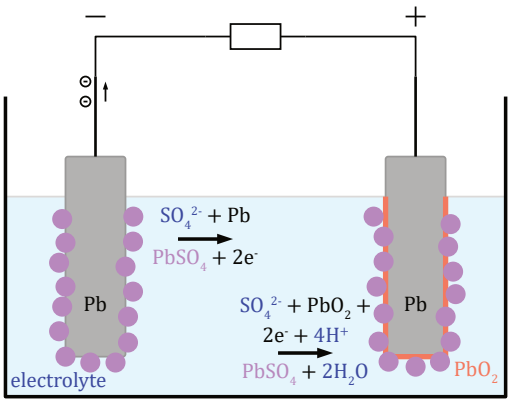

Figure 2.2: Structure of lead-acid cell.

the chemical processes that take place during charging and discharging. During discharge, the process

$$\mathrm{Pb} + \mathrm{SO_4}^{2-} \longrightarrow \mathrm{PbSO_4} + 2\,\mathrm{e}^- \tag{2.2}$$

takes place at the negative pole. Lead is oxidized with the electrolyte to lead sulfate, releasing 2 electrons. Lead sulfate is also formed at the positive electrode with the bonding of sulfuric acid in the reaction

$$\mathrm{PbO_2} + \mathrm{SO_4}^{2-} + 4\,\mathrm{H}^+ + 2\,\mathrm{e}^- \longrightarrow \mathrm{PbSO_4} + 2\,\mathrm{H_2O}. \tag{2.3}$$

But this time by a reduction of lead oxide. The formed lead sulfate deposits as a coating on the electrodes and to some extent also on the bottom of the housing. Since the sulfuric acid is utilized during the discharge process, the SoC can be determined by measuring the density of the electrolyte.
During charging, the processes take place in the opposite direction, so that the lead sulfate formed during discharging is oxidized to lead and reduced lead oxide, respectively. If the lead sulfate is completely consumed and the charging process is not stopped, electrolysis of the electrolyte begins. The cell gases hydrogen and oxygen. Sealed batteries have catalysts (Pd, Pt) above the vent where oxyhydrogen gas can recombine to water[71].
The resulting cell voltage can be determined from the galvanic series. For the two reactions, the redox potentials are at

$$\mathrm{Pb} + \mathrm{SO_4}^{2-} \longrightarrow \mathrm{PbSO_4} + 2\,\mathrm{e}^- \,|\, -0.36\,\mathrm{V} \tag{2.4}$$

$$\mathrm{PbO_2} + \mathrm{SO_4}^{2-} + 4\,\mathrm{H}^+ + 2\,\mathrm{e}^- \longrightarrow \mathrm{PbSO_4} + 2\,\mathrm{H_2O}\,|1.68\,\mathrm{V} \tag{2.5}$$

resulting in a total cell voltage of

$$E^0_{tot} = 1.68\,\mathrm{V} - (-0.36\,\mathrm{V}) = 2.04\,\mathrm{V}. \tag{2.6}$$

The nominal voltage of a cell is about 2 V, but the voltage varies between approximately 1.75 V and 2.4 V depending on the SoC and the charging or discharging current[99, 118]. The specific energy is about 35 $\frac{\mathrm{Wh}}{\mathrm{kg}}$ to 50 $\frac{\mathrm{Wh}}{\mathrm{kg}}$ and can thus be classified as low[71]. Lead acid batteries can deliver high currents for short periods, so they have a high power density. This property is for example necessary for vehicle and starter batteries, and is part of the lead acid battery's strength. On the other hand, because of this property, short circuits lead to extremely high currents, which may cause fires of the wiring.
Lead-acid batteries can achieve quite a long lifetime of several years. However, the voltage regulation is crucial here. Especially in cars as a starter battery, this is often insufficiently accurate, so that only 2 to 4 years of use are typical. Drive batteries or storage batteries can achieve a lifetime of between 5 and 15 years, depending on quality and stress. When lead acid batteries are of the same capacity and size, but of different weights, the heavier battery usually lasts longer because the lead frames are stronger. The power rating when new is not directly affected by this, as a weaker lead structure can also be designed with a large active surface area. The aging of lead acid batteries is mainly caused by internal corrosion of the lead structure of the electrodes, by the formation of fine short circuits and by sulfating of the lead. Sulfating causes the $PbSO_4$ crystals to cluster together into larger and larger compounds. Thus, the electrochemically active surface area of the $PbSO_4$ decreases and it gradually dissolves less easily. In addition, the electrical conductivity of the sulfate is lower than that of lead. The resulting increase in the internal resistance of the cell leads to a greater voltage drop under load[32].
When lead-acid batteries are recycled, they are first chopped up in several stages and separated by material. Components such as grid metal, lead paste and sulfuric acid are then treated differently. The lead is found in the grid metal and in the lead paste. The grid metal and the paste are separated in a processing plant. The paste is desulfurized and recycled into lead in a Metallurgy process. The lead quality is then sufficiently high to use it again for batteries. Sulfuric acid represents about 10 % of the weight of a battery. The acid can be separated and serves as a raw material for the chemical industry. The recycling rate of lead-acid batteries reaches almost 100 % in Germany. However, the recycling of old lead-acid batteries in developing countries is a risk to health and the environment, as the lead is recovered by hand[22, 60].

2.1.2 *Nickel-Metal Hydride Battery*

A NiMH battery is an accumulator with a positive electrode made of nickel hydroxide and a negative electrode made of a metal hydride. Like NiCd batteries, they have a nominal voltage of 1.2 V per cell with a typical end-of-discharge voltage of 1 V. Nevertheless, they are

widely used as a replacement for alkaline batteries, which have 1.5 V nominal voltage per cell, in many applications and are commonly found in standard battery designs. In some applications, however, the lower nominal voltage can be a disadvantage. For example, unregulated lights that are designed for 1.5 V operation tend to shine less brightly. Compared to alkaline batteries, the internal resistance of NiMH batteries is much lower. Because of this, they have the advantage that a higher voltage can be maintained under high load.
The layer structure of a NiMH round cell can be seen in Figure 2.3. An outer perforated foil serves as a carrier for the metal hydride powder, which forms the negative electrode. During discharge, the hydrogen bound in the metal hydride M^+H^- is oxidized to a H^+ proton and a metal of 0 oxidation state is formed:

$$MH + OH^- \longrightarrow M + H_2O + e^- \tag{2.7}$$

The resulting protons react with the OH^- hydroxide ions of the KOH solution to form water. The redox potential at a electrolyte pH value of 14 is approximately $-0.83\,V$. The separator holds the electrolyte, a 20 % KOH solution, and prevents direct contact with the positive electrode. This consists of a sheet of nickel hydroxide and black nickel oxide hydrate. Here, nickel of oxidation state +III is reduced to nickel of oxidation state +II in the reaction

$$NiO(OH) + H_2O + e^- \longrightarrow Ni(OH)_2 + OH^-. \tag{2.8}$$

During this process, free electrons are bound so that this pole becomes the positive electrode. The redox voltage of the reduction is approximately 0.49 V. The total voltage of the redox reaction is thus

$$E^o_{\text{tot,NiMH}} = 0.49\,V - (-0.83\,V) = 1.32\,V. \tag{2.9}$$

The foil combination is now wound up to ensure a high active surface area with minimal volume. The negative electrode is on the outside so that it can be directly encased in a metal cylinder. The outer casing thus forms the negative contact. An electrical connection from the nickel oxide sheet leads to the head of the cell and forms the positive pole[41, 42, 66].
The specific energy of a NiMH cell is about 80 $\frac{Wh}{kg}$, which is almost as high as that of an alkali-manganese cell and more than twice as high as that of a NiCd battery. NiMH batteries are sensitive to overcharging, overheating, incorrect polarity and, if the capacity of the electrodes is symmetrical, also to deep discharge. To prevent the metal from oxidizing instead of the hydrogen towards the end of the discharge, a negative electrode is used which is much larger than the positive electrode. The latter thus determines the capacity of the battery. This prevents the battery from being destroyed by a deep discharge. The discharge process of NiMH cells is therefore not critical. However, to

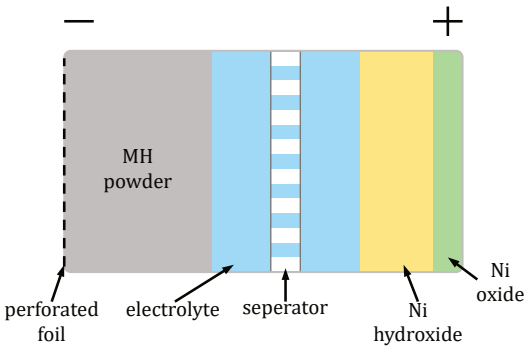

Figure 2.3: Structure of nickel-metal-hydrite battery.

achieve the desired cycle life of typically 500 cycles, an intelligent BMS is required during charging to monitor the necessary parameters. This is often integrated only inside the charger[42, 137].
The recycling of NiMH batteries relies on a vacuum distillation oven. The defective cells are placed in the oven, which is then evacuated to a vacuum of 0.1 mbar. Induction coils are used to achieve an internal temperature of 100 °C to 150 °C in the oven. This temperature is sufficient to evaporate the water and any volatile organic components present. A nickel-iron mixture remains in the furnace, which can either be separated or used, for example, in steel production. The advantages of vacuum distillation are the comparatively low costs and the very low waste gas pollution[108].

2.1.3 *Lithium-Ion Battery*

Lithium is the lightest of all metals with a density of 0.534 $\frac{g}{cm^3}$ at 20 °C. The normal potential of −3.045 V enables batteries with high energy and power. However, metallic lithium reacts strongly with water and can cause fires. Therefore, lithium is placed as ion in a liquid or polymer electrolyte system in the form of so-called intercalation electrodes, which can absorb and release lithium ions reversibly[71]. There are numerous different lithium-ion batteries. They do not only differ in size and design, but also in the chemical composition of their components and also have different voltage ranges. For about two decades, most of the lithium-based accumulators available on the market were lithium-cobalt oxide accumulators. Today, the lithium nickel manganese cobalt oxide based batteries are the most sold. The characteristics such as cell voltage, temperature sensitivity, charge and discharge end voltage and the maximum permissible charge or discharge current vary depending on the type and are essentially dependent on the electrode material and electrolyte used.
The schematic structure of a lithium-ion battery is shown in Figure 2.4. A charged lithium-ion accumulator uses the electrical potential difference between the electrodes to generate an electric current in an

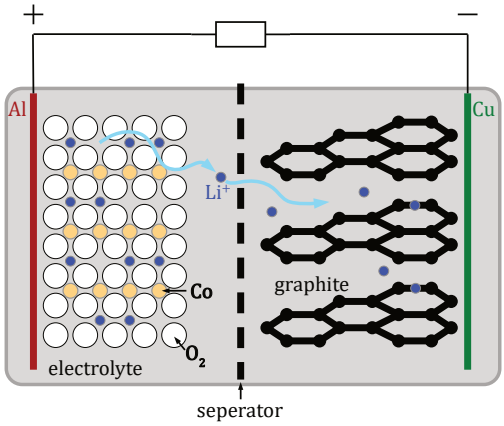

Figure 2.4: Structure of lithium-ion battery.

electrochemical process involving a change in the material of the electrodes. Li^+ lithium ions can freely move through the electrolyte between the two electrodes in the battery, hence the name of the battery. In contrast to the lithium ions, the transition metal and graphite structures of the electrodes are fixed and a separator protects them from direct contact. The movement of the lithium ions is necessary to balance the external current flow during charging and discharging, so that the electrodes themselves remain essentially electrically neutral. The negative electrode is a graphite intercalation compound with the general composition Li_xC_n, where lithium is a cation. During discharge the reaction

$$Li_xC_n \longrightarrow C_n + xLi^+ + xe^- \tag{2.10}$$

takes place at the negative electrode, so the intercalation compound emits electrons that flow to the positive electrode via the external circuit. At the same time, an equal number of Li^+ ions from the intercalation compound also migrate through the electrolyte to the positive electrode. At the positive electrode, it is not the lithium ions that accept the electrons from the external circuit, but the structures of the transition metal compounds present there. Depending on the type of battery, these can be cobalt, nickel, manganese or iron ions. For the currently most frequently sold variant, the lithium-manganese battery, the following reaction equation takes place at the positive electrode:

$$Li_{1-x}Mn_2O_4 + xLi^+ + xe^- \longrightarrow LiMn_2O_4. \tag{2.11}$$

Therefore, the lithium is still ionic at the positive electrode. Since the affinity of the lithium ions for the material of the positive electrode is greater than their affinity for the negative electrode, energy is released when lithium ions flow from the negative to the positive electrode[95, 135].
The specific energy of lithium-ion batteries is in the order of 150 $\frac{Wh}{kg}$ to 200 $\frac{Wh}{kg}$ and the energy density is in the order of 200 $\frac{Wh}{L}$ to 400 $\frac{Wh}{L}$,

which makes lithium-ion batteries particularly interesting for use as electrical energy storage devices in mobile applications and allows the construction of small and lightweight batteries[71]. The typical temperature range for use is about 30 °C to 60 °C. The problem is that the cells are not able to withstand overcharging due to their cell chemistry. When several cells are connected in series to achieve a higher voltage, cells that are as similar as possible should be connected together (binning). Nevertheless, it is usually necessary to use a BMS that enables balancing to compensate for the capacity tolerances[137]. As already mentioned, the cell voltage depends on the variant and results from the difference in the Gibbs free enthalpy of the lithium ions in the two electrode materials[71]. Conventional $LiCoO_2$ batteries provide a nominal voltage of 3.6 V, which is about three times higher than that of a NiMH battery (see section 2.1.2). The end of charge voltage is up to 4.3 V and the end of discharge voltage is about 2.5 V. Deep discharge leads to irreversible damage and loss of capacity.
Most types of lithium-ion accumulators are damaged by over temperature, since thermal runaway occurs with the commonly used oxides such as lithium cobalt oxide and lithium nickel manganese cobalt oxides at temperatures above approximately 180 °C. This is due to the decomposition of the oxide which then releases oxygen, which reacts with other cell components such as the electrolyte and thus leads to a self-boosting exothermic reaction that can no longer be stopped externally. This applies to all known cathode materials, including lithium iron phosphate, although its temperature range is considerably larger. This is because the cathode materials differ in the onset temperature, the temperature at which the exothermic reaction begins, and in the energy released in the process. Oxides such as nickel dioxide, which allow the construction of lithium-ion batteries with a high specific capacity, have a strong tendency to thermal runaway and are therefore almost not used at all.
The recycling of lithium-ion batteries is comparatively complex and there are electrical hazards, chemical hazards and fire hazards. The first step is to deactivate and discharge the battery. If necessary, this is followed by disassembly if the system consists of several cells. Pyrometallurgical processes are often used for material separation. At 450 °C to 500 °C, the cases burst open and the electrolyte burns off abruptly. However, it is then difficult to separate the remaining materials. In contrast, hydrometallurgical processes can also be used for material separation. Due to an inert atmosphere, separation can take place at lower temperatures. In total, more than 90 % of the materials in a battery cell can be recycled[53, 79].

Table 2.1: Summary of technology characteristics of conventional batteries.

PARAMETER	LEAD-ACID	NM HYDRIDE	LITHIUM-ION
Specific energy	Low	Medium	High
Power density	High	High	Very High
Lifetime	Medium	Low	High
Recyclability	Good	Medium	Bad
Handling	Easy	Medium	Difficult

2.1.4 *Comparison*

A summary of the main characteristics of the presented battery technologies is given in Table 2.1. Lead-acid batteries offer only a low specific energy, but due to the maximization of the active surface and small distances between the electrodes, very high currents are possible. Overall, the lifetime can only be rated as medium, especially since low states of charge lead to a reduction in lifetime. Even though lead is a toxic heavy metal, recyclability can still be considered good. This is because processes have already been established within Europe that allow almost complete recycling of the materials. Handling is also a plus point, because as long as the cell is not deep discharged or overcharged, which can be seen very simply from the cell voltage, lead-acid batteries are very robust.
In comparison, NiMH batteries offer more than twice the specific energy at a similar power density. However, with about 500 cycles, the cycle life is slightly reduced. Since a vacuum is required for recycling, this is more complex. Nevertheless, recycling is still possible at relatively low cost. Similar to lead-acid batteries, the discharge behavior is robust and can be performed up to the end-of-discharge voltage without much intelligence. When charging, however, a BMS is necessary.
Of the three technologies, lithium-ion technology offers the highest energy density and power density. For this reason, almost all electric cars use lithium-ion batteries. The lifetime is also better than that of other technologies. But there are also a few critical points here. Above all, recycling is costly and the processes are not yet established. In addition, a BMS is always necessary when using lithium-ion batteries to ensure a safe condition. This is because excessive currents and temperatures and overcharging can lead to fires that are difficult to extinguish.

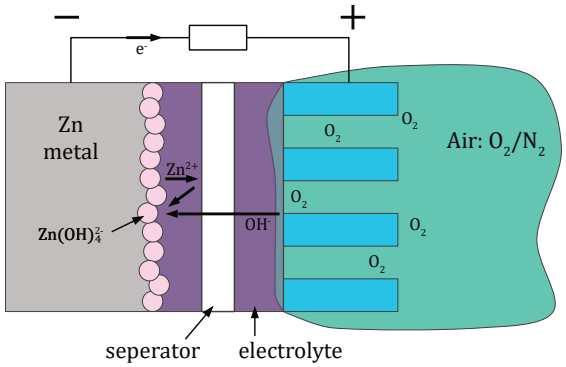

Figure 2.5: Structure of a zinc-air battery

2.2 ZINC-AIR BATTERIES

Zinc-air batteries can also be separated into primary cells and secondary cells. Primary zinc-air cells are well known and are commonly used in hearing aid devices since the 1960s[24]. Therefore, primary cells can be considered as an established technology with little need of further research.
In contrast, the technological development of rechargeable zinc-air cells is being actively researched[24, 71]. Figure 2.5 shows the general structure of a zinc-air battery. The zinc metal electrode forms the largest part of the cell and is the negative pole. A solution of KOH or caustic soda works as electrolyte and improves the standard potential[10, 24]. The separator isolates both electrodes mechanically in order to prevent a conduction of electrodes inside the cell. The positive electrode is formed by a Gas Diffusion Electrode (GDE) made of activated carbon which has a large surface area, is electroconductive and has a catalytic activating effect on cathodic oxygen reduction. In order to increase mechanical stability and electrical conductivity, the electrode is often provided with a metal mesh[10].

2.2.1 *Reactions*

Actually several different processes occur at the zinc anode in an alkaline solution. The desired discharge reaction is[24, 100]:

$$Zn \longrightarrow Zn^{2+} + 2e^{-} \tag{2.12}$$

$$Zn^{2+} + 4OH^{-} \longrightarrow Zn(OH)_4{}^{2-} \tag{2.13}$$

First, zinc is oxidized and dissolved in the electrolyte while electrons are emitted. Then the oxidized zinc ions react with hydroxide ions

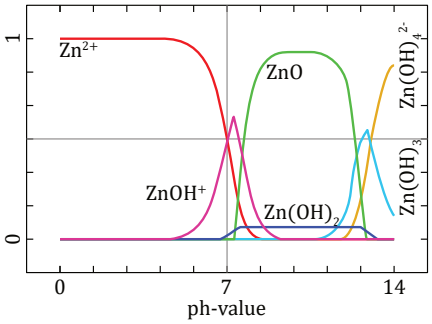

Figure 2.6: Fractions of Zn^{2+} species formed as function of pH[24, 130]

and form zincate. If possible, the zincate then accumulates again at the zinc anode. However, a partial dissolving in the electrolyte cannot be completely avoided resulting in a loss of capacity[24].
Figure 2.6 shows the resulting fractions of different Zn^{2+} species. As one can see, the $Zn(OH)_4^{2-}$ zincate is only stable for pH values higher than 13. Lower pH values result in the formation compact zinc oxide that harms the battery operation:

$$Zn(OH)_4^{2-} \longrightarrow ZnO + H_2O + 2OH^- \tag{2.14}$$

However, if the concentration of the electrolyte is too high, this also has negative consequences. Because then the electrolyte corrodes the zinc metal and hydrogen is released:

$$Zn + 2H_2O \longrightarrow Zn(OH)_2 + H_2\uparrow \tag{2.15}$$

The GDE has to be permeable for oxygen ions in order to use the oxygen of the ambient air. Furthermore, it performs the reduction of O_2. Therefore, the electrode has to be electrocatalytically active and porous[24]. For alkaline solutions as electrolytes, which are commonly used in zinc-air batteries, the reaction is given by:

$$O_2 + 2H_2O + 4e^- \longrightarrow 4OH^- \tag{2.16}$$

An advantage of zinc-air cells is that precious metal catalysts are not required at the air electrode. Thus, the cells are cheap and are easy to recycle. The usage of noble catalyst even harms the cell performance, because traces of them diffuses to the zinc anode lowering the hydrogen overvoltage[24]. This results in the production of hydrogen when the battery is being charged[133].

2.2.2 *Electrode Potential*

Mortimer uses the following model for the generation of an electrode potential[99]. When a zinc electrode is placed in a solution, for example in an electrolyte, some Zn^{2+} zinc ions migrate into the

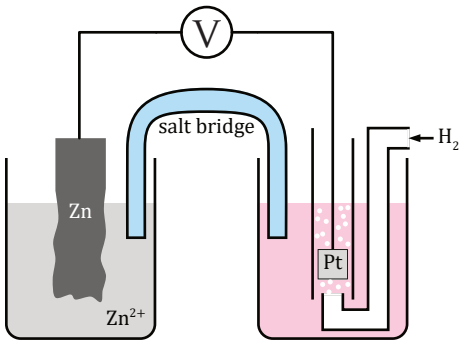

Figure 2.7: Galvanic element consisting of a standard hydrogen electrode an a $Zn^{2+}|Zn$ electrode.

solution while the free valence electrons remain in the electron gas of the electrode. An electric field is formed between the positively charged zinc ions in the solution and the negatively charged electrode, which counteracts further migration of ions. In addition, individual ions migrate back into the electrode. If the two ion currents equal each other, a state of equilibrium is reached. A defined potential now applies, which depends on the concentration of the solution and on the temperature. The level of the potential depends on how easily the metal can be oxidized.

However, the absolute value of the resulting potential cannot be measured, since a second half cell is always required for this purpose. Instead, the relative potential to a reference cell is measured. The standard hydrogen electrode serves as the reference cell. The electrode potential of the hydrogen electrode was set to be 0 V for all temperatures. It consists of a hydrogen gas flowing around a platinum electrode at normal pressure (1013 hPa) and is immersed in an acid solution with H^+ ion activity of 1. The setup of a galvanic element for determining the relative electrode potential with respect to the standard hydrogen electrode is shown in Figure 2.7. Here, the zinc electrode is connected to the hydrogen electrode via a salt bridge. The salt bridge is filled with a concentrated salt solution, allowing current conduction but preventing mixing of the two solutions. Now the potential between the zinc electrode and the standard hydrogen electrode can be measured. The potential against the standard hydrogen electrode is called the standard potential and is denoted by E^0. The potential of two different electrodes can be determined by the difference of the corresponding standard potentials.

The standard electrode potentials of the involved half-reactions are given in Table 2.2. At the zinc anode, zinc reacts with the hydroxide ions to form zincate. If an air electrode is used, oxygen and water are

Table 2.2: Standard electrode potentials in zinc-air batteries.

HALF REACTION			E^0
$Zn(OH)_4^{2+}$	$\rightleftharpoons$	$Zn + 4OH^-$	$-1.215\,V$
$O_2 + 2H_2O + 4e^-$	$\rightleftharpoons$	$4OH^-$	$+0.401\,V$
$NiO_2 + 2H_2O + 2e^-$	$\rightleftharpoons$	$Ni(OH)_2 + 2OH^-$	$+0.490\,V$

reduced to hydroxide ions at the GDE. This results in a potential for the total reaction of the zinc-air cell of

$$\Delta E^0_{ZAB} = E^0\left(O_2 + 2H_2O + 4e^- | 4OH^-\right) + \\ - E^0\left(Zn(OH)_4^{2+} | Zn + 4OH^-\right), \quad (2.17)$$

$$\Delta E^0_{ZAB,standard} = (+0.401\,V) - (-1.215\,V) = 1.6\,V. \quad (2.18)$$

As already stated at the beginning of the chapter, the resulting potential depends on the temperature and the activity of the solution. The standard potentials refer to a temperature of 25 °C and activity of 1. The question now is how to calculate the potentials for other temperatures and activities. The basis is the change in free enthalpy or Gibbs energy ΔG as a function of activity:

$$\Delta G = \Delta G^0 + RT \ln Q$$

$$Q = \frac{a^x(X) \cdot a^z(Z)}{a^a(A) \cdot a^e(E)} \quad . \quad (2.19)$$

for reaction: $aA + eE \longrightarrow xX + zZ$

The activity describes the concentration of the substance and corrects for non-ideal behavior. As an approximation, it can be assumed that the activity for solids is 1, for gases the activity corresponds to the partial pressure in relation to the normal pressure and for solutions the activity corresponds to the molarity of the solution.
The Gibbs energy describes the maximum recoverable energy of the reaction and can be linked to the electrode potential using the number of charge carriers. Since Q describes the molarity, multiplication by the Faraday Constant F gives the number of reactants. A further multiplication by the number of electrons z given in the reaction equation finally yields the number of charge carriers. Thus

$$\Delta G = -nF \cdot \Delta E, \quad (2.20)$$

$$\Delta G^0 = -nF \cdot \Delta E^0 \quad (2.21)$$

follows. After conversion to ΔE, the Nernst equation is obtained:

$$\Delta E = \Delta E^0 - \frac{RT}{nF} \ln Q. \tag{2.22}$$

First, the Nernst equation is applied to the anode reaction

$$\mathrm{Zn} + 4\mathrm{OH}^- \longrightarrow \mathrm{Zn(OH)_4}^{2-} + 2\mathrm{e}^- \tag{2.23}$$

where 2 electrons are involved. Inserting the values gives

$$E_{\text{anode}} = E^0_{\text{anode}} - \frac{RT}{nF} \cdot \ln\left(\frac{\left(a(\mathrm{Zn})\right)^1 \cdot \left(a(\mathrm{OH}^-)\right)^2}{\left(a\left(\mathrm{Zn(OH)_4}^{2+}\right)\right)^1}\right), \tag{2.24}$$

$$E_{\text{anode}} = -1.215\,\mathrm{V} - \frac{25.7\,\mathrm{mV}}{2} \cdot \ln\left(\frac{1 \cdot \left(\frac{c\left[\mathrm{OH}^-\right]}{1\,\frac{\mathrm{mol}}{\mathrm{L}}}\right)^2}{1}\right). \tag{2.25}$$

The reaction at the air electrode is

$$\mathrm{O_2} + 2\mathrm{H_2O} + 4\mathrm{e}^- \longrightarrow 4\mathrm{OH}^- \tag{2.26}$$

In contrast to the anode, a reduction takes place at the GDE during discharge. Therefore, the variable term is added instead of subtracted:

$$E_{\text{cathode}} = E^0_{\text{anode}} + \frac{RT}{nF} \cdot \ln\left(\frac{\left(a\left(\mathrm{O_2}\right)\right)^1 \cdot \left(a(\mathrm{H_2O})\right)^2}{\left(a(\mathrm{OH}^-)\right)^4}\right), \tag{2.27}$$

$$E_{\text{cathode}} = 0.401\,\mathrm{V} + \frac{25.7\,\mathrm{mV}}{4} \cdot \ln\left(\frac{\frac{p[\mathrm{O_2}]}{1013\,\mathrm{hPa}} \cdot \left(\frac{c[\mathrm{H_2O}]}{1\,\frac{\mathrm{mol}}{\mathrm{L}}}\right)^2}{\left(\frac{c\left[\mathrm{OH}^-\right]}{1\,\frac{\mathrm{mol}}{\mathrm{L}}}\right)^4}\right). \tag{2.28}$$

To calculate the voltage between both electrodes, the difference of the respective potential can be used again:

$$\Delta E = E_{\text{cathode}} - E_{\text{anode}}, \tag{2.29}$$

$$\Delta E = 1.6\,\mathrm{V} + \frac{25.7\,\mathrm{mV}}{4} \cdot \ln\left(\frac{\frac{p[\mathrm{O_2}]}{1013\,\mathrm{hPa}} \cdot \left(\frac{c[\mathrm{H_2O}]}{1\,\frac{\mathrm{mol}}{\mathrm{L}}}\right)^2}{\left(\frac{c\left[\mathrm{OH}^-\right]}{1\,\frac{\mathrm{mol}}{\mathrm{L}}}\right)^4}\right) + \\ + \frac{25.7\,\mathrm{mV}}{2} \cdot \ln\left(\frac{1 \cdot \left(\frac{c\left[\mathrm{OH}^-\right]}{1\,\frac{\mathrm{mol}}{\mathrm{L}}}\right)^2}{1}\right). \tag{2.30}$$

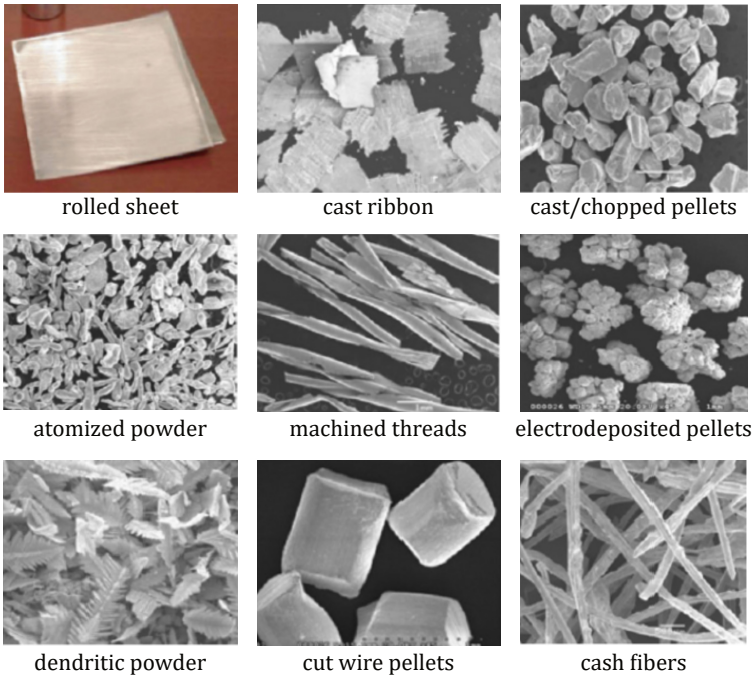

Figure 2.8: Different zinc anode structures[140]

The resulting open-circuit voltage thus depends on the temperature, oxygen content and molarity of the electrolyte. In lead-acid batteries, the electrolyte is directly involved in the redox reaction, so the electrolyte concentration changes with the SoC of the battery. This is not the case with zinc-air batteries. The hydroxide ions are formed at the air cathode by reducing oxygen and then migrate to the zinc anode. Since it is an open system, water vapor can escape through the air cathode, thus the concentration of the electrolyte can change over time due to evaporation. This then has a greater influence on the open-circuit voltage than the actual SoC.

2.2.3 *Zinc Anode*

The zinc anode simply consists of zinc. A simple zinc foil is usually not used because it offers poor performance. Instead, nano- and microstructured materials are often used to increase the surface area and efficiency. A selection of different structures is presented in Figure 2.8[140]. Thereby, typically the porosity is somewhere between 60 % and 80 % which results in a capacity density of 1.2 $\frac{\mathrm{Ah}}{\mathrm{cm}^3}$ to 1.2 $\frac{\mathrm{Ah}}{\mathrm{cm}^3}$.

Porosity not only affects the surface area and capacity of the cell, but cell performance is also strongly influenced by porosity and structure[24] (see Figure 2.9). Here, the conductivity of fibers is consistently good for a wide range of porosity values[139]. By contrast, the use of zinc powder only works with gelling agents such

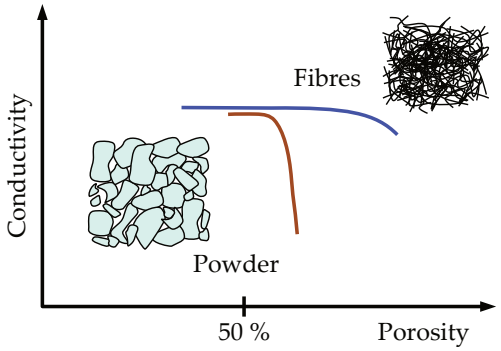

Figure 2.9: Anode conductivity depending on anode porosity[139]

as PolyTetraFluoroEthylene (PTFE), sago, and carbopol gel[72, 91, 96, 100]. Although the porosity can be adjusted fairly accurately via the binders, they lead to an increase in resistance and thus reduce cell performance[24, 73].

2.2.4 *Gas Diffusion Electrode*

The gas diffusion electrode is an air cathode that completes the redox reaction by reducing O_2 when discharging. It is possible to use several different materials. Graphene loaded with Mn_3O_4 nanoparticles is commonly used as it results in a high efficiency and performs better than noble metals[24, 73]. Thus, precious metal catalysts are not required at the air electrode. The usage of noble catalyst even harms the cell performance, because traces of them diffuse to the zinc anode lowering the hydrogen overvoltage[24]. Once again, a porous structure is used in order to increase the electrocatalytical behavior.
The different layers of a GDE are shown in Figure 2.10. Although the porous graphene should prevent the leakage of electrolyte, superhydrophobic materials are often added to the air side of the electrode for further securing against leakages. Here, PTFE has proven to be useful (white foil)[51]. Then there is current collector mesh that also works as cell contact. Since copper can be attacked by the electrolyte, a nickel or nickel coated mesh is usually used instead. The structure is completed by the gas diffusion layer.
For rechargeable zinc-air cells, an efficient oxygen reduction reaction at the air cathode is not the only important factor. During the charging process, there is an oxygen evolution reaction. Two different approaches are the subject of current research. On the one hand, there is research on bi-functional electrodes that enable both processes. However, the lifetime and efficiency of these electrodes is still very limited[24]. Another approach is the use of a separate electrode for charging. Since no oxygen from the ambient air is needed during

Figure 2.10: Structure of zinc-air gas diffusion electrode.

the charging process, a simple nickel net can also act as a positive electrode[24, 77].

2.2.5 *Electrolyte*

Since acids react with zinc, only alkaline electrolytes can be used. KOH is the most commonly used because it has a high conductivity compared to other basic electrolytes and is also very low cost[58]. KOH is very hydrophilic and is highly soluble in water. Regarding the concentration, three things need to be considered.
First, if the concentration is too high, KOH can also corrode the zinc (reaction equation 2.15). This reaction occurs when the pH-value rises above 13, which is the case at a molarity of 4 $\frac{\text{mol}}{\text{L}}$. Hydrogen is released in the process which may result in a dangerous hydrogen gas buildup[24]. In addition, the overvoltage of the electrolysis is reduced by a high concentration. This also causes accelerated hydrogen formation, here during a charging process[24].
Second, as shown in Figure 2.6, the concentration may also not be too low, since the zincate precipitates as zinc oxide at a pH below 13. The precipitated zinc oxide then passivates the anode. The occupied parts can no longer be used for battery operation and the cell dramatically loses power and capacity. A pH of 13 is approximately reached when the concentration drops below 4 $\frac{\text{mol}}{\text{L}}$[24].
The third aspect is the conductivity of the KOH solution, which has a strong dependence on the concentration. The goal is, of course, to maximize the conductivity so that the losses are as small as possible. The specific conductivity of a KOH solution as a function of its molarity is shown for various temperatures in Figure 2.11. For low concentrations, there is a linear dependence between concentration and specific conductivity. A higher number of charge carriers results in a higher conductivity. This behavior changes when the average distance between the ions becomes smaller at high concentrations. The electrostatic impact between the charge carriers stops a further gain of the conductivity and can even lower it[5]. The point of maximum conductivity also depends on the temperature. For typical battery

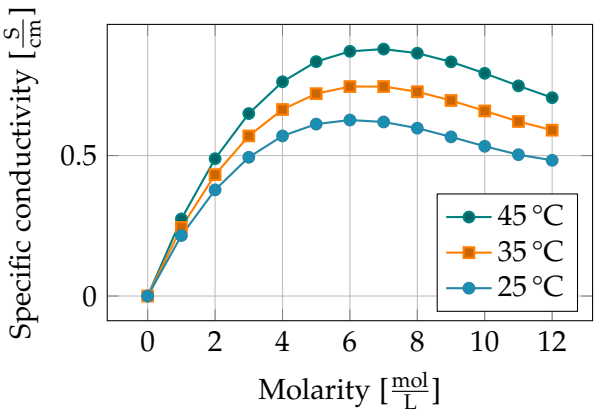

Figure 2.11: Specific conductivity of potassium hydroxide solutions at different temperatures and molarities[5, 43].

operating temperatures, however, this point is always in the range of a slightly above 6 $\frac{\text{mol}}{\text{L}}$.
Considering all aspects, a 30 % KOH solution is often used as a compromise, which corresponds to a molarity of 6.3 $\frac{\text{mol}}{\text{L}}$. At this point, the conductivity is very high and precipitation of zinc oxide is not yet a problem. Although corrosion of zinc already occurs in this range, the effect is still very small.
Other electrolytes have also been studied with zinc-air batteries. One of the most important of these is caustic soda. Operation with this solution is also possible, but larger losses usually occure due to the lower conductivity[24].
A major problem with water-based solutions is carbonation. The carbon dioxide in the ambient air leads to the formation of potassium carbonate in the electrolyte. The associated potassium ion is then no longer available as a charge carrier and the conductivity of the electrolyte decreases. Another problem is that potassium carbonate is much less soluble in water. It precipitates and clogs the pores of the GDE[58, 80, 88].
There was a recent publication that used a $Zn(OTf)_2$ solution instead of an alkaline electrolyte. It is interesting to note that the zinc anode is not oxidized to zincate during discharge, but to a reversible zinc peroxide. This has the advantage that it does not continue to precipitate as zinc oxide, which should extend the life of the cell[129].

2.2.6 *Oxygen Consumption*

Now the oxygen consumption of a zinc-air cell is analyzed to determine whether additional steps, such as ventilation, are necessary to avoid a negative impact on the cell performance and to ensure a breathable oxygen content. It is important to note that the oxygen used during the discharge process to oxidize the zinc is released during the

subsequent charge process. The oxygen is therefore not permanently taken from the ambient air. The oxygen reaction takes place at the GDE. Therefore, the corresponding reaction equation is shown here once again:

$$O_2 + 2H_2O + 4\,e^- \longrightarrow 4OH^- \tag{2.31}$$

This is a reduction, since one electron is taken up by one oxygen particle at a time. However, to a certain extent the oxygen is also used from the water of the electrolyte. Therefore, one oxygen molecule (2 oxygen atoms) of the ambient air can react with 4 electrons forming 4 hydroxide ions. To relate the reaction equation to an electric current, it is first necessary to know the number of electrons N_{1C} that transfer a charge of 1 C:

$$N_{1C} = \frac{Q}{e} = \frac{1\,C}{1.6021 \cdot 10^{-19} C} = 6.2415 \cdot 10^{18}. \tag{2.32}$$

Since 4 electrons react with one oxygen molecule at a time, the number of oxygen molecules required to discharge 1 C results in

$$N_{O_2,1C} = \frac{N_{1C}}{4} = 1.5603 \cdot 10^{18}. \tag{2.33}$$

The relationship between particle number, molar mass, volume and mass is shown in Figure 2.12. In order to calculate the necessary air volume, the molar mass must first be determined. The Avogadro constant N_A is used as a conversion factor. This gives the necessary molar mass of oxygen for 1 C as

$$n_{O_2}\,[Q = 1\,C] = \frac{N_{O_2,1C}}{N_A} = \frac{1\,C}{4 \cdot e \cdot N_A} = 2.5911 \cdot 10^{-6}. \tag{2.34}$$

The ambient air can approximately be considered as an ideal gas. This means that only hard, elastic collisions with each other and with the walls are considered as interactions between the particles. This leads to a linear relationship between the pressure and the temperature and density. It is particularly interesting that the molar volume V_{m0} of an ideal gas, which defines the ratio between the volume and the number of molecules, is a fundamental quantity constant under standard conditions and has a value of[127]

$$V_{m0} = 22.414\,\frac{L}{mol}. \tag{2.35}$$

The oxygen volume to discharge the battery by 1 C is therefore

$$V_{O_2}\,[Q = 1\,C] = V_{m0} \cdot n_{O_2} = 5.808 \times 10^{-5}\,L. \tag{2.36}$$

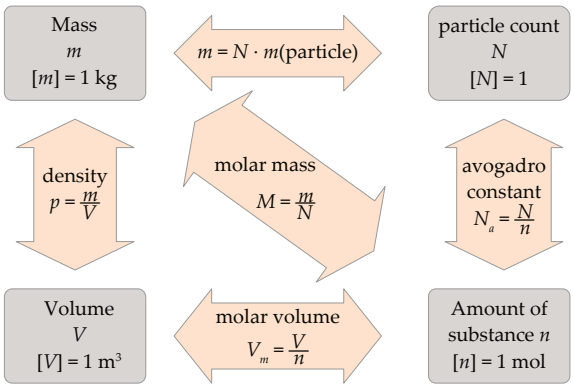

Figure 2.12: Relationship between number of particles, molar mass, volume and mass.

A charge of 1 C is transferred within one second at a discharge current of 1 A. Somewhat more concrete is certainly the necessary oxygen volume for a charge of 1 A h or

$$Q_{1\,\text{A h}} = 1\,\text{A h} \cdot \frac{3600\,\text{s}}{1\,\text{h}} = 3600\,\text{C}. \tag{2.37}$$

This charge corresponds to the volume

$$V_{\text{O}_2}\,[Q = 1\,\text{A h}] = V_{m0} \cdot n_{\text{O}_2} = \frac{V_{m0}}{4\,e \cdot N_A} \cdot 3600\,\text{C} = 0.209\,\text{L}. \tag{2.38}$$

It should be noted that zinc-air batteries are not used in a pure oxygen environment, but in normal ambient air. The required air volume is larger according to the oxygen content.

2.3 DESCRIPTION OF ZINC-AIR BATTERY UNDER DEVELOPMENT

The research project was performed in cooperation with 3E Batterie Systeme GmbH, that developed the cell chemistry and are mainly responsible for the assembly of the zinc-air cells. Figure 2.13 depicts a typical zinc-air cell being scrutinized in this thesis. The cases are injection molded and have two terminals for electrolyte circulation. If passivating zinc oxide has formed at the anode, circulating the electrolyte can help to regenerate the cell. This is possible because zinc oxide dissolves in the electrolyte and can thus be removed. The air cathode is also manufactured by machine. However, the actual assembly and production of the anode mass is still done by hand at the current stage. First, the air cathodes are glued into the sides of the case. The anode mass is pressed with a hydraulic press and then dried. There are still minor variations in the mass here. As a result, the capacity of the cells also varies. Finally, the anode wrapped with a separator and two nickel nets, which are used as charging electrodes, are inserted into the cell and the case is glued.

Figure 2.13: Photo of the zinc-air cell under development.

The characteristic properties of the cell are summarized in Table 2.3. As for other zinc-air cells as well, the open circuit voltage of 1.45 V is slightly below the theoretical cell voltage. Due to the hand manufacturing process, there is a slight variation in the cell capacity, which nevertheless keeps slightly above 100 A h. With a cell volume of 0.5 L and a weight of 0.6 kg, an average discharge voltage of 1.1 V results in an energy density and a specific energy that are already on par with lithium-ion technology in the current state of research. However, since the theoretical specific energy is 1350 $\frac{\mathrm{W\,h}}{\mathrm{kg}}$, there is still a lot of potential for improvement. The main reason for this is the large distance between the electrodes, which is currently still necessary as a safety margin against dendrite growth. A technological disadvantage is the low power density, which is caused by the long diffusion lengths in the air cathode. However, current developments show that geometry adjustments can lead to a higher power density.

2.3.1 *Structure*

Figure 2.14 shows the inner structure of the battery, which is basically known from chapter 2.2. The cell is symmetrically designed to increase the cell performance. The zinc anode forms the core of the cell, which is surrounded by electrolyte. In the electrolyte there are nickel electrodes on both sides, which are used to charge the cell. Thus, a 3-electrode technology is used here, avoiding the use of bi-functional air cathodes. The main reason is the increased lifetime of the GDE when it is only used to discharge the cell. In addition, a separate charging electrode offers the advantage that the charging power, independent

Table 2.3: Summary of technology characteristics of conventional batteries.

PARAMETER	VALUE
Off-load voltage	1.45 V
Capacity	100 A h
Volume	0.5 L
Energy density	200 $\frac{\text{W h}}{\text{L}}$
Weight	0.6 kg
Specific Energy	166 $\frac{\text{W h}}{\text{kg}}$
Charging voltage	2.1 V
Discharging voltage	1.1 V
End of discharge voltage	0.6 V
Maximal discharge Power	15 W
Power density	30 $\frac{\text{W}}{\text{L}}$

of the GDE, is much higher than the discharging power. The GDEs are then mounted on the outermost side in each case. These use porous graphite deposited on a nickel mesh to dissipate the current. To prevent leakage, a super hydrophobic layer of PTFE is also applied.

2.3.2 *Demonstrator*

Within the research project, a first small demonstrator has already been developed and assembled. Figure 2.15 shows the structure of the demonstrator. 12 cells are used, so that a total capacity of 1.32 kW h is provided. Acrylic glass walls are used to guide the air flow. The cooling concept was developed using CFD flow simulations to ensure that the temperature of all cells is as homogeneous as possible. This allows the cells to age at the same rate and prevents premature failure. Furthermore, an electrolyte management system is installed which regularly flushes the anodes and thus ensures good coating of the anode with fresh electrolyte.
As shown in Figure 2.16, the demonstrator was successfully tested on a Photo Voltaic (PV) system. The zinc-air storage system stores the PV energy during the day and releases it at night when the sun is no longer shining. For this purpose, a BMS was implemented in LabView to control the demonstrator. In addition to the actual functionality, emphasis was also placed on a safe system state, so that the cells are not overcharged and also premature aging due to too low charge levels is prevented.
I would like to take this opportunity to once again thank all the partners involved in the project. Figure 2.16 shows some of the collaborating people. From left to right, you can find Ludwig Horsthemke,

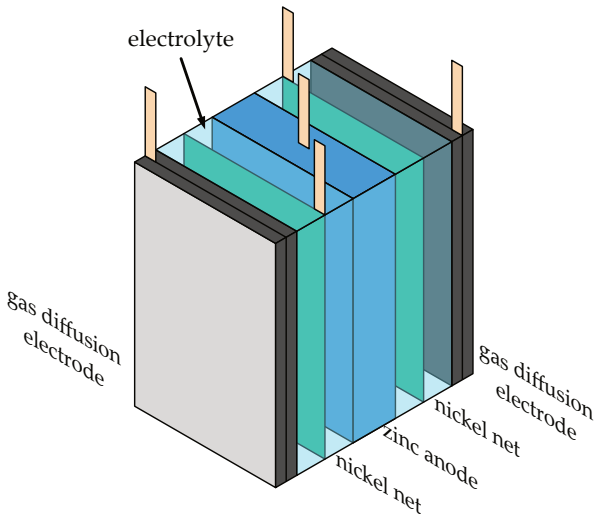

Figure 2.14: Structure of the zinc-air cell under development.

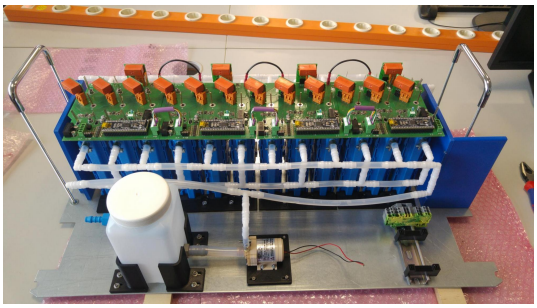

Figure 2.15: Zinc-air storage system demonstrator.

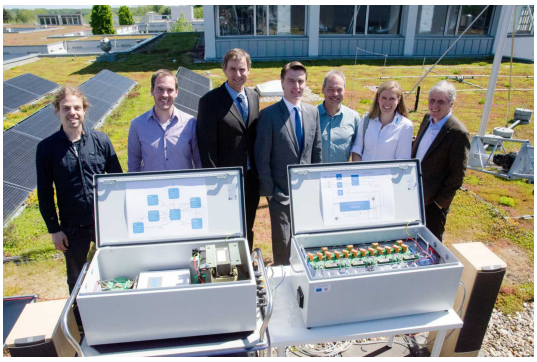

Figure 2.16: Demonstrator of a zinc-air storage system at a solar power plant.

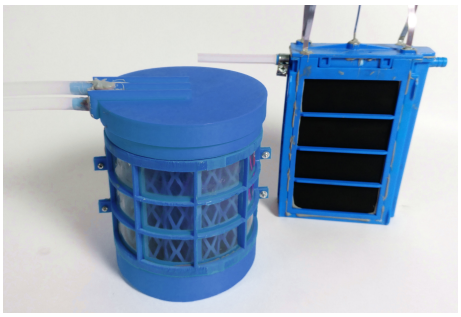

Figure 2.17: Different cell geometries that have been evaluated to optimize the power density of zinc-air cells.

Andre Löchte and Peter Glösekötter from University of Applied Sciences Münster at first, whose main focus is on the battery management and the construction of the demonstrator. Next comes Markus Kunkel, head of the companies Kunkel und Partner and 3e Batteriesysteme, that have developed the cell technology and are responsible for cell production. From the company EMG Automation there are Uwe Jaschke, Nicol Otterbach and Anno Jordan, who handled the development and construction of the electronics and power electronics. The development of the battery managemen system and the further development of the cell technology was inertially funded within the project *EFRE-0800072* by the Projektträger ETN, Leitmarktagentur.NRW. In the follow-up project *EFRE-0801585*, a cell with optimized power density is now being developed by Kunkel und Partner, 3e Batteriesysteme and University of Applied Sciences Münster in association with Stadtwerke Steinfurt.

2.3.3 *Geometry*

A technology-related disadvantage of zinc-air cells is the low discharge power caused by the GDE. While the focus of this thesis is not on optimizing the cell, electrical power is also an important aspect for battery management, which is why it is briefly discussed here. One approach to address the cell performance issue is to optimize the cell geometry. The key here is to maximize the active surface area of the GDE with respect to the cell volume. Figure 2.17 shows different geometries that have been evaluated. Round cells are particularly suitable for small diameters, since the cathode surface, which is significant for the cell performance, increases only linearly with the diameter, while the cell volume has a quadratic dependence. Prismatic cells are suitable for the larger scale. Here, the aspect ratio can be used to focus on a higher energy density or a higher power density. In the end, the active surface has increased to about twice the size using a prismatic cell. Nevertheless, the volume and capacity are unchanged by thinning the overall cell and reducing the electrode distances.

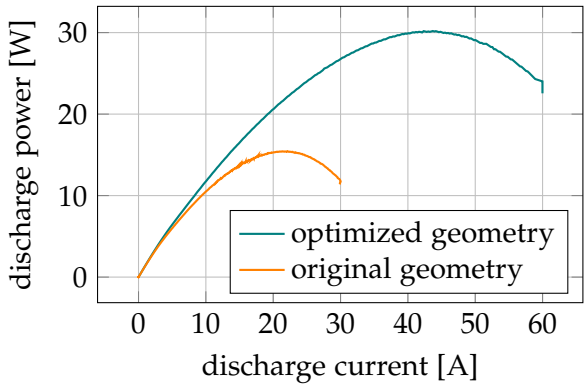

Figure 2.18: Discharge power as a function of the discharge current of a power-optimized zinc-air cell.

This also doubles the cell power. Figure 2.18 shows the cell power as a function of the discharge current. According to this, the maximum discharge power is 30 W, which is achieved at a current of 42 A. However, reducing the distances also reduces the lifetime of the cell. Thus, the cell was destroyed by a dendrite after 300 microcycles, each time the cell was discharged by 10 %.

3

CELL MODELING

The chemical processes and reactions as well as the structural design of zinc-air batteries have already been described in detail in chapter 2.2. This chapter now describes the reaction processes on the electrical level. On the one hand, a description of the static processes is given on the basis of the electrolyte and the charge transfer resistance, which define the constant relationship between cell voltage and current after the equalization processes have faded out. On the other hand, the double layer capacity and the diffusion processes are described, so that an electrical description in the frequency domain is also possible. Especially with regard to a later evaluation of the impedance data generated during an EIS measurement, this consideration is necessary and useful.

3.1 ELECTROLYTE

When an aqueous solution contains ions, it conducts electricity. Pure water contains only a few ions resulting from the reaction

$$2H_2O \rightleftharpoons H_3O^+ + OH^- \tag{3.1}$$

and is therefore a bad conductor. An electrolyte is a substance whose aqueous solution conducts the electric current better than pure water. An electrolyte is partially or completely present in aqueous solutions in the form of ions, they are partially or completely dissociated. The dissociated ions move under the influence of an electric field and thus increase the conductivity. The part that remains in the solution in the form of molecules does not increase the conductivity. Electrolytes are divided into two groups. Strong electrolytes are practically completely dissociated in aqueous solutions. The most important electrolytes are therefore either acids, bases or salts. In contrast, weak electrolytes consist of polar molecules that are only partially split into ions in aqueous solutions. At the same concentration of substance, weak electrolytes therefore conduct worse than strong electrolytes. Nevertheless, the electrical conductivity of a strong electrolyte as an ion conductor is typically lower compared to metals[99].
In zinc-air batteries, KOH dissolved in water is usually used. KOH dissociates completely in water, which means that K^+ and OH^- ions separate and the solution is conductive. The complete dissociation results in high conductivity, which is the main reason for its frequent use. In addition, this makes it a binary electrolyte because both anions (OH^-) and cations (K^+) are present as mobile species. However, only

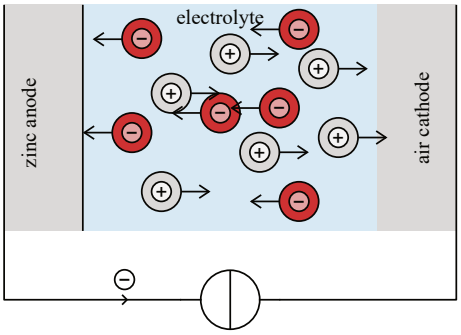

Figure 3.1: Initial state of movement of anions and cations in the electrolyte during external current.

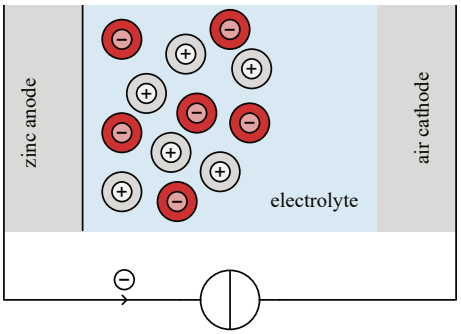

Figure 3.2: Idealized concentration gradient of the movement of anions and cations in the electrolyte with external current.

the anions pass through the electrode-electrolyte interface, as can be seen from the chemical reactions in chapter 2.2.1. As a result, a concentration gradient is formed in the electrolyte under current flow, which is accompanied by a voltage drop across the electrolyte volume[119]. Figure 3.1 shows the situation in the electrolyte shortly after an electric current is applied. At each interface, OH^- ions are transferred from the electrode into the electrolyte (air cathode on the right) and from the electrolyte into the electrode (zinc anode on the left).
Inside the electrolyte, the current is driven partly by K^+ and OH^- ions, which move to the left and to the right, respectively, according to their charge. Since the mass flow of OH^- ions at the edges corresponds to the total current, but in the center only a part of the electric current is initially driven by an equivalent mass flow of OH^- ions (the K^+ ions drive the rest), more OH^- ions are injected in the left half of the volume than are transported away. In the right half, more OH^- ions are removed than supplied. This results in a shift of the concentration of both ion types to the left[119]. Figure 3.2 shows the situation in an idealized form.
According to Fick's law, the resulting concentration gradient results in a diffusion current shown in Figure 3.3, which counteracts that concentration gradient and thus reduce the difference in concentra-

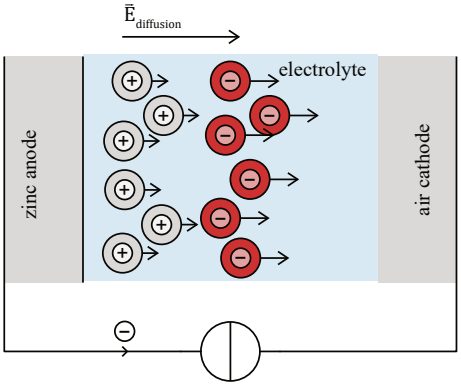

Figure 3.3: Resulting diffusion of anions and cations in the electrolyte due to the concentration gradient with external current.

tion. Due to different mobilities of the two types of ions, there is a microscopic charge separation and a resulting electric field $\overrightarrow{E}_{\text{diffuse}}$. Macroscopically, this leads to an additional voltage drop, which, however, only rises with time[119]. In addition to an ohmic resistance R_{el}, the electrolyte is thus also described by a diffusion resistance, the mathematical description of it can be found in chapter 3.4.

3.2 DOUBLE LAYER CAPACITY

3.2.1 *Helmholtz Double Layer*

The term double layer was first mentioned in 1853 by Herman von Helmholtz in a paper in which he described the electric field of two oppositely charged, infinitely close conductive areas[54]. In a later work he then explained that these double layers are formed at metallic electrodes in an electrolyte[55]. Figure 3.4 illustrates the scheme of the Helmholtz double layer that corresponds to a zinc electrode and a KOH electrolyte. The hydroxide anions displace the electrons from the surface, resulting in two oppositely charged layers of the same amount of charge. Since ions are generally much larger than electrons, the average distance between the layers is mainly defined by the size of the radius of the ion species[55, 128]. Since the caustic potash is a water based solution, solvation can occur. That means that water molecules are being attracted by the ions due to the dipole momentum resulting in a bigger hull. Thus, the average distance between the layers is increased.

Generally, the relation between space charge ρ and potential ϕ is described by the Poisson equation

$$\frac{\partial^2 \phi}{\partial^2 x} = \frac{4\pi\rho}{\epsilon}. \tag{3.2}$$

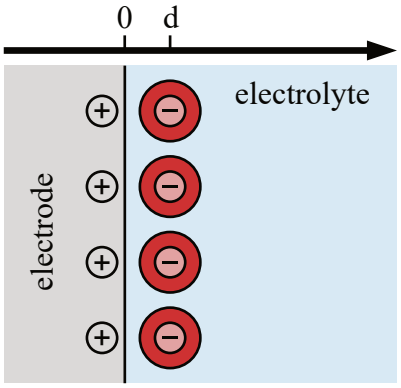

Figure 3.4: Scheme of a Helmholtz double layer

The Helmholtz layer consists of solvated ions that are directly located at the electrode. Therefore, the space charge within the two layers is zero by definition:

$$\frac{\partial^2 \phi}{\partial^2 x} = 0. \tag{3.3}$$

So that the Laplace equation

$$\frac{\partial \phi}{\partial x} = \text{const.} \tag{3.4}$$

applies. This means that the potential has a linear course as seen in Figure 3.5. The average space charge in the metallic electrode and in the electrolyte is also 0. Since the zero-current case is considered here, it can approximately be assumed that the potential in the respective species is constant. Hence the resulting potential curve is

$$\phi(x) = \begin{cases} \phi_M & \text{for } x \leq 0 \\ (\phi_L - \phi_M)\,\frac{x}{d} + \phi_M & \text{for } 0 < x < d \cdot \\ \phi_L & \text{for } d \leq x \end{cases} \tag{3.5}$$

Here ϕ_M and ϕ_L describe the potential of the electrode and the electrolyte, respectively, and d is the radius of a solvated ion. The Divergence Theorem

$$C = \frac{Q}{V} = \frac{\oint_A \overrightarrow{D}\, d\overrightarrow{A}}{\int_s \overrightarrow{E}\, d\overrightarrow{s}} \tag{3.6}$$

can be used to determine the resulting capacity. Here the dielectric displacement $\overrightarrow{D}$ is

$$\overrightarrow{D} = \epsilon_0 \cdot \epsilon_r \cdot \overrightarrow{E}, \tag{3.7}$$

so that

$$C = \epsilon_0 \cdot \epsilon_r \frac{\oint_A \overrightarrow{E}\, d\overrightarrow{A}}{\int_s \overrightarrow{E}\, d\overrightarrow{s}} \tag{3.8}$$

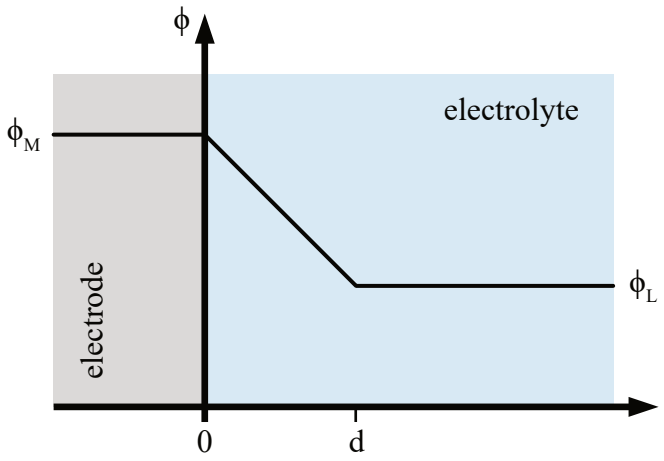

Figure 3.5: Development of potential in Helmholtz double layer[54, 55, 128]

follows. Based on Figure 3.5, the electric field can be considered approximately homogeneous. Thus, the Helmholtz layer can be regarded as a plate capacitor with a very small gap in order to determine the capacity:

$$C_H = \epsilon_0 \cdot \epsilon_R \cdot \frac{A}{d}. \tag{3.9}$$

3.2.2 *Gouy-Chapman Double Layer*

The rigid model of the Helmholtz double layer was later extended by Otto Stern with the Gouy-Chapman model. The Gouy Chapman model considers two differently directed forces. One is the electrostatic force known from the Helmholtz layer, which binds the ions to the electrode. On the other hand, there is thermal movement, because particles aim for a uniform diffusion. Gouy and Chapman modeled the resulting distribution analogous to the Barometric Elevation Formula that describes the Earth's atmosphere[128]. These movements result in a diffuse layer shown in Figure 3.6 that is wider than a single layer of molecules adjacent to the electrode[46, 47]. The Boltzmann distribution is used to determine the ion concentration based on the electrical potential at a specific point and the Laplace equation is used to model this electric potential[25]. This means that a continuous distribution is used instead of using discrete charges of ions[128]. This results in an exponentially decreasing potential as shown in Figure 3.7. The total charge in each species is

$$q_M = -q_L = 2\sqrt{2\epsilon RTc}\sinh\left(\frac{zF\left(\phi - \phi_0\right)}{2RT}\right). \tag{3.10}$$

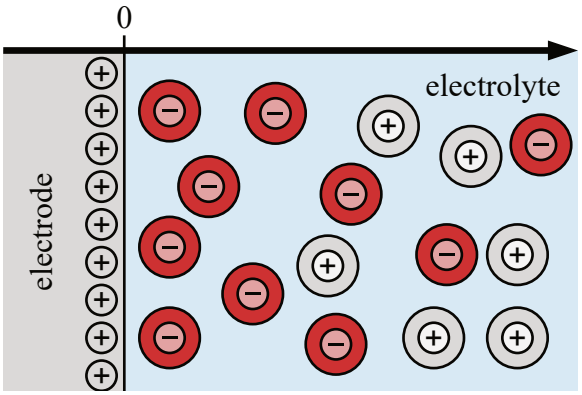

Figure 3.6: Scheme of Gouy-Chapman double layer

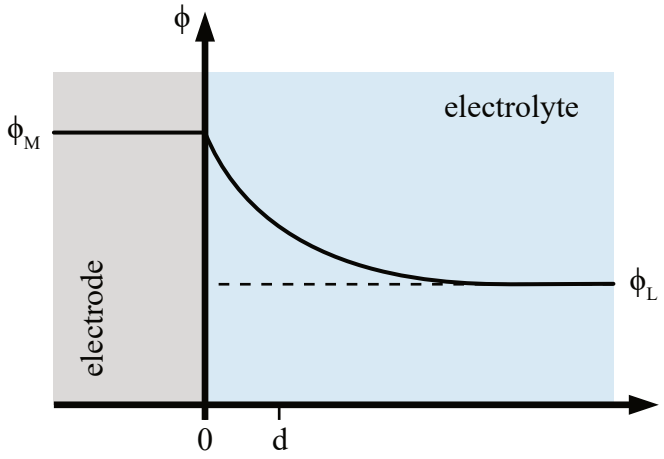

Figure 3.7: Development of potential in Gouy-Chapman double layer

Since the charge is non-linearly dependent on the potential, the capacity of the double layer is also potential-dependent and must be indicated differentially:

$$C_{GC} = -\frac{dq_L}{d\phi} = zF\sqrt{\frac{2\epsilon c}{RT}}\cosh\left(\frac{zF\left(\phi - \phi_0\right)}{2RT}\right). \tag{3.11}$$

The weakness of the model is that the charge distribution is modeled continuous so that charge carriers are modeled punctiliously instead of owning a size. Thus, this model is particularly incorrect in the area that is close to the electrode, because charge carriers would also appear at points that are closer to the electrode than the radius of the ion species. These charge carriers increase the resulting double layer capacity unrealistically.

3.2.3 *Stern Double Layer*

This means that there are now two models, each of them can describe one phenomenon, while failing at another. The Helmholtz model

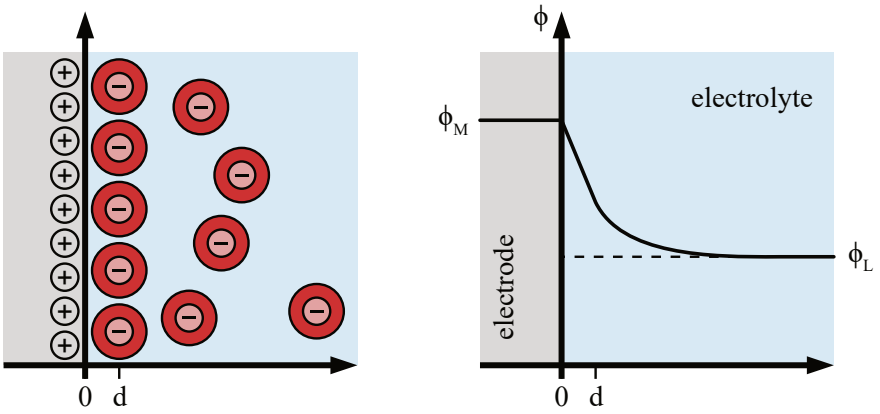

Figure 3.8: Scheme of Stern double layer and its development of potential.

produces capacity values that correspond to the measured values. However, the model does not explain the dependence of the capacity on the electrode potential. In contrast, the Gouy-Chapman model can describe this dependency, but returns values that are way too large[128]. That is why Otto Stern combined both models. According to Stern, the double layer is separated in two parts. A touching layer of ions, that is described by the Helmholtz model and a diffuse layer according to Gouy-Chapman whose charge continuously decreases to 0 (see Figure 3.8). The sum of charge in the Helmholtz layer q_H and in the diffuse layer $q_d$equals the charge in the electrode

$$q_M = q_H + q_d. \tag{3.12}$$

Although the total charge is given by the potential difference

$$q_M = \epsilon_0 \cdot \epsilon_R \cdot \frac{A}{d} \cdot (\phi_M - \phi_L), \tag{3.13}$$

the division still has to be clarified.
The charge in the Helmholtz layer is given by the number of absorbed anions n_- and cations n_+ by multiplying them by the charge per ion:

$$q_H = ze \cdot (n_- - n_+). \tag{3.14}$$

n_- and n_+ can be related to the potential in the Helmholtz layerϕ_L using the Boltzmann Distribution theorem:

$$n_+ = \frac{z_1}{1 + \frac{1}{c} e^{\frac{ze\phi_L}{kT}}} \tag{3.15}$$

$$n_- = \frac{z_1}{1 + \frac{1}{c} e^{\frac{-ze\phi_L}{kT}}} \tag{3.16}$$

The final result is

$$q_H = z \cdot \left(\frac{z_1}{1 + \frac{1}{c} e^{\frac{-ze\phi_L}{kT}}} - \frac{z_1}{1 + \frac{1}{c} e^{\frac{ze\phi_L}{kT}}} \right) \tag{3.17}$$

for the charge in the Helmholtz layer. So, q_M, q_H, and q_d of equation 3.12 can be replaced using equations 3.13, 3.17, and 3.10 which results in

$$\frac{\epsilon_0 \cdot \epsilon_R \cdot A}{d} (\phi_M - \phi_{DL}) = z \cdot \left(\frac{z_1}{1 + \frac{1}{c} e^{\frac{-ze\phi_{DL}}{kT}}} - \frac{z_1}{1 + \frac{1}{c} e^{\frac{ze\phi_{DL}}{kT}}} \right) + \\ + 2\sqrt{2\epsilon RTc} \sinh \left(\frac{z \cdot e \cdot \phi_{DL}}{2RT} \right) \quad (3.18)$$

As far as the material properties are known, ϕ_{DL} is the only unknown in the equation and is uniquely quantifiable. Hence, the total charge q_M and thus also the double layer capacity C_{DL} can be determined:

$$C_{DL} = \frac{q_M}{\phi_M} = \frac{\epsilon_0 \cdot \epsilon_R \cdot A}{d} \cdot \frac{\phi_M - \phi_{DL}}{\phi_M} \quad (3.19)$$

3.3 CHARGE TRANSFER RESISTANCE

Kinetics, that is the speed of a reaction, is the most important aspect regarding the cell performance. Chemical processes that need to overcome an activation energy at the molecular level are described by the Arrhenius equation

$$k_r = A \cdot e^{\frac{-E_a}{RT}} \quad (3.20)$$

which depends on a pre-exponential factor A that is a constant for each chemical reaction, the activation energy E_a, the universal gas constant R ,and the absolute Temperature T. The result k_r is a rate constant which describes the frequencies of collisions resulting in a reaction. Figure 3.9 illustrates the meaning of the activation energy. The energy level of the reactants is higher than the energy level of the product. Along the reaction coordinate, the transition state is defined to be the state with the highest potential energy. A successful reaction that forms the product only happens when the energy of a collusion of reactant molecules is high enough to reach the transition state, thus, the activation energy is exceeded. The Arrhenius equation states that the reaction rate increases exponentially when activation energy decreases.

The reaction rate can then be used to describe the rate of a reaction at an electrode. Generally the rate can be defined as rate constant multiplied with the molar concentration of the electroactive species $[X]$, thus the flux of material:

$$\text{flux} = k_r \cdot [X]. \quad (3.21)$$

Regarding the reactions of the zinc electrode this leads to

$$\text{rate}_{Ox} = k_c \cdot [\text{Zn}] \quad (3.22)$$

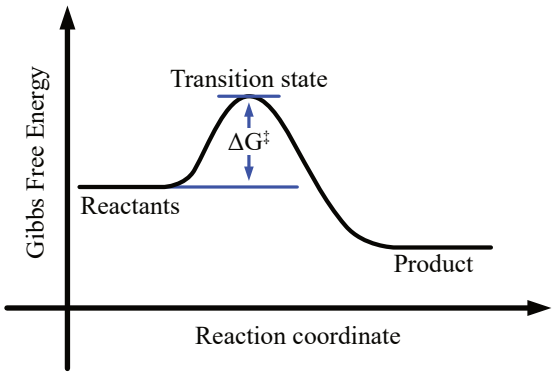

Figure 3.9: Relation of activation energy and enthalpy of an exothermic reaction.

when discharging the cell and to

$$\text{rate}_{Red} = k_a[\text{Zn(OH)}_4{}^{2-}] \tag{3.23}$$

for the charging process. Since the zinc concentration corresponds to the SoC,

$$\text{rate}_{Ox} = k_c \cdot \text{SoC}, \tag{3.24}$$

$$\text{rate}_{Red} = k_a \cdot (1 - \text{SoC}) \tag{3.25}$$

also apply. To derive the resulting current density j from the material flux, the flux must be multiplied by the charge per mole, i.e. the Faraday constant F. This leads to

$$j_c = F \cdot k_c \cdot [\text{Zn}] = FA_c \cdot [\text{Zn}] \cdot e^{\frac{-E_{a,c}}{RT}} \tag{3.26}$$

and

$$j_a = F \cdot k_a \cdot [\text{Zn(OH)}_4{}^{2-}] = FA_a \cdot [\text{Zn(OH)}_4{}^{2-}] \cdot e^{\frac{-E_{a,a}}{RT}}, \tag{3.27}$$

respectively. The net current density is their difference

$$\begin{aligned} j &= j_a - j_c, \\ j &= F \cdot k_a \cdot [\text{Zn(OH)}_4{}^{2-}] - F \cdot k_c \cdot [\text{Zn}], \\ j &= FA_a \cdot [\text{Zn(OH)}_4{}^{2-}] \cdot e^{\frac{-E_{a,a}}{RT}} - FA_c \cdot [\text{Zn}] \cdot e^{\frac{-E_{a,c}}{RT}}. \end{aligned} \tag{3.28}$$

According to Atkins[7], the influence of an electric potential on the activation energy is given by

$$E_a = E_a(0) + \alpha z F \cdot \Delta\phi. \tag{3.29}$$

Where: $E_a(0)$ is the activation energy in the absence of an electrical potential; z is the number of involved electrons of the electrode reaction, the sign of z is negative for the anodic process; the transfer

coefficient α lies in the range 0 to 1 and describes how closely the transition state resembles the product (ZnO). Thus, α is a symmetry factor that determines whether the process is more addicted to the charging or to the discharging process; Finally, $\Delta\phi$ is the potential difference between electrolyte solution and electrode metal[7, 106]

$$\Delta\phi = \phi_S - \phi_M. \tag{3.30}$$

The resulting current densities are therefore

$$j_c = FA_c \cdot [\mathrm{Zn}] \cdot e^{\frac{-E_{a,c}(0)}{RT}} \cdot e^{-\frac{\alpha z F \cdot \Delta\phi}{RT}}, \tag{3.31}$$

$$j_a = FA_a \cdot [\mathrm{Zn(OH)_4}^{2-}] \cdot e^{\frac{-E_{a,a}(0)}{RT}} \cdot e^{\frac{(1-\alpha) z F \cdot \Delta\phi}{RT}}. \tag{3.32}$$

If $\Delta\phi$ is chosen to be the open circuit electrode potential E, j_c equals j_a and the net current density j becomes 0. The remaining identical current densities at this electrode potential are summarized as parameter

$$\begin{aligned} j_0 &= FA_c \cdot [\mathrm{Zn}] \cdot e^{\frac{-E_{a,c}(0)}{RT}} \cdot e^{-\frac{\alpha z F \cdot E}{RT}}, \\ j_0 &= FA_a \cdot [\mathrm{Zn(OH)_4}^{2-}] \cdot e^{\frac{-E_{a,a}(0)}{RT}} \cdot e^{\frac{(1-\alpha) z F \cdot E}{RT}}. \end{aligned} \tag{3.33}$$

A change in potential can now be divided into open circuit electrode potential E and overpotential η:

$$\Delta\phi = E + \eta. \tag{3.34}$$

This results in the Butler-Volmer equation for the net current density:

$$j = j_0 \cdot \left(e^{\frac{(1-\alpha)F}{RT}\eta} - e^{-\frac{\alpha F}{RT}\eta} \right). \tag{3.35}$$

3.4 DIFFUSION

Diffusion describes the movement of atoms, ions, or molecules in order to balance a difference in concentration. As described earlier in Section 2.2.5, diffusion processes occur, for example, in a binary electrolyte where only one ion species is used for battery operation. We have this case in the zinc-air battery. According to Fick, the diffusion flux J is proportional to the negative of the concentration gradient:

$$J(x,t) = -D\frac{\partial c(x,t)}{\partial x}, \tag{3.36}$$

where c is the concentration of the corresponding species and D is the diffusion coefficient. x defines the one-dimensional coordinate, at which $x = 0$ corresponds to the electrode electrolyte interface. Combining equation 3.36 with continuity equation for mass conservation leads to Fick's second law which is known as Diffusion equation:

$$\frac{\partial c(x,t)}{\partial t} = -\frac{\partial J(x,t)}{\partial x} = \frac{\partial}{\partial x}\left(D\frac{\partial c(x,t)}{\partial x} \right) = D\frac{\partial^2 c(x,t)}{\partial x^2}. \tag{3.37}$$

In the later part of the thesis mainly data from EIS is used. Therefore, it makes sense to use the frequency domain. Thereby, the time derivative becomes a multiplication with $i\omega$ and the concentration is replaced by the perturbation in the concentration species $\tilde{c}$:

$$i\omega \cdot \tilde{c}(x) = D\frac{\partial^2 \tilde{c}(x)}{\partial x^2}. \tag{3.38}$$

Equation 3.38 is a second order ordinary differential equation which solution is given by

$$\begin{aligned} \tilde{c}(x) &= f_1 \exp\left(\tfrac{x}{\sqrt{D_i/i\omega}}\right) + f_2 \exp\left(-\tfrac{x}{\sqrt{D_i/i\omega}}\right), \\ \tilde{c}(x) &= f_1 \exp\left(\tfrac{x}{l_d}\right) + f_2 \exp\left(-\tfrac{x}{l_d}\right). \end{aligned} \tag{3.39}$$

$l_d = \sqrt{D_i/i\omega}$ is the frequency dependent diffusion length. f_1 and f_2 can be determined using boundary conditions. When considering the interface between the air electrode and the air, it can be assumed that the oxygen content of the air is almost constant. This assumption can be made because the maximum distance of ambient air $>> l_d$ for frequencies in the measurement range. But this assumption is also valid for the electrode electrolyte transitions, since the zinc-air cell used at this stage still uses large electrode spacing to have a buffer for dendrite formation. The bulk part of perturbation of the concentration at $x = \infty$ is therefore

$$\tilde{c}(\infty) = \tilde{c} = 0. \tag{3.40}$$

Thus, f_1 results in

$$f_1 = 0. \tag{3.41}$$

The diffusion speed at the electrode interface ($x = 0$) is given by the charge transfer reaction described in chapter 3.3 and related to the current density j:

$$D\frac{\partial \tilde{c}}{\partial x} = \pm\frac{\tilde{j}}{zF}. \tag{3.42}$$

This means that the diffusion speed increases proportional with the current density, but also depends on the charge number. A higher charge number indicates that a molecule reacts with more than one electron, so that a lower diffusion rate is sufficient to achieve the same current density. Thus,

$$f_2 = \pm\frac{l_d}{nFD} \cdot \tilde{j}. \tag{3.43}$$

It is now assumed that the perturbation of the electrode potential $\tilde{E}$ depends on the current density and on the concentration at the electrode interface:

$$\tilde{E} = Z_{int}\tilde{j} + \sum_i \beta_{d,i}\tilde{c}_i(x = 0), \tag{3.44}$$

where Z_{int} describes the interfacial impedance that consists of the charge transfer resistance and the double layer capacity, $\beta_{d,i}$ is a coefficient that describes the electrode potential change as a function of the concentration perturbation for species i. $\beta_{d,i}$ can be estimated using the Nernst equation,

$$E = E^0 + \frac{RT}{zF} \ln \left(\frac{\gamma_{ox} c_{ox}}{\gamma_{re} c_{re}} \right), \tag{3.45}$$

as long as the species concentration is not very low. E^0represents the equilibrium potential, and γ_i is the activity coefficient that describes the difference between activity and concentration. In the dilute limit ($\gamma = 1$), coefficient $\beta_{d,i}$ becomes

$$\beta_{d,i} = \frac{RT}{zF} \frac{1}{\bar{c}_i}. \tag{3.46}$$

Substituting equations 3.39, 3.46 into equation 3.44 and defining $Z = \tilde{E}/\tilde{j}$, we receive the so-called Warburg impedance

$$Z = Z_{int} + \frac{RT}{(nF)^2} \left(\frac{1}{\bar{c}_{ox}\sqrt{D_{ox}}} + \frac{1}{\bar{c}_{re}\sqrt{D_{re}}} \right) (i\omega)^{-0,5}. \tag{3.47}$$

4 REGRESSION METHODS

In chapter 3, the chemical reactions and interfaces are transferred into electrochemical models. However, unknown parameters remain in several places. Here, ranges of values can be partially defined on the basis of the literature. For example, the relative permittivity ϵ_r of the used KOH solution, which is necessary for the determination of the double layer capacitance, is about 3.3. Partly, the parameters also depend on the cell geometry. In general, the exact value of the parameters is not known and not constant. To stay with the example of the double layer capacitance, due to the open system, the concentration of the KOH solution will change with time and thus also the relative permittivity. Also, the active area of the double layer capacitance at the zinc anode is not constant, since it depends significantly on its porosity, which will decrease with increasing number of cycles. The parameters must therefore be considered unknown and need to be estimated. This chapter therefore first explains how the measured data from EIS can be used to fit the parameters of the battery model. The resulting parameter values can then be used to determine the system state, particularly the SoC. The later part of the chapter also introduces machine learning methods based on Artificial Neural Networks (ANN) and Support Vector Regression (SVR). These allow direct regression of the SoC, even without an exact knowledge of the battery model.

4.1 EQUIVALENT CIRCUIT MODELING

As indicated at the beginning of Chapter 3, the models of the chemical processes can be combined to form an equivalent circuit shown in Figure 4.1. The battery model is then a combination of a voltage source $V_{\text{off-load}}$, which applies the open-circuit voltage of the battery, and a series impedance Z_i that describes the frequency dependent losses in the cell and at the interfaces. Z_i in turn is made up of further components that describe the electrochemical model. In general, the resulting series impedance is frequency dependent. By measuring several impedance values at different frequencies, the parameter values of the individual components of the equivalent impedance circuit can then be determined or approximated.
Separate models for charging and discharging are used, since different electrode are used, respectively. While the zinc electrode is used for both processes, there are separate electrodes for charging and discharging. Like in primary bottom cells, a GDE made of graphite is used for discharging. During charging process a separate nickel grid

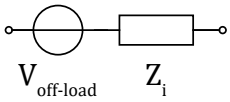

Figure 4.1: Equivalent circuit of a battery.

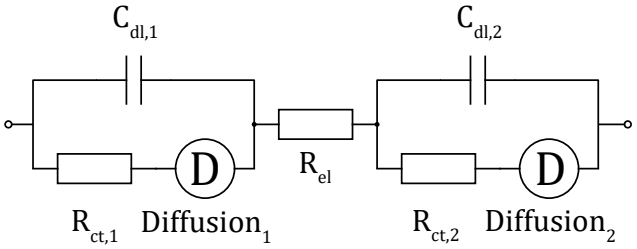

Figure 4.2: Equivalent impedance of the zinc-air battery during charging process.

is used. Both models consist of three parts, anode, electrolyte, and cathode, respectively. The electrical model of the series impedance during charging can be found in Figure 4.2, while Figure 4.3 shows the series impedance during discharging. The electrolyte works as an ion conductor and is approximated by a simple resistor R_{el}. Anode and cathode consist of three components. The capacitor C_{dl} describes the double layer capacity of the electrode while the resistor R_{ct} approximates the charge-transfer resistance[6]. The diffusion processes are marked with a D. The diffusion component describes the behavior at two different states of aggregation. So during charging there is one change between nickel net and electrolyte and one between electrolyte and zinc anode, resulting in one diffusion process per electrode (see Figure 4.2). The zinc anode is also used for discharging. However, the air electrode is now used as the counter electrode. Two diffusion processes take place here, one at the electrolyte - electrode interface and one at the electrode - ambient air interface. This is because the oxygen in the ambient air must also diffuse to the electrode[6]. In Figure 4.3, therefore, two diffusion processes are present at the right electrode, which represents the GDE. However, a separation of the influence of the respective diffusion process is not possible due to the series connection. The complex term of a diffusion process Z_d (equation 3.47) has the form

$$Z_d = a(i\omega)^{-0,5}. \tag{4.1}$$

The series connection of two diffusion processes

$$Z_{d,\text{series}} = a_1(i\omega)^{-0,5} + a_2(i\omega)^{-0,5}, \tag{4.2}$$

though, can be returned to the original form with changed values:

$$Z_{d,\text{series}} = (a_1 + a_2)\,(i\omega)^{-0,5}. \tag{4.3}$$

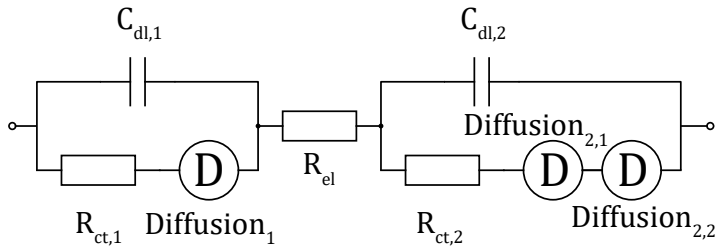

Figure 4.3: Equivalent impedance of the zinc-air battery during discharging process.

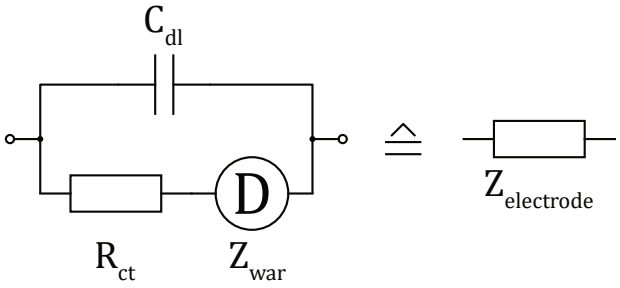

Figure 4.4: Interconnection of the impedance of an electrode.

Since only the voltage and current at the outer terminals are considered during EIS, the two diffusion processes cannot be considered separately, but act as a single diffusion process with the absolute of the impedance being added.

4.1.1 *Formation of the Equivalent Circuit*

When forming the series impedance, the well-known Kirhoff's laws can be used. This means that the total admittance of a parallel circuit is given by the sum of the admittances of the components and that the total impedance of a series circuit is given by the sum of the impedances of the individual components. The chemical processes of an electrode are interconnected as shown in Figure 4.4. The total impedance of the electrode is therefore

$$Z_{\text{electrode}} = \frac{1}{Y_{C_{\text{dl}}}(f,C,V)+\frac{1}{R_{\text{ct}}(j_0,\alpha,V,E_a)+Z_{\text{war}}(f,V,\beta)}}$$
$$Z_{\text{electrode}} = \frac{R_{\text{ct}}(j_0,\alpha,V,E_a)+Z_{\text{war}}(f,V,\beta)}{1+Y_{C_{\text{dl}}}(f,C,V)R_{\text{ct}}(j_0,\alpha,V,E_a)+Y_{C_{\text{dl}}}(f,C,V)Z_{\text{war}}(f,V,\beta)} \tag{4.4}$$

The entire cell then consists of the two representing the contact resistances of the terminals, the two electrodes and the electrolyte resistor as shown in Figure 4.5. While the two electrode impedances are formed according to equation 4.4, the contact and electrolyte resistances are approximately ohmic resistances. Since Kirchoff's laws also apply here, the ohmic resistances can be combined and it is not

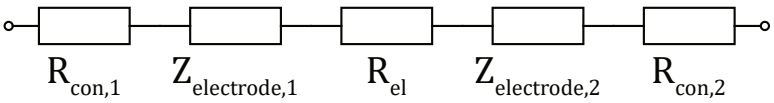

Figure 4.5: Interconnection of the impedances of the zinc-air cell.

possible to separate the measurement data to determine the respective proportions.
Some of the components of the individual processes are nonlinear functions that depend on subparameters, but also have nonlinear dependencies on the voltage itself. Here, for example, the double layer capacitance is to be mentioned. As long as only the Helmholtz model is considered, the charge of the capacitor is proportional to the applied voltage and a constant capacitance can be defined. But if the double layer is extended by the Gouy-Chapman model, there is a cosine hyperbolic dependence on the applied potential. Also the charge transfer resistance is not constant, since the resulting current increases exponentially with the applied voltage. If a linear description is required, linearization may be necessary. In this case, a linear approximation at the working point is used. The deviation of the linear approximation from the actual nonlinear model can be determined with the help of the remainder term of Taylor's theorem. According to MacDonald, the potential deviation per cell should be less than 10mV for the linearized model to be sufficiently accurate[8].

Double Layer Capacity

In section 3.2, the Stern double layer model is presented. According to equation 3.18, the charge is divided into an ion layer attached to the electrode and a diffuse ion layer. In this model, the capacitance of the adjacent Helmholtz layer is independent of the electrode potential. In contrast, the diffuse Gouy-Chapman layer shows a dependence on the potential of the electrode. Due to the parallel connection of the layers, the total capacitance is[107]

$$C_{\text{DL,Stern}}. = C_H + C_{GC}\left(\phi_0\right). \tag{4.5}$$

Since the capacitance defines the ratio of charge to voltage of a capacitor, the charge of the double layer is

$$q_{\text{DL,Stern}}\left(\phi_0\right) = C_H \cdot \phi_0 + C_{GC}\left(\phi_0\right) \cdot \phi_0 \tag{4.6}$$

The Helmholtz capacitance is constant with respect to the electrode potential ϕ, it can therefore be considered as a constant in a linearization, so that

$$\begin{gathered} C_{DL} = \frac{dq_{\text{DL,Stern}}}{d\phi_0} \mid_{\phi} = \frac{d}{d\phi_0} C_H \cdot \phi_0 + C_{GC}\left(\phi_0\right) \cdot \phi_0 \mid_{\phi}, \\ C_{DL} = C_H + C_{GC}\left(\phi\right) + \frac{dC_{GC}(\phi_0)}{d\phi_0} \mid_{\phi} \cdot \phi \end{gathered} \tag{4.7}$$

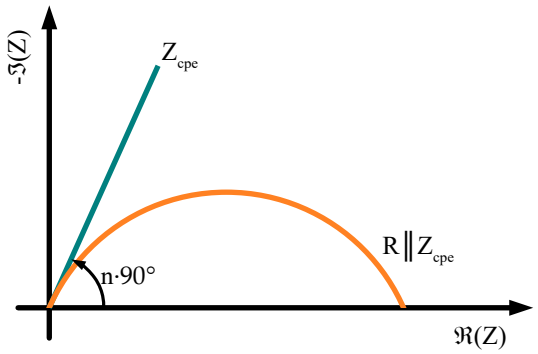

Figure 4.6: Nyquist plot illustrating the constant phase element.

results for the linearized capacitance.
In practice, the measured impedance spectra often do not show ideal behavior of the double layer capacitance. For example, as shown in Figure 4.6, the semicircles in the Nyquist plot created by paralleling the double layer capacitance and the charge transfer resistor do not start at a 90° angle to the real axis. Instead, it appears that the center of the plot is not on the real axis, so the semicircle begins at a more acute angle. Among other things, the porosity of the electrode was identified as the cause, since it is not an ideal two-dimensional geometry[97]. Another aspect concerns the edge regions of the cell in which the homogeneity of the current density cannot be guaranteed[61].
The so-called constant phase element is often used to model this behavior. Its impedance is described by equation

$$Y_{\text{cpe}} = \frac{1}{Z_{\text{cpe}}} = Q^{\circ} \cdot (i\omega)^{n}\,. \tag{4.8}$$

Here, Q approximately describes the capacitance and n determines the ratio of the angle compared to a right angle. For $n = 1$, this again results in the ideal impedance of a capacitance

$$Y_{\text{cpe}}(n = 1) = Q^{\circ} \cdot (i\omega) = i\omega C. \tag{4.9}$$

Charge Transfer Resistance

The charge transfer resistance is mainly described by the Butler-Volmer equation. An increase of the potential results in an exponential increase of the electrode current. Figure 4.7 shows the resulting current density for $\alpha = 0.5$, $j_0 = 10\,\frac{\text{mA}}{\text{m}}$ and an absolute temperature of 300 K as an example. In order to create the equivalent circuit, the charge transfer resistor will be replaced by a linearized ohmic resistor. The linearization is shown here for $\eta = 150\,\text{mV}$. The differential slope at this working point determines the linearized admittance.

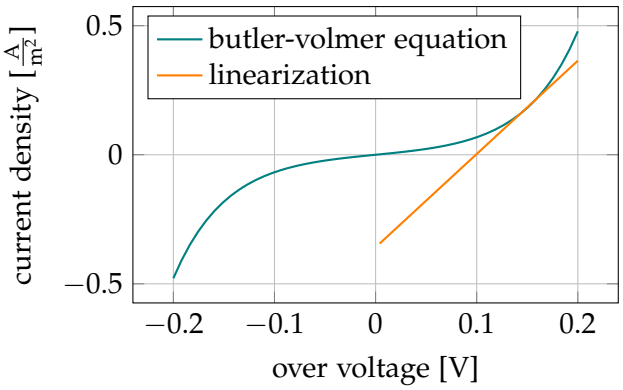

Figure 4.7: Linearization of the Butler-Volmer equation.

Since equation 3.35 is already rearranged for the current density j, it appears useful to determine the linearized admittance first:

$$\begin{aligned} Y_{ct} &= \frac{dj}{d\eta} \mid_{\eta_{wp}} = \frac{d}{d\eta} j_0 \cdot \left(e^{\frac{(1-\alpha)F}{RT}\eta} - e^{-\frac{\alpha F \eta}{RT}\eta} \right) \mid_{\eta_{wp}}, \\ Y_{ct} &= j_0 \cdot \left(\frac{(1-\alpha)F}{RT} e^{\frac{(1-\alpha)F}{RT}\eta} + \frac{\alpha F}{RT} e^{-\frac{\alpha F \eta}{RT}\eta} \right) \mid_{\eta_{wp}} . \end{aligned} \tag{4.10}$$

The associated charge transfer impedance is then determined by inverting the admittance:

$$Z_{ct} = \frac{1}{Y_{ct}} = \frac{1}{j_0} \cdot \frac{1}{\frac{(1-\alpha)F}{RT} e^{\frac{(1-\alpha)F}{RT}\eta} + \frac{\alpha F}{RT} e^{-\frac{\alpha F \eta}{RT}\eta}} \mid_{\eta_{wp}} . \tag{4.11}$$

After applying the (real) overvoltage of the working point η_{wp} in equation 4.11, a real value that is independent of the frequency also results for the charge transfer resistor. Consequently, the charge transfer resistance can be modeled by an ohmic resistor:

$$Z_{ct} = R_{ct} \left(j_0, \alpha \right) . \tag{4.12}$$

Diffusion

The Warburg impedance has already been derived in equation 3.47 in order to describe the diffusion process. This impedance can be used directly in the electrical equivalent circuit and does not require linearization.

4.1.2 *Parameter Fitting*

After having selected a matching equivalent circuit to a measured impedance spectrum, the parameters of the individual elements have to be determined. Therefore, the model parameters have to be adjusted until the differences to the measured values are minimized. This regression is called fitting. Remaining differences of the approximated solution to the measured values are residuals and are used to

measure the performance of the fit. For the calculation of impedance models, the method of least squares for nonlinear model functions is widely used. This has been extended by Macdonald et al. to a complex form which is known as the Complex-Nonlinear Least-Squares (CNLS) concept. The CNLS method uses the Kramers-Kronig relationship to perform a simultaneous calculation of the squared errors of the real and imaginary parts of the impedance[8, 105, 116, 138].
In order to have a constant electrical equivalent circuit, the linearity and time invariance for the impedance measurement must be ensured. High stimulus currents can disturb the linearity and thermal and system drifts can influence the time invariance. The Kramers-Kronig relationship can be used to check these conditions. This was derived simultaneously, but independently of Kramers and Kronig in dispersion studies in the X-ray region[67, 68]. The method was transferred by Bode to impedance measurements[15]. If the above mentioned conditions are fulfilled, a link between real and imaginary part exists, so that one property can be calculated by the other. Equations 4.13 and 4.14 show a possible method to determine the course of the real part from the course of the imaginary part and vice versa. Thus, a validation of the measured data can be performed based on the deviation to a calculated impedance quantity according to Kramer-Kronig relationship[16, 17, 62, 138].

$$\Im\{Z\}(\omega) = -\left(\frac{2\omega}{\pi}\right)\int_0^\infty \frac{\Re\{Z\}(\omega') - \Re\{Z\}(\omega)}{\omega'^2 - \omega^2}\mathrm{d}\omega' \tag{4.13}$$

$$\Re\{Z\}(\omega) = \Re\{Z\}(\omega \to \infty) + \\ + \left(\frac{2}{\pi}\right)\int_0^\infty \frac{\omega' \cdot \Im\{Z\}(\omega') - \omega \cdot \Im\{Z\}(\omega)}{\omega'^2 - \omega^2}\mathrm{d}\omega' \tag{4.14}$$

The minimization problem of the CNLS is defined as the sum of the squared errors of two dependent variables considering the real part f_r and the imaginary part f_i separately in equation 4.15. The model function $f_t(\omega_i, P)$ depends on the angular frequency ω_i and the parameter set to optimize P. $y_{r,i}$ are the corresponding measured values of the impedance spectrum and $w_{r,i}$ are corresponding weighting factors. Alternatively to real and imaginary part, absolute value and phase could be chosen as well. For the stabilization of the fitting a proportional weighting was chosen[8].

$$E_{\mathrm{CNLS}} = \sum_{l=1}^{k}\left\{w_l^r\left[f_{el}^r - f_t^r(\omega_l, P)\right]^2 + w_l^i\left[f_{el}^i - f_t^i(\omega_l, P)\right]^2\right\} \tag{4.15}$$

Numerical methods such as the Gauss-Newton method or the Newton method can be used to solve this equation. Here, the optimum is gradually approached, with the step direction and width being determined

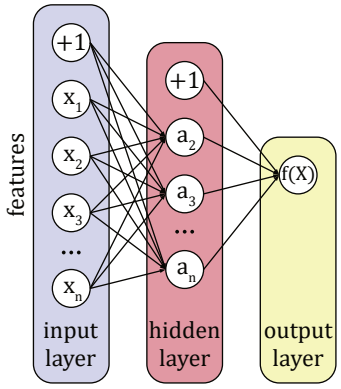

Figure 4.8: General structure of artificial neural networks.

on the basis of the first and the first two derivatives at the current point, respectively. The numerical Levenberg-Marquardt algorithm is often used. The method combines the Gauss-Newton method with a regularization technique that forces descending function values. This allows the solution to converge faster and with higher probability, even with poor initial conditions[75, 89].

4.2 ARTIFICIAL NEURAL NETWORKS

ANN are networks of artificial neurons, each of them inspired by the biological model. McCulloch and Pitts introduced a threshold element as first artificial neuron that outputs a Boolean value o_j depending on the sum of input signals x_i[92]. By now, a commonly used implementation of a neuron is the perceptron model which extends the threshold element by a weighting of the input signals w_{ij}[114]:

$$o_j = \begin{cases} 1 & \sum_i w_{ij} x_i + b > 0 \\ 0 & \text{otherwise} \end{cases} \tag{4.16}$$

The general structure of feed forward networks is shown in Figure 4.8 and allows only a signal flow in forward direction. There are also network structures that allow a feedback to a previous layer, e.g. Recurrent Neural Networks. Several neurons are organized in layers. When using perceptron neurons, these networks are called Multilayer Perceptron. The first layer is called the input layer and represents the features of an input sample extended by a constant bias. The bias can be used as a threshold value by the following layer. Here, only one hidden layer is illustrated, but multiple hidden layers are also possible. The signal flows through all hidden layers until in reaches the output layer. Each neuron in the output layer represents an output value[136].

Multilayer perceptron networks are used in applications where an input sample is associated with an output class or an output variable.

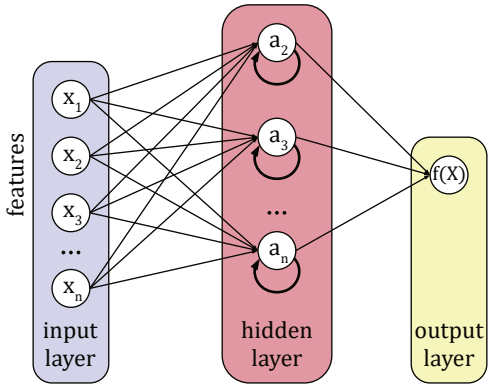

Figure 4.9: Elman structure of recurrent neural networks.

The input example can thereby be described in a higher-dimensional feature space. The structure is characterized in particular by the fact that the order in which example data are evaluated by the previously trained network has no influence on the individual result, the network has no memory.
In contrast, the structure of a Recurrent Neural Network is shown in Figure 4.9. In this concrete case it is an Elman structure, where the values of the hidden units are stored within the feedback loop and are then available as input values in the subsequent data set. The output of the network thus also depends on the internal state of the network, which is determined by the previous data. Recurrent Neural Networks are therefore very well suited for modeling sequences, as found in time series analysis. They are also successfully used for the analysis of sentences, which consist of words and letters.

4.2.1 *Activation Functions*

The activation of a neuron according to equation 4.16 has a discontinuous change of the output from 0 to 1 when crossing 0. Thus, it is not possible to use this type of activation when using gradient based training algorithms. Therefore, derivable or continuously derivable functions with a similar progression are often used. Figure 4.10 shows several common activation functions , where the input of the activation function is the weighted sum of input $v = \sum_i w_{ij} x_i$. A simple derivable function is the piece wise linear:

$$\phi^{pwl}(v) = \begin{cases} 1 & \text{if } v \geq \frac{1}{2} \\ v + \frac{1}{2} & \text{if } -\frac{1}{2} < v < \frac{1}{2} \\ 0 & \text{if } v \leq -\frac{1}{2} \end{cases} \tag{4.17}$$

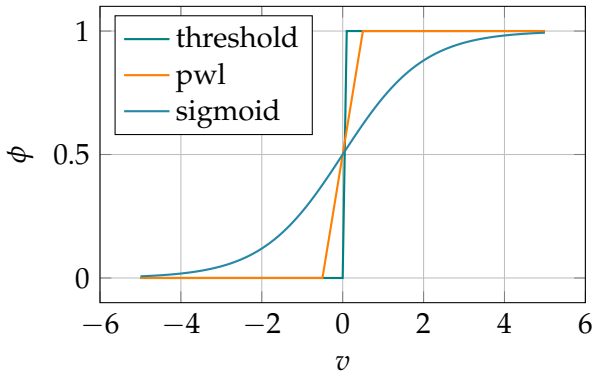

Figure 4.10: Different activation functions for perceptron neurons.

Another activation function is the Sigmoid function that represents a "S"-curve which curvature can be controlled by parameter a. It is commonly used, because it is easily derivable[136]:

$$\phi^{sig}(v) = \frac{1}{1+\exp(-av)} = \frac{\exp(av)}{1+\exp(av)} = \frac{1}{2}\left(1+\tanh\frac{av}{2}\right) \quad (4.18)$$

Radial basis function networks use an entirely different activation function. These are networks with exactly one hidden layer. The activation functions of the neurons in the hidden layer are based on the Gaussian radial basis function:

$$\phi^{rbf}(x;\mu,\sigma^2) = \frac{1}{\sqrt{2\pi\sigma^2}}\exp\left(-\frac{(x-\mu)^2}{2\sigma^2}\right) \quad (4.19)$$

While x is input vector of the network, the parameters μ and σ^2 represent the mean and the variance activation function. In fact, ϕ^{rbf} correspond to probability density of a Gaussian or Normal distribution[136]. The course of the one-dimensional function is shown in Figure 4.11. It is a symmetric function which center can be shifted using parameter μ. The variance can be used to change the width of the distribution. This means that the activation is high whenever the input vector is similar to the mean value.

4.2.2 *Training Algorithms*

Training algorithms are used to set weights of each neuron. When small logic functions (AND, OR, etc.) are patterned, it is possible to manually set those weights. However, ANNs are frequently used in applications with huge datasets. Therefore, an algorithms have been developed that autonomously optimize the weights of the network. These algorithms can be divided into supervised and reinforced learning. In this thesis, supervised learning is used exclusively which means that the training samples also contain target values t_j for the

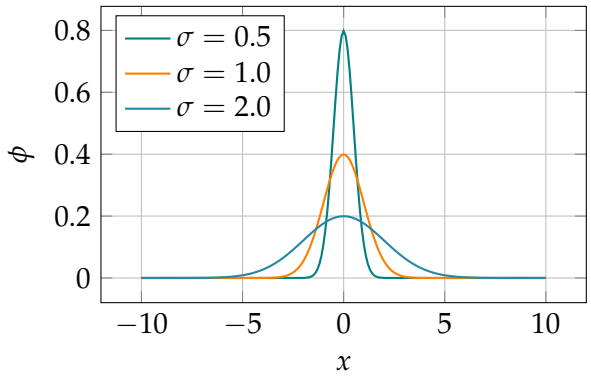

Figure 4.11: Gaussian distribution used in RBF networks.

output j.
One example is the Perceptron Learning Rule that works for binary input and output signals. The idea is that the weight is incremented when the output is 0, but should be 1; the weight is decremented when the output is 1, but should be 0 ;and the weight left unchanged, when the output corresponds to the expectation[114]:

$$\begin{aligned} \Delta w_{ij}^{perceptron} &= \alpha \cdot \left(t_j - o_j\right) \cdot x_i \\ w_{ij}(k+1) &= w_{ij}(k) + \Delta w_{ij} \end{aligned} \quad . \tag{4.20}$$

Where t_j is the target value and α sets the learning rate. However, this approach only works when all training data is linear separable.
The delta rule overcome this problem by minimizing the error function

$$E_\Delta = \sum_j \frac{1}{2} \left(t_j - o_j\right)^2 \tag{4.21}$$

using a gradient decent. This means that the activation function have to be derivable. The weight space of the neurons is moved against the direction of the gradient of E_Δ with respect to each weight

$$\frac{\partial E_\Delta}{\partial w_{ij}} = \frac{\partial \frac{1}{2} \left(t_j - o_j\right)^2}{\partial w_{ij}}. \tag{4.22}$$

Since we differentiate with respect to the weights of jth neuron, the weights of the other neurons in the sum vanishes. Inserting

$$o_j = \phi \left(\sum_i w_{ij} x_i \right) = \phi \left(v \right) \tag{4.23}$$

and applying the chain rule results in

$$\frac{\partial E_\Delta}{\partial w_{ij}} = - \left(t_j - o_j\right) \cdot x_i \cdot \phi'(v). \tag{4.24}$$

Once again a learning rate is used for weight update and the minus sign is eliminated for moving in the direction of the minimum. This results in update equation

$$\Delta w_{ij}^{delta} = \alpha \left(t_j - o_j\right) \cdot x_i \cdot \phi'(v). \tag{4.25}$$

The delta rule is only applicable to single layer-layer neural networks. A generalized form is the Error Backpropagation learning. It uses the very same error function to minimize:

$$E_{ebp} = \sum_j \frac{1}{2} \left(t_j - o_j\right)^2. \tag{4.26}$$

However, the adjustment of the weights depends on whether the neuron is in the output layer or in the hidden layer:

$$\Delta w_{ij}^{ebp} = -\alpha \frac{\partial E}{\partial w_{ij}} = \alpha \delta_j o_i \tag{4.27}$$

and

$$\delta_j = \begin{cases} \phi'(v) \left(t_j - o_j\right) & \text{if } j \text{ corresponds to an output neuron} \\ \phi'(v) \sum_k \delta_k w_{jk} & \text{if } j \text{ corresponds to hidden neuron} \end{cases}. \tag{4.28}$$

Here i corresponds to prior neurons of j and k corresponds to subsequent neurons. This means that o_i is the input of neuron j, for the first layer o_i equals x_i. Moreover, for hidden neurons the weight adjustment depends on the error of the subsequent neurons. Thus, the error is back propagated to hidden neurons. The Error Backpropagation algorithm is also a gradient decent based, which makes it vulnerable for finding local minima. Therefore, different solutions are possible for different weight initialization.
There are some other weaknesses that are tackled by some extensions to that algorithm. Firstly, the weight adjustment is based on the derivative of the activation function. As one can see in Figure 4.12, the derivative of the Sigmoid function is very small in the outer areas which can lead to small adjustment for large errors. The heuristic approach extension instead uses a linear curve between output and target values for calculating the weight adjustment[136].
Secondly, the algorithm tends to oscillate when the learning rate is too large (see Figure 4.13). Several approaches make use of a momentum term in order to smooth the solution process. This means that the Weight increment depends not only on the error, but also on the increment of the previous step[115, 122, 136]:

$$\Delta w_{ij}(n+1) = \beta \Delta w_{ij}(n) + \gamma \Delta w_{ij}(n-1). \tag{4.29}$$

The tendency to oscillations can also be tackled by lowering the learning rate constant. However, this also decreases the training speed.

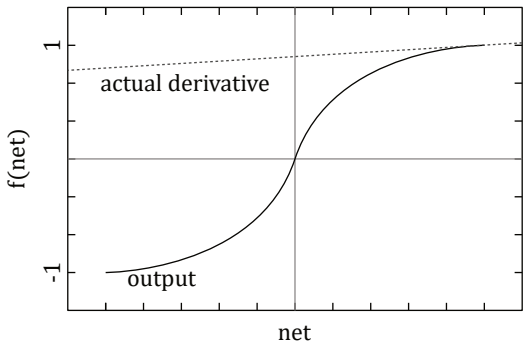

Figure 4.12: Lack of Error Backpropagation for very large error.

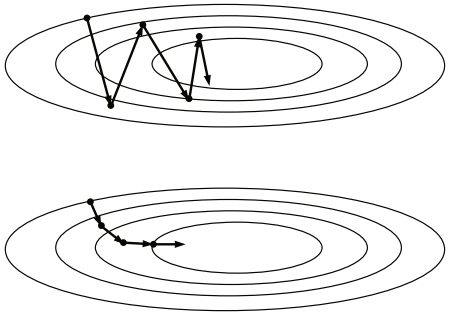

Figure 4.13: Solution process of Error Backpropagation without and with momentum term.

In contrast, the directional search extension can speed up the solution process. The idea is to look for a minimum in gradient direction before the calculation for a new gradient. The minimum in gradient direction can be found using the Newton-Raphson method.
The Levenberg-Marquardt algorithm can improve the convergence speed as well and is based on the Gauss-Newton algorithm. According to that, for sum of squares performance functions like equations 4.21and4.26 the Hessian can be approximated as

$$H \approx J^T J. \tag{4.30}$$

Where J is the Jacobi matrix of the performance function that can be calculated using the Error Backpropagation algorithm. Close to the minimum of the error function, the Gauss-Newton algorithm tend to be faster and more accurate. However, the gradient decent algorithm is

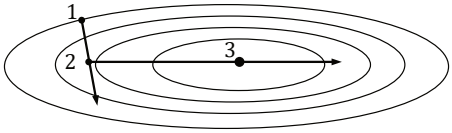

Figure 4.14: Directional search on the gradient direction when using Error Backpropagation algorithm.

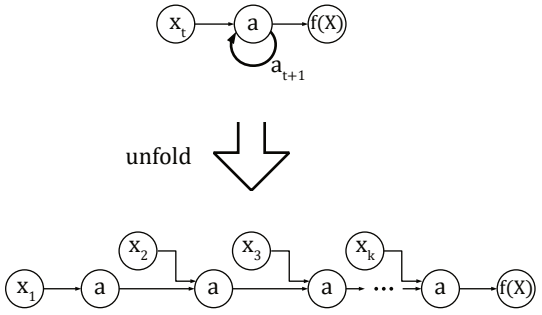

Figure 4.15: Illustratin of backpropagation through time method.

faster at the beginning. Therefore, the Levenberg-Marquardt algorithm extends the weight increment to

$$\Delta w_{ij}^{lm} = -\left[J^T J + \beta I\right] E \tag{4.31}$$

where I is the identity matrix and E correspond to the matrix of error values. At the beginning of the training β is set to a larger value resulting in a gradient decent. When reaching the optimal solution, β becomes closer resulting in the Gauss-Newton algorithm[75, 89, 136].
In Recurrent Neural Networks, the Error Backpropagation algorithm cannot be used in its original form because the recurrent loops preventing it. With the help of the Backpropagation Through Time method, this problem can be overcome. Backpropagation Through Time is a method based on Backpropagation. Here, the Error Backpropagation method is extended by a time factor. Since the output of a Recurrent Neural Network depends on the order of the data, the training data is an ordered sequence of k input and output pairs $\langle x_1, y_1\rangle, \langle x_2, y_2\rangle, \ldots, \langle x_k, y_k\rangle$. In order to subsequently apply the original Backpropagation algorithm, the Recurrent Neural Network must be unfolded. This approach is illustrated in Figure 4.15, where the unfolded network now processes the input sequence entirely in one run, rather than sequentially. The unfolded network thus contains k inputs. The recurrent components of the original network are completely duplicated for each required time step. The Backpropagation algorithm is then applied to the expanded network.
The complexity of the resulting unfolded network increases drastically when increasing the length of the training sequence. This can lead to problems when using the Backpropagation algorithm because, as shown in the corresponding equation 4.28, the variations of the weights depend also on the gradients of the errors of the subsequent neurons. In case of a long sequence, the error term of the unfolded network is multiplied accordingly many times. Provided that the error term is smaller than 1, a frequently repeated multiplication results in a value close to 0 (vanishing gradient problem). On the other hand, the magnitude of the error term could also be larger than 1, so that after repeated multiplication the resulting gradients explode and the

gradient descent becomes unstable. For deep recurrent neural networks the Backpropagation Through Time Algorithm is therefore not suitable, instead other structures like the Long Short-Term Memory module should be used.

4.3 SUPPORT VECTOR REGRESSION

The basic idea of ϵ-SVR is finding the flattest function $f(x)$ whose deviation from the training data is not larger than a given parameter ϵ. In case of a linear function

$$f(x) = \langle w, x \rangle + b \tag{4.32}$$

where $\langle \cdot, \cdot \rangle$ denotes the dot product, the resulting optimization problem is given by:

$$\begin{aligned} &\text{minimize} \quad \tfrac{1}{2} \parallel w \parallel^2 \\ &\text{subject to} \quad \begin{Bmatrix} y_i - \langle w, x_i \rangle - b & \leq & \epsilon \\ \langle w, x_i \rangle + b - y_i & \leq & \epsilon \end{Bmatrix} \end{aligned} \tag{4.33}$$

Here, the flatness is defined as norm of the parameter vector, $\parallel w \parallel^2 = \langle w, w \rangle$. The constraints mean, that training data with an error smaller than ϵ is not taken into account while errors larger than ϵ are not acceptable[123, 131].
However, depending on the type of function it is not always feasible to find a function that keeps the deviation small enough for all training data. Under certain circumstances, this function does not exist. Therefore, the margin can be softened depending on the training data by using slack variables ξ_i and ξ_i^* which belong to a positive or negative error, respectively:

$$\begin{aligned} &\text{minimize} \quad \tfrac{1}{2} \parallel w \parallel^2 + C \sum_{i=1}^{l} (\xi_i + \xi_i^*) \\ &\text{subject to} \quad \begin{Bmatrix} y_i - \langle w, x_i \rangle - b & \leq & \epsilon + \xi_i \\ \langle w, x_i \rangle + b - y_i & \leq & \epsilon + \xi_i^* \\ \xi_i, \xi_i^* & \geq & 0 \end{Bmatrix} \end{aligned} \tag{4.34}$$

The margin is extended by the slack variables, so that deviations larger than ϵ are now acceptable, but penalized. Figure 4.16 illustrates the development of the penalty. As long as the deviation is within the ϵ margin, no penalty is applied. If the deviation becomes larger than ϵ, the penalty increases with a slope defined by the parameter C. Thus, there is a trade-off between the flatness of the resulting function and the size of remaining deviation that can be set by constant C. This trade-off is especially important because flatter functions tend to be

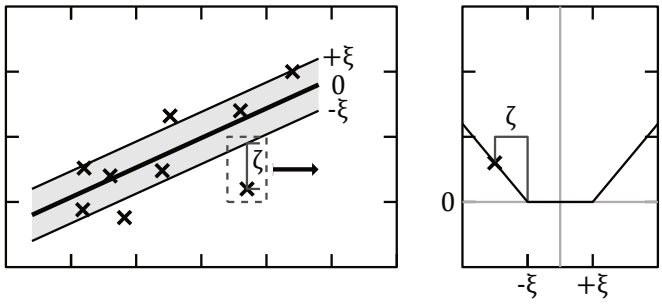

Figure 4.16: Penalization of training data with a deviation larger as ϵ

more robust to unseen data.
Lagrange multipliers can be used to find the extremum of a (optimization) function $f(x)$ with constraints $g(x)$. The basic idea is that at the point of extremum the gradients of $f(x)$ and $g(x)$ need to point in the same direction. Otherwise it would be possible to increase or decrease the value of $f(x)$ by moving along $g(x)$. However, while the gradient vectors have to point in the same direction, they don't necessarily have the same length. Therefore, the Lagrange multiplier λ is added to the gradient of $g(x)$ in order to re-scale its vector length. The resulting constraint for an extremum of $f(x)$ at $g(x)$ is

$$\nabla f(x) = \lambda \nabla g(x). \tag{4.35}$$

Applied to equation 4.34 $f(x) - \lambda g(x)$ gives the so-called Lagrangian:

$$\begin{aligned} L := \frac{1}{2} \parallel w \parallel^2 + C \sum_{i=1}^{\iota} (\xi_i + \xi_i^*) - \sum_{i=1}^{\iota} (\eta_i \xi_i + \eta_i^* \xi_i^*) + \\ - \sum_{i=1}^{\iota} \alpha_i \left(\epsilon + \xi_i - y_i + \langle w, x_i \rangle + b\right) + \\ - \sum_{i=1}^{\iota} \alpha_i^* \left(\epsilon + \xi_i^* + y_i - \langle w, x_i \rangle - b\right) \end{aligned} \tag{4.36}$$

where η_i, η_i^*, α_i, α_i^* represent the Lagrange multipliers. According to the saddle point condition of equation 4.35 the partial derivatives of L with respect to ω, b, ξ_i ,and ξ_i^* have to be zero:

$$\frac{\partial L}{\partial b} = \sum_{i=1}^{\iota} (\alpha_i^* - \alpha_i) = 0 \tag{4.37}$$

$$\frac{\partial L}{\partial \omega} = \omega - \sum_{i=1}^{\iota} (\alpha_i - \alpha_i^*) \, x_i = 0 \tag{4.38}$$

$$\frac{\partial L}{\partial \xi_i} = C - \alpha_i - \eta_i = 0 \tag{4.39}$$

$$\frac{\partial L}{\partial \xi_i^*} = C - \alpha_i^* - \eta_i^* = 0 \tag{4.40}$$

Constants α_i and α_i^* define the resulting support vectors. η_i and η_i^* can be eliminated through equations 4.39 and 4.40 as $\eta_i^{(*)} = C - \alpha_i^{(*)}$. Furthermore, ω can also be expressed as

$$\omega = \sum_{i=1}^{\iota} (\alpha_i - \alpha_i^*)\, x_i \tag{4.41}$$

which is known as Support Vector expansion, since ω can completely be described by a linear combination of the training data[123].The substitution of equations 4.37 to 4.40 into 4.36 results in the optimization problem

$$\begin{aligned} \text{maximize} \quad & -\tfrac{1}{2} \textstyle\sum_{i,j=1}^{\iota} (\alpha_i - \alpha_i^*) \left(\alpha_j - \alpha_j^*\right) \langle x_i, x_j \rangle + \\ & -\epsilon \textstyle\sum_{i=1}^{\iota} (\alpha_i + \alpha_i^*) + \sum_{i=1}^{\iota} y_i (\alpha_i - \alpha_i^*) \\ \text{subject to} \quad & \textstyle\sum_{i=1}^{\iota} (\alpha_i - \alpha_i^*) = 0 \text{ and } \alpha_i, \alpha_i^* \in [0, C] \end{aligned} \quad . \tag{4.42}$$

The result of the optimization problem determines the linear combination of the training data that is used to describe ω. Finally, the complete algorithm can be described using the data, even the evaluating $f(x)$:

$$f(x) = \sum_{i=1}^{\iota} (\alpha_i + \alpha_i^*) \langle x_i, x \rangle + b. \tag{4.43}$$

According to the Karush-Kuhn-Tucker conditions, the product of the primal variables and the constraints vanishes at the point of solution:

$$\begin{aligned} \alpha_i (\epsilon + \xi_i - y_i + \langle \omega, x_i \rangle + b) &= 0 \\ \alpha_i^* (\epsilon + \xi_i^* + y_i - \langle \omega, x_i \rangle - b) &= 0 \end{aligned} \tag{4.44}$$

and

$$\begin{aligned} (C - \alpha_i)\, \xi_i &= 0 \\ (C - \alpha_i^*)\, \xi_i^* &= 0 \end{aligned} \quad . \tag{4.45}$$

Firstly, equation 4.45 means that only samples (x_i, y_i) with $\alpha_i^{(*)} = C$ lie outside the ϵ-tube[123], because either $\xi_i^{(*)}$ is zero which means that the sample lies inside the ϵ-tube or $\xi_i^{(*)} > 0$, but then $\alpha_i^{(*)}$ has to equal C in order to fulfill the equation. Secondly, according to equation 4.44 $\alpha_i^{(*)} = 0$ for samples that lie inside the ϵ-tube. The inner part of the brackets is non-zero when the sample lies in the tube, because $\xi_i^{(*)} \geq 0$. Thus, $\alpha_i^{(*)}$ have to be zero in order for the equation to vanish.

In conclusion, only samples outside the ϵ-tube have non vanishing coefficients and are used to create the regression model. They are called Support Vectors.
Until now, this chapter only described the linear function case. A simple method for archiving a nonlinear algorithm is a preprocessing map Φ of the input space into a higher dimensional feature space[4]. However, this approach can quickly become computationally infeasible for higher dimensional input space or feature space[123]. As already seen in equation 4.42, it is sufficient to know the result of the dot product of the mapped input samples instead of explicitly calculate the mapped samples. The result of the dot product of the mapped input samples is called kernel

$$k\left(x_i, x_j\right) = \langle \Phi(x_i), \Phi(x_j) \rangle. \tag{4.46}$$

and substitutes the former dot product in the optimization problem:

$$\begin{aligned} \text{maximize} \quad & -\tfrac{1}{2} \textstyle\sum_{i,j=1}^{l} \left(\alpha_i - \alpha_i^*\right) \left(\alpha_j - \alpha_j^*\right) k\left(x_i, x_j\right) + \\ & -\epsilon \textstyle\sum_{i=1}^{l} \left(\alpha_i + \alpha_i^*\right) + \sum_{i=1}^{l} y_i \left(\alpha_i - \alpha_i^*\right) \\ \text{subject to} \quad & \textstyle\sum_{i=1}^{l} \left(\alpha_i - \alpha_i^*\right) = 0 \text{ and } \alpha_i, \alpha_i^* \in [0, C] \end{aligned} \quad . \tag{4.47}$$

There are several types of kernels that fulfill the necessary conditions, but note that the optimization now finds the flattest function in feature space not in input space[123].

4.4 HYPERPARAMETER TUNING

In ANN as well as in SVR, there are parameters that have to be defined before fitting or training and that are not automatically optimized. In the case of ANN, these are, for example, the number of layers or the number of neurons. In SVR, the epsilon band has to be specified or the factor C, which determines the amount of costs for points outside the band, must be specified before fitting. These types of parameters are called hyperparameters. Hyperparameters can have a significant impact on model quality.
One way to define the hyperparameters is to use brute forcing. Ideally, the user already has experience and can estimate in which parameter range good results are obtained. Now different parameter changes are tested and if possible the performance is checked for unseen data. The procedure is quite easy to perform, but it is unclear whether an optimum is really found. In addition, it is difficult to understand how the resulting hyperparameters were found[3, 124].

The Grid Search method follows a similar principle. Here, value sequences are specified for all parameters to be tuned:

$$N_{\text{layer}} = [1, 2, 3]$$
$$N_{\text{neuron}} = [1, 3, 5] \tag{4.48}$$

The value sequences of the various parameters are then combined to form a grid. Each grid element corresponds to a different parameter combination of the number of layers N_l and the number of neurons N_n:

$$\text{Grid} = \begin{bmatrix} N_{\text{l}} = 1, N_{\text{n}} = 1 & N_{\text{l}} = 1, N_{\text{n}} = 3 & N_{\text{l}} = 1, N_{\text{n}} = 5 \\ N_{\text{l}} = 2, N_{\text{n}} = 1 & N_{\text{l}} = 2, N_{\text{n}} = 3 & N_{\text{l}} = 2, N_{\text{n}} = 5 \\ N_{\text{l}} = 3, N_{\text{n}} = 1 & N_{\text{l}} = 3, N_{\text{n}} = 3 & N_{\text{l}} = 3, N_{\text{n}} = 5 \end{bmatrix} \tag{4.49}$$

Each combination is then used to fit the model and to determine the resulting performance. The advantage of this procedure is that the combinations are already predefined and thus the testing can be processed in parallel. However, there is no optimization of the combination selection, all elements of the grid are evaluated. Depending on the number of hyperparameters and the length of the value sequences, a huge grid can be formed, so that the tuning takes a lot of time[3].
In contrast, Bayesian Optimization only tests the parameter combinations that are expected to improve the performance. Here, a Gaussian process is used to approximate generalized performance function $f(x)$ (performance on unseen data) as a function of the hyperparameters X. The Gaussian process detects the typical behavior of the performance function, which can be used to derive the optimal approximation for the problem. The result is a probability distribution of possible approximation functions and the solution with the highest probability. In principle, alternatives to the Gaussian process are also possible, but due to its high flexibility and tractability, it has proven to be very effective. A Gaussian process is completely defined by a mean function $m(x)$ and a positive definite covariance function $k(x, x')$. The mean function is the a-priori estimate of the regression problem and describes an offset or trend of the data known in advance. In many cases, the mean function can be estimated by the covariance function or a constant mean is sufficient.
Accordingly, the results for a successful approximation depend mainly on the covariance function. In the regression problem, only discrete grid points, namely the already evaluated hyperparameters, of the generalized performance function which is to be approximation or smoothed, are known. In such a case, a Gaussian process can also be determined. For this purpose, instead of this single function, a set of many copies of the function shifted to each other are considered.

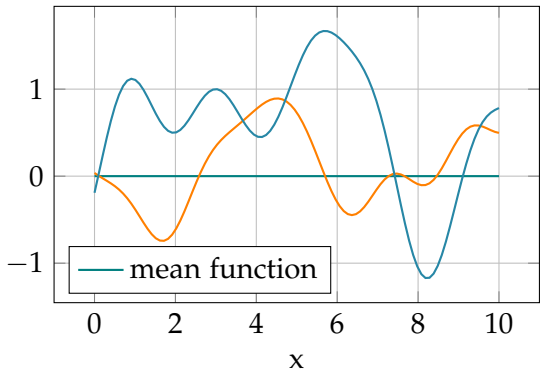

Figure 4.17: Prior approximation functions resulting from squared exponential kernel.

This distribution can now be described with the help of a covariance function. Usually it can be expressed as a relative function of this shift by

$$K(x, x\prime) = K(x\prime - x) = K(r). \tag{4.50}$$

It then applies equally to all locations of the function and describes the always same (i.e. stationary) correlation of a point to its neighborhood, as well as the correlation of neighboring points to each other.
Although there are infinitely many possible resulting performance functions for all non-degenerate covariance functions, the nature of the kernel can also specify certain properties of the performance function. The most commonly used kernel is the squared exponential kernel

$$K_{\mathrm{SE}}(r) = \Theta_0 \exp\left(-\frac{1}{2}r^2\right). \tag{4.51}$$

Figure 4.17 shows random instances of associated approximation functions for the one-dimensional case. As can be seen, the associated interpolation functions are very smooth and the changes tend to be small. These properties usually prevent overfitting, but also lead to a low convergence speed[124].
Snoek at el. recommend the Matérn 5/2 kernel

$$K_{\mathrm{M52}}(r) = \Theta_0 \left(1 + \sqrt{5r^2} + \frac{5}{3}r^2\right) \exp\left(-\sqrt{5r^2}\right) \tag{4.52}$$

instead[124]. The Matérnrn kernel is smooth and twice derivable, so that Quasie-Newton methods can be used to determine the optimum. At the same time, faster changes are possible as can be seen from sample approximation functions in Figure4.18.
At the beginning of the Bayesian optimization some grid points are already known. This means that the generalized performance for several values of hyperparameters has already been determined. These grid points can either have been determined within a grid search or the

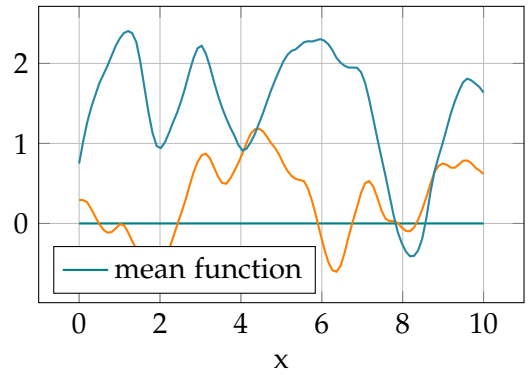

Figure 4.18: Prior approximation functions resulting from Matérn kernel.

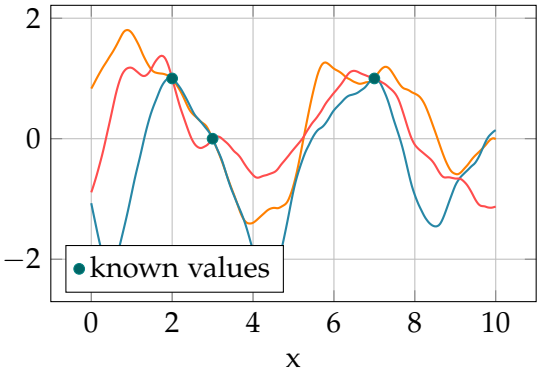

Figure 4.19: Posterior approximation functions resulting from Matérn kernel.

values have been determined randomly. The conditional a-posteriori Gaussian process with known measured values y_n at the coordinates x_n can be determined with the help of Bayes' theorem:

$$(f(x) \mid x_n, y_n) \sim \mathcal{GP}\left(m_{post}, k_{post}\right) \tag{4.53}$$

with

$$\begin{aligned} m_{\text{post}}(t) &= m(t) + k^{\top}(x, x_n)K(x_n, x_n)^{-1}(y_n - m(x_n)), \\ k_{\text{post}}(x, x') &= k(x, x') - \underline{k}^{\top}(x, x_n)K(x_n, x_n)^{-1}\underline{k}(x, x'). \end{aligned} \tag{4.54}$$

Here, K is a covariance matrix obtained by evaluating the covariance function $k(x, x')$ at the discrete rows x_i and columns x_j. Furthermore, $\underline{k}$ was formed as a vector of functions by evaluating k only at discrete rows or discrete columns. Three random resulting posterior approximation functions are shown in Figure 4.19. The markers show the known support points that are matched by all functions.
Between the saddle points, the approximation functions differ, of course. In addition, Figure 4.20 shows the resulting mean value function $m(x)$ together with the standard deviation. At the support points, the standard deviation is 0 due to the known y_n. With larger distance,

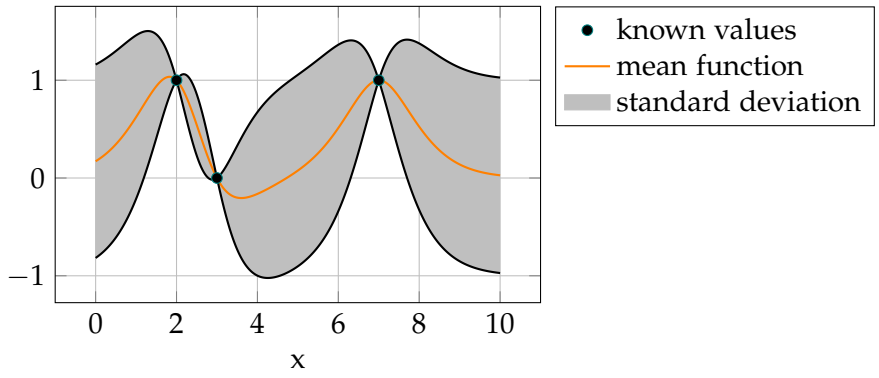

Figure 4.20: Posterior mean function and standard deviation resulting from Matérn kernel.

however, it grows. Now the question arises, which point should be evaluated next.
At this point, the Acquisition Function determines the further procedure. It decides between exploration, i.e. searching at locations with high variance, and exploitation, i.e. searching at locations where low performance values have already been found. In fact, there are several approaches to this. For the tuning of hyperparameters, two commonly used acquisition functions a exists as they can be calculated analytically in closed form. Both functions evaluate the improvement of the generalized performance compared to the current minimum at x_{best}:

$$\gamma(x) = \frac{f\left(x_{\text{best}}\right) - m\left(x\right)}{\sigma\left(x\right)}. \tag{4.55}$$

In the probability of improvement method, the cumulative distribution Φ of γ is evaluated and maximized:

$$a_{\text{PI}}(x) = \Phi\left(\gamma(x)\right). \tag{4.56}$$

Alternatively, the expected improvement can be maximized. In this case, not only the probability of an improvement serves as a decision criterion, but also its amount:

$$a_{\text{EI}}(x) = \sigma(x) \cdot \left(\gamma(x)\Phi\left(\gamma(x)\right)\right) + \mathcal{N}\left(\gamma(x); 0, 1\right). \tag{4.57}$$

The more unknown the sections are, the larger the variance σ, so that the width of the bell also becomes larger. In comparison to the gradient descent, all known points are used for the determination of the next point, so that jumps in the space of the hyperparameters are also possible.
The selected point is then evaluated by fitting the model and determining the generalized performance. Next, the entire process is then repeated, with the new evaluated point also being used in determining the posterior. And the process is repeated until a specified number of repetitions is reached or the generalized performance is sufficiently accurate.

Part III

RESULTS AND ANALYSIS

5 BATTERY CYCLING

This chapter takes a closer look at the operating behavior of zinc-air batteries. For this purpose, typical charging and discharging processes are presented and important points are explained. It will be explained once again why the state estimation of conventional battery technologies cannot be transferred to zinc-air batteries. Finally, possible problems are shown and how they can be treated.

5.1 CHARGING BEHAVIOR

First, the complete charging processes of the zinc-air battery being used are analyzed. Figure 5.1 shows the charging process of a cell with a capacity of 50 A h. The electrolyte which is used is a 30 % KOH solution, the typical electrolyte which is also often mentioned in the literature. The cell was charged with a constant current of 2 A. Therefore, after a time of 25 h, a charge equal to the cell capacity is reached. To counteract possible self-discharge, the impressed charge is increased by 10 %.
The first thing to notice is the overvoltage required to hold the charge current. While the open circuit voltage of the cell is

$$V_{\text{off-load}} = 1.45\,\text{V}, \tag{5.1}$$

the cell voltage increases to

$$V_{\text{bat}}(I = 2.0\,\text{A}) = 2.1\,\text{V}, \tag{5.2}$$

at a charge current of 2 A. The efficiency during charging is therefore

$$\eta_{\text{charge}}(I = 2.0\,\text{A}) = \frac{V_{\text{off-load}}}{V_{bat}(I = 2.0\,\text{A})} = \frac{1.45\,\text{V}}{2.1\,\text{V}} = 69\,\%. \tag{5.3}$$

Apart from the voltage increase at the beginning of the charging process, however, the voltage curve is remarkably flat and almost constant. During the entire charging process, the battery voltage increases by just 40 mV. On the one hand, this is an advantage because the voltage curve is significantly more constant than with other cell technologies. This means that the power electronics used to charge the cells can be optimized specifically for this voltage range and thus work particularly efficiently. On the other hand, it should be noted that the cell in the figure has already been overcharged to a small extent. However, the fact that the cell is already fully charged cannot be determined at all from the voltage. The problem here is that in addition to the reduction of the zinc anode, an electrolysis process also

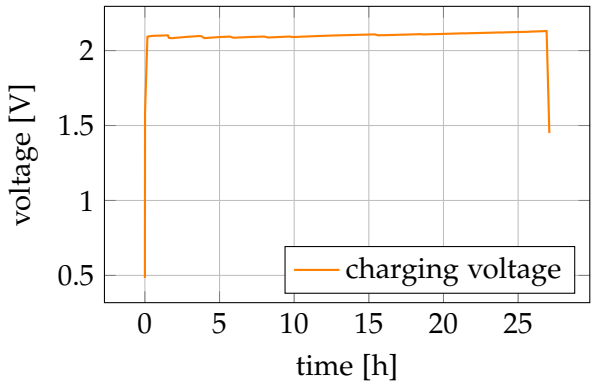

Figure 5.1: Charging cycle using potassium hydroxide electrolyte.

takes place. The voltage required to start the electrolysis is the same as the charging voltage. As a result, the rate of hydrogen formation increases when the cell reaches its charge termination.
Figure 5.2 shows the charging process of a cell that was identically constructed but uses a different electrolyte. Accordingly, this cell also has a capacity of 50 A h and is charged with a current of 2 A. Additionally, the cell was operated at the same time and in close proximity to the other cell, so the temperature of the two cells should also be identical. However, the electrolyte used is not a pure KOH solution, but a solution of KOH, Potassium Fluoride (KF) and Lithium Fluoride (LiF) dissolved in water. According to Fu et al., this mixture is supposed to slow down dendrite growth. However, since the amount of KOH is lower, the electrolyte also has a lower conductivity, which should result in a reduced efficiency[39].
A lower conductivity should actually be reflected in a higher charging voltage or a lower discharging voltage. However, an increase in the charging voltage at the start of the charging process is not evident. The charge voltage is also at 2.1 V here. One possible reason is that the conductivity of the electrolyte only contributes a small part of the voltage difference between the off-load voltage and the charging voltage. This would mean that the charge transfer resistance is much larger than the resistance formed by the electrolyte:

$$R_{ct} \gg R_{el}. \tag{5.4}$$

It should be noted that the absolute resistance values are meant here (capital letters) and not the differential resistances.
In the further course, the voltage also remains constant at first. However, after about 25 h, when the cell is fully charged, an increase in voltage can now be seen. Compared to other cell technologies, the voltage increase of 110 mV is still quite small, but could now be used to detect charge termination of the battery. From the increase of the voltage it can be concluded that the voltage for starting the electrolysis with the used solution is higher in comparison with the 30 % KOH

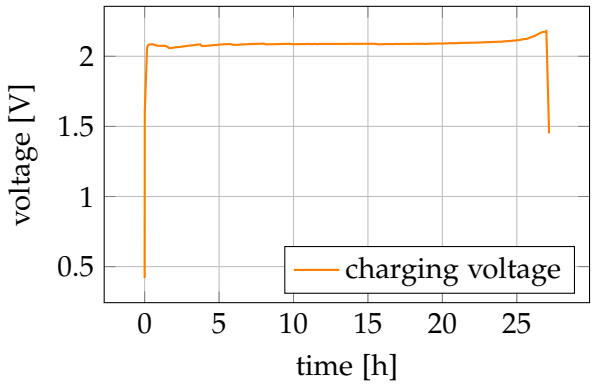

Figure 5.2: Charging cycle using a mixture of potassium hydroxide, lithium fluoride, and potassium fluoride electrolyte.

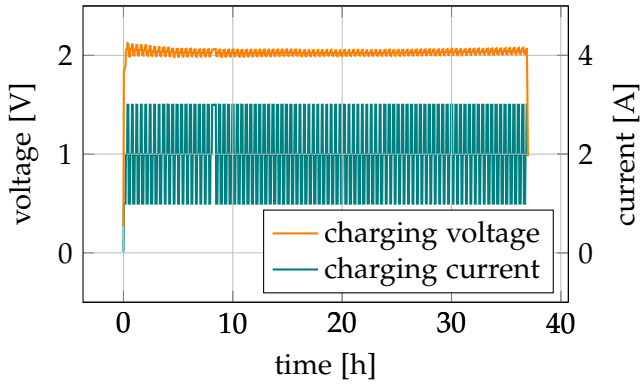

Figure 5.3: Charging cycle at varying charge currents.

solution.
In order to verify whether the influence of the electrolyte conductivity really is so small, a further charging process with varying charging currents was performed. This is shown in Figure 5.3. As one can see, the charging current was regularly changed between 1 A, 2 A and 3 A. As expected, this also results in a change in the battery voltage. At the beginning, the difference between the voltages at 1 A and at 3 A is greater at approx. 130 mV than in the later course from approx. 10 h. The difference has then decreased to approximately 70 mV.
Now it has to be clarified by which extend each parameter contributes to the voltage change. If only the steady state after a current change is considered, a quasi-stationary case can be approximately assumed. Thus, the model of the cell can be simplified by eliminating the double layer capacities and the diffusion processes. What remains are the charge transfer resistances and the resistance of the electrolyte (see Figure 5.4).
As already explained in chapter 3, the resistance of the electrolyte depends on the temperature and the concentration of the alkaline solution. However, since each current level was only applied for 10

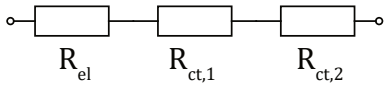

Figure 5.4: Stationary impedance model of a zinc-air battery.

minutes at a time, a constant temperature and concentration can be assumed. Thus, a linear resistance can be assumed for R_{el}:

$$V_{el} = R_{el} \cdot I_{ch} \tag{5.5}$$

In contrast, the charge-transfer resistances R_{ct} are based on the nonlinear Butler-Volmer equation which results in a current that increases exponentially to the overvoltage η:

$$j = j_0 \cdot \left(e^{\frac{F}{2RT}\eta} - e^{-\frac{F\eta}{2RT}\eta} \right). \tag{5.6}$$

Since we only consider the charging process here, the exponential function being subtracted can be neglected. Conversion of the truncated Butler-Volmer equation after the overpotential results in:

$$\begin{aligned} &\eta = \tfrac{1}{a} \left[\ln(I) - \ln(j_0) \right] \\ &\text{with:} \quad a = \tfrac{F}{2RT} \quad , I = j \cdot A \end{aligned} \quad . \tag{5.7}$$

As shown in Figure 5.4, the model contains two charge-transfer resistors, one for each electrode. However, the sum of the two logarithmic functions again results in a logarithmic function and can therefore be simplified:

$$\eta_{tot} = \eta_1 + \eta_2, \tag{5.8}$$

$$\eta_{tot} = \frac{1}{a_1} \left[\ln(I) - \ln(j_{0,1}) \right] + \frac{1}{a_2} \left[\ln(I) - \ln(j_{0,2}) \right], \tag{5.9}$$

$$\eta_{tot} = \left(\frac{1}{a_1} + \frac{1}{a_2} \right) \ln(I) - \left(\frac{1}{a_1} \ln(j_{0,1}) + \frac{1}{a_2} \ln(j_{0,2}) \right), \tag{5.10}$$

$$\eta_{tot} = a_{tot} \cdot \ln(I) - c. \tag{5.11}$$

Since this is a series circuit, the total measured voltage difference is

$$U_{\text{bat}} - U_{\text{off-load}} = V_{el} + \eta_1 + \eta_2 = V_{el} + \eta_{tot}, \tag{5.12}$$

$$U_{\text{bat}} - U_{\text{off-load}} = R_{el} \cdot I_{ch} + a_{tot} \cdot \ln(I_{ch}) - c. \tag{5.13}$$

This results in an equation with 3 parameters. The parameters are all linear. 3 measuring points are therefore sufficient to set up a linear system of equations to determine the parameters. The system of equations is structured as follows:

$$\underline{I} \cdot \underline{p} = \underline{V} \tag{5.14}$$

$$\begin{bmatrix} I_1 & \ln(I_1) & 1 \\ I_2 & \ln(I_2) & 1 \\ I_3 & \ln(I_3) & 1 \end{bmatrix} \cdot \begin{bmatrix} R_{el} \\ a_{tot} \\ c \end{bmatrix} = \begin{bmatrix} U_{\text{bat}}(I_1) - U_{\text{off-load}} \\ U_{\text{bat}}(I_2) - U_{\text{off-load}} \\ U_{\text{bat}}(I_2) - U_{\text{off-load}} \end{bmatrix} \tag{5.15}$$

Since the charge curve was recorded at 3 different currents, the following values can be determined at the beginning of the charging cycle:

$$\begin{aligned} U_{\text{bat}}(I_{bat} = 1\,\text{A}) - U_{\text{off-load}} &= 1.99\,\text{V} - 1.45\,\text{V} = 0.54\,\text{V} \\ U_{\text{bat}}(I_{bat} = 2\,\text{A}) - U_{\text{off-load}} &= 2.064\,\text{V} - 1.45\,\text{V} = 0.614\,\text{V} \\ U_{\text{bat}}(I_{bat} = 3\,\text{A}) - U_{\text{off-load}} &= 2.109\,\text{V} - 1.45\,\text{V} = 0.659\,\text{V} \end{aligned} \cdot \tag{5.16}$$

After solving the system of equations, the parameters

$$\begin{aligned} R_{el} &= 4.12\,\text{m}\Omega \\ a_{tot} &= 0.100 \\ c &= -0.536\,\text{V} \end{aligned} \tag{5.17}$$

are obtained. The largest deviation from the open-circuit voltage is thus caused by the constant parameter c, which in turn is formed by the sum of the parameters j_0 of the two charge-transfer resistors. At a charge current of 2 A, the charge transfer resistor is also responsible for an overvoltage of

$$\eta_{tot} = a_{tot} \cdot \ln(2\,\text{A}) = 69.9\,\text{mV} \tag{5.18}$$

due to the logarithmic dependence on the current. The part of the voltage difference that is caused by the conductivity of the electrolyte is very small in comparison and is

$$V_{el} = R_{el} \cdot 2\,\text{A} = 8.3\,\text{mV}. \tag{5.19}$$

A fresh electrolyte thus causes about 1.4 % of the overvoltage needed to charge the battery.

5.2 DISCHARGING BEHAVIOR

Figure 5.5 shows the voltage curve of a complete discharge cycle of the zinc-air battery used. First again with the standard 30 % KOH electrolyte. This is the same cell from Figure 5.1, which has a nominal capacity of 50 A h. The cell was discharged at a current of 2 A, so the current had to be held for 25 h to fully discharge the cell. In fact, the end-of-charge voltage of 0.6 V was already reached after 23.04 h, which corresponds to a discharged capacity of 46.1 A h.
Right at the beginning of the discharge process, there is a drop in the cell voltage. This is caused by the necessary overvoltage required to reach the discharge current and has a size of

$$V_{\text{off-load}} - V_{\text{bat}}(I = -2.0\,\text{A}) = 1.45\,\text{V} - 1.265\,\text{V} = 185\,\text{mV}. \quad (5.20)$$

Compared to the charging process, where the overvoltage was 650mV for a charging current of the same magnitude, the value is much lower during the discharging process. This is also reflected in the efficiency, which is also significantly higher at

$$\eta_{dis} = \frac{V_{bat}}{V_{\text{off-load}}} = \frac{1.265\,\text{V}}{1.45\,\text{V}} = 87.2\,\% \quad (5.21)$$

than when charging the cell. In the further process of the discharge characteristic, the cell voltage initially decreases slowly. Thus, the cell voltage is still 1.15 V after the cell has been discharged by 80 %. Accordingly, the voltage drops by 0.115 V in this range. In comparison, the voltage of a lithium-ion cell drops by about 0.6 V when80 % of its capacity is discharged. Although the voltage of a zinc-air cell is more influenced by the SoC during discharge than during charge, one can still say that the discharge voltage is very constant compared to other battery technologies. Only at the end of the discharge process there is a much greater drop in the cell voltage until the final discharge voltage is reached. The average discharge voltage is 1.2 V, resulting in an overall efficiency of

$$\eta_{tot} = \frac{V_{bat,dis}}{V_{bat,ch}} = \frac{1.265\,\text{V}}{2.1\,\text{V}} = 60.2\,\%. \quad (5.22)$$

As already explained in chapter charging, measurements were also performed with an alternative electrolyte for the discharge process. To ensure good comparability, the zinc-air cell itself was manufactured in an identical process and has the same geometry, capacity and layer thickness. However, the electrolyte was replaced with a mixture of KOH, KF and LiF, which according to Fu et al. leads to an improved cycle life of the battery, since dendrite growth is expected to be slowed down[39]. Figure 5.6 shows a corresponding discharge curve. The cell was also discharged with a discharge current of 2 A. The end

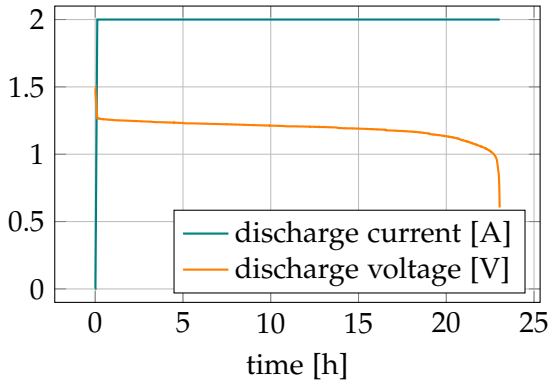

Figure 5.5: Discharge cycle using potassium hydroxide electrolyte.

of charge was reached after 22.7 h, which thus corresponds to a discharged capacity of 45.4 A h. The capacity is thus 0.7 A h less than for the cell with 30 % caustic potash. The difference is caused by the manufacturing process, as the cell was manufactured by hand. In particular, the zinc anode was also pressed by hand, so the amount of zinc can only be influenced to a certain extent.
The modified electrolyte solution has a reduced molarity of KOH, so that the conductivity is reduced. Lower conductivity then leads to higher voltage drops. For the charging process, it was shown that the conductivity of the electrolyte has only a small effect on the efficiency and cell performance, as the charge-transfer resistances have a much larger influence. However, the discharge curve with normal 30 % KOH has already shown that the overvoltages are lower during discharge than during charge, so the situation must now be re-evaluated for the discharge process. Here, at the beginning of the discharge process, there is now a differential voltage of

$$V_{\text{off-load}} - V_{\text{bat}}(I = -2.0\,\text{A}) = 1.45\,\text{V} - 1.195\,\text{V} = 255\,\text{mV}, \quad (5.23)$$

which is therefore 37 % greater than with conventional electrolyte. The discharge efficiency is thus reduced from 87.2 % to

$$\eta_{dis} = \frac{V_{bat}}{V_{\text{off-load}}} = \frac{1.195\,\text{V}}{1.45\,\text{V}} = 82.4\,\%. \quad (5.24)$$

The further course of the curve is similar to the cell with previous electrolyte at a accordingly lower level. Again, the discharge curve is very flat compared to other cell technologies. After the cell was discharged by 80 %, the voltage dropped by 135 mV to 1.06 V. Thereafter, a faster voltage drop occurs until finally the end of discharge voltage of 0.6 V is reached.
In order to find out how the losses are divided between the charge-transfer resistors and the electrolyte conductivity during discharge as well, a discharge process was recorded in which the discharge current was regularly alternated between 1 A, 2 A and 3 A. The resulting

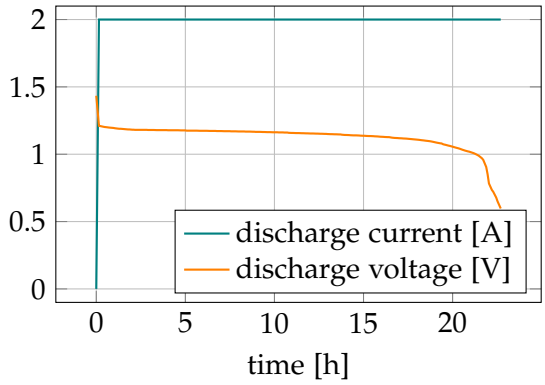

Figure 5.6: Discharging cycle using a mixture of potassium hydroxide, lithiu fluoride, and potassium fluoride electrolyte.

voltage curve and the corresponding discharge current are shown in Figure 5.7. According to chapter 3, the conductivity of the electrolyte varies depending on the temperature and the concentration of the solution. Therefore, each current value is applied only for 10 min at a time in order to guarantee a constant temperature and concentration per slot.
The dynamic processes of the cell decay after about 60 s, so that stationary behavior can be assumed thereafter. The diffusion processes and double layer capacities can therefore be neglected. Thus, the battery model for the stationary discharging process corresponds very closely to the model for charging, which is shown in Figure 5.4. However, since the processes are now reversed, the negative term of the Butler-Volmer equation must be considered instead of the positive term. In the resulting system of equations, the voltage difference is therefore inverted:

$$\begin{bmatrix} I_1 & \ln(I_1) & 1 \\ I_2 & \ln(I_2) & 1 \\ I_3 & \ln(I_3) & 1 \end{bmatrix} \cdot \begin{bmatrix} R_{el} \\ a_{tot} \\ c \end{bmatrix} = \begin{bmatrix} U_{\text{off-load}} - U_{\text{bat}}(I_1) \\ U_{\text{off-load}} - U_{\text{bat}}(I_2) \\ U_{\text{off-load}} - U_{\text{bat}}(I_2) \end{bmatrix}. \quad (5.25)$$

Thus, 3 measured values are necessary to solve the system of equations. For this purpose, the values of the battery voltage corresponding to the 3 different currents are used:

$$\begin{aligned} U_{\text{off-load}} - U_{\text{bat}}(I_{bat} = 1\,\text{A}) &= 1.45\,\text{V} - 1.245\,\text{V} = 0.205\,\text{V} \\ U_{\text{off-load}} - U_{\text{bat}}(I_{bat} = 2\,\text{A}) &= 1.45\,\text{V} - 1.198\,\text{V} = 0.252\,\text{V} \\ U_{\text{off-load}} - U_{\text{bat}}(I_{bat} = 3\,\text{A}) &= 1.45\,\text{V} - 1.152\,\text{V} = 0.298\,\text{V} \end{aligned} \quad (5.26)$$

After solving the system of equations, the parameters

$$\begin{aligned} R_{el} &= 44.6\,\text{m}\Omega \\ a_{tot} &= 0.0035 \\ c &= -0.160\,\text{V} \end{aligned} \quad (5.27)$$

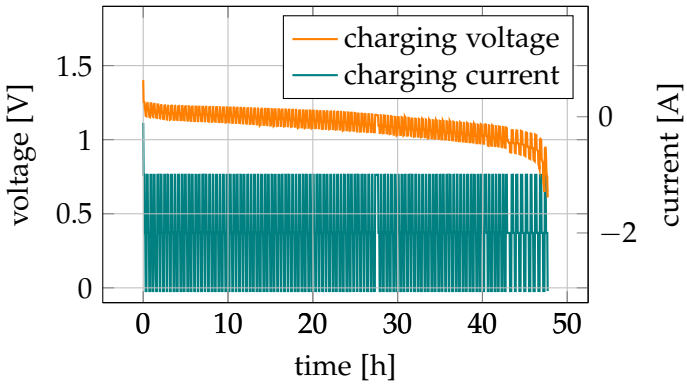

Figure 5.7: Discharging cycle at varying charge currents.

are obtained. The largest part of the voltage difference is now taken up by the current-independent part of the charge transfer. This results in a loss of approximately 160 mV. After that, the voltage loss due to the charge transfer is only slightly influenced by the discharge current. Thus, a current of 2 A leads to a further voltage loss of

$$\eta_{tot} = a_{tot} \cdot \ln(2\,\mathrm{A}) = 2.4\,\mathrm{mV}. \tag{5.28}$$

In contrast, the resistance of the electrolyte is now much larger compared to when charging, so that a current of 2 A causes a voltage difference of about

$$V_{el} = R_{el} \cdot 2\,\mathrm{A} = 89.2\,\mathrm{mV}. \tag{5.29}$$

This corresponds to a percentage of 35.4 %. In fact, the resistance R_{el} of the battery model also represents the resistance of the metallic contact in addition to the electrolyte resistance. Since both components behave identically, a separation of the impact is not possible. It is therefore probable that the contacting of the air cathode is worse than the contacting of the separate nickel electrode used for charging and this leads to an increase in the series resistance.

5.3 MICROCYLING

Cycle tests were performed to further analyze cell behavior. This involves stressing the cell by constantly charging and discharging it in order to obtain an accelerated aging profile. A one-hour discharge duration at nominal current was set as the parameter. The subsequent charging process also takes place at nominal current, but the charging time is increased by 10 % to prevent gradual discharge of the cell due to self-discharge. Figure 5.8 shows the course of the cell voltage and cell current of such a cycle test. A total of 100 cycles are shown, so that the individual changes can no longer be seen. However, it can be seen that the current periodically changes between 2 A (charging) and −2 A

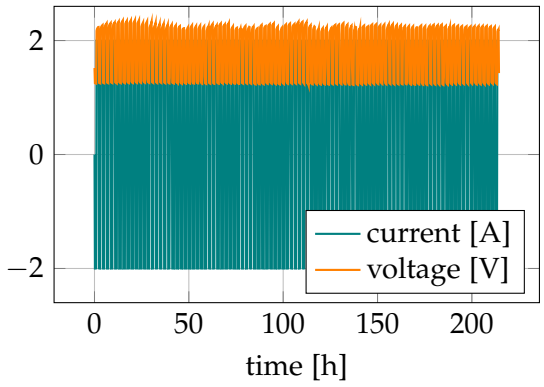

Figure 5.8: Cycle test results of zinc-air battery using 30 % potassium hydroxide electrolyte.

(discharging). Negative currents therefore represent a discharge current here. The plotted voltage corresponds to the respective electrode. This means that during charging the voltage between anode and nickel electrode is used, while during discharging the voltage between anode and air electrode is used. It can be seen that the resulting discharge voltage is very constant over the entire time range. In contrast, the charge voltage fluctuates considerably between individual cycles with up to 200 mV. The difference between the cycles is thus higher than the voltage difference of a complete charge cycle, which once again highlights the problem of state-of-charge detection. The prognosis of the cell voltage is not sufficient for this.
Figure 5.9 takes a closer look at the first five cycles. The voltage and current curves can now be seen properly. During a discharge cycle, the cell voltage is very constant. After the overvoltage has dissipated, the voltage drops by just 10 mV within one hour. A different behavior can be seen during charging. Here, there is a voltage increase of 2.2 V. Looking at the absolute values, voltages of 2.2 V during charging and 1.25 V during discharging can be determined. The efficiency at the beginning of the cycle test is thus

$$\eta_{\text{cycling, KOH, start}} = \frac{V_{ch}}{V_{dis}} = \frac{1.25\,\text{V}}{2.2\,\text{V}} = 56.8\,\%. \tag{5.30}$$

In comparison, Figure 5.10 shows the cell characteristic of the first five cycles using an electrolyte solution of KOH, KF and LiF. The differences that were already observed in the full charge cycles are also found here. The cell voltage increases towards the end of the charging process in the microcycles as well. This behavior indicates that the overvoltage for starting electrolysis is higher here than with the 30 % KOH solution. Towards the end of the charging process, the percentage of electrolysis increases slowly until finally the charging current is used for electrolysis only, and the voltage reaches a limit value. The discharge curve is very flat, as before, but drops with 30 mV within a discharge process slightly more than it is the case with

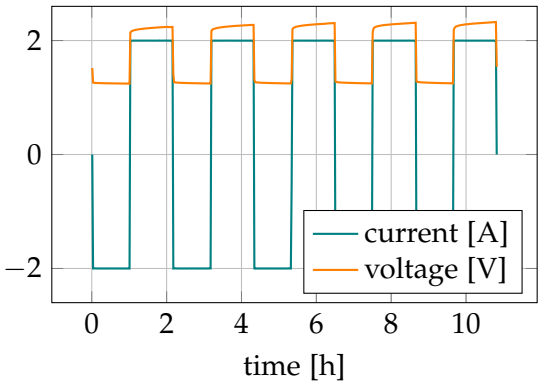

Figure 5.9: First cycles of cycling test using 30 % potassium hydroxide electrolyte.

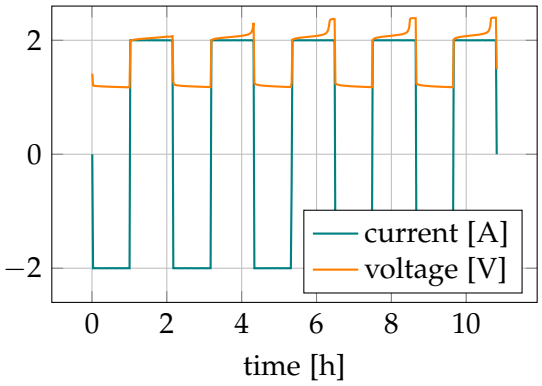

Figure 5.10: First cycles of cycling test using an electrolyte solution of potassium hydroxide, lithium fluoride, and potassium fluoride.

the cell with KOH as electrolyte. Overall, the efficiency increased due to the lower charge voltage, but is at a similar level:

$$\eta_{\text{cycling, special, start}} = \frac{V_{ch}}{V_{dis}} = \frac{1.185\,\text{V}}{2.04\,\text{V}} = 58.1\,\%. \tag{5.31}$$

A slightly wider view in terms of time is shown in Figure 5.11, which shows the cycle sequence for several days. As can be seen from the temperature, the room temperature drops at night and rises during the day. It can be clearly seen that the charging voltage does not correlate with the temperature, or only to a very small extent. Therefore, the temperature cannot be used to eliminate the voltage fluctuations.
The discharge voltages do not follow the course of the ambient temperature at the beginning either. In Figure 5.12, the voltage scale is therefore adjusted in such a way that the fluctuation of the discharge voltage can be seen. At the beginning, the discharge voltage increases independently of the temperature. After 15 cycles, the discharge voltage follows the temperature, as expected from the Nernst equation. One possible explanation is that the formatting process of the cell is only completed after a certain number of cycles.

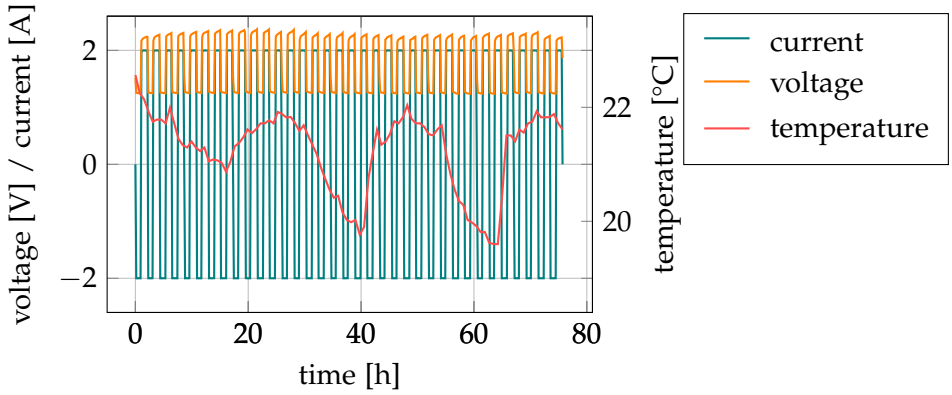

Figure 5.11: Medium range cycles of cycling test using 30 % potassium hydroxide electrolyte.

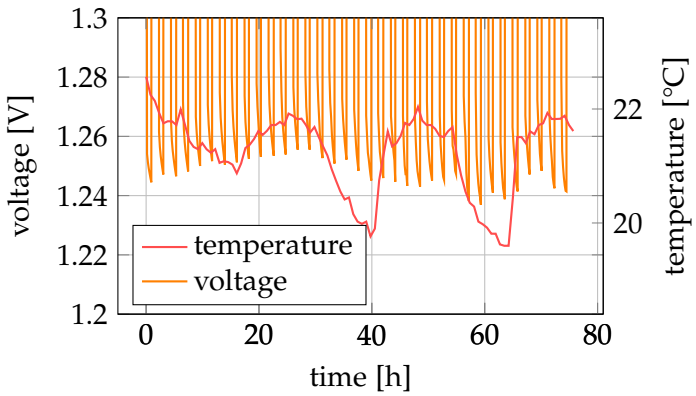

Figure 5.12: Medium range cycles of cycling test using 30 % potassium hydroxide electrolyte zoomed to see discharge voltage fluctuations.

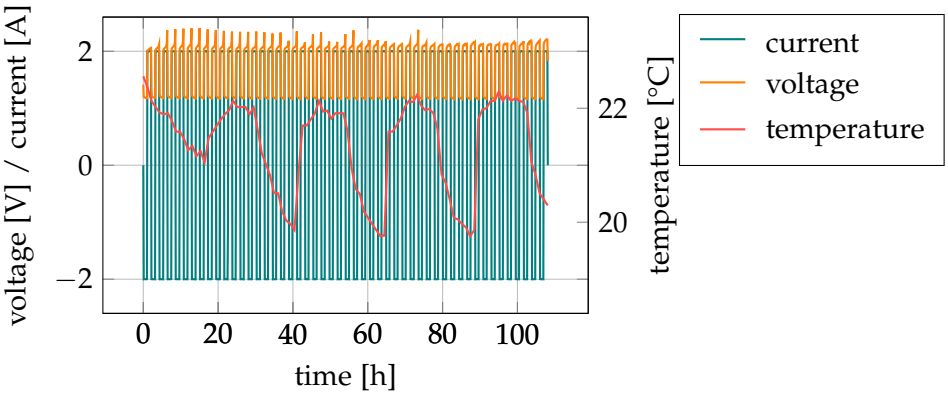

Figure 5.13: First 100 cycles cycles of cycling test using an electrolyte solution of potassium hydroxide, lithium fluoride, and potassium fluoride.

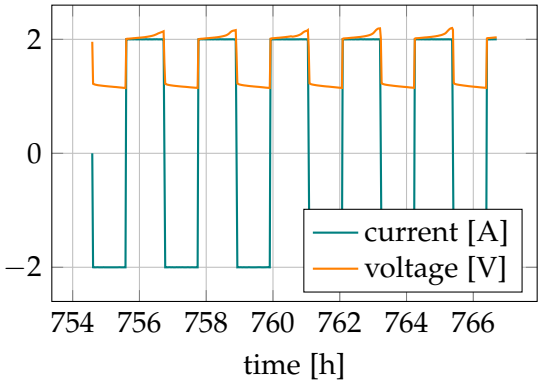

Figure 5.14: Last cycles of cycling test using an electrolyte solution of potassium hydroxide, lithium fluoride, and potassium fluoride.

The characteristic of the first 100 cycles of the cell with the electrolyte solution of KOH, KF and LiF can be seen in Figure 5.13 6. The observations of the normal electrolyte are confirmed here. Voltage fluctuations occur between cycles, especially during charging. Once again, the fluctuations do not correlate with the temperature and therefore cannot be removed by calculation. Figure 5.14 shows the voltage and current characteristics of the same cell after 350 cycles. In general, the behavior is still identical. A difference can be seen in the voltage peaks, which are now no longer so pronounced. Here, the carbonization and aging of the electrolyte can lead to a reduction in the overvoltage of the electrolysis. The efficiency has dropped to

$$\eta_{\text{cycling, special, end}} = \frac{V_{ch}}{V_{dis}} = \frac{1.17\,\text{V}}{2.05\,\text{V}} = 57.1\,\%. \tag{5.32}$$

The value has therefore changed only marginally.

Figure 5.15: Zinc dendrites penetrating the seperator.

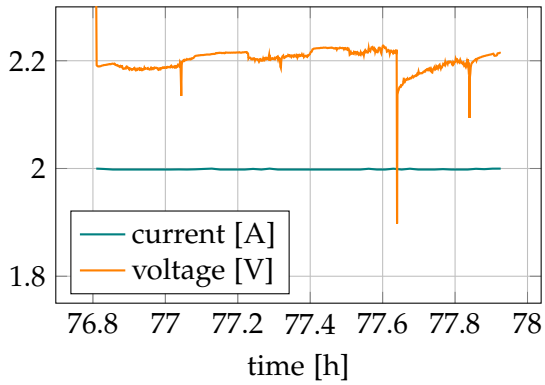

Figure 5.16: Voltage characteristic of zinc dendrites.

5.4 IDENTIFYING CELL DEFECTS

As already explained in the state of the art, the growth of dendrites is still one of the biggest problems of the rechargeable zinc-air technology. When the cell is charged, zinc crystals are formed which grow in the direction of the counter-electrode. As soon as they reach it, a short circuit occurs that prevents further battery operation. Figure 5.15 shows the beginning of the formation of dendrites. The separator foil has already been penetrated here.
The effects of a dendrite on the cell voltage are shown in Figure 5.16. As soon as the dendrite reaches the nickel electrode, the charge voltage suddenly drops due to the short circuit. At this moment, the applied current is no longer used to drive the redox reaction, so the SoC of the battery is not increasing. Instead, there is now a conductive metallic connection between the two electrodes. As long as the dendrites are very small and thin, the applied current causes the dendrites to burn. This can also be seen in the voltage curve. The dendrites initially cause a voltage drop, but then burn and the voltage recovers very quickly.
The 3-electrode technology with a separate electrode for charging also

has advantages when treating dendrites. The additional electrode is located between the zinc anode and the air cathode. This means that dendrites first reach the nickel mesh and can thus be detected by the drop in the charge voltage before they reach the air electrode. In a first step, one can try to burn the dendrite. Here, the chances of success are higher if the applied current is increased to twice the nominal value. However, this procedure no longer works for larger dendrites. The resistance of the dendrite is then so small that the applied current is no longer sufficient to burn the dendrite. Now the advantage of the additional electrode comes into play. The dendrite has not yet managed to reach the discharge electrode. This means that it is still possible to discharge the cell. Since the dendrite is closest to the GDE, it is significantly more oxidized than the actual zinc anode and falls to the bottom. The cell can then be charged again. The associated pseudocode of the dendrite treatment is shown in Listing 5.1.

Listing 5.1: Treatment of dendrites.

```
% Check for dendrite
if(t_charge > 5 min && v_charge < 2.0 V)
        % Start burning dendrite
        i_charge = 2 * i_nominal
        wait(10 min)

        % Check dendrite status
        if(v_charge > 2.0 V)
                i_charge = i_nominal
                return

        % Start discharge
        i_charge = 0
        i_discharge = i_nominal
        wait(30 min)

        % Return
        return
```

In so doing, it is still possible to use the cell for a longer period of time. However, the dendrites are becoming more and more massive with time, so that they cannot be completely eliminated even during the discharge process. Figure 5.17 shows a dendrite formation that could not be destroyed in the end.
Another feature that must be taken into account in the case of a zinc-air cell with 3-electrode technology is the possibility of short-circuiting the charging and discharging cathodes. Since no dendrite growth takes place here, the two electrodes are usually not separated by a separator. This would only lower the conductivity unnecessarily. However, there is a risk that the nickel electrode may come into contact with the

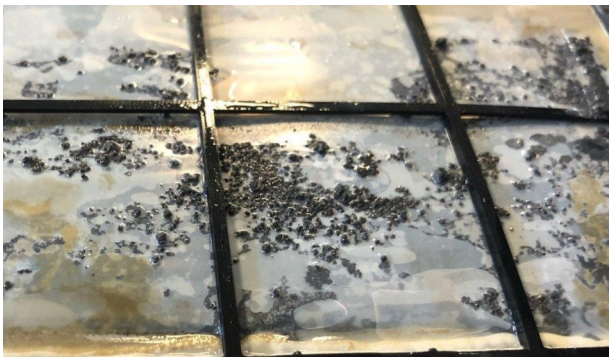

Figure 5.17: Zinc dendrites penetrating the seperator.

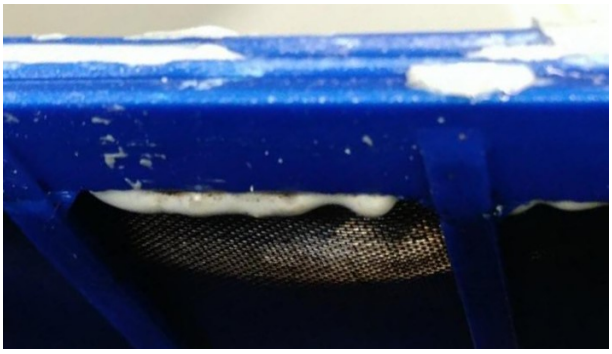

Figure 5.18: Dissolving of air cathode.

GDE. As a result, the GDE, which is not bifunctional, is also used to charge the cell. The oxygen that is then produced at the GDE reacts to a large extent with the carbon of which the electrode is made. It therefore dissolves. Initially, this reduces the active surface area and cell performance decreases. However, leakage of the cell also occurs relatively soon. Figure 5.18 shows a partially dissolved GDE.

6

PARASITIC EFFECTS

In this chapter, two parasitic effects will now be analyzed. First, the influence of the oxygen content of the ambient air is evaluated. On the one hand, a practical experiment is used to evaluate whether the theoretical considerations on oxygen consumption are correct. In addition, the influence of the oxygen content on the cell performance is investigated. The is also a dedicate paper dealing with this topic[85]. The second effect involves electrolyte management. Since a metal-air cell is necessarily an open system for gases, simple evaporation of the water content may occur. Therefore, it is necessary to look for solutions to ensure an electrolyte concentration that is as constant as possible.

6.1 OXYGEN CONTENT

6.1.1 *Theoretical Aspects*

Oxygen consumption

As described in chapter 2.2.6, the amount of oxygen used during the discharge process can be theoretically determined from the reaction equation

$$O_2 + 2H_2O + 4\,e^- \longrightarrow 4OH^- \tag{6.1}$$

at the GDE. 4 electrons as charge carriers thus react with one oxygen molecule. Since

$$N_{1C} = \frac{Q}{e} = \frac{1\,C}{1.6021 \cdot 10^{-19} C} = 6.2415 \cdot 10^{18}. \tag{6.2}$$

charge carriers transfer a charge of 1 C, a total of

$$N_{O_2,1C} = \frac{N_{1C}}{4} = 1.5603 \cdot 10^{18}. \tag{6.3}$$

oxygen molecules are required to discharge 1 C. The Avogadro constant can be used to convert the number of molecules into the molar mass. Since the ambient air can be considered in good approximation as an ideal gas, which has a defined volume per molar mass, the oxygen consumption is

$$V_{O_2}\,[Q = 1\,C] = V_{m0} \cdot n_{O_2} = 5.808 \times 10^{-5}\,L. \tag{6.4}$$

However, the ambient air does not consist of pure oxygen, but only to the extent of 20.95 %. Therefore, to discharge the cell a 1 A h, an air volume of

$$V_{\text{air}}\left[Q = 1\,\text{Ah}\right] = 5.808 \times 10^{-5}\,\frac{\text{L}}{\text{C}} \cdot \frac{3600\,\text{A h}}{1\,\text{C}}\frac{100}{20.95} = 0.998\,\text{L} \quad (6.5)$$

is needed.

Electrode Potential depending on Oxygen Content

Theoretical approaches already exist for lithium-air primary cells that analyze the power loss due to low oxygen content[98]. In this chapter, the theoretical behavior of zinc-air batteries is considered in more detail. Lower oxygen content leads to a reduced battery voltage, which is described by the Nernst equation[104]:

$$E = E_0 + \frac{R \cdot T}{n \cdot F} \cdot \ln\left(\frac{(a_{\text{Ox}})^v}{(a_{\text{Red}})^v}\right). \quad (6.6)$$

The electrode potential E increases with the activity of the oxidizing agent and decreases with the activity of the corresponding reducing agent. Equation 6.6 can be simplified under SATP conditions:

$$E = E_0 + \frac{0.059159V}{n} \cdot \log\left(\frac{a_{\text{Ox}}}{a_{\text{Red}}}\right). \quad (6.7)$$

The activities should be interpreted depending on the state of aggregation. The activity for aqueous solutions, such as the electrolyte, is the concentration of the solution in $\frac{\text{mol}}{\text{L}}$ (molarity):

$$a\left[\text{solution}\right] = \frac{c\left[\text{solution}\right]}{1\,\frac{\text{mol}}{\text{L}}}. \quad (6.8)$$

For gases, the partial pressure is used instead:

$$a\left[\text{gas}\right] a = b. = \frac{p\left[\text{gas}\right]}{1013\,\text{hPa}}. \quad (6.9)$$

Since only the air cathode is in contact with the ambient air, its reaction equation is relevant here. Adding the appropriate oxidizing and reducing agents and the standard electrode potential to equation 6.6 leads to equation

$$E_{\text{O}_2} = 0.401\,\text{V} + \frac{59.159\,\mu\text{V}}{4} \cdot \log\left(\frac{\frac{p[\text{O}_2]}{1013\,\text{hPa}} \cdot \left(\frac{c[\text{H}_2\text{O}]}{1\,\frac{\text{mol}}{\text{L}}}\right)^2}{\left(\frac{c\left[\text{OH}^-\right]}{1\,\frac{\text{mol}}{\text{L}}}\right)}\right), \quad (6.10)$$

which gives the relationship between electrode voltage and oxygen concentration. The partial pressure of oxygen is in the numerator. Therefore, the voltage level of the battery increases logarithmically with the oxygen content.

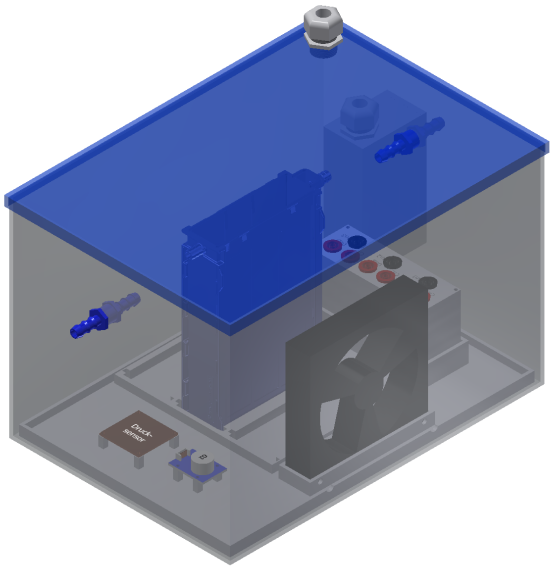

Figure 6.1: Test chamber for determining the oxygen addiction

6.1.2 *Test Setup*

The theoretical analysis was verified by developing a test chamber. The structure of the chamber is shown in Figure 6.1. It provides space for up to three batteries and sensors to measure the air pressure and the oxygen content in the chamber. Moreover, a fan is used to average the oxygen concentration in the chamber by mixing the contents. Multiple sealed cutouts serve as feedthroughs and can be used to wire components or circulate the battery electrolyte. A 3D CAD software is used to determine the volume of air required by the components, which must be subtracted from the chamber volume.
Figure 6.2 shows the complete measurement setup. Its main component is the presented test chamber. The currents are applied via relays and measured via Hall-effect based current sensors for safety. Moreover, the battery voltage is measured via separate lines to avoid a measurement error due to the applied current. Since the zinc-air battery system is an open system, water can evaporate from the electrolyte solution, resulting in a change in electrolyte concentration. Since this also affects the voltage level, a separate electrolyte circulation system is used to control the concentration.
Two batteries are used for the actual tests. One cell discharges and consumes oxygen from the chamber. The second cell is used to measure the open circuit voltage.

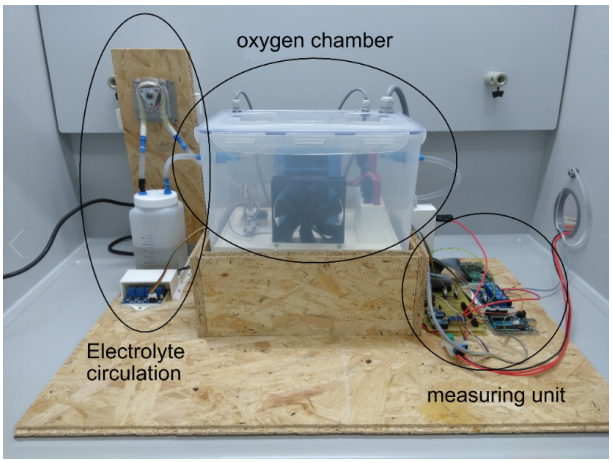

Figure 6.2: Measurement setup for determining the oxygen addiction

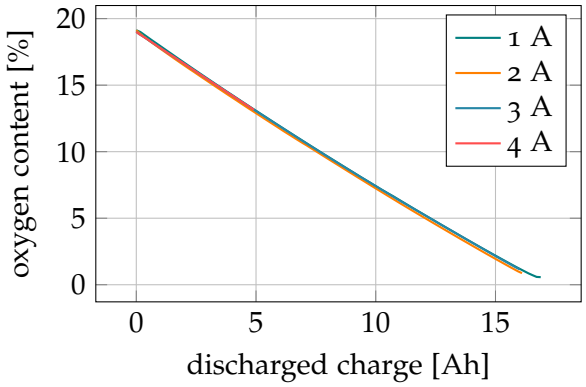

Figure 6.3: Oxygen content in the chamber as a function of the the discharged charge

6.1.3 *Results*

Figure 6.3 shows the course of the oxygen content of a closed chamber while a battery is discharged with different currents. The oxygen content is plotted against the discharged charge. The differences between the curves are within the measurement tolerances. Thus, oxygen consumption is actually linearly dependent on the discharged charge and is not dependent on the current. Compared to the theoretically estimated value, the oxygen consumption is about 19 % lower than expected. One possible reason for this behavior are small leakages in the test chamber.
In Figure 6.4, the open-circuit voltage of the second battery as a function of oxygen content is plotted. In addition, the estimated cell voltage predicted by the Nernst equation is also plotted. Considering that the ordinate axis includes only 12 mV, we can see that the general behavior is consistent with theory. The drop-off of the measured curve starts a little earlier. Again, this is probably due to the tolerance of the oxygen sensor.

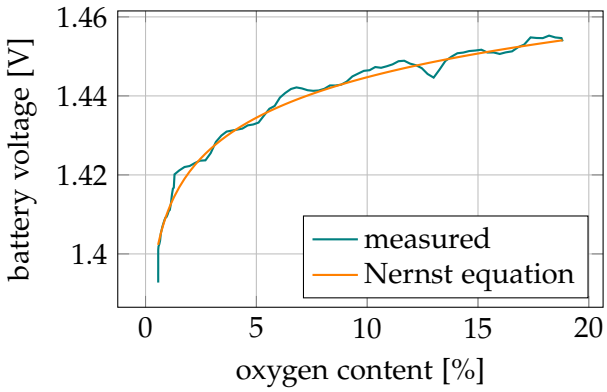

Figure 6.4: Measured off-load voltage compared to the theoretical estimation based on Nernst equation

Figure 6.5 compares the characteristics between an open and a closed chamber of the same battery. The results of the open chamber are shown by dashed lines. The capacity of the battery is quite large, so for an open chamber with a constant oxygen content of 19 %, the battery voltage does not change when the battery is discharged over 1 h with 1 A, As the current is kept constant, the oxygen content in the closed chamber decreases again linearly. The voltage of the charged battery is initially only slightly affected. At about 2.5 % oxygen content, a sharp drop occurs that significantly degrades battery performance. Therefore, it is recommended to ensure that the ambient air of zinc-air batteries has an oxygen content of at least 5 %, fixing a minimum percentage of power. The amount of fresh air required to maintain a minimum oxygen content $c_{O_2,\min}$ after discharging a charge of Q is

$$V_{\text{air}}(c_{O_2,\min}, Q) = 0.2312\,\text{L} \cdot \frac{100\,\%}{20.95\,\% - c_{O_2,\min}} \cdot \frac{Q}{\text{A h}}. \tag{6.11}$$

Assuming that the average discharge voltage of a zinc-air battery is 1 V, about 1.5 m^3 of fresh air are needed to discharge 1 kW h.
The same measurement was repeated with other discharge currents. In Figure 6.6, the voltage levels for different discharge currents are plotted against the oxygen content. Our test setup's maximum discharge current is 4.2 A. General voltage levels are lower at higher currents due to the internal series resistance. Plus, the sudden voltage drop occurs a bit earlier at higher loads. Nevertheless, the recommendation of an oxygen content of 5 % still fits.

6.2 ELECTROLYTE CONCENTRATION

Metal air batteries in general use oxygen from the surrounding air. In order to make use the oxygen of the surrounding air, electrodes that are permeable for air but impermeable for liquids like the electrolyte are used[109]. Normally aqueous solutions, like potassium hydroxide,

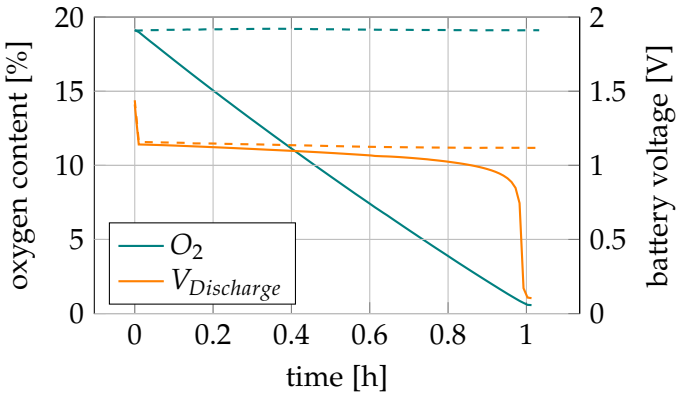

Figure 6.5: Comparing the performance during discharging with a working point of 1 A between an open oxygen chamber (solid lines) and a closed chamber (dashed lines)

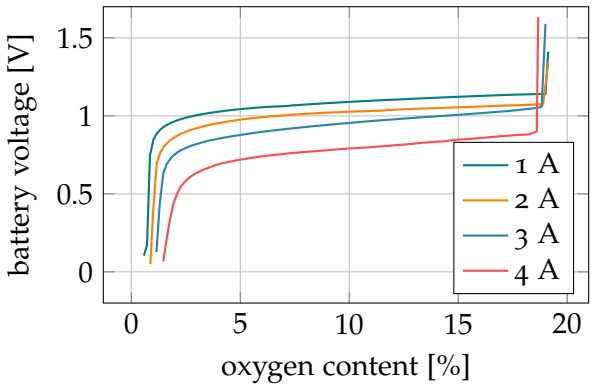

Figure 6.6: Comparing the performance during discharging at different working points

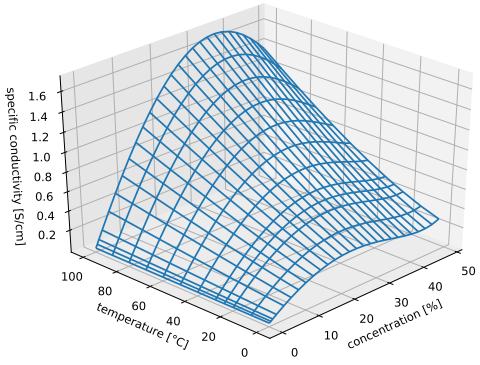

Figure 6.7: Correlation of the specific conducitivty, temperature and concentration of potassium hydroxide according to data of Gilliam et al.[43]

are used as electrolyte. However, its water content can evaporate and escape through the permeable electrode leading to unwanted high electrolyte concentrations.
On the one hand the electrolyte concentration is chosen to have the maximum conductivity which corresponds to the least power losses. The specific conductivity of potassium hydroxide depending on its temperature and concentration is shown in Figure 6.7. As one can see the conductivity depends on both properties. Nevertheless the maximum conductivity for all temperatures is close to 30 % making it an optimal value[43]. If we concentrate on the correlation between the concentration and the specific conductivity, we see a linear dependence for low concentrations. A higher number of charge carriers results in a higher conductivity. This behavior changes when the average distance between the ions becomes smaller at high concentrations. The electrostatic impact between the charge carriers stops a further gain of the conductivity and can even lower it. Therefore, the series resistance of the battery will increase when the concentration changes resulting in a lower battery voltage when using high discharge currents[5].
On the other hand the electrolyte solution becomes more aggressive when the concentration increases. The permeable electrode is a weaker part in most cases and can therefore be destroyed by these higher concentrated electrolytes. This can lead to dangerous situations since aggressive materials permeate outer walls and become released. Figure 6.8 shows a destroyed GDE of the zinc-air battery. The concentration of the potassium hydroxide rapidly increased and crystallized while the battery was stressed with high temperatures. The resulting inner crystals then cut the electrode.
Both problems have to be avoided. Therefore, this chapter covers the development of a new self-acting system for controlling the electrolyte concentration.

Figure 6.8: Gas diffusion electrode of a zinc-air battery that is damaged by a high electrolyte concentration.

6.2.1 *Measurement System*

One of the most important property of a controller is the ability to measure the actual value of the desired property. So for this system a measurement of the concentration of the solution is essential. Different approaches are viable. One idea to think of is to measure the pH value. However, in general the concentrations of electrolytes are too high to measure a change of the pH value. At a concentration of 30 % the pH value will always be 14. Moreover, pH measurement electrodes are quite expensive and need to be calibrated regularly.
Another feasible method for measuring the concentration of the electrolyte is to measure its conductivity as already seen in Figure 6.7.
The schematic of the conductivity measurement circuit is shown in Figure 6.9 and is based on a reference design of analog devices[74]. A voltage is applied to the sensing electrode and the resulting current is measured by an operational amplifier circuit. The op-amp implements an inverting amplifier whose input resistor is represented by the electrolyte link within the measurement electrode. Because of the negative feedback and the ground connection at the positive input pin, the negative input pin node forms a virtual ground. Therefore, the resulting output voltage of the op-amp is linear to the current through the measurement electrode. Both, the voltage and the current signal are then processed to suit the Analog Digital Converter (ADC) of a STM32 microcontroller. In the first stage a Programmable Gain Amplifier (PGA) is used to amplify the signals. The selectable gains are 1, 10, 100, and 1000. Thus, a wide range of conductivities can be measured. During the last processing step, the input signals are shifted to the middle of the ADC input voltage range.

6.2.2 *Reduction of Passivation Effects*

As one can see analog multiplexers are used to create and measure a modulated signal. The reason is that an Alternating Current (AC) modulated signal hinders the formation of passivation layers[20]. When

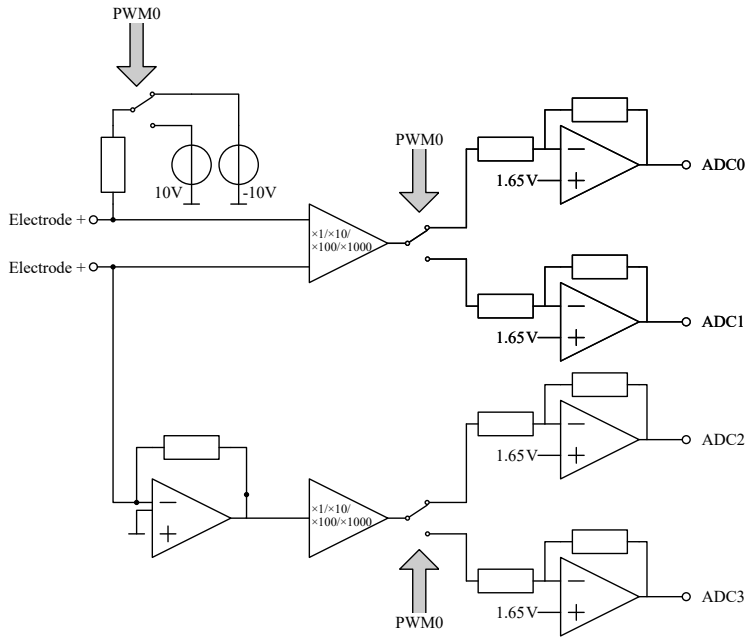

Figure 6.9: Schematic of the conductivity measurement circuit.

applying a constant voltage to electrodes within an electrolyte, corresponding ions move and accumulate at the opposed charged electrode and create a contrary electric field that works against a further movement of ions to this electrode. Therefore, the measured current would decrease. By periodically changing the voltage direction, passivation effects are being avoided. The signal processing for the ADC uses both, the non-inverting and the inverting signal. The actual voltage and current values can be measured by subtracting both values.
One important question is the required modulation frequency. When the frequency is too low, polarization effects still exist which means that the measured conductivity G is lower than the actual conductivity that correspond to the specific conductivity κ. However, if the frequency is too high, the current might increase due to parasitic capacities resulting in a higher measured conductivity[20]. Figure 6.10 illustrates that the ideal frequency is somewhere between both effects. Finding an optimal frequency is possible by sweeping the frequency and looking for an area where the measured conductivity does not change.
Another way for minimizing the effect is making use of four-terminal sensing. Interfering resistances due to polarization or wiring are compensated by a separate currentless voltage measurement[5, 20].

6.2.3 *Measurement Electrode*

The final measurement electrode is built by a 3D printer and shown in Figure 6.11. Both outer electrodes are used to apply the modulated

Figure 6.10: Characteristics of the ratio of the measurement conductivity and the actual conductivity depending on the modulation frequency.

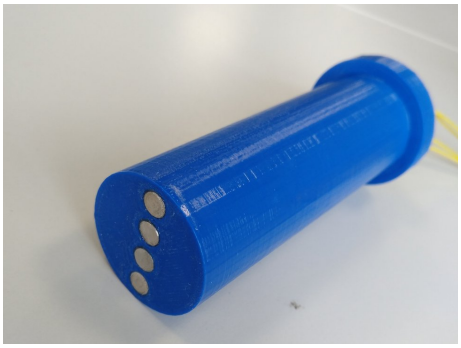

Figure 6.11: 3D printed measurement electrode used to determine the conductivity of the electrolyte.

alternating current while the inner electrodes are used to measure the resulting voltage response. Moreover, a temperature sensor is located within the measurement cell since it is not resistant to an alkali.
In order to create a liquid-tight case for the measurement electrode, different filament and varnish combinations have been tested. In general, a slight over extrusion helps the different layers to better combine with each other. ABS (Acrylonitrile Butadiene Styrene), PLA (polylactide) and PETG (PolyEthylene Terephthalate Glycol-modified) filaments were analyzed for liquid-tightness. Furthermore each filament was also tested with a varnish of epoxy resin. Small boxes for each combination were printed and filled with a 30 % potassium hydroxide solution (Figure 6.12). During the next days the underlying tissues were observed to identify leaking boxes.
The results are summarized in Table 6.1. While all of the filament materials are liquid-tight in combination with the epoxy varnish, only ABS is also alkali-proof. Even the varnished boxes made of PLA and PETG started to leak after 2 d. One probable reason is that the so called vase mode cannot be used for printing the measurement cell. In vase mode, only the outer surface is printed in a spiralized mode. The height of the nozzle is continuously increased instead of printing complete layers one by one. Printing the measurement cell in vase mode is not possible since it has an inner structure. However, ABS filament can be used for the measurement electrode.

Figure 6.12: Test setup for verifying the liquid- and alkali-tightness of different filament and varnish combinations.

Table 6.1: Test results of liquid-tightness

FILAMENT MATERIAL	VARNISH	RESULT
ABS	None	Sealed
ABS	Epoxy	Sealed
PLA	None	Permeable
PLA	Epoxy	Permeable
PETG	None	Permeable
PETG	Epoxy	Permeable

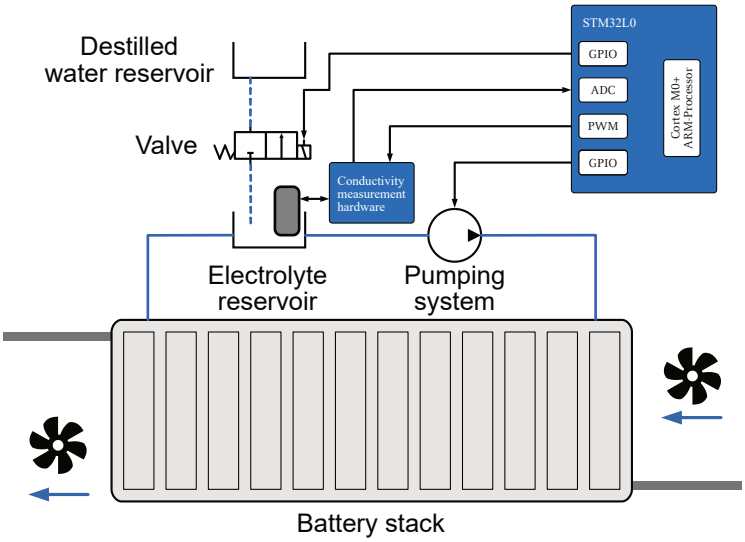

Figure 6.13: Setup for self-acting controlling of electrolyte concentrations.

6.2.4 *Setup*

The structure of the resulting measurement and control setup is shown in Figure 6.13. The biggest component of the setup is the battery stack. Its batteries are interconnected in series. It is quite complex to measure the electrolyte concentration in each battery cell separately. Therefore, a reservoir and a pumping system is used to create one central place for measuring the concentration. The electrolyte interconnection can be assembled in series and in parallel connection. The advantage of a parallel connection is that electrolyte can flow back to the reservoir when stopping the pump resulting in lower shunt currents. Due to the serial connection of the batteries, filled electrolyte hoses form a shunt resistor connecting cells at different potentials. However, the resulting currents are rather small. The measured resistances never dropped below 1 kΩ.
There is another reservoir that is used to store distilled water. Since it is located at a higher position, a simple 2/2 directional control valve can be used to control the flow of fresh water into the electrolyte reservoir. The adding of new water to the electrolyte compensates the evaporation and leads to an optimal performance.
The sequence for controlling the electrolyte concentration always starts with activating the pumping system in order to transport the electrolyte from within the cells to the central electrolyte reservoir. After 5 min of pumping the concentration measurement takes place. By knowing the measured concentration c_m, the desired concentration c_t and the volume of electrolyte in the system at the desired concentrationV_T, the volume of water that needs to be added $V_{H_2O,add}$

can be approximated. The target and the measured electrolyte concentrations are defined as follows:

$$c_t = \frac{n_{sub}}{V_t}, \tag{6.12}$$

$$c_m = \frac{n_{sub}}{V_m} \tag{6.13}$$

where n_{sub} describes the amount of the active component and V_m the volume of the measured electrolyte. Assuming that the apparent molar property is negligible, the target concentration can be obtained by adding a volume $V_{H_2O,add}$ of water:

$$c_t \approx \frac{n_{sub}}{V_m + V_{H_2O,add}}. \tag{6.14}$$

Solving to $V_{H_2O,add}$ and substituting both upper equations results in

$$V_{H_2O,add} \approx V_t \left(1 - \frac{c_t}{c_m}\right). \tag{6.15}$$

In order to drop the need for a mass flow controller when adding water to electrolyte reservoir, Torricelli's law can be used to approximate the speed of the water flowing out of its reservoir. The activation time of the valve t_{sw} can then be calculated by

$$t_{sw} = V_{H_2O,add} \cdot \frac{1}{A_H \cdot \mu \cdot \sqrt{2gh}}. \tag{6.16}$$

Here A_H, g and h correspond to the cross section of the hose, to the gravitational acceleration and the difference in height between the upper edge of the water and the valve.

6.2.5 *Implementation*

In order to implement the self-acting controlling of the electrolyte concentration, data collection of conductivity measurements took place for a set of different concentrations and temperatures. The gained data is then stored within a 2D lookup table that correspond to Figure 6.7. This table links conductivity and temperature data to a concentration value.
Figure 6.14 shows the software flowchart for implementing the controlling of the electrolyte concentration. The process begins by settings a General Purpose Input Output (GPIO) output pin in order to control a MOSFET that activates the pumping system. About 5 min are needed to circulate and average the electrolyte of the stack. Therefore, before going to deep sleep mode an alarm of the built-in Real Time Clock (RTC) is set to 5 min in the future.

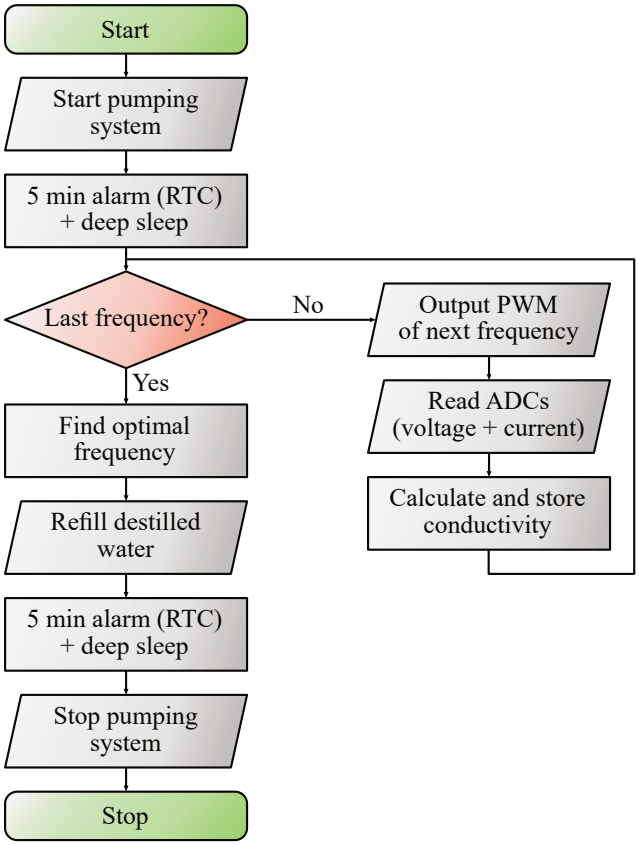

Figure 6.14: Process of controlling the electrolyte concentration.

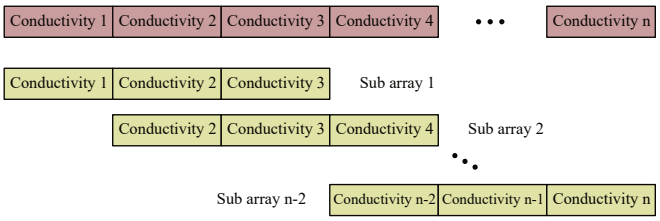

Figure 6.15: Process of choosing the optimal chopper frequency

When the microcontroller wakes up the actual conductivity measurement takes place for a set of different modulation frequencies ranging from 100 Hz to 10 kHz. The modulated current is applied to the measuring cell by outputting a pulse width modulation with a duty cycle of 50 % at the corresponding frequencies. The internal ADC is then used to measure the resulting voltage and current values. Depending on these values, suitable gain factors for the PGA are set and a Direct Memory Access (DMA) transfer of 1024 current and voltage ADC values is initiated. The actual current and voltage values used to determine the conductivity are calculated by averaging all of the measured values in order to increase precision. The derived conductivity is then stored in an array whose elements represent the measured conductivity for each frequency in the set. These steps are repeated for each frequency in the set.
Next step is to find the measurement with the optimal modulation frequency. Hence, the variance of each 3 element sub array of the conductivity array is calculated. According to Figure 6.10 the sub array with the least variance is the optimal frequency. The conductivity value in the middle of this sub array is used (see Figure 6.15).
The pregenerated 2D lookup table is then used to determine the electrolyte concentration from the measured conductivity and temperature. Values between list items in the lookup table are linearly interpolated. Another timer is then used to precisely control a MOSFET that activate the valve to fill distilled water into the electrolyte reservoir.
In order for the water to mix with the electrolyte, the pumping system is left on for another 5 min. Once again, the RTC is used to wake up the microcontroller from deep sleep and for deactivating the pump. Last step is to activate the RTC alarm for the next controlling cycle. The time depends on the temperature and on the amount of evaporated water and can be a value between 10 min and 12 h. Then the microcontroller is put in deep sleep mode to save energy until the next controlling step takes place.

7 STATE ESTIMATION

BMS are electronic circuits that ensure the safe condition of battery systems and monitor and control the charging and discharging processes of batteries. For these essential functions to work safely, both the SoC and the SoH of the respective cell must be known or determinable. In current cell technologies, the cell voltage is usually used for this purpose, because typically the cell voltage of an empty cell is lower than that of a full cell.
As already described in chapters 3 and 5, the cell voltage profile of zinc-air batteries is so flat that state estimation in this way is not possible. For this reason, this chapter examines alternative ways of determining the SoC and the SoH. Here, electrochemical impedance spectra are a promising approach. First, possibilities to measure impedance spectra in a simple and accurate way are presented and then methods to determine the SoC and the SoH from an impedance spectrum are explained.

7.1 TEST SETUP

EIS determines the impedance, i.e. the AC resistance, of electrochemical systems as a function of the frequency of an AC voltage or current. Electrochemical systems are, for example, batteries. EIS can be used to obtain precious information about the system under investigation and the processes taking place in it. Usually, EIS is performed on batteries by imposing an alternating current, that is, the current of the working electrode is sinusoidally modulated and the resulting voltage and its phase are measured. The Direct Current (DC) component of the modulated current is usually set to 0 so that the EIS is charge neutral and the SoC of the cell is not influenced. Due to the 3-electrode technology used in our zinc-air cells, the charge-neutral method cannot be used, since the DC component must be at least as large as the AC amplitude so that there is no switching between charging and discharging during an impedance measurement. As an alternative to the galvanostatic measurement method, EIS can also be performed using an applied AC voltage; in this case, the current and its phase are measured. The concept of impedance and the complex alternating current theory assume that there is a linear relationship between the amplitudes of voltage and current. In electrochemical systems, this is only the case approximately for small amplitudes, e.g., 1 mV to 10 mV[8]. Significantly larger voltage amplitudes must therefore not be used for measurement.

In particular, the necessary DC component during an impedance measurement and the 3-electrode technology prevent the use of an existing instrument for the measurement of impedance spectra. Therefore, developments for the measurement of impedance spectra of zinc-air cells as well as adaptations for existing measuring instruments are presented in this section.

7.1.1 *PicoEIS*

Commercially available and universally applicable measuring instruments for EIS are financially very expensive. At the beginning of the zinc-air project, there was no funding to purchase such a measuring device as part of the project. On the other hand, there are considerably less expensive instruments available that are designed for usage with lithium-ion cells. This means that the frequency range is limited from 1Hz to 1kHz and that the impedance range is designed for low values and becomes inaccurate at higher values. In addition, the 3-electrode technology requires a system that can perform the impedance measurement while a DC current is applied so that the working area of the charging or discharging electrode is not exceeded.
For this reason, it has been necessary to build a dedicated measurement system. The first approach is based on the PicoEIS, which Kiel presented in his dissertation. The name is derived from a Pico Technology PC oscilloscope being used. The structure of the customized setup is shown in Figure 7.1. The oscilloscope has two analog inputs and one analog output. The analog output is used to specify the current, which means that a sine wave is output there. A current controller now applies a current proportional to this voltage signal. The two analog inputs measure the actual current and the resulting voltage response of the cell. With these both information it is now possible to calculate the impedance[63]. According to MacDonald et. al, the voltage response should not exceed an amplitude of 10 mV per cell[8]. However, the AC response overlaps the DC cell voltage. Therefore, to increase the accuracy of the voltage measurement, the DC offset is removed. In the original setup, this is done by manually adjusting a potentiometer, which is impractical for periodic measurements. The setup was therefore extended with a microcontroller controlled compensation of the offset voltage. Now a computer program can automatically measure impedance spectra on a regular basis using an algorithm that was implemented in Matlab.
Beside the oscilloscope, the circuit can be separated into two parts. The first part of the circuit implements a current controller and is shown in Figure 7.2. The setpoint of the current can be defined via a voltage signal proportional to it at the coaxial socket. The operational amplifier OA_1 implements a PID controller that handles the current control. The difference between the reference voltage and the ampli-

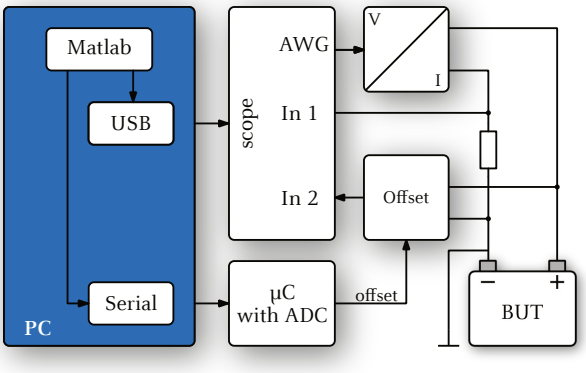

Figure 7.1: Schematic structure of the PicoEIS impedance spectroscopy measurement instrument.

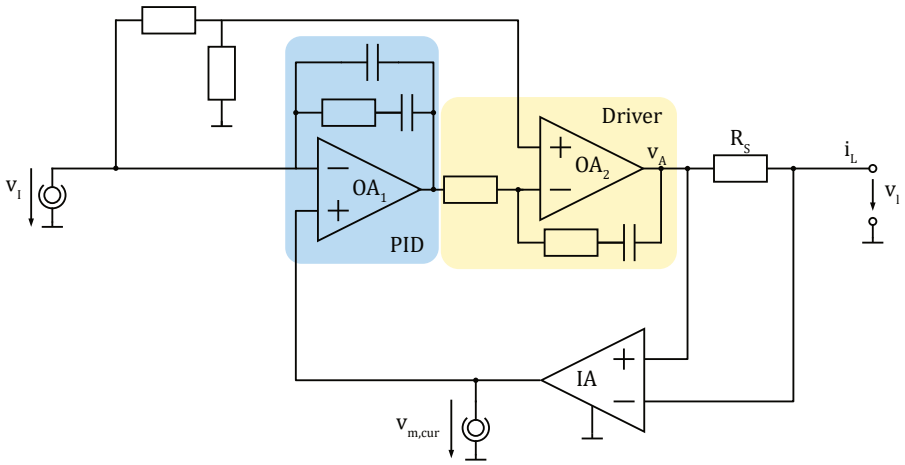

Figure 7.2: Circuit for current control of the PicoEIS instrument.

fied voltage of the shunt resistor R_S is compensated. The amplified voltage of the shunt resistor is also connected to another coaxial socket, so that a measurement of the actual current is possible. OA_2 is an OP549 power operational amplifier. This allows an output current of up to 8 A, so that an additional driver stage is not necessary.
The circuit for offset compensation is shown in Figure 7.3. The battery voltage is measured with an instrumentation amplifier. It has an input for the voltage reference, i.e. the measured battery voltage is output with respect to the reference potential. For offset compensation, this reference voltage input has to be assigned with the negative cell voltage. The measured voltage is then passed through a low-pass filter to prevent alias errors in the subsequent acquisition of the signal with the PicoScope.
A STM32 microcontroller is used to automate the offset compensation as soon as the main program of the computer initiates it using the serial interface. The reference contact of the instrumentation amplifier is controlled via a Digital Analog Converter (DAC). The resulting output

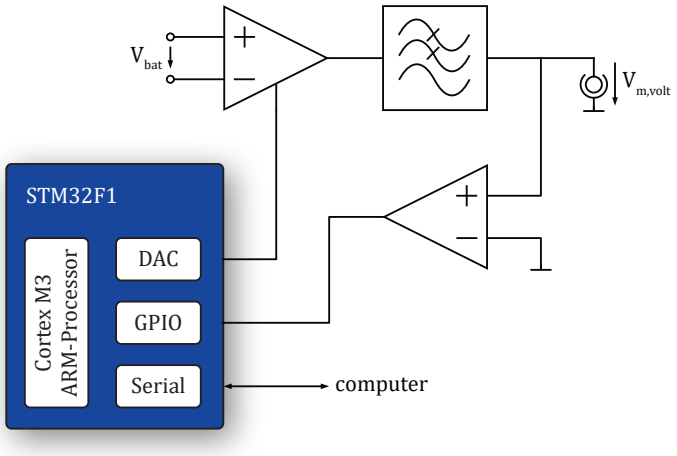

Figure 7.3: Circuit for offset compensation of the battery voltage of the PicoEIS.

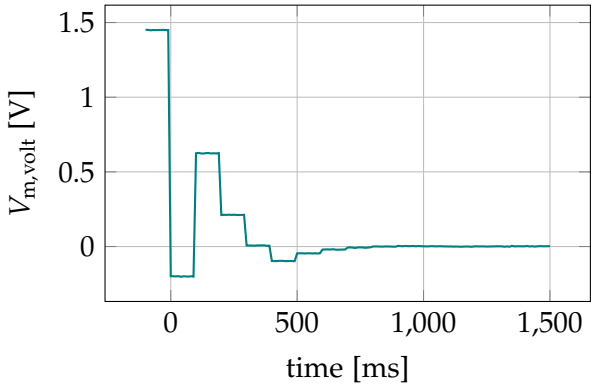

Figure 7.4: Progress of the successive approximation to compensate for the DC component of the cell voltage.

voltage is then compared with ground potential using a comparator. The actual compensation is done by successive approximation. The bits of the DAC are set consecutively from Most Significant Bit (MSB) to Least Significant Bit (LSB). If the resulting voltage is lower than ground, the bit is reset, otherwise it remains set. The development of the resulting voltage $v_{m,volt}$ is shown in Figure 7.4. The distance to the ground potential becomes smaller with each step.

Due to the 3-electrode technology, the measurement of the impedance spectra can only be performed during a charging process and during a discharging process, respectively, so that the SoC of the cell changes to a certain extent during the measurement. Since the measurement time at low frequencies is up to 30 s, the DC component of the voltage measurement may change during the measurement. The voltage change is particularly large at the beginning of charging or discharging processes because the slowest processes have yet to decay. The voltage signal of such a case is shown in Figure 7.5 as an example.

The resulting error is minimized by modeling the DC voltage compo-

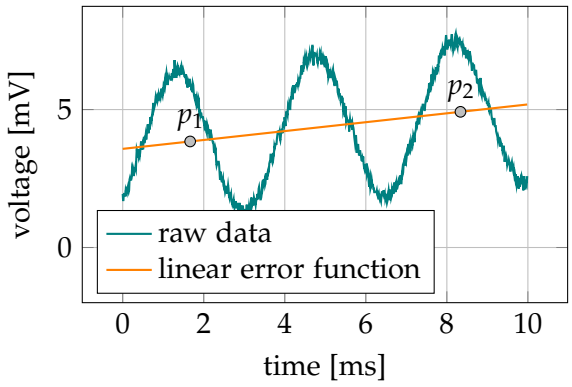

Figure 7.5: Measured voltage signal of an impedance measurement whose direct component increases during the charging process.

nent in a linear way and subtracting it from the characteristic of the voltage. Linear functions are determined by two points. Thus, the mean values of the first sine period (p_1) and the last sine period (p_2) of the voltage signal are being determined. The mean value of a sine period without offset is zero. Therefore, for the evaluated periods, the mean value can be used to determine the offset value $p_{i,v}$. The associated time component $p_{i,t}$ of the points corresponds to the midpoint of each period. Thus, the point (p_1) of the first period is given by its components

$$p_{i,v} = \sum_{s=0}^{s_p} \frac{v_s}{s_p}, \tag{7.1}$$

$$p_{i,t} = \sum_{s=0}^{s_p} \frac{t_s}{s_p} = \frac{1}{2 \cdot f}. \tag{7.2}$$

Here s implements a control variable that passes through the voltage samples v_s\$ and their corresponding time pointst_s. The number of values corresponding to the period is given by s_p and the measured frequency by f_k. The equation of a line described by p_1 and p_2 is then subtracted from the raw measurement data. As can be seen in Figure 7.6, the error is almost completely eliminated.
Afterwards the corrected voltage signal and the measured current signal are Fourier transformed to $\underline{V}$ and$\underline{I}$. Since only one frequency is applied at a time, only this frequency has to be evaluated. To save computational effort, the Goertzel algorithm can therefore be used[45]. Finally, the impedance $\underline{Z}$ of frequency k is calculated by

$$\underline{Z}_k = \frac{\underline{V}_k}{\underline{I}_k}. \tag{7.3}$$

Several impedances for different frequencies are measured quickly one after the other and can be combined to a spectrum.

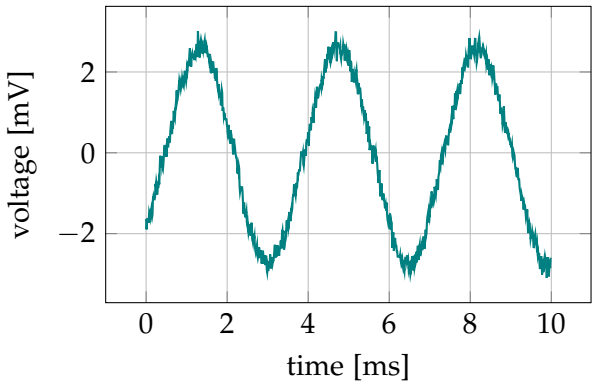

Figure 7.6: Adjusted voltage signal of an impedance measurement after subtracting the linear DC voltage function.

Exemplary measured impedance spectra are shown in Figure 7.7. Both spectra were measured directly one after the other during a discharge process, so that the states of charge differ minimally. Large inaccuracies can be found especially in the low-frequency right-hand region. The big disadvantage of the PicoEIS is the poor accuracy of the impedance measurements. The reason for this is the limited resolution of the current setpoint signal. The resolution of the DAC of the PicoScope offers a resolution of 12 bit at a fixed reference voltage of ± 1 V. On the one hand, the resolution of the output signal thus depends on the amplitude of the current, since the current amplitude is selected such that the amplitude of the voltage response is less than 10 mV. This means that one loses some of the resolution of the DAC, particularly with larger impedances, since a reduced current amplitude is used. These larger impedances can be found on the right-hand side of the spectra which corresponds to low frequencies. On the other hand, the signal output by the DAC consists not only of the AC component, but also of the DC component, which determines the charge or discharge current of the cell during the measurement. If the DC component is particularly large, a scaled-down signal first has to be output so that the voltage range of the DAC is not violated. Subsequently, this signal is amplified again to obtain the desired current. The initial scaling also reduces the resolution of the generated sine wave.

7.1.2 *MicroEIS*

These problems are eliminated in a new circuit. The overall structure of the circuit is shown in Figure 7.8. The entire EIS process is now controlled by a microcontroller, so that the setup is much smaller and field applications are also possible. The STM32F4 microcontroller represents the centerpiece of the schematic that controls all of the other peripherals. One of its two DACs is used to output a sine wave

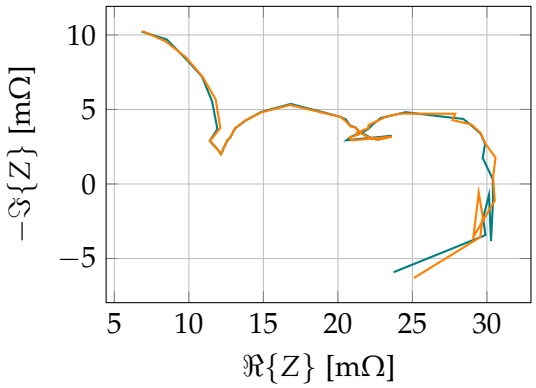

Figure 7.7: Samples of measured spectra with PicoEIS measurement system.

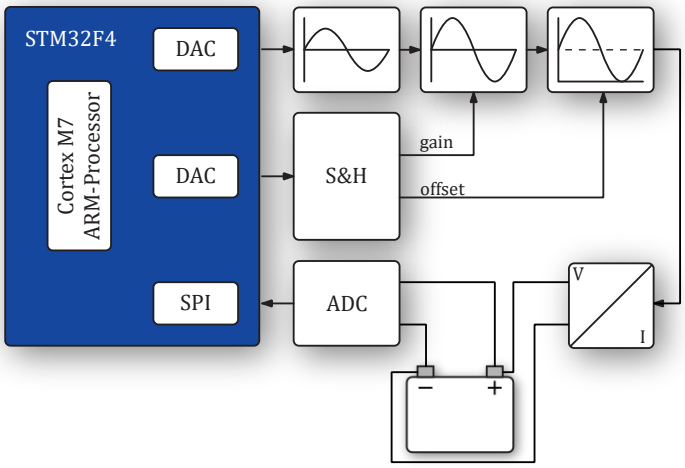

Figure 7.8: Schematic of developed circuit for measuring impedance spectra

at the frequency that is measured. The other DAC creates several constant voltages using a Sample-and-Hold (S&H) circuit that enables the duplication of numbers of outputs as long as constant voltages are being output. These voltages control the amplitude and the offset of the signal. The accuracy of the output signal is kept high, because amplitude and offset are controlled separately. A galvanostatic impedance measurement is preferred because the SoC of the battery is kept unchanged. Therefore, the output signal is used as input of a current controller that applies the AC current to the Battery Under Test (BUT). Last but not least, an external ADC is used to measure both the actual applied AC current and the resulting voltage response of the BUT. According to MacDonald the amplitude of the voltage response has to remain less than 10 mV[8]. Therefore, a high precision, high speed ADC, AD7768-4, is used so that the voltage response can be measured with sufficient accuracy despite the voltage offset of the battery. Offset compensation is thus no longer necessary.

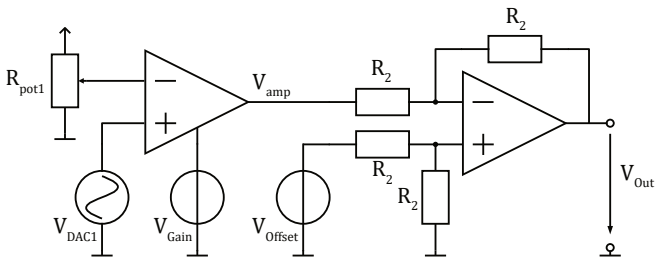

Figure 7.9: Schematic signal generation

7.1.2.1 *Signal Generation and Measurement Unit*

Figure 7.9 takes a closer look to the signal generation. The sine voltage V_{DAC1} is the DAC output of the microcontroller which oscillates between 0 V and 3.3 V. The left amplifier is the voltage controlled gain amplifier LMH6503. It amplifies its differential input voltage. Therefore, R_{pot1} sets the negative input voltage to 1.65 V so that the differential input voltage is a symmetrical sine wave. The amplitude of the output signal V_{amp} can by controlled by V_{Gain}.
The components on the right-hand side implement a difference amplifier. Since all resistors that belong to this circuit have an equal resistance

$$V_{out} = V_{offset} - V_{amp}$$

applies to the output voltage. Accordingly, voltage V_{amp} is inverted and shifted by an offset. Since V_{amp} is a symmetrical sine wave and only the phase difference between the applied current and the voltage response is evaluated for determining the impedance, an inversion of V_{amp} does not have any impact on the measurement.
V_{Gain} and V_{Offset} are generated by a single DAC output using a S&H circuit shown in Figure 7.10. The first amplifier implements a voltage buffer that decreases the current of the DAC. The following voltage divider shifts the DAC output range to symmetrical ± 1 V range by referencing the lower pin of R_2 to a negative voltage. Thereby, the offset voltage of V_{out} can correspond to either a constant charging or a constant discharging current. The actual sampling is implemented by a digitally controlled analog switch S_1 while the capacitors hold the sampled voltages. The circuit is controlled by the microcontroller that uses a timer with three output compare channels that cyclically generate interrupts at three different time points. During the first interrupt the switch is set to middle position that is not connected. The second interrupt changes the output of the DAC output voltage to the value of the next clamp. Finally, the switch is switched to this very clamp charging the corresponding capacitor. The final voltage buffers output the voltage that is stored in the capacity. Since the input current of an operational amplifier is rather small, the voltage of

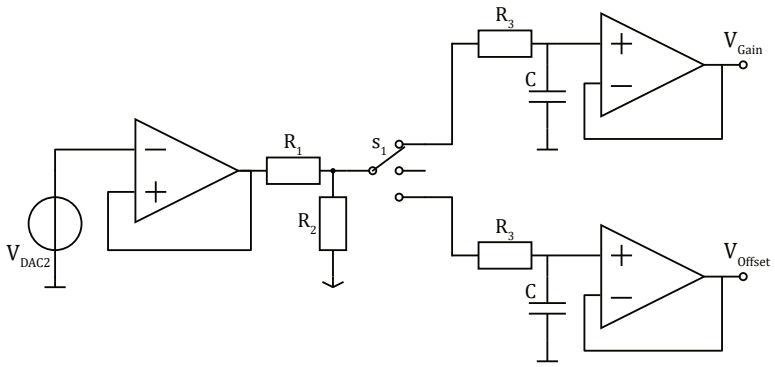

Figure 7.10: Schematic of Sample and Hold component

the capacity is almost constant, even when the DAC signal is removed when switching to the other path.

7.1.2.2 *Current Controller*

Since the galvanostatic impedance measurement method allows impedance measurements that do not affect the SoC of the battery, a current controller needs to be developed. The first question that arises here is whether digital or analogue control is better. Although it is much easier to adapt the controller parameters to the system being measured, the time constants are very small, so that the sampling intervals of a digital control would lead to instabilities. Therefore, an analog control system that is based on operational amplifier is used. The OPA549 is again used as the output operational amplifier, which can directly drive the required currents.
One possible method for implementing a current controller is Howland's current pump. The schematic of the basic Howland current pump is shown in Figure 7.11. An advantage of the current pump is that the current can flow in both directions. However, this original version has two crucial disadvantages. On the one hand, the output resistance depends strongly on the matching of the resistors R_1 to R_4. On the other hand the load current i_L flows to a large extent also through R_4. For EIS of batteries several amperes are necessary. Accordingly, extremely precise resistors with a high nominal power are required.
These weaknesses can be corrected by slight adjustments. Figure 7.12 shows an improved version of the current pump. The necessary loop and node equations are given by

$$0 = \frac{V_1 - V_C}{R_1} - i_1, \tag{7.4}$$

$$0 = \frac{V_2 - V_C}{R_3} - i_3, \tag{7.5}$$

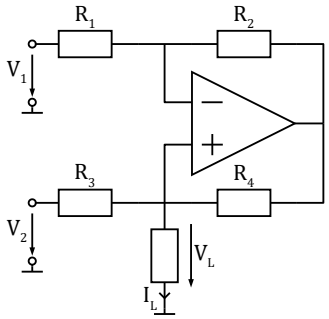

Figure 7.11: Schematic of Howland current pump

$$0 = V_1 - R_1 i_1 - R_2 i_1, \tag{7.6}$$

$$0 = V_2 - R_3 i_3 - R_4 i_3 - V_L, \tag{7.7}$$

$$0 = V_A - R_5 i_5 - V_L, \tag{7.8}$$

$$0 = i_5 + i_3 - i_L. \tag{7.9}$$

Separating $i_L$in equation 7.9 and substituting i_5 and i_3 using equations 7.4 to 7.8 results in

$$i_L = \frac{V_2 \left(R_1 R_4 + R_1 R_5 + R_2 R_4\right) - V_1 \left(R_2 R_3 + R_2 R_4\right)}{R_1 R_5 \left(R_3 + R_4\right)} + \\ + \frac{V_L \left(R_2 R_3 - R_1 R_5 - R_1 R_4\right)}{R_1 R_5 \left(R_3 + R_4\right)}. \tag{7.10}$$

The circuit implements a voltage controlled current source if the load current i_L is independent of the voltage of the load V_L. Therefore the constraint

$$R_2 R_3 = R_1 R_5 + R_1 R_4 \tag{7.11}$$

has to be satisfied which means that the ratio of R_1 and R_2 needs to equal the ratio of R_3 and $(R_4 + R_5)$:

$$\frac{R_1}{R_2} = \frac{R_3}{R_4 + R_5}. \tag{7.12}$$

Substituting R_3 and R_2 for $R_1$and $(R_4 + R_5)$, respectively, results in

$$i_L = \left(\frac{R_4 + R_5}{R_1} \cdot \frac{1}{R_5}\right) \left(U_2 - U_1\right). \tag{7.13}$$

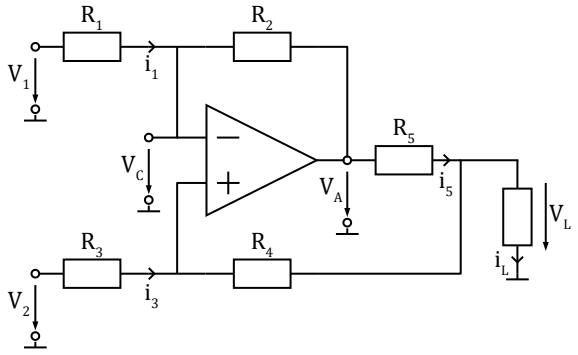

Figure 7.12: Schematic of improved Howland current pump

The output current of the improved Howland circuit depends on the input voltage difference and the gain is set by R_5 and modified by the ratio of R_1 and R_2.

One advantage of the improved Howland current pump is that the resistor R_5 that sees the output current can be small while maintaining the gain of the circuit by modifying the other resistors of the circuit. However, the control loop does not use an integral component, so that a high gain of the operational amplifier is necessary to ensure the smallest possible control deviation. Especially when high frequency signals are used, this condition is no longer guaranteed, since the gain of the OPA549 has already dropped by 5 orders of magnitude at a frequency of 1 kHz. For this reason, the Howland current pump approach was discarded.

Another possible current controller implementation is shown in Figure 7.13. Here,an instrumental amplifier is used to measure the load current i_L and two operational amplifier implement a differential amplifier and a PID controller. The main purpose of the instrumentation amplifier is to measure and amplify the differential voltage of the shunt resistor R_S and to reference its output voltage

$$v_S(t) = (v_A(t) - v_L) \cdot G_S = R_S i_L(t) \cdot G_S \tag{7.14}$$

to ground potential. The value $v_I(t)$ sets the desired load current i_L multiplied by R_S and G_S. Therefore, the operational amplifier on the left-hand side implements the differential amplifier with a gain of 1 and determines the negative of the measured error $e(t)$:

$$v_E(t) = v_S(t) - v_I(t) = -e(t). \tag{7.15}$$

The actual controller is implemented by the op amp on the right-hand side. As an approximation, the inputs of an operational amplifier can be regarded as current-less, so that the current flowing through R_2 and C_2 can be assumed to equal $i_1(t)$. Therefore, i_{11} and i_{12} form two components of the regulating variable:

$$i_2(t) = i_1(t) = i_{11}(t) + i_{12}(t) \tag{7.16}$$

Due to the negative feedback, both input terminals of the operational amplifier are forced to ground potential. Therefore, the current $i_{11}(t)$ can be calculated by

$$i_{11}(t) = \frac{1}{R_1} v_E(t) = -\frac{1}{R_1} e(t). \tag{7.17}$$

Furthermore, i_{12} is defined by

$$i_{12}(t) = C_1 \frac{d\, v_E(t)}{dt} = -C_1 \frac{d\, e(t)}{dt}. \tag{7.18}$$

The output voltage v_A is determined by the current i_2 :

$$v_A(t) = -i_2 R_2 - \frac{1}{C_2} \int i_2(t)\, dt. \tag{7.19}$$

Inserting equations 7.16 to 7.18 results in

$$v_A(t) = -\frac{R_2}{R_1} v_E(t) - \frac{1}{R_1 C_2} \int v_E(t)\, dt + \\ - R_2 C_1 \frac{d\, v_E(t)}{dt} - \frac{C_1}{C_2} v_E(t), \tag{7.20}$$

$$v_A(t) = -\left(\frac{R_2 C_2 + R_1 C_1}{R_1 C_2} \right) v_E(t) + \\ - \frac{1}{R_1 C_2} \int v_E(t)\, dt - R_2 C_1 \frac{d\, v_E(t)}{dt}, \tag{7.21}$$

$$v_A(t) = \left(\frac{R_2}{R_1} + \frac{C_1}{C_2} \right) e(t) + \frac{1}{R_1 C_2} \int e(t)\, dt + R_2 C_1 \frac{d\, e(t)}{dt}. \tag{7.22}$$

Comparing the last equation with the equation of a PID controller

$$y(t) = K_p \cdot e(t) + K_i \int e(\tau)\, d\tau + K_d \frac{d\, e(t)}{dt} \tag{7.23}$$

results in the following parameters:

$$K_p = \frac{R_2}{R_1} + \frac{C_1}{C_2}, \tag{7.24}$$

$$K_i = \frac{1}{R_1 C_2}, \tag{7.25}$$

$$K_d = R_2 C_1. \tag{7.26}$$

In the next step the controller parameters were optimized. Since the load R_L represents the BUT, which cannot be described sufficiently

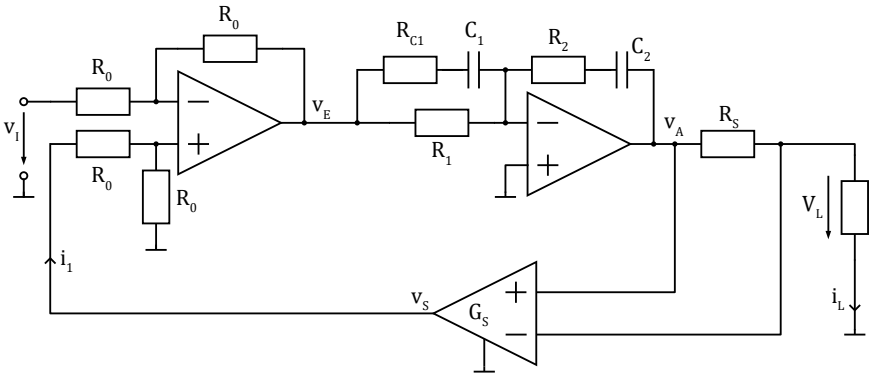

Figure 7.13: Schematic of the PID current controller

accurately by a resistor, an equivalent circuit consisting of a voltage source, a series resistor and a RC parallel circuit was used as R_L. The circuit simulator Microcap already includes an optimizer. During the optimization the controller parameters were tuned to minimize the expression RMS(v(VE)) when a step function is applied to the input. Thus, the root mean square of the voltage V_e, which in turn represents the control deviation should be as small as possible. The optimized circuit was then produced on a Printed Circuit Board (PCB). Care must

sure to taken be

the BUT are sufficiently sized.

For testing of the current controller, a test impedance was designed according to the recommendations in Kiel's dissertation, which models the impedance behavior of a battery[63]. The main problem in reproducing the impedance behavior of a battery is the necessary capacitance, which is usually larger than a few farads. The production of such large capacitance is very expensive, unless double layer capacitors are used, which, however, show a strong dependence on temperature, state of charge and aging and are thus far from constant[31]. Figure 7.14 shows Kiel's approach, in which the impedance Z, which can consist for example of an R ∥ C element, is reduced by a voltage divider circuit with R_{shunt} and R_v, so that available capacitors can be used.

First, the step response of the current controller was measured using the test impedance, whereby the target signal was generated with the aid of a function generator. The voltage V_S is used to measure the current and shown in Figure 7.15. The step response of the current controller asymptotically follows the input signal without overshoot and thus demonstrates the behavior of a first order low pass filter. The test signal transitions to 500 mV, so that the time constant can be read when 315 mV is reached. This occurs after 43 µs and thus corresponds to a cutoff frequency of 23 kHz. The current regulator is thus sufficiently fast for frequencies usually measured during EIS.

Figures 7.16 and 7.17 show the results when combining the signal generation unit and the current controller. Once again, the test impedance

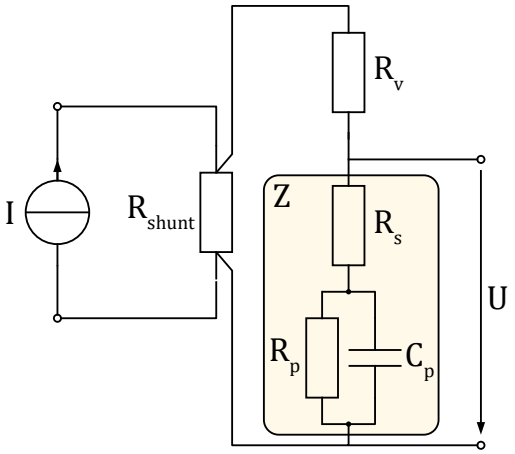

Figure 7.14: Schematic of test impedance according to Kiel used to verify the MicroEIS setup[63].

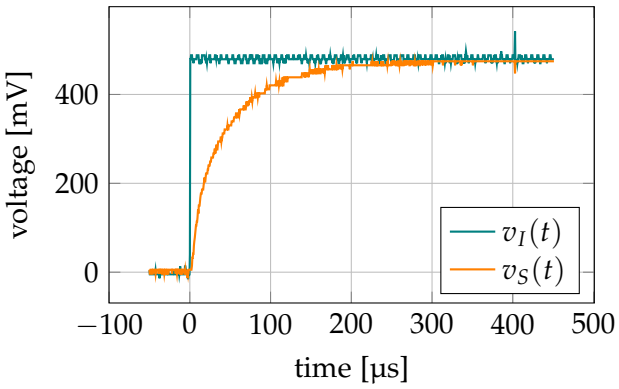

Figure 7.15: Step response of the PID current controller.

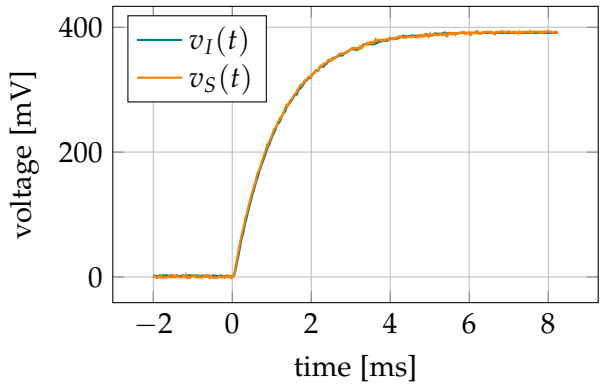

Figure 7.16: Step response of the signal generation unit and current controller response.

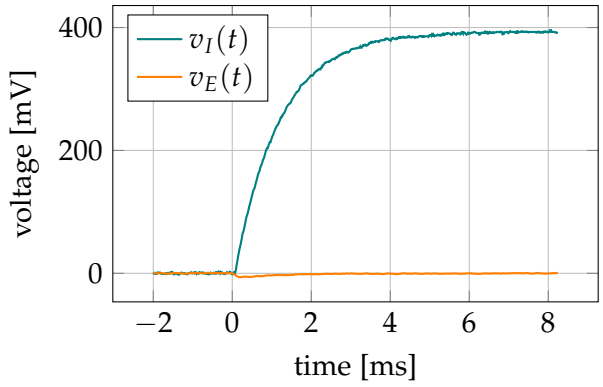

Figure 7.17: Control deviation of the PID current controller when applying signal generation step function.

was used as R_L, which was designed on the basis of Kiel's dissertation[63]. First of all, it is noticeable that there is no visible difference between these two signals. However, the signals correspond rather to a first order delay element than a step function. This is due to the fact that the input signal is generated by the signal generation. The charging of the capacitor in the S&H part is mainly responsible for the slow rise of the voltage. Therefore, the current controller is dimensioned sufficiently fast to output the generated signals.

Figure 7.17 takes a closer look at the control deviation V_E. At the beginning of the step, when the slope is at its maximum, there is a small control deviation. In relation to the step height of 400 mV, the maximum deviation of 6.3 mV is still relatively small.

7.1.3 *EISmeter*

During the project, funding was obtained for a commercial impedance spectroscope. The most difficult challenge in the search for a suitable product is the simultaneous application of a DC current during the

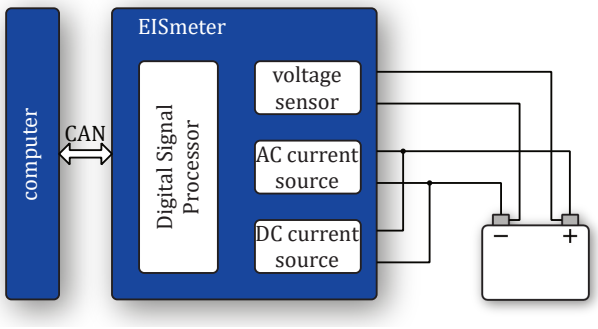

Figure 7.18: Schematic structure of the Digatron EISmeter[14].

impedance measurement. This is essential for the developed zinc-air cell, because it uses a 3-electrode technology and the respective charge or discharge region must not be left during the impedance measurement. If no DC current is applied, the cell would be charged during the first half-period of the sine wave and discharged during the second half-period.
The EISmeter from the Digatron company was finally chosen. This was developed together with the Institute for Power Electronics and Electrical Drives (ISEA) of RTWH Aachen university. The basic structure of the device is shown in Figure 7.18. The parameters of the measurement are set on a computer. The parameter set includes the frequency range being measured, the desired amplitude of the voltage response, the DC current that will be used, and maximum values for the current amplitude and cell voltage[28]. The data is transmitted to the EISmeter via a CAN bus. A digital signal processor coordinates the generation of the current signal and measures the resulting cell voltage. AC part and DC part of the current are generated separately. The impedance is then determined from the data and sent back to the computer[14, 28].The impedance range of 300 µΩ to 3 Ω is sufficiently large, because as seen with the previous measuring instruments, the impedances of the zinc-air cells are between 5 mΩ and 100 mΩ. Also the frequency range is generally applicable, especially it is possible to measure at frequencies lower than 1 Hz[29].
Figure 7.19 shows some example measured data of the EISmeter. Between the measurements the cell was discharged for 45 minutes, therefore the spectra are not exactly identical. Especially in comparison to the Picoeis, much smaller inaccuracies can be found. It can already be seen here that especially the low-frequency components, which are found on the right-hand side, are influenced by the SoC.

7.1.3.1 *Electrode Changer*

However, the EISmeter has the disadvantage that it is designed for using two-pole battery cells. Besides the manual reconnection, one way to still use zinc-air cells with 3-electrode technology is to use two

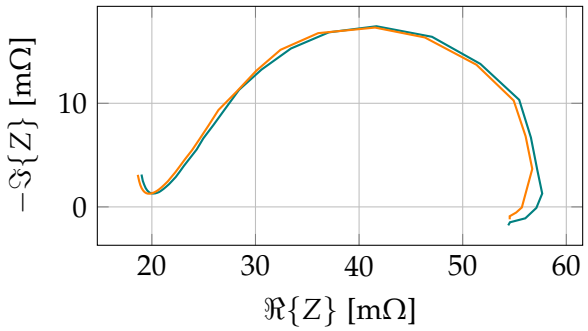

Figure 7.19: Samples of measured spectra with EISmeter measurement system.

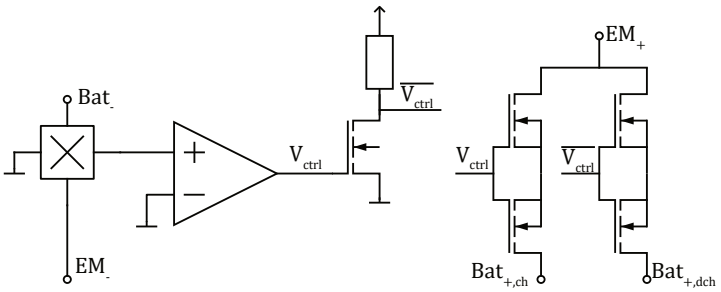

Figure 7.20: Schematic of the electrode changer board used to drive 3 electrode technology cells with EISmeter impedance spectroscope.

channels of the EISmeter for one cell. One channel is taken exclusively during charging of the cell and is connected to the charging electrode and one channel is connected to the air cathode is used only during discharging of the cell. Of course, the method has the disadvantage that it reduces the number of simultaneous tests by half. To overcome this, an electrode changer board was developed. The corresponding circuit is shown in Figure 7.20. It is based on a Hall-effect current sensor from Allegro Microsystems. An operational amplifier, which works as a comparator, detects the direction of the current, i.e. whether the cell is being discharged or charged. Depending on the case, a different current path is enabled to the appropriate electrode. An identical control is also available for the path of the voltage measurement, whereby smaller transistors are used here.

7.2 STATE OF CHARGE ESTIMATION

Probably the most important information that a battery mangament system relies on is the SoC of the cell. A too low SoC leads to a significant reduction in the lifetime of zinc-air cells, since the proportion of zincate in the anode is particularly high. On the one hand, it dissolves in the electrolyte, which simply reduces the amount of material in

the anode and thus the cell capacity. This can be counteracted by already adding zinc to the electrolyte beforehand. Nevertheless, the zinc anode in the discharged state is in the form of a paste and is displaced downwards by the force of gravity. At the bottom, the anode mass can then expand, reaching as far as the counter-electrode. The resulting short circuit prevents further battery operation.
On the other hand, overcharging of the cell is also a problem. The gassing voltage of the cell is on the same level as the charging voltage. When charging at higher states of charge, an accompanying electrolysis of the electrolyte therefore already begins, resulting in the release of hydrogen. As soon as the cell is fully charged, the applied current is actually used completely for electrolysis. On the one hand, this is problematic because an atmosphere with more than 5 % hydrogen is an explosive environment. However, this problem can be overcome with a fan. On the other hand, the electrolyte loses hydrogen and oxygen during electrolysis, while the amount of potassium hydroxide remains the same. The concentration of the electrolyte therefore increases. This is accompanied by a decrease in the conductance of the electrolyte and the efficiency of the cell. In addition, the higher concentration of potassium hydroxide is more aggressive and can attack the other cell components.
In current cell technologies, the cell voltage is typically used to determine the SoC. For both lead-acid batteries and lithium-ion cells, the open-circuit voltage is strongly dependent on the SoC. This also enables the Constant Current Constant Voltage (CCCV) charging method, where a maximum current and voltage is specified. As long as the cell is fairly empty, the charging voltage is below the end-of-charge voltage and the cell is charged with the specified maximum current. Towards the end of the charging process, the charge voltage then reaches the end-of-charge voltage. Voltage regulation now takes place and the charge current continues to drop.
As already described in sections 4.1 and 5.2, the voltage range is almost constant for a large part of the discharge process. At the end, however, there is a rapid drop in cell voltage, so that an empty cell can be easily detected. During charging, the dependence of the cell voltage on the SoC is also much smaller for zinc-air batteries. Charging in CCCV mode is thus impractical, since the cell voltage already reaches the gassing voltage at the beginning of the charging process. Staying away from the gassing voltage is only possible by drastically reducing the charging power, in which case there would be no practical use for the cell. For this reason, zinc-air cells are charged at a constant current.
In particular, the course of the microcycles shows that the influence of temperature and electrolyte condition on the cell voltage is greater than the influence of the SoC. For example, the voltage differences between cycles are greater than during a cycle. Thus, it is impossible

to determine the SoC based on the cell voltage. Instead, the impressed charge is often counted. When the cell is used continuously, this is a totally practicable method. However, when the cell is left unused for long periods, an unknown self-discharge comes into play. For this reason, this chapter examines alternative ways of determining the SoC. Here, electrochemical impedance spectra are a promising approach.

7.2.1 *Modeling of Equivalent Circuits*

A frequently used analysis method of impedance spectra is the parameterization of an electrical equivalent circuit, as it was created in Section 4.1. There is also a dedicated paper dealing with SoC dependent fitting of equivalent circuits[84].

7.2.1.1 *Model Verification*

From each measured spectrum, an electrical battery model is derived whose parameters depend on the SoC. The parameters of the corresponding equivalent circuit are varied so that the sum of the squared error

$$E_{square} = \sum_{i=1}^{n} [Z_{measured}(f_i) - Z_{model}(f_i)]^2 \tag{7.27}$$

between the measured impedance $Z_{measured}$ and the model impedance Z_{model} for the measured frequencies f is minimized. Numerical solution methods as described in Section 4.1 from Matlab or Python can be used to solve the minimization problem. The developed Python program to fit the model can be found in Appendix A.2.
Figure 7.21 shows a measured impedance spectrum during the charging process and the impedance curve of the fitted battery model. Both curves have a very similar course. Although models of different cell reactions often provide similar impedance behavior, it can be seen that the battery model created in Section 4.1 is suitable for successfully modeling the tested zinc-air cell. Colored highlights are used to mark various properties of the measured spectrum. First of all, the green area shows that at particularly high frequencies an inductive component can also be measured, which is indicated by a positive real part. The subsequent semicircle of the impedance curve, which results from the parallel connection of the charge transfer resistance and the double layer capacity, does not start at a 90° angle to the real axis (red area). As mentioned in Section 4.1, the porosity of the two electrodes is a potential reason. Therefore, the double layer capacity in this battery model is described by a constant phase element. While the double layer capacity also significantly defines the frequency distribution on the semicircle, the charge transfer resistance defines the radius marked in yellow. Both electrodes act in the same frequency range during the charging process, so that both semicircles overlap and are difficult to

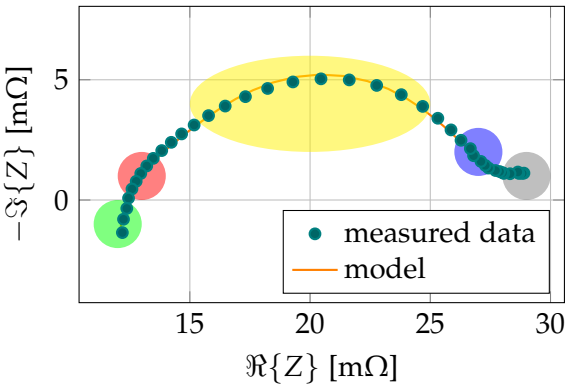

Figure 7.21: Impedance spectrum of the zinc-air battery measured during a charge process and impedance curve of the fitted model.

distinguish. However, a closer look reveals that the curvature of the semicircle changes during the course (red and blue area), so that only a model that describes both electrodes allows a sufficiently accurate fitting. In the gray area of the particularly low frequencies, the first impact of the Warburg impedance can be seen.
In Figure 7.22, the battery model is verified with the measured spectrum during a discharge process. Again, the developed model is suitable for modeling the measured data. Compared to the charge process, especially the impedance values at the low frequencies are about twice as high. This confirms once again that the separate nickel electrode used for charging not only leads to an increased cycling life, but also allows higher charging currents with lower power dissipation. The semicircles based on the parallel connection of the double layer capacitance and the charge transfer resistor are more separated here. In the left part of the curve, there is initially a smaller circle for the higher frequencies, which is created by the zinc anode. Subsequently, this merges into a much larger semicircle. The radius of the semicircle is essentially formed by the charge-transfer resistor. Because the air electrode is several millimeters thick, the diffusion length of the oxygen ions is also correspondingly long, so that the discharge power of the cell depends mainly on the surface of the GDE.
While in this section the battery models were verified first with the measurement data from the conventional EISmeter instrument, the next section investigates whether embedded measurement devices that can be used in a demonstrator, with their limited resolution, are sufficient to determine the SoC based on the battery model.

7.2.1.2 *Results*

Since the model structure of the equivalent circuit of the anode and cathode is identical, the assignment of the diffusion processes to the electrodes in the model can be random. Thus, the reactions of the zinc anode in Figure 4.5 can be assigned either to the left electrode

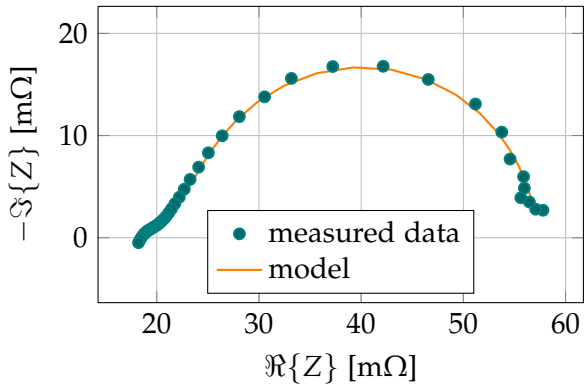

Figure 7.22: Impedance spectrum of the zinc-air battery measured during a discharge process and impedance curve of the fitted model.

impedance or to the right. To provide a fixed assignment for periodic impedance measurements, the parameters of the previous impedance spectrum are used as initial values for the Levenberg-Marquardt algorithm. Since this performs a gradient descent, a strong tendency is thus established for the same electrode pairing.
Initially, the PicoEIS setup was used to perform the EIS. Selected examples of the measured spectra during discharge of a 50 A h zinc-air cell are shown in Figure 7.23. Using the low-budget setup is sufficient to measure spectra that differ with respect to the SoC. Especially in the right region of the impedance spectrum, clear differences between the charge states can be seen; these are the low frequencies in the range from 100 mHz to 1 kHz. The reason for this behavior is probably that the diffusion processes at the GDE are rather slow. Spectra at higher charge states tend to have higher absolute values for both the imaginary and real parts. This can be explained by increasing charge transfer resistance. At higher frequencies, the impedance is mainly determined by the conductivity of the electrolyte, since the double layer capacitors of the anode and cathode act as a short circuit. Therefore, all spectra end with almost the same impedance value.
In Figure 7.24, two different spectra of a charging cycle are shown. For each spectrum, only one semicircle is shown here. While the spectrum of a half-charged battery matches the equivalent circuit, the behavior of a fully charged battery does not match the equivalent circuit. Probably in this case electrolysis is dominant, which leads to a completely different behavior. At low frequencies, the impedance spectrum tends to drift away with constant phase, which can be explained by a dominant Warburg element[134]. Again, the highest variance is found at the low frequencies.
In Figure 7.25 some of the determined parameter values of the equivalent circuit during the course of a discharge cycle are shown. These values are normalized with respect to the mean value in order to illustrate the characteristic. However, their variance is still small and is therefore

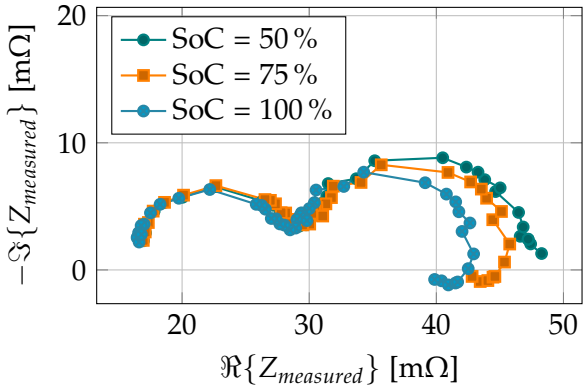

Figure 7.23: Some measured sample spectra of a discharging cycle at different states of charge

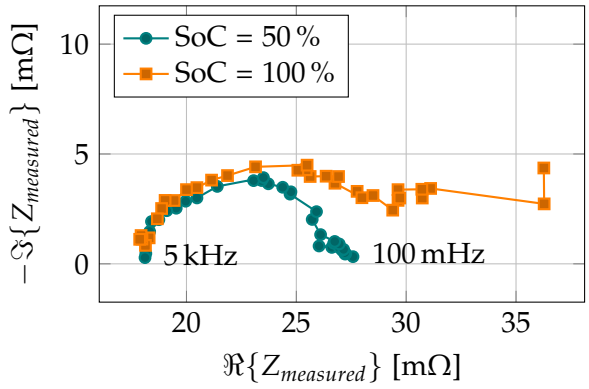

Figure 7.24: Two measured spectra of a charging cycle comparing a battery a half charged and at overcharged state

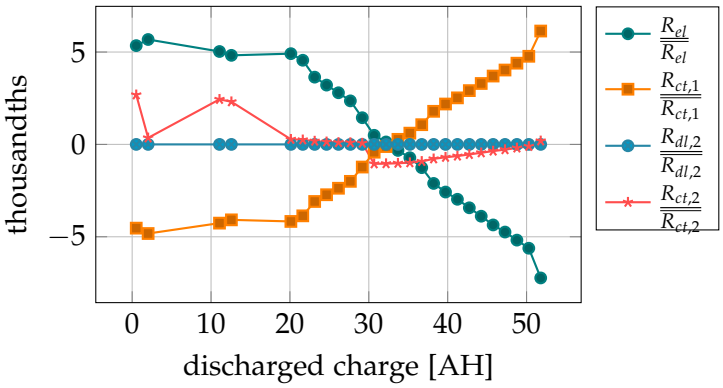

Figure 7.25: Development of the normalized parameter of the equivalent circuit during a discharge cycle

plotted in parts per thousand. The assignment of the electrodes is selected so that $C_{dl,2}$ and $R_{ct,2}$ belong to the GDE. Their parameter values are quite constant, since both the oxygen concentration of the ambient air and the electrolyte concentration and temperature change only slightly during the discharge process. The absolute change in R_{el} is also quite small, since resistivity is the minimum impedance of each spectrum. Therefore, the most unambiguous parameter for assessing the charge state is the charge transfer resistance $R_{ct,1}$ of the zinc anode.

Figure 7.26 takes a closer look at the course of $R_{ct,1}$. As before, the absolute change in the parameter value is rather small, but a precise trend can still be seen. At the beginning of the discharge cycle, the resistance hardly changes. The zinc concentration is still high enough not to affect the charge transfer. But it increases linearly after 20 A h have been discharged. A quadratic polynomial model $M_{\mathrm{ECM,dch}}$ provides a good approximation in both parts of the characteristic curve. So, calculating back the determined charge transfer resistance $R_{ct,1}$ to the SoC results in a Root Mean Squared Error (RMSE) of

$$\begin{aligned} RMSE_{\mathrm{EC,dch}} &= \sqrt{\tfrac{1}{n}\left(\textstyle\sum_{i=1}^{n}\left(M_{\mathrm{ECM,dch}}\left(R_{ct,1}(i)\right) - Q_{\mathrm{dch}}\left(R_{ct,1}(i)\right)\right)^2\right)} \\ RMSE_{\mathrm{EC,dch}} &= 2.03\,\mathrm{A\,h}. \end{aligned} \tag{7.28}$$

Figure 7.27 shows the determined parameters of the model with respect to the SoC during an entire charge cycle. These values are also normalized to the respective mean value here. It should be noted that the cell was massively overcharged and that the change in the parameter values is so large that these are not given in parts per thousand. Most parameters show a significant change at 68 A h. Taking into account that during the discharge process 51 A h could be discharged before the final discharge voltage was reached, the secondary

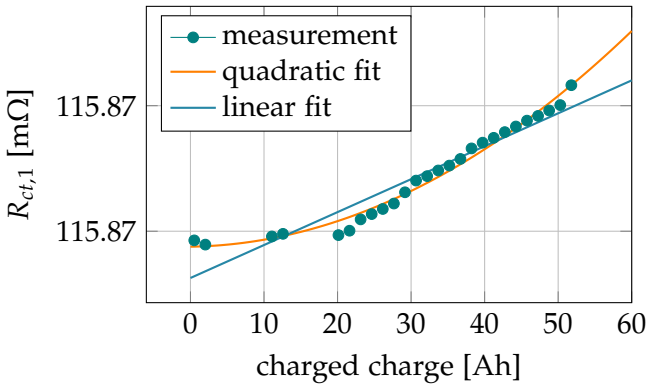

Figure 7.26: Closer look to the charge transfer resistance of the anode during a discharge cycle

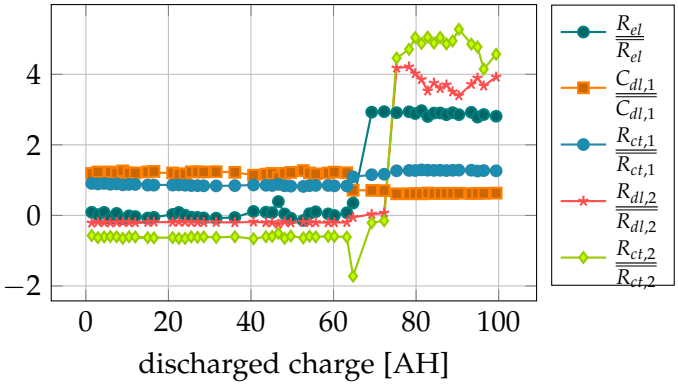

Figure 7.27: Development of the normalized parameter of the equivalent circuit during a charging cycle

electrolysis process, which occurs when the cell is overcharged, is probably the reason for the massive change of the parameters. The assumption is strengthened by the fact that the ohmic resistance of the electrolyte also experiences a strong change. Battery operation no longer takes place, electrolysis becomes dominant at the end of the charging process and the model simply no longer fits. The difference between the charged and the discharged charge can be explained by the coulombic efficiency.

So while measuring the cell voltage is not sufficient to determine a charge termination of zinc-air batteries, measuring impedance spectra and fitting the created electrical equivalent circuit of the cell makes it easy to detect the end of charge.

Determining the current SoC, on the other hand, is more problematic. The reason is that there is no clear dependence of any parameter on the SoC when considering the range in which the battery is not yet fully charged and no dominant electrolysis takes place. Nevertheless 7.28 provides a more detailed representation of the course of the charge transfer resistance of the anode $R_{ct,1}$ in the region where the battery is not yet full. Again, there is a correlation with the SoC, which can

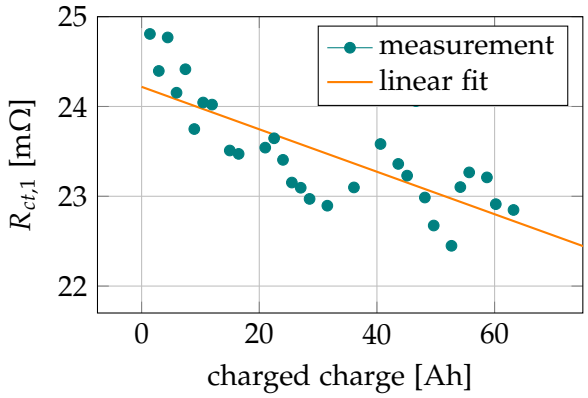

Figure 7.28: Development of the charge transfer resistance during a charging cycle while the battery is not overchaged

be approximated by a linear fit $M_{\text{ECM,ch}}$. However, the noise of the parameters fitted from the measured data is so large that no exact assignment to a SoC is possible. Therefore, a RMSE of

$$\begin{aligned} RMSE_{\text{EC,ch}} &= \sqrt{\frac{1}{n}\left(\sum_{i=1}^{n}\left(M_{\text{ECM,ch}}\left(R_{ct,1}(i)\right) - Q_{\text{ch}}\left(R_{ct,1}(i)\right)\right)^2\right)} \\ RMSE_{\text{EC,ch}} &= 13.51\,\text{A h} \end{aligned} \tag{7.29}$$

is obtained.
With the parameterization of the electrochemical model based on measured electrochemical impedance spectra, it is therefore possible to determine both the charge termination and the SoC during discharge. In particular, detection of the charge termination purely on the basis of the cell voltage was not possible before. However, the noise during charging is too high to allow reliable detection of the SoC based on the electrical equivalent circuit.

7.2.2 *End of Charge Detection*

Section 7.2.1 presents how the measurement of an electrochemical impedance spectrum can be used to detect a charge termination of rechargeable zinc-air batteries. It is shown that a strong change in the low frequency diffusion process occurs when the full state is reached. This is well illustrated in Figure 7.24 by the much larger radius of the overcharged spectrum. In this chapter, a robust method is now presented that uses the change in impedance spectra as a cutoff criterion and therefore works reliably even in the presence of strong manufacturing tolerances, such as those that are expected when cells are manufactured by hand. A detailed publication covering this topic can be found in [82].
The idea behind the new end-of-charge criterion is to observe the

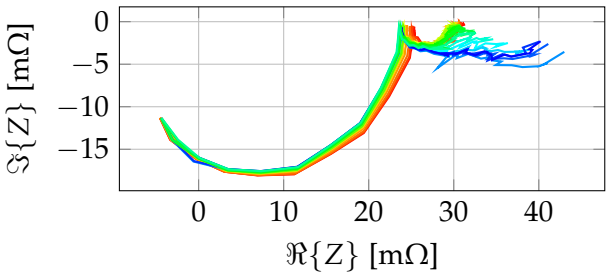

Figure 7.29: Impedance spectrum colour weighted from red (SoC=0) to blue (SoC=100)

rate of change of the electrochemical impedance spectra. The spectra describe the chemical processes in the cell and depend, for example, on the charge state or the SoH. Of course, the spectra are also affected by parameter tolerances. Therefore, not the absolute impedance values are evaluated, but their rate of change. The measured spectra of a charge cycle are shown in Figure 7.29. The color of each characteristic curve specifies the time of the impedance measurement. Since a constant charge current is used, the color also represents the SoC of the battery. Red spectra indicate an empty battery (SoC=0 %), while blue spectra belong to a fully charged or even overcharged battery (SoC=100 %). While the differences in spectra between a full and an empty battery are rather small at high frequencies (left part of the Nyquist plot), the largest deviation in impedance values is found at the low frequencies that form the semicircle on the right. To reduce the computational cost as much as possible, no electrochemical model is fitted in this approach. Instead, the proposed method generates circular models of the right semicircles and uses the evolution of their radii[81].

There are two challenges in creating a circle model based on a measured spectrum. On the one hand, the right semicircle must be separated. The phase ϕ of the impedance values can easily be used for this purpose. This indicates the angle between the impedance values and the real axis. The evolution of ϕ over all frequencies in a spectrum is shown in Figure 7.30. The first frequency index $k = 0$ corresponds to the lowest measured frequency. Therefore, the values on the left side in Figure 7.30 correspond to the values on the right side of Figure7.29. Since the radii of the high-frequency circles have a tendency to be much larger than the radii of the important semicircles, the angle values decrease significantly as the frequencies of the left semicircle are reached.
The aim of the method is to be as robust as possible and therefore to be able to generalize to new battery prototypes. Hence, the use of absolute values is omitted. Instead, the derivative of the course of ϕ with respect to the frequency is used. Since the impedances are

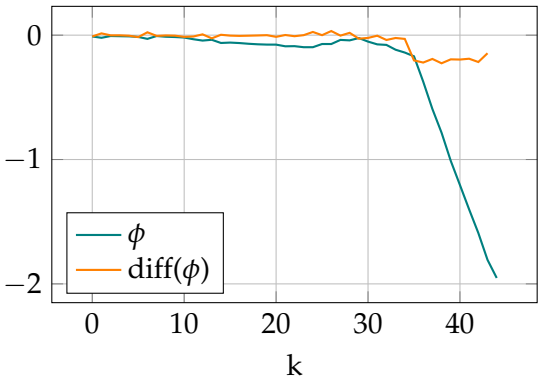

Figure 7.30: Development of the charge transfer resistance during a charging cycle while the battery is not overchaged

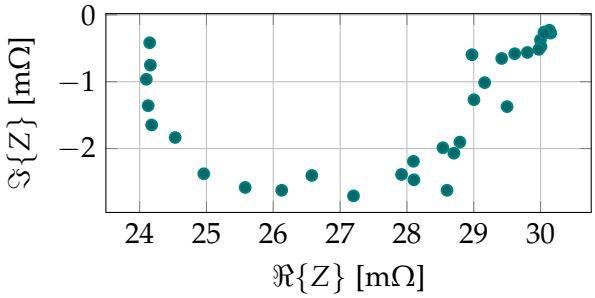

Figure 7.31: Resulting spectrum after separating the right semicircle.

measured only at discrete frequencies, the derivative can be specified as the difference quotient of two subsequent impedance values with an interval of 1 (diff function). Also the threshold value used to determine the index of the splitting point is not based on an absolute value, but is determined by averaging the spectrum itself. The index of the splitting point is chosen so that

$$k_{split} = \frac{\partial \phi(Z_k)}{\partial k} > \left[5 \cdot RMS(\frac{\partial \phi(Z_k)}{\partial k}) \right], \tag{7.30}$$

more precisely

$$k_{split} = \phi(Z_k) - \phi(Z_{k-1}) > [5 \cdot RMS(\phi(Z_k) - \phi(Z_{k-1}))]. \tag{7.31}$$

Figure 7.31 shows a separated spectrum after the cutting process. As can be seen, the cutting algorithm works quite well. However, the data is also contaminated with a lot of noise during the charging process. Therefore, the second challenge is to remove outliers from the spectrum before modeling the circles.
Here, good results have been achieved with the RANSAC (Random Sample Consensus) algorithm. Figure 7.32 helps to illustrate the algorithm. The basic idea is to fit multiple models and use the best-fitting model with the fewest outliers[37]. Three points are sufficient to define a circle, so three impedance points are first randomly selected

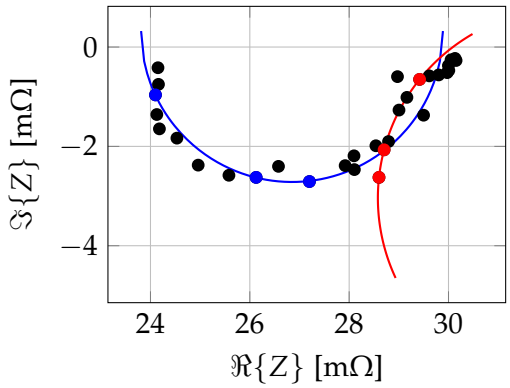

Figure 7.32: Visualisation of RANSAC algorithm.

and used to create an initial circle model. These three points can either result in a good model (blue points) or a bad model (red points). The resulting model is then tested against all other impedance values. If the distance between an impedance value and the circular model is less than 2 % of the maximum absolute value of that spectrum, it is considered an inlier and the number of inliers is summed up. Good models are characterized by a high number of inliers. These steps are repeated for 15 sets of randomly chosen initial values. Finally, the algorithm selects the model with the highest number of inliers.
Next, an optimized circular model is determined using all impedance values that are considered inliers by minimizing the mean squared error according to Bucher[21]. The relation of a circle is given by

$$(x - x_c)^2 + (y - y_c)^2 = r^2 \tag{7.32}$$

where x_c and y_c denote the center of the circle and r the radius. Substituting

$$A = x_c^2 + y_c^2, \tag{7.33}$$

$$B = 2 \cdot x_c, \tag{7.34}$$

$$C = 2 \cdot y_c \tag{7.35}$$

results in a linear system of equations:

$$\begin{bmatrix} 1 & -x_1 & -y_1 \\ 1 & -x_2 & -y_2 \\ 1 & -x_3 & -y_3 \\ \vdots & \vdots & \vdots \end{bmatrix} \cdot \begin{bmatrix} A \\ B \\ C \end{bmatrix} = \begin{bmatrix} x_1^2 + y_1^2 \\ x_2^2 + y_2^2 \\ x_3^2 + y_3^2 \\ \vdots \end{bmatrix} \tag{7.36}$$

that is solved using the least-squares solution of the system. Finally, the actual radius is determined by inserting the solution into the equations above.

The idea of the algorithm is to detect the transition of chemical processes from charging the battery to overcharging with accompanying electrolysis. Considered separately, the spectra change only moderately during the charging process. At the beginning of the charging process, the zincate is reduced to zinc. This process leads to an increase in the SoC of the cell. When the charging process is about to end, an accompanying electrolysis process starts, which separates the water part of the electrolyte to hydrogen and oxygen. The concept is that the spectra of these two reactions are very different, as the reactions are completely different. Therefore, there is a detectable transition when the cell reaches its charge termination. At this stage, the fraction of impressed current used for zinc reduction decreases, while the fraction used for electrolysis increases. For this reason, the derivative of the radii is analyzed with respect to the charged energy. Since the measurements of the impedance spectra were performed time discrete with a fixed charging current and a fixed sampling interval of 30 min, the difference between two following radii at measurement index n is used as the derivative:

$$r'(n) = \frac{\partial r(n)}{\partial Q_{charged}(n)} = \frac{r_n - r_{n-1}}{Q_{charged,n} - Q_{charged,n-1}}. \tag{7.37}$$

The development of the magnitude of the derivative during a charging cycle is shown in Figure 7.33. It is quite small at the beginning of the charging cycle, which means that the change in radii during the charging process is actually quite small. Then after 60 A h has been charged into the cell, the gradient increases sharply. At this point, the transition of the chemical reactions begins. After 85 A h, the gradient then decreases again. Here the reduction process stops completely and only the electrolysis process takes place. Since this is relatively constant, the change in the impedance radii is also accordingly small. The threshold is determined based on the values of the derivative at the beginning of the charging cycle. Even if the evaluated battery has large tolerances, it can be assumed that at least 33 % of the targeted capacity is reached. Therefore, the values of the derivative from the first third of the nominal capacity are used to calculate the limit Δr_{limit}. More precisely, the algorithm uses the average the absolute values in this range:

$$\Delta r_{limit} = \sqrt{\frac{3}{N} \sum_{n=1}^{N/3} \left| r'(n) \right|} \cdot 8. \tag{7.38}$$

Here N indicates the number of impedance spectra within the complete nominal capacitance. The complete method thus operates free of

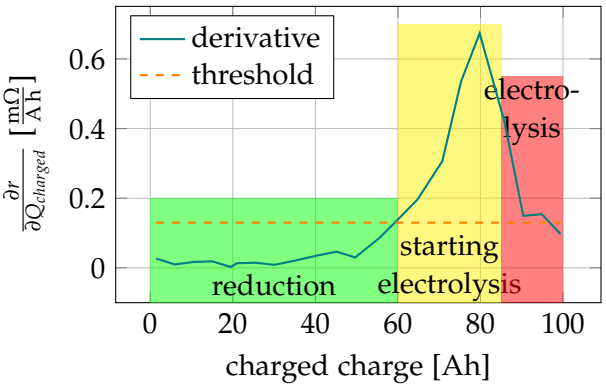

Figure 7.33: Development of the gradient of the radii of the circle models. The characteristic is divided into several chemical processes.

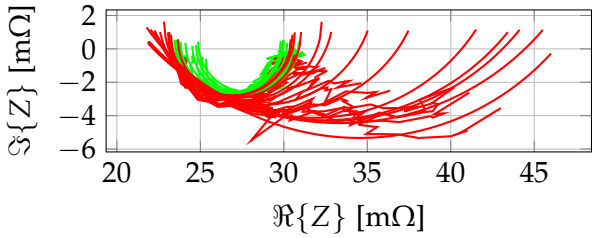

Figure 7.34: Impedance spectrum split in charging (green) and overcharging (red) - transition at roughly 60 A h

absolute values. The resulting threshold is also included in Figure 7.33. A battery is now considered full when the absolute derivative of the radius exceeds the comparison value:

$$\frac{\partial r(Q_{charged})}{\partial Q_{charged}} > \Delta r_{limit} \rightarrow \begin{cases} True & \text{Battery is full} \\ False & \text{Battery is not full} \end{cases} \tag{7.39}$$

The battery used in this example was supposed to be manufactured with a capacity of 100 A h. However, although the battery was charged for 50 h with 2 A, which corresponds to a charge of 100 A h, only 56 A h could be discharged during the subsequent discharge cycle. Assuming that this difference is caused by coulombic losses, the criterion holds in practical tests even in cases of particularly large deviation. Figure 7.34 shows the classification of the individual spectra of the charging cycle. As expected, the spectra of a charged battery are densely arranged in a small range. In contrast, the spectra of the overcharged battery vary greatly. The reason for this is that the spectra of the transition are also assigned to the overcharged state.

7.2.3 *Regression using Artificial Neural Networks*

With the methods presented in Sections 7.2.1 and 7.2.2, a robust determination of the end of charge and a SoC determination during the

discharge process is possible. Since the end of charge can be determined from the cell voltage, which drops sharply towards the end of the discharge process, the only thing missing for a reliable detection of the SoC is the possibility to determine it during the charging process as well. In this section, it is therefore evaluated whether a regression of the SoC based on ANN is possible[27, 35]. Among other things, different methods of preprocessing the impedance data to generate the feature space are presented and evaluated. A detailed publication covering this topic can be found in [83].
Typically, the measured electrochemical impedance spectra are used to fit the parameters of an equivalent circuit similar to Section 7.2.1. Mainly due to the diffusion process, minimizing the squared error does not result in a system of equations that allows a direct solution using linear regression. Instead, a Newton-Raphson like algorithm must be used to iteratively approach the minimum of the error function (see Section 4.1). This step is necessary for each evaluation of a newly measured spectrum and therefore takes a lot of computational resources. To avoid an underdetermined system of equations it is also necessary to measure at least as many frequencies as parameters[40]. This may also increase the time needed. Following the identification of the parameters of the electrical equivalent circuit, it is then still necessary to relate the model parameters to the desired SoC, for example with a quadratic approximation.
An analysis of the electrochemical impedance data based on the electrochemical model does provide insights into the chemical processes of the cell. However, insofar as the goal is only to determine the SoC, this comes at the expense of speed and the necessary computing power for each evaluation. ANN can offer an advantage here. While training the network still takes its time, evaluation in the field is fast and easy, not least because the SoC can be modeled directly. Thus, in a short experiment on a desktop PC, a speedup of about 3 orders of magnitude could be achieved. An evaluation of the equivalent circuit, for example, takes on average 82.23 ms, while the evaluation of the trained neural network took only 51.86 µs. Typically, BMS use microcontrollers with much less computing power, making the evaluation there require correspondingly more computing time. Moreover, ANN have already been used successfully for the analysis of electrochemical impedance spectra[27, 35].

Data Generation and Feature Extraction

Figure 7.35 shows the structure of the measured impedance data used to train the neuronal networks. While parameter fitting of an electrical equivalent circuit always uses one impedance spectrum to fit an equivalent circuit, a large number of impedance spectra are used for training an ANN. To generate the data, the zinc-air cell is charged and discharged periodically while an electrochemical impedance spec-

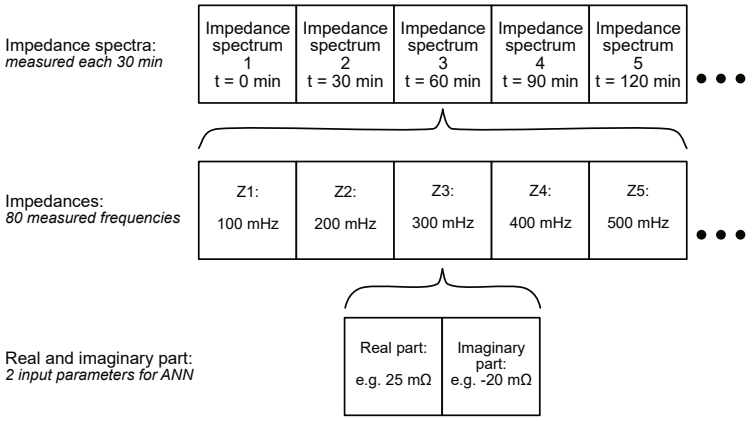

Figure 7.35: Structure of generated measurement data for state of charge estimation using artificial neural networks.

trum is measured every 30 min (Figure 7.35 top). Since the cell is used continuously and without interruptions, a known SoC can be assigned to each measured spectrum by counting the charged and discharged charges, respectively. Each individual spectrum in turn contains 40 impedancemeasurements, each taken at different frequencies (Figure 7.35 center). Since the impedance is the complex AC resistance, the real and the imaginary part define an impedance in each case (Figure 7.35 bottom).
Features now have to be defined from the generated measurement data, which are supposed to work as input data of the ANN. In a first approach, which is called raw in the further course, simply the unchanged real and imaginary parts of a spectrum are used as input vector x_{raw} of the neural network. x_{raw} thus results in

$$x_{\text{raw}} = \left[\Re\left\{Z_1\right\}, \ldots, \Re\left\{Z_m\right\}, \Im\left\{Z_1\right\}, \ldots, \Im\{Z_m\}\right]. \tag{7.40}$$

The generation of the measurement data took place over a longer period of time, so that the degradation and the SoH also influence the measured impedance spectra. Therefore, two other types of features are additionally evaluated. In a first approach, the real and imaginary parts x_{raw} measured at the SoC being evaluated are combined with the real and imaginary parts of the last measured spectrum of an empty cell $x_{\text{raw,SoC=0}}$. This approach is called diff in the following part, since it is intended to allow the evaluation of the difference of the spectrum of the current SoC to an empty cell with the same aging condition. Accordingly, the associated feature vector is formed by

$$\begin{aligned} x_{\text{diff}} &= \left[x_{\text{raw}}, x_{\text{raw,SoC=0}}\right], \\ x_{\text{diff}} &= \left[\Re\left\{Z_1\right\}, \ldots, \Re\left\{Z_m\right\}, \Im\left\{Z_1\right\}, \ldots, \Im\{Z_m\}, .\right. \\ &\quad \Re\left\{Z_{1,\text{SoC=0}}\right\}, \ldots, \Re\left\{Z_{m,\text{SoC=0}}\right\}, \\ &\quad \left.\Im\left\{Z_{1,\text{SoC=0}}\right\}, \ldots, \Im\{Z_{m,\text{SoC=0}}\}\right]. \end{aligned} \tag{7.41}$$

The idea of the second approach is called grad and, similar to the method presented in Section 7.2.2, it does not try to use the absolute values of the spectra, but the change of the impedances Z and Z' of two successive spectra is evaluated. Since the impedance spectra are measured regularly at 30 min intervals, the gradient of the spectra can be approximated by the difference of two successive spectra. Thus,

$$\begin{aligned} x_{\text{grad}} &= [x_{\text{raw}} - x'_{\text{raw}}], \\ x_{\text{grad}} &= [\Re\{Z_1\} - \Re\{Z'_1\}, \ldots, \Re\{Z_m\} - \Re\{Z'_m\}, \\ &\quad \Im\{Z_1\} - \Im\{Z'_1\}, \ldots, \Im\{Z_m\} - \Im\{Z'_m\}]. \end{aligned} \tag{7.42}$$

results for the feature vector here.
For the regression of the SoC, multilayer perceptron networks are used, which have a hidden layer in addition to the input and output layer. Due to the manual fabrication of the test cells, there are still strong differences between the electrochemical impedance spectra of different cells. Therefore, the neural networks are only trained with the data of one cell, which results in a small data set. To avoid overfitting, Bayesian regularization is used in the training algorithm. This tends to improve generalization ability, since the sum of network weights E_w is included in the objective function to be minimized[30, 87]:

$$F = \alpha \cdot \frac{1}{N} \sum_{i=1}^{N} (e_i)^2 + \beta \cdot E_w. \tag{7.43}$$

Figure 7.36 illustrates the process for evaluating the ANN. In order to evaluate the generalization capability, at the beginning, the measurement data is randomly divided into training and validation data. Meaning, the networks are trained with 90 % of the data set. After training is complete, the remaining data is used to verify generalization by predicting the state of loading of the unseen validation data by the trained network and determining the resulting mean error. This result also depends, to some extent, on the random partitioning of the measured data. Therefore, to obtain a meaningful result, the procedure is repeated five times using a heuristic technique. Furthermore, the optimal number of neurons in the hidden layer is searched within a grid search. The presented procedure is therefore repeated for the number of neurons between 1 and 10.
Furthermore, the time required for the measurement is also subject to optimization. The measured spectrum consists of a total of 40 different frequencies, so 80 parameters are used as features (real and imaginary part). Since a strong correlation is likely between impedances of neighboring frequencies, it is investigated whether a smaller subset of the whole spectrum is also sufficient to model the SoC. To test this idea, the networks are also evaluated with spectra reduced to 40 and 20 features, respectively.

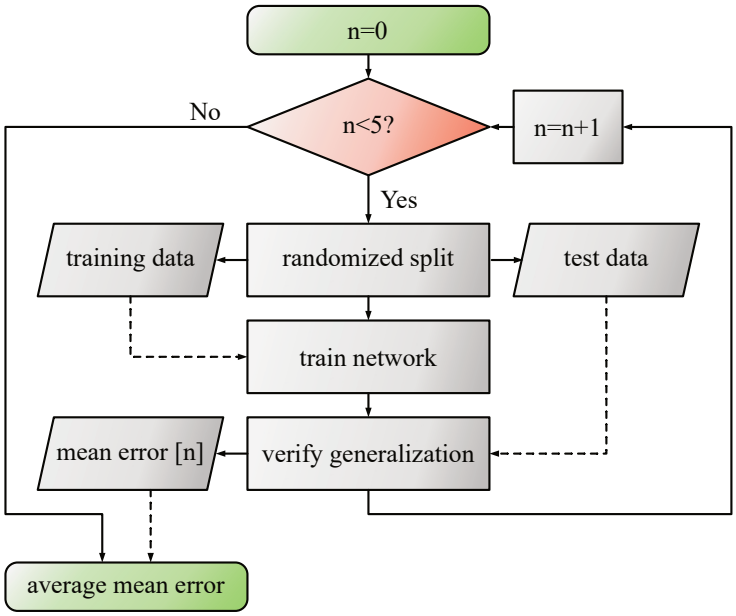

Figure 7.36: Flowchart that describes the process of training and validation of one combination of number of frequency and neurons

Analysis

A total of three cells are analyzed, each using a different DC component during electrochemical EIS. Table 7.1 shows the mean absolute error when the cell is charged with 1000 mA. The DC component of the charging current is defined below as the working point. The results are divided according to the method used, the number of frequencies selected and the number of neurons in the hidden layer. The best combination of each method is highlighted in green. The best overall result is obtained using all 80 features of the 40 frequencies and 10 neurons when the spectra are combined with the impedances of the empty cell as features (diff method). This leads to a mean absolute error of 56.5 mAh. The results of the raw method are slightly higher, but at a similar level. Although the result is also best here when all frequencies are used, a reduction of the measured frequencies still seems possible, since the error then does not increase dramatically. The average error is still smaller than 1 % of the cell capacity, which here is 100 A h. In contrast, the error of the gradient-based method is quite high for most combinations. One possible reason is a high noise level of the impedance measurement itself.
Applying ANN to the cells charged with other DC currents show similar characteristics. As can be seen in the associated Tables 7.2 and 7.3, the error values are at a slightly higher level overall. One reason is that the PicoEIS instrument is used. In this case, both the charging current and the AC current of the EIS are modulated via one DAC. Higher DC currents therefore result in a reduction of the resolution of

Table 7.1: Mean absolute error in mA h at working point = 1000 mA with respect to the used method, number of neurons (#n) and the number of measured frequencies (#f). Best result of each method is highlighted in green.

METHOD	Orig		
#n \ #f	80	40	20
1	118.5	180.7	590.1
3	122.0	124.0	140.0
6	117.0	4956	191.3
10	114.4	309.3	267.9

METHOD	Diff		
#n \ #f	80	40	20
1	141.3	237.2	4932
3	114.7	183.1	135.0
6	65.6	205.3	186.8
10	56.5	170.2	165.0

METHOD	Grad		
#n \ #f	80	40	20
1	643.9	925.8	4804
3	1233	2041	3222
6	3596	1747	236.7
10	1604	3486	272.5

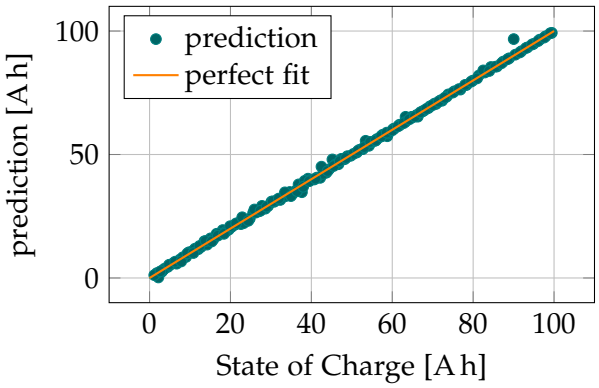

Figure 7.37: Regression plot that compares all output values of the trained artificial neural network with its corresponding target value.

the sine wave. Overall, the diff method, which combines the current impedance spectrum with the spectrum at the beginning of the charge cycle, provides the best results. Furthermore, a small reduction of the used features to 40 and 20 frequencies, respectively, is also possible here without strongly degrading the regression quality. It can be clearly seen that the third method, which uses the difference between two measurements, is not suitable as feature extraction.
Figure 7.37 shows the states of charge estimated by the best network f_i as a function of the actual states of charge y_i for the DC charging current of 3 A. This corresponds to the nominal current of the cells under investigation. A straight line corresponding to a perfect prediction is also plotted in the Figure. However, due to the good prediction, this line only overlays the predicted data. Accordingly, the coefficient of determination

$$R^2 = 1 - \frac{SS_{res}}{SS_{tot}} = 1 - \frac{\sum_i (y_i - f_i)^2}{\sum_i (y_i - \bar{y}_i)^2} \tag{7.44}$$

which is used to assess the goodness of fit of a regression, also has a good value of 0.999.
In summary, EIS in combination with an artificial neural network is also suitable for estimating the SoC of a zinc-air battery during a charging process.

7.2.4 *Regression using Support Vector Regression*

In a next step, the SVR method is investigated as an alternative to determine the charge state from an impedance spectrum. Two things are special about this method. First, the cost function that is minimized is designed so that small deviations that fall within a defined range do not result in a cost. For example, it is possible to define the size of the margin in such a way that the design of the cost function alone prevents overfitting to the measured data. On the other hand, the

Table 7.2: Mean absolute error in mA h at working point = 2000 mA with respect to the used method, number of neurons (#n) and the number of measured frequencies (#f). Best result of each method is highlighted in green.

METHOD	Orig		
#n \ #f	80	40	20
1	6520	8327	7368
3	862.9	1579	1995
6	458.7	907.0	1312
10	801.2	557.5	1434

METHOD	Diff		
#n \ #f	80	40	20
1	4288	5172	5467
3	863.8	2158	1432
6	572.7	692.9	1047
10	572.9	425.8	1192

METHOD	Grad		
#n \ #f	80	40	20
1	23062	23014	22903
3	10806	15414	22968
6	8927	15529	17809
10	8391	13929	17378

Table 7.3: Mean absolute error in mA h at working point = 3000 mA with respect to the used method, number of neurons (#n) and the number of measured frequencies (#f). Best result of each method is highlighted in green.

METHOD	Orig		
#n \ #f	80	40	20
1	5746	6310	6706
3	949.3	3189	3130
6	1270	1066	2017
10	610.1	669.1	984.8

METHOD	Diff		
#n \ #f	80	40	20
1	4852	6266	6335
3	1035	1488	2466
6	866.1	529.4	1132
10	907.2	537.1	680.2

METHOD	Grad		
#n \ #f	80	40	20
1	23223	23204	23163
3	9424	23185	23192
6	7363	10292	23162
10	6206	10332	12885

quality criterion is designed so that the parameters of the objective function are as small as possible. This control is the basis of SVR and has been adopted to some extent by other methods for controlling overfitting. Since $\| w \|^2$ is minimized, the flatest possible function is chosen. The idea is that a flat function makes good predictions even on unseen data.
The first aspect of using SVR is the underlying model function. In principle, this is always a linear scalar product between the weight vector w and the vector of input data x. However, by applying a kernel that maps the input data to a higher dimensional feature space, other functions can be used as well. Nevertheless, the model remains linear in the feature space. Two commonly used model functions are the polynomial function and the radial basis function. The degree of the polynomial function can be parameterized, but must be specified before model fitting. Thus, it is a hyperparameter that is not optimized by the actual cost function. For the radial basis function, the function value is formed via a weighted sum of grid points. The weighting is usually determined via a Gaussian radial basis function, with the associated parameters \sigma and \mu found during optimization.
The input vector x resulting from EIS is very high dimensional, since for each measured impedance Z_k at frequency f_k up to four values are generated (real and imaginary part, absolute and angle). The structure of the underlying input vector is

$$\begin{aligned} x_i \quad = \quad & [\Re\{Z_{i,1}\}, \ldots, \Re\{Z_{i,m}\}, \Im\{Z_{i,1}\}, \ldots, \Im\{Z_{i,m}\}, \\ & |Z_{i,1}|, \ldots, |Z_{i,m}|, \phi(Z_{i,1}), \cdots, \phi(Z_{i,m})]. \end{aligned} \tag{7.45}$$

It is simply the concatenated values of the real parts, the imaginary parts and the magnitude and phase of the impedance spectra. Here, Z_1 represents the lowest measured frequency and Z_m is the highest measured frequency. i differs the observations at different states of charge. It is therefore difficult to represent the curve of the SoC as a function of all values of the input vector. Instead, the progressions of the four values of frequency 1 kHz over the SoC are shown in Figure 7.38. The steps are probably difficult to model using a polynomial. Nevertheless, both methods presented were tested to select the model function. Since only a model function is to be selected here, the data has not yet been preprocessed.
The values are also not yet scaled to a variance of 1 in this step and still have an offset. In order to compare the two models, the data set was split and only a portion of 80 % was used fitting the model. The other part was then used to determine the performance using the Root Mean Squared Error of Prediction (RMSEP). Before fitting the model, the hyperparameters have to be defined first. These are still optimized iteratively and manually in this step. The resulting values

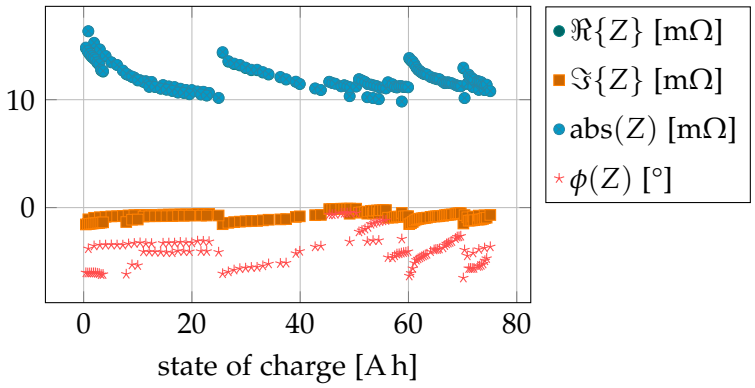

Figure 7.38: Development of real and imaginary part, absolute and angle of the impedance at 1 kHz depending on the state of charge.

Table 7.4: Used hyperparameters of the Support Vector Regression for original data.

PARAMETER	POLYNOMIAL	RADIAL BASIS
C	0.1	15
ϵ	0.001	0.01
Degree of Polynomial	2	-
σ	-	0.006

can be found in Table 7.4. For the model based on the polynomial function, a resulting metric is

$$\mathrm{RMSEP}_{\mathrm{poly,original}} = 3.67\,\mathrm{A\,h}. \tag{7.46}$$

In contrast, the RMSEP of the radial basis function was slightly lower at

$$\mathrm{RMSEP}_{\mathrm{rbf,original}} = 2.07\,\mathrm{A\,h}. \tag{7.47}$$

The difference between the predicted SoC values and the actual values for both models are shown in Figure 7.39. As can be seen, not only is the mean deviation lower for the radial basis function model, but the maximum deviations are also smaller.
Even in their current state, with no pre-processing done yet, both models already deliver good results on unseen data. Although the radial basis function model performs better, the difference is not particularly high. Therefore, the next steps will also be performed with both models in order to select the better model at the end.
In the next step a scaling of the input data takes place. As already mentioned, in the cost function, which is minimized in the SVR, both the deviations outside the ϵ range and large weights are penalized. This is also linked to a dependence on the variance of the input data,

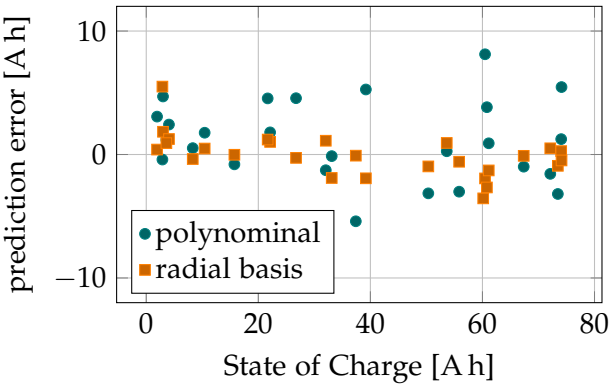

Figure 7.39: Difference between predicted state of charge values of polynomial and radial basis SVR model and the actual values with manual optimization of hyperparameters.

since large variances result in smaller weights. Although this can be partially compensated for by the hyperparameter C, the parameter does not affect differences of variances of the different features. It can therefore be useful to subtract the mean of the individual features and then scale the variance to 1. The mean vector μ is formed by averaging all observations of a feature:

$$\begin{aligned}\mu \quad = \quad & [\overline{\Re\{Z_1\}}, \ldots, \overline{\Re\{Z_m\}}, \overline{\Im\{Z_1\}}, \ldots, \overline{\Im\{Z_m\}}, \\ & \overline{|Z_1|}, \ldots, \overline{|Z_m|}, \overline{\phi(Z_1)}, \cdots, \overline{\phi(Z_m)}].\end{aligned} \tag{7.48}$$

It should be noted that the mean vector is formed only using the training data to prevent leakage from the test data. Then the mean vector μ is subtracted from each observation vector x_i resulting in the zero mean vector

$$x_{z,i} = x_i - \mu. \tag{7.49}$$

Next, the variance of each feature is scaled to 1 by dividing each value by the variance of the feature's values in the training dataset. The zero mean and variance 1 observation vectors thus result in

$$\begin{aligned}x_{zv,i} \quad = \quad & x_{z,i} / [\sigma^2(\Re\{Z_1\}), \ldots, \sigma^2(\Re\{Z_m\}), \\ & \sigma^2(\Im\{Z_1\}), \ldots, \sigma^2(\Im\{Z_m\}), \\ & \sigma^2(|Z_1|), \ldots, \sigma^2(|Z_m|), \sigma^2(\phi(Z_1)), \cdots, \sigma^2(\phi(Z_m))].\end{aligned} \tag{7.50}$$

In which an element-wise division is performed. The rescaling of the data requires of course also an adjustment of the hyperparameters. However, the hyperparameters are now no longer optimized to produce the smallest possible error on the test data. Instead, the hyperparameters are specified from the training data alone to obtain maximum separation between training and test data and to verify generalization to unseen data. For this purpose, the cross-validation

procedure is used. In this procedure, the training data is once again divided into 5 equal splits. Then 4 of the splits are used to fit a model. The fitted model is then validated by determining the RMSEP of the observations of the remaining split. These steps are repeated a total of 5 times, so that each split has been used four times to fit the model and once for validation. The resulting metrics can be averaged at the end and even a standard deviation can be determined. Listing 7.1 summarizes the procedure once again.

Listing 7.1: Pseudocode of cross-validation procedure.

```
data_splits[5] = split(data_training)
for k=1 to 5
        model = fit(data_splits[all except k])
        metric[k] = test(model,data_split[k])
end for
mean_metric = mean(metric)
```

So cross-validation already provides a good analysis of how well the model can generalize even though all the data is also used for training. However, the hyperparameters are not yet optimized by this method. There are also automated procedures for doing this, so that the parameters are not optimized manually in a try and error procedure. One example is the so-called grid search method. A grid of predefined parameter combinations is created and each combination is separately evaluated. Here, of course, a trade-off arises. If the parameter values are very densely meshed, a huge grid is created, which requires a lot of time. On the other hand, the optimum can be missed if the parameter values are too coarse.
Therefore, Bayesian optimization was applied, using a Gaussian process to model the performance function as a function of the hyperparameters. Based on Snoek et al. recommendation, the Matèrn 5/2 kernel was used as the covariance function and the evaluation points were selected based on the expected improvement[124]. Bayesian optimization was applied to the training data for 50 iterations via cross-validation procedure. The hyperparameter combination with the best RMSEP metric are shown in Table 7.5. The combinations were then used to train a model with the complete training data set. The generalized performance on the unseen training data results in

$$\mathrm{RMSEP}_{\mathrm{poly,scaled}} = 5.09\,\mathrm{A\,h}. \tag{7.51}$$

for the polynomial model and

$$\mathrm{RMSEP}_{\mathrm{rbf,scaled}} = 1.93\,\mathrm{A\,h}. \tag{7.52}$$

for the radial basis function model.
Performance on unseen scaled data from the polynomial model, although Bayesian optimized, is now worse than the model that uses

Table 7.5: Used hyperparameters of the Support Vector Regression for scaled data.

PARAMETER	POLYNOMIAL	RADIAL BASIS
C	0.616	30.6
ϵ	0.105	0.0006
Degree of Polynomial	1	-
σ	-	0.005

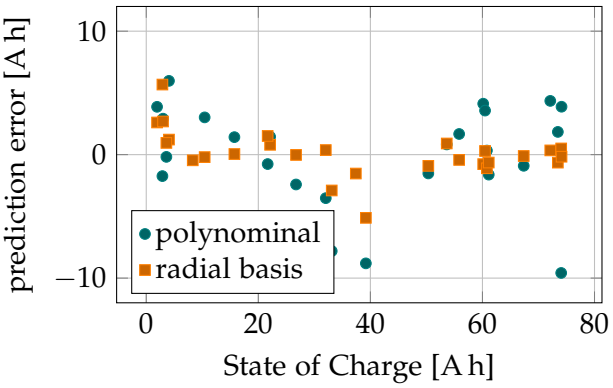

Figure 7.40: Difference between predicted state of charge values of polynomial and radial basis SVR model and the actual values with hyperparameters being optimized by Bayesian Optimization.

unscaled data but was manually optimized to minimize test error. This strongly indicates that the previous performance by optimizing the hyperparameters on the test data resulted in a data leakage. In contrast, the RMSEP has become even smaller with the radial basis function model. This impression is further confirmed when looking at the differences in the predicted test data in Figure 7.40. Because also the maximum deviations are much smaller for the Radial Basis Function Model. Therefore, the polynomial model is discarded for further consideration.

The impedance spectra form a continuous course. As a result, the differences in impedance values for neighboring frequencies are rather small and there is a strong correlation. Therefore, to reduce the dimensionality of the feature vector, the Principle Component Analysis (PCA) is applied. PCA is a statistical technique that allows you to combine many variables into a few principal components. Its aim is to combine the variance of the data from many individual variables into few principal components. These principal components are stochastically independent of each other. As shown in Figure 7.41, this creates a new coordinate system whose axes each map the direction of maximum variance and are orthogonal to each other. The essential tool of this procedure is the diagonalization of a symmetric matrix with the help

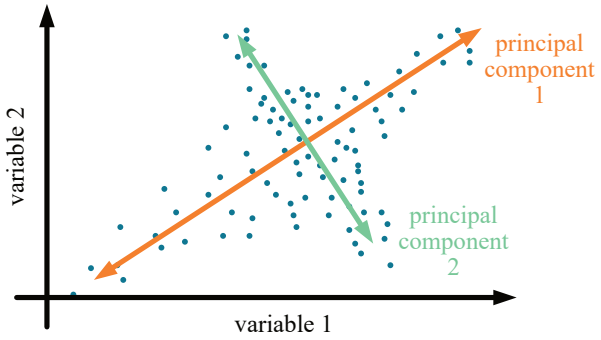

Figure 7.41: Illustration of the principal component transformation.

Table 7.6: Explained variance depending on number of principle components.

NO. PRINC. COMP.	EXPLAINED VARIANCE
1	46 %
2	76 %
3	90 %
4	95 %
5	97 %
7	98 %
9	99 %

of an orthogonal matrix.
When using the principle component transformation, the question arises about how many components should finally be taken over. One approach is to specify the number of components directly. Another approach is the definition of the portion of the explained variance. This portion can be determined by the eigenvalues of the principal components. Table 7.6 shows the explained variance depending on the number of principal components when applying the principal component transformation to the training data. As can be seen, the assumption that there is a strong variance between the measurement frequencies is confirmed. Already three principal components are sufficient to describe 90 % of the variance.
For the numbers of principal components from Table 7.6, optimized hyperparameters are now determined again using the combination of Bayesian optimization and cross-validation. The best resulting RMSEP for each number of principal components is shown in Table 7.7. The error increased for all numbers of principal components compared to the results without applying PCA. The reason why this was to be expected is that in SVR good generalization can already be achieved by adjusting the hyperparameters, and these very hyperparameters have already been fixed beforehand by Bayesian optimization on unseen

Table 7.7: RMSEP on unseen testdata and optimized hyperparameters depending on number of principal components.

NO. PRINC. COMP.	RMSEP	ϵ	σ	C
1	15.4 A h	0.2	0.045	0.45
2	6.64 A h	0.2	0.446	1.45
3	2.73 A h	0.0041	0.276	13.8
4	4.53 A h	0.02	0.169	27.8
5	4.70 A h	0.027	0.135	31.5
7	4.18 A h	0.037	0.067	28.1
9	4.80 A h	0.0015	0.032	31.9

data in the cross-validation procedure. Apart from that, generalization can certainly improve performance if the variance of the data is reduced by a principal component transformation. For example because the reduced variance can eliminate measurement noise and prevent overfitting.The best metric was achieved with a component number of 3, so 10 % of the variance was removed. The RMSEP only slightly increased. Moreover, the optimized hyperparameters changed by several orders of magnitude. In particular, the epsilon band and sigma are now much larger, which should make the model more stable.

Now having described the procedure, adapted features are evaluated. This means that the raw impedance data is used in advance to extract new features and to adjust the spectra, respectively. The use of the feature extraction methods from Section 7.2.3 is omitted here because they have either yielded very poor results (grad method) or rely significantly on the fact that the impedance spectrum of an empty cell is also measured regularly, but this SoC leads to premature damage of the cell (diff method). Instead, in a first approach, the true ohmic resistance of each spectrum is removed. According to the battery model, this is mainly caused by the resistance of the electrolyte in addition to the contact resistance. Ideally, there is no dependence on the SoC for the true ohmic component at all, but rather on the concentration and temperature of the electrolyte. The algorithm for modifying the features is described in Listing 7.2 using R language. First, the data is grouped based on the measurement id. Since each spectrum has its own ID, the following command is applied to each spectrum separately. An ohmic resistance results in a right shift on the real axis. Especially at high frequencies the double layer capacities appear like a short circuit, so that the ohmic resistance and possibly even the inductive part of the cable remains. Because the inductive part only affects the imaginary part, the ohmic part can be determined by the minimum real part value of the spectrum and can then be

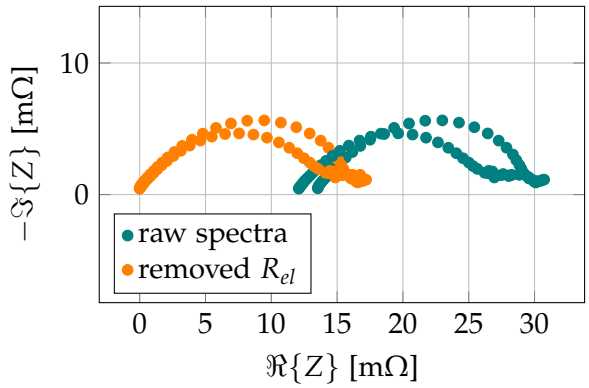

Figure 7.42: Illustration of removing true ohmic resistance from impedance spectra.

subtracted from all real parts.

Listing 7.2: Removing true ohmic resistance from impedance spectra.

```
eis_wo_rel_dataframe <-
  raw_eis_dataframe %>%
  group_by(measurement_id) %>%
  mutate_which(select realparts,
               realpart = realpart - min(realparts)
              )
```

The effect of the transformation is shown in Figure 7.42. Here, two unchanged impedance spectra can be seen. The two spectra have been recorded after different periods of time, so that the electrolyte of one spectrum has already aged, which is reflected in a shift of the spectrum to the right. Due to the transformation the ohmic part is subtracted, so that now both spectra start at the imaginary axis.
For different numbers of principal components, the hyperparameters have now been optimized using Bayesian optimization and cross-validation, then the RMSEP performance has been determined. The resulting performance and the hyperparameters used are summarized in Table 7.8. It is noticeable that the best performance using the original spectrum data, which was achieved with a component number of 3, is now no longer achieved. However, the overall results are now at a lower level when using other component numbers.
In summary, SVR can also be used to determine the SoC of a zinc-air cell with sufficient accuracy during the charging process. However, the error values are slightly higher compared to the application of artificial neural networks.

Table 7.8: RMSEP on unseen testdata where R_{el} has been removed and resulting optimized hyperparameters depending on number of principal components.

NO. PRINC. COMP.	RMSEP	ϵ	σ	C
No PCA	4.09 A h	0.02	0.007	31.8
1	16.1 A h	0.051	0.120	0.26
2	6.60 A h	0.2	0.851	0.28
3	3.12 A h	0.0344	0.302	12.0
4	2.92 A h	0.0062	0.247	26
5	2.69 A h	0.023	0.187	26.9
7	4.04 A h	1.42e-5	0.155	26.7
9	3.18 A h	0.004	0.077	30.1

7.3 CURRENT GENERALIZATION

The previous approaches always specified a fixed DC current that was used to measure the impedance spectra. This principle can theoretically also be applied in practice. However, then the current working point must be left in order to use the working point that was used for training the models. When charging, this can lead to situations where energy generated by a photovoltaic system cannot be utilized at this point in time. When discharging, the energy of the new working point may not be sufficient and additional energy from the grid is needed reach the desired working point. In both cases, there is a monetary loss. This chapter therefore analyzes whether it is also possible to create a model that generalizes the DC current or the working point. In detail, this means that the models are trained with data from different working points and thus an evaluation with different direct currents is also possible.

The problem that arises is well illustrated in Figure 7.43. It shows impedance spectra at different currents and states of charge. One can see, an increase in the DC current behaves similar to a change in the SoC. This behavior can be explained with the battery model from chapter 3. At high frequencies, the double layer capacities act like short circuits, so that the total impedance is mainly formed by the resistance of the electrolyte and the contacting. Since this resistance is independent of the SoC of the cell and the current, the differences of the curves on the left side are rather small. In contrast, the impedance for small frequencies depends mainly on the charge transfer resistances described by the Butler-Volmer equation. According to this, the electrode current increases exponentially with the voltage. The differential resistance therefore decreases for higher currents, since smaller

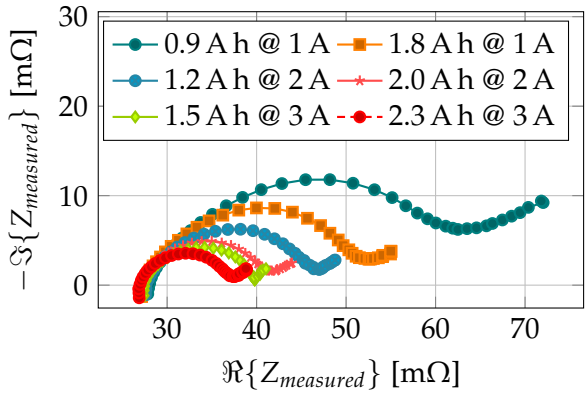

Figure 7.43: Impedance spectra of zinc-air batteries at different working points and state of charges.

voltage differences are now sufficient to achieve an equal change in current.

7.3.1 *Data generation*

To generate measurement data, a procedure shown in Figures 5.3 and 5.7 is picked up again. Here, zinc-air cells are continuously charged or discharged with an alternating current of 1 A, 2 A or 3 A. This means that the charging process starts with 1 A. A short delay is made until the cell voltage has become familiar with the current and a measurement of the impedance spectrum is started. After that, the charging current is increased to 2 A, again a short delay is made and the next impedance measurement is started. The same is done for 3 A and then it starts again at 1 A. Meanwhile, the applied charge is counted so that the actual SoC is known. Once the cell is full, the discharge process starts using the identical technique.
After several charge and discharge cycles, there is no random division of the resulting data into training data and test data this time, but the measurements at 1 A and 3 A form the training data set and the measurements at 2 A form the test data set. This ensures that the results correspond to an actual generalization of the working point. The hyperparameters are optimized by cross-validating the training set to prevent data leakage. Of course, the feature vector must be extended to include the DC current value, so that the following vector is now obtained:

$$x_i = [I_{\text{bat,DC}}, \Re\{Z_{i,1}\}, \ldots, \Re\{Z_{i,m}\}, \Im\{Z_{i,1}\}, \ldots, \Im\{Z_{i,m}\}, |Z_{i,1}|, \ldots, |Z_{i,m}|, \phi(Z_{i,1}), \cdots, \phi(Z_{i,m})]. \quad (7.53)$$

7.3.2 *Regression Using Artificial Neural Networks*

The general procedure for model generation based on neural networks has already been described in chapters 7.2.3 and 7.2.3. Since at this point it is intended to investigate whether the models also generalize to an unseen DC current component (= working point), the training data consist of all measurements which have taken place at the working points 1 A and 3 A, while the spectra which have been measured at a DC current of 2 A form the test data set. Since the measurements have been performed alternating, the ratio of training to test data is 2/3.

In a first approach, the feature vector, as described in equation 7.53, is obtained from the DC working point and from the measured impedance data. Since the neural network is sensitive to feature scaling, for each feature the mean is removed and scaled to a variance of $\sigma^2 = 1$. Impedance values at similar frequencies correlate strongly with each other. Therefore, it is additionally analyzed whether a reduction of the feature vector by means of a principal component transformation leads to better results or to a better generalization, respectively. Here, the principal component transformation is only applied to the measurement data of the spectrum, since the DC operating point is very important for the generalization, but has only a small variance due to the two different values in the training dataset.

The quality of the resulting model depends, among other factors, significantly on the hyperparameters used. However, the use of a principal component transformation also affects the optimal values of the hyperparameters. Therefore, for each number of principal components, optimized values for the number of neurons and the L2 regularization term α are found using the Grid Search procedure in combination with cross-validation. In Grid Search, a grid is spanned containing all defined combinations of parameter values. These are used sequentially by cross validation to train a model and test on unseen data. In this process, the training data is divided into five groups. The model is fitted with the data from four groups and tested against the unseen data from the fifth group. This process is repeated a total of five times, so each group is used once to determine performance. The average of the five runs of the RMSEP is then used as the performance of the Grid Search hyperparameter combination.

The optimized hyperparameter values depending on the number of principal components are shown in Table 7.9. In addition, the performance values for the best model in each case can also be found there. The level of information when using a single principal component is not sufficient to produce a good model. As a result, the RMSEP for cross-validation with training data is 26.22 A h, which corresponds to more than 25 % of the nominal capacity. Using two principal components and more, the performance values are much better. It is

Table 7.9: Mean RMSEP of cross-validated training data and optimized hyperparameters in current generalization when using artificial neural networks depending on the number of principal components.

NO. PRINC. COMP.	RMSEP	HIDDEN NEURONS	α
0	2.76 A h	6	$6.4 \cdot 10^{-4}$
1	26.22 A h	7	$5.5 \cdot 10^{-3}$
2	3.43 A h	9	$2.6 \cdot 10^{-8}$
3	2.92 A h	7	$2.9 \cdot 10^{-3}$
4	3.45 A h	4	$6.6 \cdot 10^{-7}$
5	2.11 A h	8	$7.1 \cdot 10^{-3}$
7	1.79 A h	9	$3.2 \cdot 10^{-3}$
9	1.94 A h	5	$3.4 \cdot 10^{-8}$

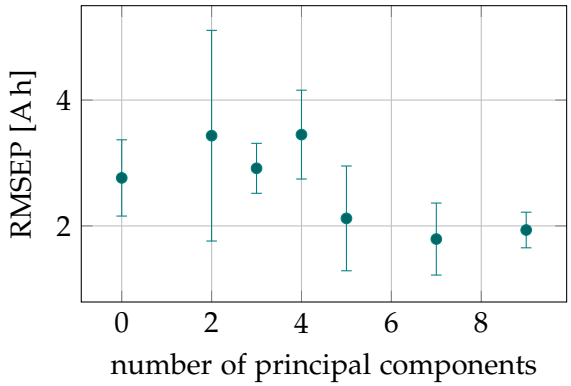

Figure 7.44: RMSEP and standard deviation of crossvalidated training data depending on number of principal components for current generalization using ANN.

interesting to note that the optimal number of neurons in the hidden layer is below 10 in all cases. Higher values lead to poorer generalization due to overfitting.

Figure 7.44 illustrates the cross-validation performance for the training data again graphically. While too few principal components initially lead to a poorer performance, a partial reduction of the input dimensionality can also lead to an improvement of the model. For example, the RMSEP is below the value when PCA is not applied, starting with a number of 5 principal components. The best result is obtained with 7 principal components, although the standard deviation is larger here than with 9 principal components.

In the next step, models are now fitted with the complete set of training data using the optimized hyperparameters. Then the prediction of the test data takes place and the prediction is compared with the target values. The difficulty is now much higher compared to the

Table 7.10: RMSEP on unseen test data during current generalization using artificial neural networks depending on number of principal components.

NO. PRINC. COMP.	RMSEP
No PCA	3.20 A h
1	2.45 A h
2	0.16 A h
3	3.24 A h
4	0.17 A h
5	3.98 A h
7	1.32 A h
9	24.1 A h

cross-validation of the training data, because the training data set consists of spectra at a DC component of 1 A or 3 A, but now predictions have to be made to measurements at a working point of 2 A.
Nevertheless, the resulting performance is sufficiently accurate for the most part, as can be seen in Table 7.10, which summarizes the RMSEP as a function of the number of principal components. In most cases, the performance on the unseen working point is at a similar level or even better than when cross-validating the training data. The network with 2 principal components performs best. Here the RMSEP with a value of 0.16 A h is even significantly better than for the training data. An outlier is the network that uses 9 principal components, where the performance is significantly worse.
Figures 7.45 and 7.46 show the predicted data and the difference from the target value when no principal component transformation is performed and for the best fit (2 components). Here it can be seen again particularly well that the generalization of the DC working point for the model with 2 components works very well. The network trained with the complete impedance set of the spectrum also shows good results, but there are larger deviations, especially for values at the beginning of the charging process.

7.3.3 *Regression Using Support Vector Regression*

The procedure for modeling based on SVR has already been explained in detail in chapter 7.2.4. During training, the data of the training dataset are used in the cross-validation procedure. For this purpose, the data set is divided into five equal parts. Within five runs, four parts are used to train one model at a time and the remaining part is used to determine performance. By using a different part for performance evaluation in each run, an average performance can be determined

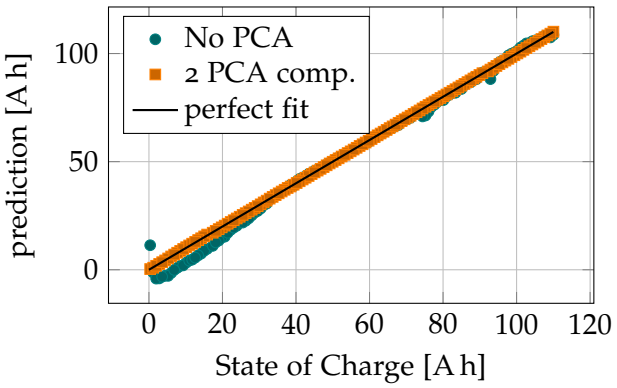

Figure 7.45: Influence of PCA on the predicted state of charge values of ANN models during current generalization.

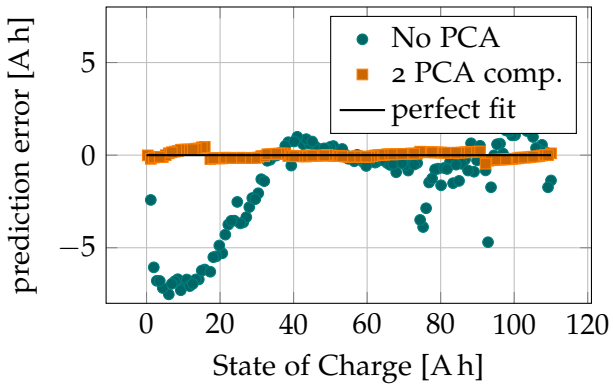

Figure 7.46: Influence of PCA on the difference between predicted state of charge values and the actual values of ANN models during current generalization.

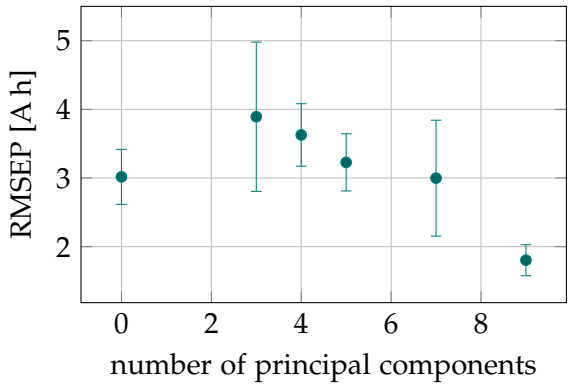

Figure 7.47: RMSEP and standard deviation of crossvalidated training data depending on number of principal components for current generalization using SVR.

afterwards. Before training, the mean value of each feature of the training parts is removed and the variance is scaled to 1. In addition, the influence of a principal component transformation, in particular the number of principal components used, is examined. A change in the number of principal components also affects the optimal value of the SVR hyperparameters. Therefore, Bayesian optimization is used to obtain optimized hyperparameters for each number of principal components that is analyzed. Again, the optimization is performed using only the mean performance of the cross-validation with the training data to prevent data leakage. Finally, after the optimal hyperparameters have been found, the complete set of training data is used for fitting the model and the performance on the test data is determined. The RMSEP is used as the performance metric.
Figure 7.47 shows the RMSEP values of the cross-validation with training data. Additionally, the error bars represent the standard deviation of the RMSEP within the five parts. The performance using a single principal component is out of scale with a value of 30 A h. This is no surprise, since the constant current is now also part of the feature vector and the principal component transformation has to bring in this information as well. If the principal component transformation is not applied, the results here are at a similar level as when analyzing a constant working point. After applying PCA, the mean error decreases with increasing number of principal components. At a number of 7 or more principal components, even better performance is achieved than when the principal component transformation is not applied.
Table 7.11 shows the resulting metrics when using the optimized hyperparameters to fit a model using all training data and predicting the test data depending on the number of principal components used. Again, model accuracy is very poor when only one principal component is used. It is interesting to note that the results of the test data are in most cases even better than the results of the cross-validation with

Table 7.11: RMSEP on unseen test data and optimized hyperparameters of current generalization using Support Vector Regression depending on number of principal components.

NO. PRINC. COMP.	RMSEP	ϵ	σ	C
No PCA	1.90 A h	0.0094	0.00067	31.6
1	31.8 A h	0.19	1.1E-10	5.19
2	2.73 A h	0.12	0.98	30.2
3	4.38 A h	0.002	0.64	2.21
4	0.465 A h	0.0084	0.02	30.2
5	0.881 A h	0.043	0.018	31.6
7	1.37 A h	0.029	0.013	28.8
9	1.17 A h	0.0088	0.0085	31.3

the training data. This may be due to the fact that the number of training data used is now 20 % larger without cross-validation. Another aspect is that the results seem to be better when the value of the DC current falls within the range of the training data. Because while in the previous cross-validation only 1 A and 3 A data were available that mark the current limits, now only 2 A charging current data is tested. In some cases, the reduced information content through the PCA even provides an improvement in performance compared to the original data. Thus, the best result is achieved with a principal component number of 4.
Figures 7.48 and 7.49 show the predicted data and the difference from the target value when no principal component transformation is performed and for the best fit (4 components). Especially the first data point directly marks the largest deviation. This is most likely due to the fact that the diffusion processes have not yet settled. Thus, at the beginning the cell voltage still increases by approximately 15 mV during the measurement of the complete spectrum, while later the cell voltage only changes by 2 mV-5 mV. The remaining test data are approximated very well, but there is a slight tendency to too low predictions.

7.3.4 *Comparison*

In this chapter, it has been shown that it is possible to determine the SoC from impedance spectra at unseen DC working points using both ANN and SVR. In principle, both methods are sufficiently accurate. By means of a principal component transformation, the dimensionality of the feature space was reduced with very little loss of information. Provided that a particularly strong reduction of the dimensionality is used, ANN show a better performance. Thus, the RMSEP is smaller

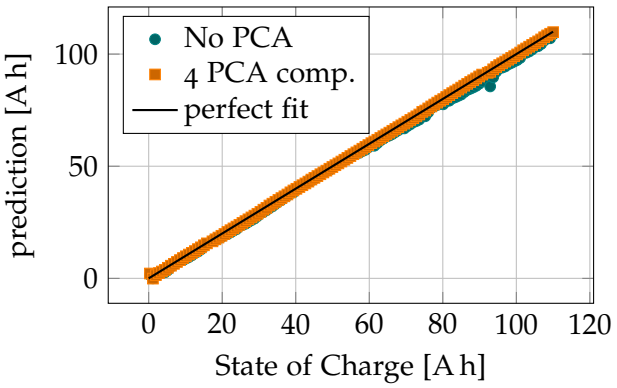

Figure 7.48: Influence of PCA on the predicted state of charge values of SVR models during current generalization.

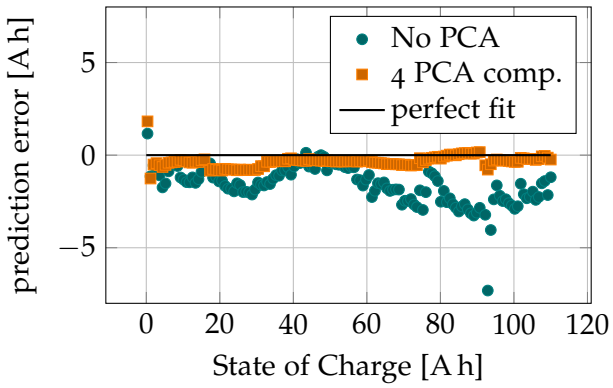

Figure 7.49: Influence of PCA on the difference between predicted state of charge values and the actual values of SVR models during current generalization..

when using one to four principal components inclusive than with SVR. The best result is obtained when using two principal components. With a higher dimensionality of the input data the SVR is ahead. Even when the principal component transformation is not used, SVR shows a smaller tendency to overfit, so that the metric is only about half as large.

7.4 STATE OF HEALTH ESTIMATION

The SoH describes the degradation of the cell. Typically, the SoH of an energy storage device is defined, for example in IEC62391-2, as a function of the remaining capacity or the internal resistance[26]. The first criterion is based on the capacity of the cell. For instance, considering a lead-acid cell, sulfating of the electrodes can result in less anode material being available for battery operation. The lack of material results in a loss of usable cell capacity. According to DIN 2020, a cell is considered defective when that cell has lost 30 % of its nominal capacity. A possible definition of the SoH based on the current cell capacity Q_{cell} is therefore

$$\text{SoH}_{\text{cap}} = 1 - \frac{Q_{\text{nom}} - Q_{\text{cell}}}{0.3 \cdot Q_{\text{nom}}}. \tag{7.54}$$

The second criterion is based on the internal resistance of the cell. The sulfating of the lead electrodes also leads to a reduction of the active surface of the cell and thus the internal resistance increases. If the internal resistance doubles compared to the starting value, the cell is also considered broken. A possible definition of the SoH by comparing the current internal resistance $R_{i,\text{cell}}$ with the initial value $R_{i,0}$ is

$$\text{SoH}_{\text{Ri}} = 2 - \frac{R_{i,\text{cell}}}{R_{i,0}}. \tag{7.55}$$

In order to apply these criteria to zinc-air cells, however, measurement data are still not available at the current stage of cell development. This means that for the zinc-air batteries under development, only dendrites and leakages lead to cell defects, even before there is a significant loss of cell capacity or an increase in internal resistance. Nevertheless, in order to investigate whether it is possible to determine the degradation state of zinc-air cells with the aid of EIS, measurement results from existing publications are used. A detailed publication covering this topic can be found in [83, 86].

7.4.1 *Data generation*

Publications already exist that analyze the impedance spectra of zinc-air batteries as a function of the SoH. Arai et al., for example, evaluated the impedance spectra of the cathodic part of zinc-air batteries and

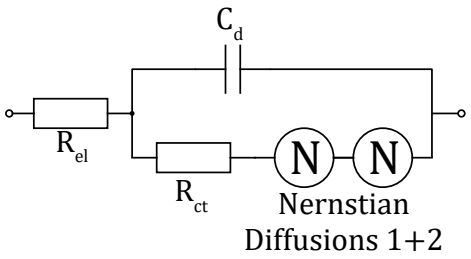

Figure 7.50: Equivalent circuit of the battery which is parametrized by the impedance spectra according to Arai et al.[6]

performed an evaluation using an electrical equivalent circuit[6]. Based on the data of Arai et al. an optimized SoH determination usingANN is now developed. The electrical model of the air electrode used by Arai et al. is shown in Figure 7.50. It is very similar to the model presented in Section 4.1. While the resistance R_{el} describes the electrolyte as an ion conductor, R_{ct} describes the energy needed to start the charge transfer. The double layer capacitance that appears at the electrode-electrolyte interface is modeled by the capacitor C_d. Similar to Section 4.1, there are two diffusion components, as two changes in phase occur at the air cathode. Like the Warburg impedance, the diffusion process of the ions is described by the solution of Fick's second law for complex rotating pointers. The solution used here is called Nernst diffusion and depends on two parameters, the diffusion resistance R_d and the diffusion factor K[120]:

$$Z_{Nernst} = R_d \frac{[\sinh(x)+\sin(x)]-i[\sinh(x)-\sin(x)]}{x[\cosh(x)+\cos(x)]} \qquad x = \sqrt{\frac{2\omega}{K}} \tag{7.56}$$

The impedances of the capacitor and the Nernst diffusion components depend on the frequency, whereas the impedances of the resistors are not affected.
The air cathode was degraded by continuous operation and impedance spectra were measured at three different states of health. The resulting measured data were used to fit the parameters of the presented electrical equivalent circuit. The resulting parameters depending on the SoH are shown in Table 7.12. Thus, the evaluation based on the electrical equivalent circuit has already been successfully performed. As can be seen, the values change with the SoH[6].
These three data points are not sufficient to perform an evaluation using ANN. Therefore, they serve as a base to generate further training data. The intermediate values of the parameters of the equivalent circuit are linearly interpolated for this purpose. For example, the equation

$$R_{el,SoH=75\%} = \frac{75-50}{50} \cdot R_{el,SoH=100\%} + \frac{100-75}{50} \cdot R_{el,SoH=50\%} \tag{7.57}$$

Table 7.12: Resulting parameter values of the equivalent circuit derived by the measured impedance spectra.

SoH [%]	R_{el} [Ω]	C_d [mF]	R_{ct} [Ω]
100	0.15	2.0	0.02
50	0.20	1.8	0.02
0	0.25	1.5	0.03

SoH [%]	R_{d1} [Ω]	K_1 [$\frac{1}{s}$]	R_{d2} [Ω]	K_2 [$\frac{1}{s}$]
100	0.14	20	0.25	98
50	0.22	30	0.29	110
0	0.25	9.1	0.55	140

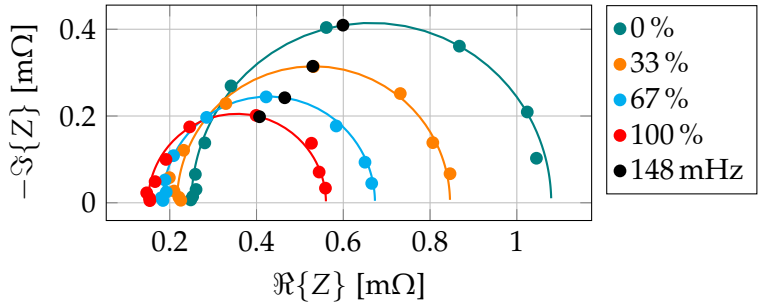

Figure 7.51: Nyquist plot of impedance depending on state of health.

is used to determine the electrolyte resistance at a SoH of 75 %. A total of 1000 data points for each parameter was generated in this way.
The resulting parameter combinations are then used to calculate an impedance spectrum for each interpolated SoH using the electrical equivalent circuit. For this purpose, the frequency range was set from 100 mHz to 1 kHz. So, again, the evaluation with the ANN is done using the data of an impedance spectrum. Figure 7.51 shows several examples of the resulting interpolated data in a Nyquist plot. Higher degradation leads to semicircles with larger radius and a slight shift to the right. Also, impedance points of a constant frequency of 148 mHz are highlighted in each spectrum. One goal of the following analysis is to optimize the timing of the state-of-health determination. Among other things, the selection of the frequencies to be measured is important for this purpose. Therefore, the data points used for the analysis are selected based on their frequencies, using 2 values per decade from 100 mHz to 1 kHz.

7.4.2 *Analysis*

The goals in evaluating the SoH using neural networks are, on the one hand, high accuracy and, on the other hand, the shortest possible time required for the estimation. Both goals depend on the selection of frequencies ω that are measured and used for estimation. A smaller number of frequencies n_f that are measured leads to a shorter evaluation time, since each measurement requires a time t_{init}, which is needed for the initiation and calculation of the real and imaginary parts of the impedance. On the other hand, the selected frequencies themselves are also an important factor, since smaller frequencies require a longer time to measure $t_{measure}$, since at least one full period must be measured. In order to determine the SoH as fast as possible, a cost function is defined and optimized, which depends on the vector of measured frequencies $\underline{\omega}$ and the number of measured frequencies n_f:

$$t = t_{init}(n_f) + t_{measure}(\underline{\omega}, n_f). \tag{7.58}$$

A set-up and evaluation time of 120 ms is used for t_{init}:

$$t_{init}(n_f) = 120\,\text{ms} \cdot n_f \tag{7.59}$$

$t_{measure}$ is the accumulated time for data acquisition. Supposed that 2 periods are used for one measurement $t_{measure}$ results in

$$t_{measure}(\underline{\omega}) = 2 \cdot \sum_{i=1}^{n} \frac{2\pi}{\omega_i} = 4\pi \sum_{i=1}^{n} \frac{1}{\omega_i}. \tag{7.60}$$

Another goal of the SoH estimation is a good accuracy. Therefore, another function λ_{error} is used to evaluate the precision of the estimation by looking for the maximum difference between the output value y and the target value T.

$$\lambda_{error}(y) = \max(\text{abs}(y - T)) \tag{7.61}$$

For each frequency combination, a multilayer perceptron network is trained. The size of the input layer depends on the number of frequencies in each combination, since for each frequency the real and imaginary parts are used as features. In the hidden layer, 10 neurons have been shown to be practical, so this value is used for all combinations. To ensure the highest possible generalization, the cross-validation procedure was also used here. For each frequency combination, both the needed time and the resulting error λ_{error} is determined. The results are plotted in Figure 7.52. As there are two targets to minimize, a compromise has to be used. Combination where one property cannot be improved without downgrading the other property (pareto front) are shown in a different color. In order to find good compromises these pareto optimal combinations are presented

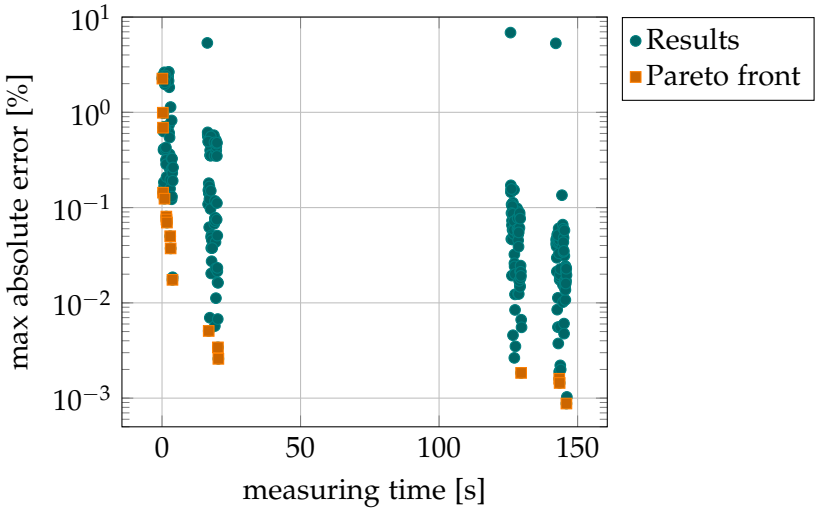

Figure 7.52: Pareto front combining measuring time and precision of estimation. A total number of 255 frequency combination are proved, while 18 combinations fell within the Pareto front.

Table 7.13: Frequency combinations of Pareto front and the resulting measuring time and error

f_1 [Hz] - f_7 [Hz]							t [s]	λ_{error} [%]
1000	-	-	-	-	-	-	0.133	2.26
129	359	-	-	-	-	-	0.372	0.14
129	1000	-	-	-	-	-	0.35	0.69
359	1000	-	-	-	-	-	0.288	0.99
45	129	359	1000	-	-	-	0.896	0.12
17	46	359	1000	-	-	-	1.55	0.08
17	46	129	1000	-	-	-	1.61	0.075
6	46	129	1000	-	-	-	2.96	0.05
0.77	129	359	1000	-	-	-	16.8	0.0051
17	46	129	359	1000	-	-	1.77	0.07
6	46	129	359	1000	-	-	3.11	0.037
6	16	46	359	1000	-	-	3.77	0.017
0.1	0.77	17	129	359	-	-	143.4	0.0016
0.77	6	17	46	129	1000	-	20.2	0.0034
0.1	6	17	46	129	1000	-	129.6	0.0018
0.1	0.77	17	129	359	1000	-	143.5	0.0014
0.77	6	17	46	129	359	1000	20.3	0.0026
0.1	0.77	6	17	46	129	1000	146	0.00088

in Table 7.13.
As one can see, using all the frequencies results in the best accuracy, but needs the longest measurement time of all (146 s). As the difference of the measuring time is higher for lower frequencies, these times lead to clusters. While the main part of the measuring time of a combination is defined by its lowest frequency, the error of a combination depends on all its frequency components. Therefore, the absolute error within a cluster varies quite much with respect to the measuring time. The fastest results can be received by using only the highest frequency, which is 1 kHz. The resulting maximum error is 2.26 %. The fastest way to estimate the SoH with a precision of 1 %, is to use a combination of the frequencies 359 Hz and 1 kHz. This results in a total estimation time of 288 ms.

Part IV

CONCLUSION

8 CONCLUSION

8.1 ADDRESSED QUESTION

In this thesis, it has first been shown why a massive expansion of battery technology can be expected in the future. One important point here is certainly the electrification of vehicles. At the moment, the transport sector within the EU is still largely based on fossil fuels and is responsible for more than 25% of greenhouse gas emissions in Europe. If one leaves aside the Corona crisis, this share is even growing. Climate research predicts that global warming will result in the melting of sea ice and glaciers, rising sea levels, thawing of permafrost soils with the release of methane hydrate, growing areas of drought, and increasing weather extremes. To some extent, the consequences are already being observed. According to current estimates, the current human-caused extinction rate of species exceeds the natural rate by a factor of 100 to 1000. In addition to global warming, vehicles with internal combustion engines also contribute significantly to air pollution. In particular, the proportion of ultrafine particles and nitrogen dioxide increases as a result of combustion engines. In numerous European cities, driving bans have therefore been introduced for vehicles with high emissions. All these points are leading more and more people to see all-electric and partially electrified vehicles as a feasible alternative and make use of them. As a result, the demand for battery capacity is also rising rapidly.

Nevertheless, electric cars are particularly climate-friendly only if the electricity they use is also generated ecologically. To counteract global warming, the share of renewable energies must therefore be massively expanded in the future. However, electricity from PV systems and wind turbines, which account for a large proportion of renewable energies, is only available intermittently or irregularly. At the moment, the stabilization of the transmission grid can still be maintained with power plants and their rotating masses. If the expansion of renewable energies leads to the shutdown of the majority of power plants, system stabilization must be made possible in an alternative way. PV and wind power plants can only provide positive control power if they are permanently throttled. This is not very efficient, so that instead a massive expansion of battery technology is to be expected in this point as well. The provision of electrical energy is thereby made possible sufficiently quickly.

This massive expansion of battery technology cannot be based on existing battery technologies alone for several reasons. First, the raw

materials of existing technologies are limited and are mainly found in countries that do not allow safe working conditions. Foremost among these is the Congo, where much of the cobalt needed for lithium-ion batteries is mined under miserable conditions. Zinc, on the other hand, is more often found in countries that do not exploit their employees, such as Australia and North America. Another point concerning raw materials is the recyclability cycle. Lithium-ion accumulators can only be recycled at great expense and with the risk of explosion. The simple construction of zinc-air batteries helps here. They can be opened without danger and the components can be separated without great effort. Secondly, the theoretical energy density of metal-air batteries is much greater than existing battery technologies. For example, the theoretical energy density of zinc-air cells is three times greater than that of lithium-ion cells. The potential of the cell prices is even substantially larger, since the cell production of zinc-air cells is simpler and the raw materials are cheaper by a factor of 10.Therefore, metal-air batteries and especially rechargeable zinc-air batteries are a crucial factor to enable the energy transition.

However, the operation of zinc-air cells is more complex, since existing BMS cannot be used. The reason for this is the small voltage differences that occur during charging and discharging. When a zinc-air cell is charged, the cell voltage increases by only 40 mV during the charging process, i.e. by an order of magnitude less than in other battery technologies where the cell voltage can be used to detect the state of charge. State of charge detection based on cell voltage is not possible in particular because the influence of temperature and electrolyte concentration on cell voltage is greater than the state of charge itself. The charging process is further complicated by the fact that an accompanying electrolysis process starts at about the same voltage level as the battery charge voltage when the cell is overcharged. This means that overcharging cannot be detected from the cell voltage. Both overcharging and deep discharging damage the cell. However, when discharging, a large voltage drop occurs towards the end of the discharge process, which can be used to detect the end of discharge. At the start of the thesis, it was therefore not possible to use zinc-air batteries without coulomb counting. The typical application scenarios are excluded by this obstacle, because the cell must be operated continuously in order not to lose the known SoC due to self-discharge. The coulomb counting method thus excludes in particular the use for storage of non-continuous regenerative energies, since it is especially important there to be able to adjust to the situation. In order to take advantage of the benefits of zinc-air batteries, a BMS based on EIS has therefore been developed that enables the detection of the end of charge or the state of charge.

8.1.1 *Method*

Thereby, the development of the BMS is based on a fundamental description of the cell chemistry. For this purpose, the individual cell components and their current state of the art were presented. Based on the reaction equations and the structure of the cell, an electrochemical model was created. The static behavior of the cell is defined by the open circuit voltage of the cell, the electrolyte as ion conductor and the charge transfer resistance. The open-circuit voltage model includes the state of charge and the temperature as well as the oxygen content and the electrolyte concentration. Thus, all relevant parameters have been included in the static model. As far as possible, practical experiments were also carried out to confirm the model predictions. For example, an oxygen chamber was set up in which it is possible to control the oxygen content in order to investigate the influence of the oxygen concentration on cell voltage and cell performance. In the practical experiment, on the one hand, the model could be confirmed and, on the other hand, it was shown that even a low oxygen content, which at 5% is far below the normal oxygen content of the atmosphere, does not significantly affect cell performance. Since the static behavior is not affected sufficiently to derive the state of charge, the methods developed for determining the SoC and charge termination are based on the dynamic behavior of the cell. Therefore, dynamic components were added to the cell model to obtain a frequency domain description of the cell. While the Warburg impedance describes the diffusion of the charge carriers, the Stern double layer models the capacitive behavior of the boundary layers of the electrodes.

8.2 RESULTS

Based on the electrochemical model, an frequency dependent electrical equivalent circuit of the cell was developed. Typically, impedance spectra can be used to fit the parameters of the electrical equivalent circuit. However, the unique electrode arrangement of zinc-air secondary cells means that conventional EIS measurement systems are not suitable for use with zinc-air batteries. Therefore, this work demonstrates the development of an adapter board that allows existing EIS measurement systems to be used with zinc-air batteries. Since stand-alone EIS measurement systems are usually very cost-intensive, a small and low-cost measurement system was also developed, which makes the integration of the measurement technology financially attractive even for smaller energy storage systems, such as those used in the private sector for intermediate storage of solar energy. By fitting the electrical equivalent circuit with measured impedance spectra of the developed zinc-air cell, it is already possible to determine the state of charge during discharge with adequate accuracy. The determination of the

charge termination is also possible without any problems, since the parameters of the equivalent circuit show large steps when the full state is reached. However, the accuracy via fitting the parameters is not sufficient to also determine the SoC during the charging process, since the resulting parameters only change in a very small range during the course of the charging process.
Therefore, other methods, in particular artificial intelligence methods, were also used to check the capability of determining the state of charge on the basis of the measured EIS spectra. Artificial neural networks and SVR turned out to be particularly promising. Both methods use the raw measured data of the measured impedance spectra as input data, so that the exact knowledge of the battery model is not necessary and they can be applied particularly easily. The hyperparameters of the two methods were optimized in the grid search procedure and via a Bayesian optimization on the basis of the training data set in order to prevent data leakage. As a result, both methods are also suitable for determining the state of charge of zinc-air batteries during the charging process.
Regression using artificial neural networks was able to determine the state of charge with an error of 0.53 % of the battery capacity on unseen data. It has been shown that generalization to unseen data improves when the size of the input vector is reduced by using just impedance values at prominent frequencies as inputs. Compared to the parameterization of the electrical equivalent circuit, the regression of the state of charge using artificial neural networks is thus much more accurate and sufficient for use in a BMS.
In comparison, the application of SVR shows a slightly higher error of 2.69 % on unseen data. Nevertheless, even an error of this dimension is sufficiently small to be applied in a BMS. One advantage that is shown when using the SVR is that the regulation works better and thus an overfitting has only a very small influence even with higher dimensional input data.
A crucial point and a highlight is that both artificial intelligence methods can also be applied to unknown DC currents during impedance measurement. A change in the charge or discharge current, for example, leads to a shift in the working point during the linearization of the charge transfer resistance and thus to a completely different differential resistance. Provided that the training data constrain the charging current selected from the outer limits of possible charging currents, the determination of the state of charge when interpolating the charging current within these limits is even more accurate than when the regression takes place for a defined charging current. Thus, the ANN achieves an error of 0.16 % and the SVR achieves an error of 0.47 % on unseen data. In practice, this success is of great relevance, since no defined charge current, which was trained beforehand, has to be applied for the determination of the state of charge, but any con-

stant currents may occur during the measurement, which are within the fitted limits

Another less computationally intensive method for detecting the charge termination was also successfully tested. Here, the variation of the low-frequency diffusion process over time is tracked in the impedance data. The transition between reduction to zinc and electrolysis can thus clearly be detected. Although only charge termination is detected here, the method has the advantage that it is extremely robust and can also be applied to new cells without prior training.

The possibility of determining the SoH based on electrochemical impedance spectra by applying ANN was also investigated. The cell under development degrades mainly due to the formation of dendrites rather than a reduction in capacity or an increase in the internal resistance, so existing data from other publications was used. The detection of the state of degradation could be successfully performed with the help of neural networks and even an optimization of the measurement duration by identifying the important frequencies was possible.

In addition to state detection, there are other hurdles facing the operation of zinc-air batteries. First, electrolyte management is a crucial aspect. Since the GDE is permeable to gases, the water content can evaporate from the electrolyte and diffuse to the outside through the air cathode. The electrolyte concentration is thus negatively influenced with an impact on cell performance and lifetime. Therefore, a measurement and control system based on the electrolyte conductivity was developed, which ensures a constant electrolyte concentration. Thus, an important step has been achieved that allows zinc-air batteries to operate in an extended temperature range.

Finally, the oxygen consumption of zinc-air cells was investigated. To do this, a theoretical statement on oxygen consumption as a function of the discharged charge was first made on the basis of the chemical reaction equations. In a practical experiment, in which the cells were operated in an airtight box while the oxygen content was measured, the theoretical statements were confirmed very precisely. It was shown that only the discharged charge is responsible for the oxygen consumption and that other factors, such as the current intensity, have no influence. The results thus allow a concrete design of the ventilation of a zinc-air storage system based on the cell capacity.

In summary, the primary challenges of operating zinc-air batteries have been solved and the success has been shown in practical experiments. This step is also significant with regard to the energy transition, as it is now possible to store renewable energy with a safe, environmentally friendly and at the same time highly energetic battery technology. The developed processes could already be tested in a demonstrator with 12 cells on a PV system. Currently, a setup with more than 70 zinc-air cells is being developed, built and tested.

8.3 OUTLOOK

Of course, research and development is not yet at an end. An important point here is the further development of the actual zinc-air cell. By using the 3-electrode technology, in which a separate nickel electrode is used for charging, the durability of the GDE could be increased to such an extent that it survives several zinc anodes. Instead, the focus should now be on reducing dendrite formation. Strong improvements have already been achieved here by modifying the electrolytes. One aspect that affects the lifetime of the electrolyte is carbonization. CO_2 from the ambient air enters the electrolyte and forms potassium carbonate. This can lower the pH of the electrolyte to a point where zinc oxide precipitates and forms a passivating layer. Further battery operation of the cell then requires complete replacement of the electrolyte so that the passivating layer dissolves in the fresh electrolyte. There is also further development potential with regard to the power density and energy density of zinc-air cells. The key factor here is the cell geometry, which is currently still designed for maximum safety against dendrites. The first tests of a geometry with increased cell performance are already taking place.

However, different cell geometries also lead to modified impedance spectra. The state estimation methods presented in this work, however, all require a known cell geometry, and the data from this geometry were used to fit the models. In a next step, it should be investigated whether the regression methods can also approximate different cell geometries, for example with the aid of additional parameters such as the active surface. The goal here is that the methods can be applied to unknown cells. To strengthen robustness, it would be possible, for example, not to perform a regression, but to classify the SoC in 10 % steps.

A further potential for optimization, which is particularly useful in monetary terms, is the development of integrated circuits that enable galvanically isolated voltage measurement on battery systems with 3-electrode technology. While integrated circuits already exist for conventional battery technologies with 2 electrodes, which enable galvanically isolated voltage measurement even in systems with a high number of cells, discrete circuit structures had to be developed and built for the zinc-air demonstrators. On the one hand, this results in a high space requirement. On the other hand, the discrete setup is also much more expensive. Therefore, the development of an integrated circuit, in which two voltages can be measured with one reference potential, is an economically very important step.

Finally, battery systems, despite their importance, cannot alone manage the energy transition. Therefore, other technologies should be further studied. One promising approach is the production of green hydrogen from surplus renewable energy in an electrolysis process.

With the help of fuel cells, the energy can then be returned to the grid or used in a cars.

Part V

APPENDIX

APPENDIX

A.1 SCHEMATIC OF PID CURRENT CONTROLLER

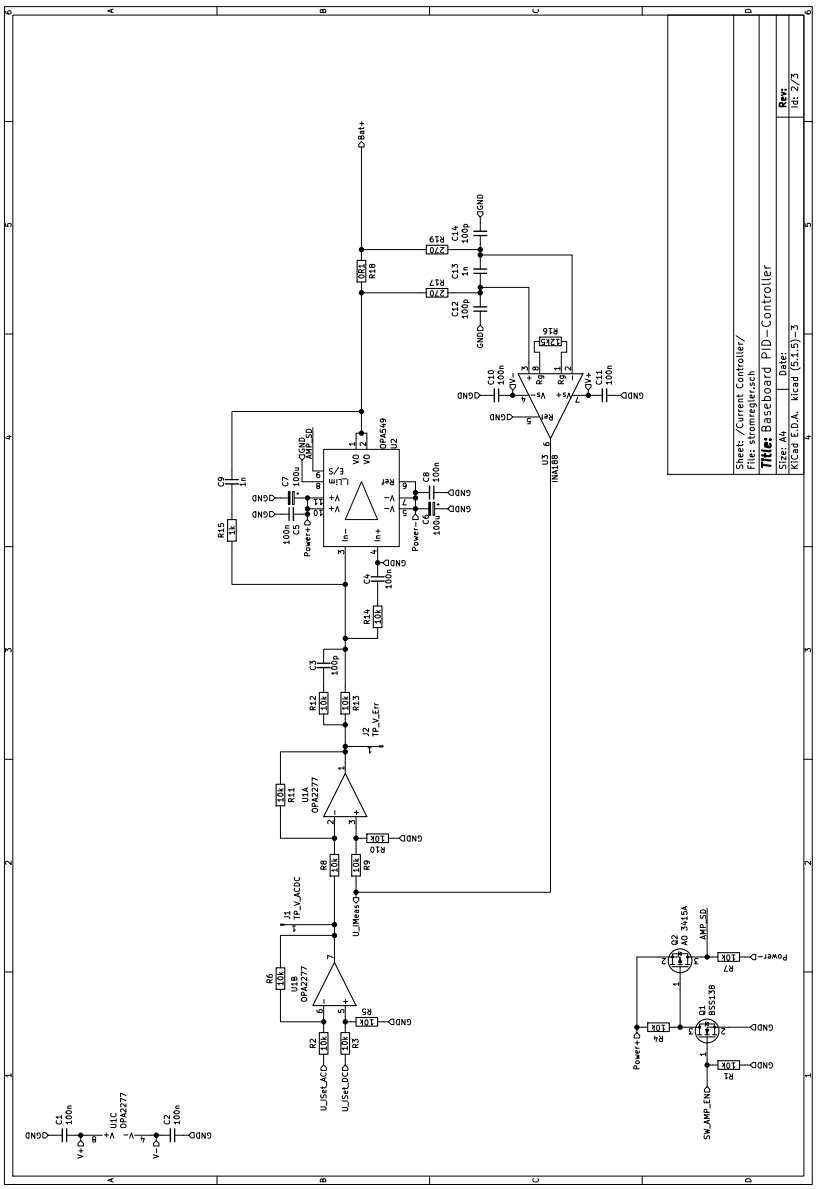

A.2 SOFTWARE: MODEL FITTING

The Python module scikit-optimize was used to fit the battery model. The fitting is divided into three steps. First, the battery model is defined, which determines the impedance depending on the model parameters and the frequency being evaluated (Listing A.1). In order to use the optimization functions from the scikit-optimize module, a cost function must be defined whose cost increases with increasing deviation between the measured data and the model data (Listing A.2). The actual optimization then takes place in Listing A.3.

Listing A.1: Definition of the battery model in Python.

```
# Define Battery model
def z_model_charge(f,param):
    w = 2*np.pi*f
    # Split up parameters
    Rel = param[0]
    Rct1 = param[1]
    ad1 = param[2]
    cpe_q = param[3]
    cpe_n = param[4]
    Rct2 = param[5]
    ad2 = param[6]
    Cdl2 = param[7]
    L = param[8]

    # Calculate Warburg impedance
    Zwar1 = ad1 * ((1j*w)**(-0.5))
    Zwar2 = ad2 * ((1j*w)**(-0.5))

    # Calculate CPE
    Ycpe1 = cpe_q * ((1j*w)**cpe_n)

    # Calculate electrode impedance
    Zelectrode1 = 1 / (Ycpe1 + (1/(Rct1+Zwar1 )))
    Zelectrode2 = 1 / ((1j*w*Cdl2) + (1/(Rct2+Zwar2)))

    # Return complete Impedance
    return (Rel + Zelectrode1   + Zelectrode2 + (1j*w*L))
```

Listing A.2: Definition of the error function in Python to fit the battery mode.

```
# Define cost function
def squared_error_charge(eisdata,param):
    residual_sum = 0.
    for k in range(len(eisdata)):
        Zm = eisdata.Z[k]
        f = eisdata.ActFreq[k]
        Zc = z_model_charge(f, param)*1E3
        residual = Zm-Zc
        residual_sum += residual.real**2 +residual.imag**2
    return residual_sum

def f_cost(param):
    return models.squared_error_charge(eis_data, param)
```

Listing A.3: Python program used to fit the battery model against measured impedance spectra.

```
# Define initial guess
param0 = [1.0-2,    # Rel
          1.0E-2,   # Rct1
          5e-12,    # ad1
          4.0E0,    # cpe_q
          5.0E-1,   # cpe_n
          8.0E-3,   # Rct2
          9.0E-5,   # ad2
          4.0E-1,   # Cdl2
          4.0E-8]   # L

# Define boundaries
bounds = scipy.optimize.Bounds(np.ones([len(param0)])*1e-20,
                               np.ones([len(param0)])*5)

# Optimize
cnt = 0
while (res.fun > 2 or cnt < 10):
    res = scipy.optimize.minimize(f_cost,
                                  param0,
                                  bounds=bounds,
                                  options={"maxiter":1E2})
    param0 = res.x
    cnt +=1

# Store results
params_charge = res.x
```

BIBLIOGRAPHY

[1] K. M. Abraham. "Rechargeable Batteries for the 300-Mile Electric Vehicle and Beyond." en. In: *ECS Transactions* 41.31 (Dec. 2019), pp. 27–34. DOI: 10.1149/1.3702853. URL: https://iopscience.iop.org/article/10.1149/1.3702853 (visited on 04/24/2021) (cit. on p. 13).

[2] ADAC. *Zufahrtsbeschränkungen in Europa*. de. Jan. 2021. URL: https://www.adac.de/verkehr/abgas-diesel-fahrverbote/fahrverbote/fahrv/ (cit. on p. 8).

[3] Ryan P Adams. *A Tutorial on Bayesian Optimization! for Machine Learning*. en. University of Toronto, 2018 (cit. on pp. 78, 79).

[4] M. A. Aizerman, È. M. Braverman, and L. I. Rozonoèr. "Theoretical foundation of potential functions method in pattern recognition." ru. In: *Avtomat. i Telemekh.* 25.6 (1964), pp. 917–936 (cit. on p. 78).

[5] Frank Allebrod, Christodoulos Chatzichristodoulou, Pia Lolk Mollerup, and Mogens Bjerg Mogensen. "Electrical conductivity measurements of aqueous and immobilized potassium hydroxide." en. In: *International Journal of Hydrogen Energy* 37.21 (Nov. 2012), pp. 16505–16514. DOI: 10.1016/j.ijhydene.2012.02.088. URL: https://linkinghub.elsevier.com/retrieve/pii/S0360319912004521 (visited on 01/03/2021) (cit. on pp. 39, 40, 107, 109).

[6] Hajime Arai, Stefan Mueller, and Otto Haas. "AC Impedance Analysis of Bifunctional Air Electrodes for Metal-Air Batteries." en. In: *Journal of The Electrochemical Society* 147.10 (2000), p. 3584. DOI: 10.1149/1.1393943. URL: http://jes.ecsdl.org/cgi/doi/10.1149/1.1393943 (visited on 07/22/2019) (cit. on pp. 62, 173).

[7] Peter Atkins, Julio de Paula, and James Keeler. *Atkins' Physical Chemistry*. 11th Edition. Oxford, United Kingdom: OXFORD, Dec. 2017 (cit. on pp. 57, 58).

[8] Evgenij Barsoukov and J. Ross Macdonald, eds. *Impedance spectroscopy: theory, experiment, and applications*. en. Third edition. Hoboken, NJ: Wiley, 2018 (cit. on pp. 64, 67, 117, 118, 123).

[9] Fachverband Batterien. *Anforderungen an Batterie-Entladeanzeiger für Blei-Antriebsbatterien zur Erreichung einer hohen Wirtschaftlichkeit*. de. July 2008. URL: https://www.zvei.org/fileadmin/user_upload/Verband/Fachverbaende/Batterien/Merkblaetter/Industriebatterien/13_Anforderungen_an_Batterie-Entladeanzeiger_

fuer_Bleiantriebsbatterien_2008-07.pdf (visited on 04/27/2021) (cit. on p. 15).

[10] Werner Baumann and Anneliese Muth. *Batterien: Daten und Fakten zum Umweltschutz*. de. OCLC: 913804409. 1997. URL: http://link.springer.com/openurl?genre=book&isbn=978-3-642-64442-9 (visited on 07/23/2019) (cit. on p. 32).

[11] Hans-Peter Beck, Bernd Engel, Lutz Hofmann, Roland Menges, Thomas Turek, and Hartmut Weyer. *Studie Eignung von Speichertechnologien zum Erhalt der Systemsicherheit*. de. Abschlussbericht FA 43/12. Goslar: Energie-Forschungszentrum Niedersachsen, Mar. 2013. URL: https://www.bmwi.de/Redaktion/DE/Publikationen/Studien/eignung-von-speichertechnologien-zum-erhalt-der-systemsicherheit.pdf?__blob=publicationFile&v=9 (visited on 04/20/2021) (cit. on p. 12).

[12] FU Berlin. *Kfz energetisch betrachtet*. de. Mar. 2017. URL: http://kirste.userpage.fu-berlin.de/chemistry/general/kfz-energetisch.html (visited on 03/18/2021) (cit. on p. 9).

[13] Harry H. Binder. *Lexikon der chemischen Elemente - das Periodensystem in Fakten, Zahlen und Daten*. Stuttgart: S. Hirzel Verlag, 1999 (cit. on p. 12).

[14] Holger Blanke, Tilman Sanders, Martin Kiel, Thorsten Baumhöfer, Birger Fricke, and Dirk Uwe Sauer. "EISmeter – The Art of Impedance Spectroscopy on Batteries and Fuel Cells." en. In: *Technische Mitteilungen* (2006), p. 11 (cit. on p. 132).

[15] H. W. Bode. *Network Analysis and Feedback Amplifier Design*. Vol. Princeton. New Jersey: D. Van Nostrand Company, Inc., 1945 (cit. on p. 67).

[16] Bernard A. Boukamp. "A Linear Kronig-Kramers Transform Test for Immittance Data Validation." en. In: *Journal of The Electrochemical Society* 142.6 (June 1995), pp. 1885–1894. DOI: 10.1149/1.2044210. URL: https://iopscience.iop.org/article/10.1149/1.2044210 (visited on 02/19/2021) (cit. on p. 67).

[17] Bernard A. Boukamp. "Impedance Spectroscopy, Strength and Limitations (Impedanzspektroskopie, Stärken und Grenzen)." In: *tm - Technisches Messen* 71 (Sept. 2004), pp. 454–459. DOI: 10.1524/teme.71.9.454.42758 (cit. on p. 67).

[18] Hans Breuer. *Dtv-Atlas Chemie*. 9th ed. Vol. 1. München: Deutscher Taschenbuch Verlag (dtv), 2000 (cit. on p. 12).

[19] Max P. Brinker. "Strategische Vermarktungsanalyse eines Zink-Luft-Akkumulators zur Speicherung von Solarstrom." de. Bachelorthesis. Steinfurt, Germany: University of Applied Sciences Muenster, Apr. 2017 (cit. on p. 14).

[20] P. Bruttel and C. Thielen. *Konduktometrie - Leitfähigkeitsmessung*. 2004 (cit. on pp. 108, 109).

[21] I. Bucher. *Circle fit*. 2004. URL: https://de.mathworks.com/matlabcentral/fileexchange/%205557-circle-fit?focused=5059278%5C&tab=function (cit. on p. 144).

[22] Naturschutz und nukleare Sicherheit (BMU) Bundesministerium für Umwelt. *Statistiken: Verkäufe, Sammlung, Sammelquote*, Recyclingeffizienz und Recyclingniveau Altbatterien*. de. Sept. 2020. URL: https://www.bmu.de/themen/wasser-abfall-boden/abfallwirtschaft/statistiken/statistik-altbatterien/ (visited on 03/15/2021) (cit. on pp. 5, 6, 26).

[23] Pieremanuele Canepa, Gopalakrishnan Sai Gautam, Daniel C. Hannah, Rahul Malik, Miao Liu, Kevin G. Gallagher, Kristin A. Persson, and Gerbrand Ceder. "Odyssey of Multivalent Cathode Materials: Open Questions and Future Challenges." en. In: *Chemical Reviews* 117.5 (Mar. 2017), pp. 4287–4341. DOI: 10.1021/acs.chemrev.6b00614. URL: https://pubs.acs.org/doi/10.1021/acs.chemrev.6b00614 (visited on 04/24/2021) (cit. on p. 13).

[24] Vincenzo Caramia and Benedetto Bozzini. "Materials science aspects of zinc–air batteries: a review." en. In: *Materials for Renewable and Sustainable Energy* 3.2 (June 2014), p. 28. DOI: 10.1007/s40243-014-0028-3. URL: http://link.springer.com/10.1007/s40243-014-0028-3 (visited on 07/19/2019) (cit. on pp. 32, 33, 37–40).

[25] David Leonard Chapman. "A Contribution to the Theory of Electrocapillarity." en. In: *Philosophical Magazine Series 6* 25.148 (1913), pp. 475–481 (cit. on p. 53).

[26] International Electrotechnical Commission. *IEC62391-2*. en. Apr. 2006 (cit. on p. 172).

[27] Claudia Conesa, Javier Ibáñez Civera, Lucía Seguí, Pedro Fito, and Nicolás Laguarda-Miró. "An Electrochemical Impedance Spectroscopy System for Monitoring Pineapple Waste Saccharification." en. In: *Sensors* 16.2 (Feb. 2016), p. 188. DOI: 10.3390/s16020188. URL: http://www.mdpi.com/1424-8220/16/2/188 (visited on 01/04/2021) (cit. on p. 147).

[28] Digatron, ed. *EIS-METER – Impedanzspektroskop Bedienungsanleitung V2.4.4* (cit. on p. 132).

[29] Digatron. *Electrochemical Impedance Spectroscopy EIS-METER datasheet*. en (cit. on p. 132).

[30] Chi Dung Doan and Shie-Yui Liong. "GENERALIZATION FOR MULTILAYER NEURAL NETWORK BAYESIAN REGULARIZATION OR EARLY STOPPING." en. In: (), p. 8 (cit. on p. 149).

[31] J. Drillkens, Y. Yurdagel, Kowal, J., and D. U. Sauer. "Maximizing the lifetime of electrochemical double layer capacitors at given temperature conditions by optimized operating strategies." In: *4th European Symposium on Supercapacitors and Applications, ESSCAP*. Bordeaux, France, Oct. 2010 (cit. on p. 129).

[32] Rodolfo Dufo-López, Tomás Cortés-Arcos, Jesús Sergio Artal-Sevil, and José L. Bernal-Agustín. "Comparison of Lead-Acid and Li-Ion Batteries Lifetime Prediction Models in Stand-Alone Photovoltaic Systems." en. In: *Applied Sciences* 11.3 (Jan. 2021), p. 1099. DOI: 10.3390/app11031099. URL: https://www.mdpi.com/2076-3417/11/3/1099 (visited on 06/18/2021) (cit. on p. 26).

[33] G. Eason, B. Noble, and I. N. Sneddon. *Zink und seine chemischen Eigenschaftenzink*. de. Oct. 2012. URL: http://chemikalien.de/zink-und-seine-chemischen-eigenschaften/ (visited on 07/23/2019) (cit. on p. 3).

[34] U.S. Department of Energy. *Energy Storage Database*. end. 2021. URL: https://www.sandia.gov/ess-ssl/global-energy-storage-database/ (visited on 04/20/2021) (cit. on p. 12).

[35] Faculty of Electrical and Computer Engineering, University of Tabriz, Tabriz, Iran, Hossein Komijani, Sepideh Rezaeihassanabadi, Faculty of Electrical Engineering, Ghiasodin Jamshid Kashani Higher Education Institute, Ghazvin, Iran, Mohammad Reza Parsaei, Department of Computer Engineering and Information Technology, Shiraz University of Technology, Shiraz, Iran, Saeed Maleki, and Faculty of Chemical and Petroleum Engineering, University of Tabriz, Tabriz, Iran. "Radial Basis Function Neural Network for Electrochemical Impedance Prediction at Presence of Corrosion Inhibitor." en. In: *Periodica Polytechnica Chemical Engineering* (Sept. 2016). DOI: 10.3311/PPch.9295. URL: https://pp.bme.hu/ch/article/view/9295 (visited on 01/04/2021) (cit. on p. 147).

[36] Donal P. Finegan et al. "In-operando high-speed tomography of lithium-ion batteries during thermal runaway." en. In: *Nature Communications* 6.1 (Nov. 2015), p. 6924. DOI: 10.1038/ncomms7924. URL: http://www.nature.com/articles/ncomms7924 (visited on 04/28/2021) (cit. on p. 15).

[37] Martin A. Fischler and Robert C. Bolles. "Random Sample Consensus: A Paradigm for Model Fitting with Applications to Image Analysis and Automated Cartography." In: *Commun. ACM* 24.6 (June 1981). Place: New York, NY, USA Publisher: Association for Computing Machinery, pp. 381–395. DOI: 10.1145/358669.358692. URL: https://doi.org/10.1145/358669.358692 (cit. on p. 143).

[38] Kaspar Fraunhofer IEE. *Kombikraftwerk 2*. Dec. 2013. URL: www.kombikraftwerk.de (visited on 04/19/2021) (cit. on p. 11).

[39] Jing Fu, Zachary Paul Cano, Moon Gyu Park, Aiping Yu, Michael Fowler, and Zhongwei Chen. "Electrically Rechargeable Zinc-Air Batteries: Progress, Challenges, and Perspectives." en. In: *Advanced Materials* 29.7 (Feb. 2017), p. 1604685. DOI: 10.1002/adma.201604685. URL: http://doi.wiley.com/10.1002/adma.201604685 (visited on 05/08/2021) (cit. on pp. 86, 90).

[40] Paul Geladi and Bruce R. Kowalski. "Partial least-squares regression: a tutorial." en. In: *Analytica Chimica Acta* 185 (1986), pp. 1–17. DOI: 10.1016/0003-2670(86)80028-9. URL: https://linkinghub.elsevier.com/retrieve/pii/0003267086800289 (visited on 01/04/2021) (cit. on p. 147).

[41] H.F. Gibbard. "Nickel metal hydride battery technology." en. In: *Proceedings of WESCON '93*. San Francisco, CA, USA: IEEE, 1993, pp. 215–219. DOI: 10.1109/WESCON.1993.488437. URL: http://ieeexplore.ieee.org/document/488437/ (visited on 06/18/2021) (cit. on p. 27).

[42] H.F. Gibbard. "Nickel metal hydride battery applications." en. In: *Proceedings of 9th Annual Battery Conference on Applications and Advances*. Long Beach, CA, USA: IEEE, 1994, p. 127. DOI: 10.1109/BCAA.1994.283603. URL: http://ieeexplore.ieee.org/document/283603/ (visited on 06/18/2021) (cit. on pp. 27, 28).

[43] R Gilliam, J Graydon, D Kirk, and S Thorpe. "A review of specific conductivities of potassium hydroxide solutions for various concentrations and temperatures." en. In: *International Journal of Hydrogen Energy* 32.3 (Mar. 2007), pp. 359–364. DOI: 10.1016/j.ijhydene.2006.10.062. URL: https://linkinghub.elsevier.com/retrieve/pii/S0360319906005428 (visited on 01/03/2021) (cit. on pp. 40, 107).

[44] finanzen.net GmbH. *finanzen.net Rohstoffe*. de. Apr. 2021. URL: https://www.finanzen.net/rohstoffe (visited on 04/22/2021) (cit. on p. 12).

[45] Gerald Goertzel. "An Algorithm for the Evaluation of Finite Trigonometric Series." en. In: *The American Mathematical Monthly* 65.1 (Jan. 1958), p. 34. DOI: 10.2307/2310304. URL: https://www.jstor.org/stable/2310304?origin=crossref (visited on 05/11/2021) (cit. on p. 121).

[46] Louis Georges Gouy. "Sur la constitution de la charge électrique à la surface d'un electrolyte." fr. In: *Comptes Rendus de l'Académie des sciences* 149 (1909), pp. 654–657 (cit. on p. 53).

[47] M. Gouy. "Sur la constitution de la charge électrique à la surface d'un électrolyte." fr. In: *Journal de Physique Théorique et Appliquée* 9.1 (1910), pp. 457–468. DOI: 10.1051/jphystap:019100090045700. URL: http://www.edpsciences.org/10.1051/jphystap:019100090045700 (visited on 09/15/2020) (cit. on p. 53).

[48] N. N. Greenwood and A. Earnshaw. *Chemie der Elemente*. 1st ed. Weinheim: VCH, 1988 (cit. on p. 12).

[49] Marian Greßhoff. "Wirtschaftlichkeitsanalyse von Zink-Luft-Akkusim Vergleich zu Lithium-Ionen-Akkus für zukünftige Energiespeicher." de. MA thesis. Steinfurt, Germany: University of Applied Sciences Muenster, 2021 (cit. on p. 14).

[50] grs-batterien.de. *Stiftung Gemeinsames Rücknahmesystem Batterien - Jahresbericht 2019*. Tech. rep. May 2020. URL: grs-batterien.de (visited on 03/03/2021) (cit. on p. 5).

[51] Katrin Harting, Kunz Ulrich, and Thomas Turek. "Zinc-air Batteries: Prospects and Challenges for Future Improvement." In: *Zeitschrift für Physikalische Chemie* 226.2 (2012), pp. 151–166 (cit. on p. 38).

[52] Pascal Hartmann, Conrad L. Bender, Miloš Vračar, Anna Katharina Dürr, Arnd Garsuch, Jürgen Janek, and Philipp Adelhelm. "A rechargeable room-temperature sodium superoxide (NaO_2) battery." en. In: *Nature Materials* 12.3 (Mar. 2013), pp. 228–232. DOI: 10.1038/nmat3486. URL: http://www.nature.com/articles/nmat3486 (visited on 04/25/2021) (cit. on p. 13).

[53] Yaqun He, Xue Yuan, Guangwen Zhang, Haifeng Wang, Tao Zhang, Weining Xie, and Liping Li. "A critical review of current technologies for the liberation of electrode materials from foils in the recycling process of spent lithium-ion batteries." In: *Science of The Total Environment* 766 (2021), p. 142382. DOI: https://doi.org/10.1016/j.scitotenv.2020.142382. URL: https://www.sciencedirect.com/science/article/pii/S0048969720359118 (cit. on p. 30).

[54] Hermann von Helmholtz. "Ueber einige Gesetze der Vertheilung elektrischer Ströme in körperlichen Leitern, mit Anwendung auf die thierisch elektrischen Versuche." In: *Annalen der Physik und Chemie*. 3rd ser. 89 (1853), pp. 211–233. DOI: 10.1002/andp.18531650603 (cit. on pp. 51, 53).

[55] Hermann von Helmholtz. "Studien über electrische Grenzschichten." In: *Annalen der Physik und Chemie* 243 (1879), pp. 337–382. DOI: 10.1002/andp.18792430702 (cit. on pp. 51, 53).

[56] Klaus Heuck, Klaus-Dieter Dettmann, and Detlef Schulz. *Elektrische Energieversorgung: Erzeugung, Übertragung und Verteilung elektrischer Energie für Studium und Praxis*. de. 8., überarb. und aktualisierte Aufl. Studium. OCLC: 669170746. Wiesbaden: Vieweg + Teubner, 2010 (cit. on p. 12).

[57] Eric Hirst. "Price-Responsive Demand as Reliability Resources." en. In: *Consulting in Electric-Industry Restructuring* (Apr. 2002), p. 23 (cit. on p. 11).

[58] Soraya Hosseini, Salman Masoudi Soltani, and Yuan-Yao Li. "Current status and technical challenges of electrolytes in zinc–air batteries: An in-depth review." In: *Chemical Engineering Journal* 408 (2021), p. 127241. DOI: https://doi.org/10.1016/j.cej.2020.127241. URL: https://www.sciencedirect.com/science/article/pii/S1385894720333660 (cit. on pp. 39, 40).

[59] Christina Imobersteg. *Zink hat viele Talente*. de. June 2019. URL: https://www.umweltnetz-schweiz.ch/themen/ressourcen/3196-zink-hat-viele-talente.html (visited on 04/22/2021) (cit. on p. 12).

[60] R. Jolly and C. Rhin. "The recycling of lead-acid batteries: production of lead and polypropylene." en. In: *Resources, Conservation and Recycling* 10.1-2 (Apr. 1994), pp. 137–143. DOI: 10.1016/0921-3449(94)90046-9. URL: https://linkinghub.elsevier.com/retrieve/pii/0921344994900469 (visited on 06/18/2021) (cit. on p. 26).

[61] Jean-Baptiste Jorcin, Mark E. Orazem, Nadine Pébère, and Bernard Tribollet. "CPE analysis by local electrochemical impedance spectroscopy." en. In: *Electrochimica Acta* 51.8-9 (Jan. 2006), pp. 1473–1479. DOI: 10.1016/j.electacta.2005.02.128. URL: https://linkinghub.elsevier.com/retrieve/pii/S0013468605008285 (visited on 05/21/2021) (cit. on p. 65).

[62] S. R. Käbitz. *Untersuchung der Alterung von Lithium-Ionen-Batterien mittels Elektroanalytik und elektrochemischer Impedanzspektroskopie*. de. Aachener Beiträge des ISEA. Dec. 2016 (cit. on p. 67).

[63] Martin Kiel. *Impedanzspektroskopie an Batterien unter besonderer Berücksichtigung von Batteriesensoren für den Feldeinsatz*. de. Aachener Beiträge des ISEA 67. OCLC: 852507405. Aachen: Shaker, 2013 (cit. on pp. 118, 129–131).

[64] Florian Knobloch, Steef V. Hanssen, Aileen Lam, Hector Pollitt, Pablo Salas, Unnada Chewpreecha, Mark A. J. Huijbregts, and Jean-Francois Mercure. "Net emission reductions from electric cars and heat pumps in 59 world regions over time." en. In: *Nature Sustainability* 3.6 (June 2020), pp. 437–447. DOI: 10.1038/s41893-020-0488-7. URL: http://www.nature.com/articles/s41893-020-0488-7 (visited on 03/18/2021) (cit. on p. 8).

[65] Kaspar Knorr. "Abschätzung der Netzstabilität einer rein regenerativen Stromversorgung." In: Kassel: Fraunhofer Institut für Windenergie und Energiesystemtechnik IWES, 2012, p. 12 (cit. on pp. 10–12).

[66] John J.C. Kopera. *Inside the Nickel Metal Hydride Battery*. en. Tech. rep. Cobasys, MI: Citeseer, 2004. URL: http://www.cobasys.%20com/pdf/tutorial/inside%5C_nimh%5C_battery%5C_technology.pdf (visited on 04/18/2021) (cit. on p. 27).

[67] H. A. Kramers. "Die Dispersion und Absorption von Röntgenstrahlen." In: *Physikalische Zeitschrift* 30 (1929), pp. 522–523 (cit. on p. 67).

[68] R. de L. Kronig. "On the Theory of Dispersion of X-Rays." In: *Journal of Optical Society of America* 12.6 (1926), pp. 547–557 (cit. on p. 67).

[69] Lothar Kuhn. *Expertenstreit: Ist Brennstoffzelle oder Akku klimafreundlicher?* de. July 2019. URL: https://edison.media/erklaeren/expertenstreit-ist-brennstoffzelle-oder-akku-klimafreundlicher/24844360.html (visited on 03/18/2021) (cit. on p. 8).

[70] P. Kurzweil. "Gaston Planté and his invention of the lead–acid battery—The genesis of the first practical rechargeable battery." In: *Journal of Power Sources* 195.14 (2010), pp. 4424–4434. DOI: https://doi.org/10.1016/j.jpowsour.2009.12.126. URL: https://www.sciencedirect.com/science/article/pii/S0378775310000546 (cit. on p. 4).

[71] Peter Kurzweil and Otto K. Dietlmeier. *Elektrochemische Speicher: Superkondensatoren, Batterien, Elektrolyse-Wasserstoff, Rechtliche Rahmenbedingungen*. de. Wiesbaden: Springer Fachmedien Wiesbaden, 2018. DOI: 10.1007/978-3-658-21829-4. URL: http://link.springer.com/10.1007/978-3-658-21829-4 (visited on 08/31/2021) (cit. on pp. 4, 5, 24–26, 28, 30, 32).

[72] C.W. Lee, S.W. Eom, K. Sathiyanarayanan, and M.S. Yun. "Preliminary comparative studies of zinc and zinc oxide electrodes on corrosion reaction and reversible reaction for zinc/air fuel cells." In: *Electrochimica Acta* 52 (2006), pp. 1588–1591 (cit. on p. 38).

[73] Jang-soo Lee, Taemin Lee, Hyun-Kon Song, Jaephil Cho, and Byeong-Su Kim. "Ionic liquid modified graphenenanosheets anchoring manganese oxide nanoparticles as efficient electrocatalysts for Zn–air batteries." In: *Energy & Environmental Science* 4 (2011), pp. 4148–4154 (cit. on p. 38).

[74] Robert Lee and Walt Kester. "Fully Automatic Self-Calibrated Conductivity Measurement System." en. In: *Analog Dialogue Technical Journal 50-11* (2016), p. 7 (cit. on p. 108).

[75] Kenneth Levenberg. "A method for the solution of certain non-linear problems in least squares." en. In: *Quarterly of Applied Mathematics* 2.2 (July 1944), pp. 164–168. DOI: 10.1090/qam/10666. URL: http://www.ams.org/qam/1944-02-02/S0033-569X-1944-10666-0/ (visited on 01/05/2021) (cit. on pp. 68, 74).

[76] Yanguang Li and Hongjie Dai. "Recent advances in zinc-air batteries." en. In: *Chem. Soc. Rev.* 43.15 (2014), pp. 5257–5275. DOI: 10.1039/C4CS00015C. URL: http://xlink.rsc.org/?DOI=C4CS00015C (visited on 07/23/2019) (cit. on p. 14).

[77] Yanguang Li, Ming Gong, Yongye Liang, Ju Feng, Ji-Eun Kim, Hailiang Wang, Guosong Hong, Bo Zhang, and Hongjie Dai. "Advanced zinc-air batteries based on high-performance hybrid electrocatalysts." en. In: *Nature Communications* 4.1 (June 2013), p. 1805. DOI: 10.1038/ncomms2812. URL: http://www.nature.com/articles/ncomms2812 (visited on 01/10/2021) (cit. on p. 39).

[78] Yanguang Li and Jun Lu. "Metal-Air Batteries: Future Electrochemical Energy Storage of Choice?" en. In: (), p. 23 (cit. on p. 13).

[79] Chunwei Liu, Jiao Lin, Hongbin Cao, Yi Zhang, and Zhi Sun. "Recycling of spent lithium-ion batteries in view of lithium recovery: A critical review." In: *Journal of Cleaner Production* 228 (2019), pp. 801–813. DOI: https://doi.org/10.1016/j.jclepro.2019.04.304. URL: https://www.sciencedirect.com/science/article/pii/S0959652619314015 (cit. on p. 30).

[80] Xiao-yi Liu and Xian-zhi Xu. "Mesoscopic numerical computation model of air-diffusion electrode of metal/air batteries." en. In: *Applied Mathematics and Mechanics* 34 (Apr. 2013), pp. 571–176 (cit. on p. 40).

[81] Andre Loechte, Ole Gebert, and Peter Gloesekoetter. "End of charge detection of batteries with high production tolerances." en. In: Granada, Sept. 2019, p. 6 (cit. on p. 142).

[82] Andre Loechte, Ole Gebert, and Peter Gloesekoetter. "End of Charge Detection by Processing Impedance Spectra of Batteries." In: *Theory and Applications of Time Series Analysis*. Ed. by Olga Valenzuela, Fernando Rojas, Luis Javier Herrera, Héctor Pomares, and Ignacio Rojas. Cham: Springer International Publishing, 2020, pp. 163–176 (cit. on p. 141).

[83] Andre Loechte, Ole Gebert, Daniel Heming, Klaus T. Kallis, and Peter Gloesekoetter. "State estimation of zinc air batteries using neural networks." en. In: *Neural Computing and Applications* (Sept. 2018). DOI: 10.1007/s00521-018-3705-9. URL: http:

//link.springer.com/10.1007/s00521-018-3705-9 (visited on 07/22/2019) (cit. on pp. 147, 172).

[84] Andre Loechte, Ole Gebert, Ludwig Horsthemke, Daniel Heming, and Peter Gloesekoetter. "State of Charge Depended Modeling of an Equivalent Circuit of Zinc Air Batteries Using Electrochemical Impedance Spectroscopy." en. In: *Proceedings ITISE 2018*. Vol. 3. Granada, Spain: Universidad de Granada, Sept. 2018, pp. 625–636. URL: http://itise.ugr.es/ITISE2018_Papers_Vol_3.pdf (cit. on p. 135).

[85] Andre Loechte, Daniel Heming, Ole Gebert, Ludwig Horsthemke, and Peter Gloesekoetter. "Oxygen consumption of zinc-air batteries and their performance at low oxygen concentration levels." en. In: *2018 16th Biennial Baltic Electronics Conference (BEC)*. Tallinn: IEEE, Oct. 2018, pp. 1–4. DOI: 10.1109/BEC.2018.8600972. URL: https://ieeexplore.ieee.org/document/8600972/ (visited on 06/17/2021) (cit. on p. 101).

[86] Andre Loechte, Daniel Heming, Klaus T. Kallis, and Peter Gloesekoetter. "State of Health Estimation of Zinc Air Batteries Using Neural Networks." In: *Advances in Computational Intelligence*. Ed. by Ignacio Rojas, Gonzalo Joya, and Andreu Catala. Cham: Springer International Publishing, 2017, pp. 641–647 (cit. on p. 172).

[87] David J. C. MacKay. "A Practical Bayesian Framework for Backpropagation Networks." en. In: *Neural Computation* 4.3 (May 1992), pp. 448–472. DOI: 10.1162/neco.1992.4.3.448. URL: https://www.mitpressjournals.org/doi/abs/10.1162/neco.1992.4.3.448 (visited on 01/04/2021) (cit. on p. 149).

[88] Aroa Mainar, Luis Colmenares, Hans-Jürgen Grande, and J. Blázquez. "Enhancing the Cycle Life of a Zinc–Air Battery by Means of Electrolyte Additives and Zinc Surface Protection." en. In: *Batteries* 4.3 (Sept. 2018), p. 46. DOI: 10.3390/batteries4030046. URL: http://www.mdpi.com/2313-0105/4/3/46 (visited on 06/18/2021) (cit. on p. 40).

[89] Donald Marquardt. "An Algorithm for Least-Squares Estimation of Nonlinear Parameters." en. In: *SIAM Journal on Applied Mathematics* 11.2 (1963), pp. 431–441 (cit. on pp. 68, 74).

[90] Peter Marx. "Wirkungsgrad-Vergleich zwischen Fahrzeugen mit Verbrennungs- und mit Elektromotor: Harte Fakten." de. In: *Elektronik automotive Sonderausgabe Elektromobilität 2018* (2018), pp. 44–48. URL: http://www.mx-electronic.com/pdf-texte/link-e-mobility/Wirkungsgrad-Vergleich%20Marx%202018.pdf (visited on 03/18/2021) (cit. on p. 9).

[91] M.N Masri and A.A. Mohamad. "Effect of adding potassium hydroxide to an agar binder for use as the anode in Zn–air batteries." In: *Corrosion Science* 51 (2009), pp. 3025–3029 (cit. on p. 38).

[92] Warren S Mcculloch and Walter Pitts. "A LOGICAL CALCULUS OF THE IDEAS IMMANENT IN NERVOUS ACTIVITY." en. In: *Bulletin of Mathematical Biology* 52.1/2 (1990), pp. 99–115 (cit. on p. 68).

[93] Transport and Environment Reporting Mechanism. *Transport: increasing oil consumption and greenhouse gas emissions hamper EU progress towards environment and climate objectives*. Tech. rep. 15/2019. European Environment Agency, Feb. 2020. URL: https://www.eea.europa.eu/publications/transport-increasing-oil-consumption-and (visited on 03/17/2021) (cit. on pp. 7, 8).

[94] Armin Melzer. *Materialien für Zink und Zink-Luft Batterien*. de. Münster, Feb. 2010. URL: https://docplayer.org/5093744-Materialien-fuer-zink-und-zink-luft-batterien.html (visited on 04/25/2021) (cit. on p. 14).

[95] K. Mizushima, P. C. Jones, P. J. Wiseman, and J. B. Goodenough. "LixCoO2 (o<x<-1): A new cathode material for batteries of high energy density." In: *Materials Research Bulletin* 15.6 (1980), pp. 783–789. DOI: https://doi.org/10.1016/0025-5408(80)90012-4. URL: https://www.sciencedirect.com/science/article/pii/0025540880900124 (cit. on p. 29).

[96] A.A. Mohamad. "Zn/gelled 6 M KOH/O2 zinc–air battery." In: *Journal of Power Sources* 159.1 (Sept. 2006), pp. 752–757 (cit. on p. 38).

[97] W. H. Molder, J. H. Sluyters, T. Pajkossy, and L. Nytkos. "Tafel current at fractal electrodes - Connection with admittance spectra." en. In: *Journal of Electroanalytical Chemistry and Interfacial Electrochemistry* 285.1-2 (June 1990), pp. 103–115. DOI: https://doi.org/10.1016/0022-0728(90)87113-X (cit. on p. 65).

[98] Charles W. Monroe. "Does Oxygen Transport Affect the Cell Voltages of Metal/Air Batteries?" en. In: *Journal of The Electrochemical Society* 164.11 (2017), E3547–E3551. DOI: 10.1149/2.0521711jes. URL: http://jes.ecsdl.org/lookup/doi/10.1149/2.0521711jes (visited on 07/23/2019) (cit. on p. 102).

[99] Charles E. Mortimer. *Chemie - Das Basiswissen der Chemie*. 6th ed. New York: Georg Thieme Verlag Stuttgart, 1996 (cit. on pp. 24, 26, 33, 49).

[100] S Mueller, F Holzer, and O Haas. "Optimized zinc electrode for the rechargeable zinc-air battery." en. In: (Nov. 1997), p. 4 (cit. on pp. 32, 38).

[101] Martin Murnane and Adel Ghazel. "A Closer Look at State Of Charge (SOC) and State Of Health (SOH) Estimation Techniques for Batteries." en. In: (2017), p. 8. URL: www.analog.com (visited on 12/19/2017) (cit. on p. 16).

[102] Adolf Neckel, Christoph Fabjan, and Kurt Selden. *Chancen für das Elektrofahrzeug?* Ed. by Bundesministerium für Handel, Gewerbe und Industrie in Wien. Vol. 6. Energiepolitische Schriftenreihe. Vienna: Springer Vienna, 1980. DOI: 10.1007/978-3-7091-3661-4. URL: http://link.springer.com/10.1007/978-3-7091-3661-4 (visited on 07/23/2019) (cit. on p. 3).

[103] Julia Mareike Neles and Christoph Pistner, eds. *Kernenergie: Eine Technik für die Zukunft?* de. Technik im Fokus. Berlin, Heidelberg: Springer Berlin Heidelberg, 2012. DOI: 10.1007/978-3-642-24329-5. URL: http://link.springer.com/10.1007/978-3-642-24329-5 (visited on 04/18/2021) (cit. on p. 10).

[104] Walther Nernst. *Die elektromotorische Wirksamkeit der Jonen*. de. Wilhelm Engelmann, 1889. DOI: 10.3931/e-rara-10994. URL: http://www.e-rara.ch/doi/10.3931/e-rara-10994 (visited on 07/23/2019) (cit. on pp. 16, 24, 102).

[105] Mark E. Orazem and Bernard Tribollet. *Electrochemical impedance spectroscopy*. en. 2nd edition. Hoboken, New Jersey: John Wiley & Sons, Inc, 2017 (cit. on p. 67).

[106] Grzegorz Piłatowicz, Heide Budde-Meiwes, Julia Kowal, Christel Sarfert, Eberhard Schoch, Martin Königsmann, and Dirk Uwe Sauer. "Determination of the lead-acid battery's dynamic response using Butler-Volmer equation for advanced battery management systems in automotive applications." en. In: *Journal of Power Sources* 331 (Nov. 2016), pp. 348–359. DOI: 10.1016/j.jpowsour.2016.09.066. URL: https://linkinghub.elsevier.com/retrieve/pii/S0378775316312289 (visited on 08/05/2020) (cit. on p. 58).

[107] Ludwig Pohlmann. *Elektrochemie*. de. Berlin, Nov. 2005. URL: http://userpage.fu-berlin.de/%7Elap/PCIII_EC_4.pdf (visited on 05/07/2021) (cit. on p. 64).

[108] Antti Porvali, Severi Ojanen, Benjamin P. Wilson, Rodrigo Serna-Guerrero, and Mari Lundström. "Nickel Metal Hydride Battery Waste: Mechano-hydrometallurgical Experimental Study on Recycling Aspects." en. In: *Journal of Sustainable Metallurgy* 6.1 (Mar. 2020), pp. 78–90. DOI: 10.1007/s40831-019-00258-2. URL: http://link.springer.com/10.1007/s40831-019-00258-2 (visited on 06/18/2021) (cit. on p. 28).

[109] M. Prabu and S. Shanmugam. "NiCo2O4 - Graphene oxide hybrid as a bifunctional electrocatalyst for air breathing cathode material in metal air batteries." en. In: *International Conference on Advanced Nanomaterials & Emerging Engineering Technologies*. Chennai: IEEE, July 2013, pp. 468–470. DOI: 10.1109/ICANMEET.2013.6609319. URL: http://ieeexplore.ieee.org/document/6609319/ (visited on 01/03/2021) (cit. on p. 105).

[110] Volker Quaschning. *Regenerative Energiesysteme Technologie – Berechnung – Simulation*. de. 9th ed. Carl Hanser Verlag, 2015 (cit. on pp. 9, 10).

[111] M C Rao. "Novel Cathode Materials for Rechargeable Batteries." en. In: (2013), p. 3 (cit. on p. 15).

[112] Anette Regelous and Jan-Peter Meyn. "Erneuerbare Energien - eine physikalische Betrachtung." de. In: *Erneuerbare Energien* (), p. 5 (cit. on p. 9).

[113] Johan Rockström et al. "A safe operating space for humanity." en. In: *Nature* 461.7263 (Sept. 2009), pp. 472–475. DOI: 10.1038/461472a. URL: http://www.nature.com/articles/461472a (visited on 03/17/2021) (cit. on p. 7).

[114] F. Rosenblatt. "The perceptron: A probabilistic model for information storage and organization in the brain." en. In: *Psychological Review* 65.6 (1958), pp. 386–408. DOI: 10.1037/h0042519. URL: http://doi.apa.org/getdoi.cfm?doi=10.1037/h0042519 (visited on 01/04/2021) (cit. on pp. 68, 71).

[115] David E. Rumelhart, Geoffrey E. Hinton, and Ronald J. Williams. "Learning representations by back-propagating errors." In: *Nature* 323.6088 (Oct. 1986), pp. 533–536. DOI: 10.1038/323533a0. URL: https://doi.org/10.1038/323533a0 (cit. on p. 72).

[116] Andrej Sadkowski. "CNLS fits and Kramers–Kronig validation of resonant EIS data." In: *Journal of Electroanalytical Chemistry* 573.2 (Dec. 2004), pp. 241–253. DOI: https://doi.org/10.1016/j.jelechem.2004.07.009 (cit. on p. 67).

[117] Sarwan S Sandhu, George W Brutchen, and Joseph P Fellner. "Lithium/air cell: Preliminary mathematical formulation and analysis." en. In: *Journal of Power Sources* (2007), p. 14 (cit. on p. 13).

[118] Klaus Schmidt-Rohr. "How Batteries Store and Release Energy: Explaining Basic Electrochemistry." en. In: *Journal of Chemical Education* 95.10 (Oct. 2018), pp. 1801–1810. DOI: 10.1021/acs.jchemed.8b00479. URL: https://pubs.acs.org/doi/10.1021/acs.jchemed.8b00479 (visited on 01/07/2020) (cit. on pp. 24, 26).

[119] Michael Schönleber. *Verfahren zur Charakterisierung des Niederfrequenzverhaltens von Lithium-Ionen-Batterien*. de. Vol. 32. Schriften des Instituts für Angewandte Materialien – Werkstoffe der Elektrotechnik. Karlsruher Institut für Technologie, July 2017 (cit. on pp. 50, 51).

[120] J. Schule and P. Drossbach. "Elektrochemische Untersuchungen an Kohleelektroden I - Die Ueberspannung des Wasserstoffs." de. In: *Electrochimica Acta* 9 (1964), pp. 1391–1404 (cit. on pp. 16, 173).

[121] Adolf J. Schwab. *Elektroenergiesysteme: Erzeugung, Übertragung und Verteilung elektrischer Energie*. de. Berlin, Heidelberg: Springer Berlin Heidelberg, 2017. DOI: 10.1007/978-3-662-55316-9. URL: http://link.springer.com/10.1007/978-3-662-55316-9 (visited on 04/19/2021) (cit. on p. 10).

[122] Terrence J. Sejnowski and Charles R. Rosenberg. "Parallel Networks that Learn to Pronounce English Text." en. In: *Complex Systems* 1 (1987), pp. 145–168 (cit. on p. 72).

[123] Alex J. Smola and Bernhard Schölkopf. "A tutorial on support vector regression." en. In: *Statistics and Computing* 14.3 (Aug. 2004), pp. 199–222. DOI: 10.1023/B:STCO.0000035301.49549.88. URL: http://link.springer.com/10.1023/B:STCO.0000035301.49549.88 (visited on 12/07/2020) (cit. on pp. 75, 77, 78).

[124] Jasper Snoek, Hugo Larochelle, and Ryan P. Adams. "Practical Bayesian Optimization of Machine Learning Algorithms." en. In: *arXiv:1206.2944 [cs, stat]* (Aug. 2012). arXiv: 1206.2944. URL: http://arxiv.org/abs/1206.2944 (visited on 02/03/2021) (cit. on pp. 78, 80, 158).

[125] Zentrum für Sonnenenergie- und Wasserstoff-Forschung Baden-Württemberg (ZSW). *Bestand an Elektro-Pkw weltweit*. de. Mar. 2021. URL: https://www.zsw-bw.de/mediathek/datenservice.html (visited on 03/18/2021) (cit. on p. 9).

[126] R. Spotnitz and J. Franklin. "Abuse behavior of high-power, lithium-ion cells." en. In: *Journal of Power Sources* 113.1 (Jan. 2003), pp. 81–100. DOI: 10.1016/S0378-7753(02)00488-3. URL: https://linkinghub.elsevier.com/retrieve/pii/S0378775302004883 (visited on 04/28/2021) (cit. on p. 15).

[127] Deutsches Institut Fur Normung E.V. (German National Standard). "DIN 1343 - Reference conditions, normal conditions, normal volume; concepts and values." de. In: Beuth Verlag GmbH, Jan. 1990. DOI: https://dx.doi.org/10.31030/2333155 (cit. on p. 41).

[128] Otto Stern. "Zur Theorie der elektrolytischen Doppelschicht." In: *Zeitschrift für Elektrochemie* 30 (Nov. 1924), pp. 508–516 (cit. on pp. 51, 53, 55).

[129] Wei Sun et al. "A rechargeable zinc-air battery based on zinc peroxide chemistry." en. In: *Science* 371.6524 (Jan. 2021), pp. 46–51. DOI: https://doi.org/10.1126/science.abb9554 (cit. on p. 40).

[130] S. Thomas, N. Birbilis, M.S. Venkatraman, and I.S. Cole. "Self-repairing oxides to protect zinc: Review, discussion and prospects." en. In: *Corrosion Science* 69 (Apr. 2013), pp. 11–22 (cit. on p. 33).

[131] Vladimir Naumovich Vapnik. *The nature of statistical learning theory*. en. 2nd ed. Statistics for engineering and information science. New York: Springer, 2000 (cit. on p. 75).

[132] VuMA and Statista. *Anzahl der Smartphone-Nutzer in Deutschland in den Jahren 2009 bis 2020 (in Millionen)*. 2020. URL: https://de.statista.com/statistik/daten/studie/198959/umfrage/anzahl-der-smartphonenutzer-in-deutschland-seit-2010/ (visited on 03/16/2021) (cit. on p. 8).

[133] Keliang Wang, Pucheng Pei, Yichun Wang, Cheng Liao, Wei Wang, and Shangwei Huang. "Advanced rechargeable zinc-air battery with parameter optimization." In: *Applied Energy* 225 (2018), pp. 848–856. DOI: https://doi.org/10.1016/j.apenergy.2018.05.071. URL: https://www.sciencedirect.com/science/article/pii/S0306261918307906 (cit. on p. 33).

[134] E. Warburg. "Ueber das Verhalten sogenannter unpolarisirbarer Elektroden gegen Wechselstrom." de. In: *Annalen der Physik und Chemie* 303.3 (1899), pp. 493–499. DOI: 10.1002/andp.18993030302. URL: http://doi.wiley.com/10.1002/andp.18993030302 (visited on 07/22/2019) (cit. on p. 137).

[135] John T. Warner. "Chapter 4 - Overview and comparison of different lithium-ion chemistries." In: *Lithium-Ion Battery Chemistries*. Ed. by John T. Warner. Elsevier, 2019, pp. 79–97. DOI: 10.1016/B978-0-12-814778-8.00004-1. URL: https://www.sciencedirect.com/science/article/pii/B9780128147788000041 (cit. on p. 29).

[136] B.M. Wilamowski. "Neural network architectures and learning." en. In: *IEEE International Conference on Industrial Technology, 2003*. Maribor, Slovenia: IEEE, 2003, TU1–T12. DOI: 10.1109/ICIT.2003.1290197. URL: http://ieeexplore.ieee.org/document/1290197/ (visited on 01/04/2021) (cit. on pp. 68, 70, 72, 74).

[137] Martin Winter, Brian Barnett, and Kang Xu. "Before Li Ion Batteries." en. In: *Chemical Reviews* 118.23 (Dec. 2018), pp. 11433–11456. DOI: 10.1021/acs.chemrev.8b00422. URL: https://pubs.acs.org/doi/10.1021/acs.chemrev.8b00422 (visited on 06/18/2021) (cit. on pp. 28, 30).

[138] Martin Wünsch. *Separation der Kathodenalterung in Lithium-Ionen-Batteriezellen mittels elektrochemischer Impedanzspektroskopie*. de. Vol. 134. Aachener Beiträge des ISEA. Nov. 2019 (cit. on p. 67).

[139] X. Gregory Zhang. "Fibrous zinc anodes for high power batteries." en. In: *Journal of Power Sources* 163.1 (2006), pp. 591–597 (cit. on pp. 37, 38).

[140] X.G. Zhang. "SECONDARY BATTERIES – ZINC SYSTEMS | Zinc Electrodes: Overview." en. In: *Encyclopedia of Electrochemical Power Sources* (2009), pp. 454–468 (cit. on p. 37).